Thomas Røste

Monitoring overburden and reservoir changes from prestack time-lapse seismic data - applications to chalk fields

Thesis for the degree doktor ingeniør

Trondheim, March 2007

Norwegian University of Science and Technology
Faculty of Engineering Science and Technology
Department of Petroleum Engineering and Applied Geophysics

NTNU
Innovation and Creativity

NTNU
Norwegian University of Science and Technology

Thesis for the degree doktor ingeniør

Faculty of Natural Sciences and Technology
Department of Petroleum Engineering and
Applied Geophysics

ISBN 978-82-471-0797-3 (printed version)
ISBN 978-82-471-0802-4 (electronic version)
ISSN 1503-8181

Doctoral theses at NTNU, 2007:37

Printed by NTNU-trykk

Abstract

Reservoir compaction due to hydrocarbon production has been observed in several North Sea reservoirs, especially the chalk reservoirs in the southern part. This compaction leads to changes in porosity and permeabilities which have implications for production and the production performance. In addition, reservoir compaction is often associated with stretching and arching of the overburden rocks and subsidence of the sea bed. The change in geomechanical stress state for the overburden rocks might cause damage in existing wells. It is therefore of significant importance to monitor these changes during production not only for the reservoir itself but also for the overburden rocks. This information can be obtained from well logs; however, wells in most reservoirs are sparse and widely spread, making time-lapse seismic data an important complementary tool.

Since compaction and stretching cause changes in both layer thickness as well as seismic velocities, it is crucial to develop methods to distinguish between the two effects. A new method based on detailed analysis of prestack time-lapse seismic data is introduced to discriminate between layer thickness and velocity changes. A key parameter in this discrimination process is the dilation factor, α, which is the relative velocity change divided by the relative thickness change within a given layer. This method incorporates lateral variations in relative velocity changes by utilizing zero-offset and offset-dependent time shifts.

Monitoring fault movements is important to avoid the complications associated with wells crossing faults that might be reactivated due to reservoir production. In addition, reactivation of overburden faults near the reservoir zone might lead to leakage of hydrocarbons and affect the reservoir drainage patterns. This thesis shows that growing faults can be obtained from prestack time-lapse seismic data. A growing fault tip appears as a distortion pattern with characteristic time shift versus offset signatures. From raypath considerations and modeling, the position and vertical extent of a distortion zone can be determined. The distortion patterns disappear if the time-lapse data is stacked, meaning that prestack data contains crucial information. The correlation between a time-lapse distortion zone and a growing fault tip is investigated on high quality prestack time-lapse seismic ocean bottom cable (OBC) data from the Valhall Field. A compacting reservoir zone

exists directly beneath this fault tip, validating that a growing fault might cause the observed anomalies. Growing faults complicate the interpretation of time-lapse data since large vertical (in addition to lateral) variations in thickness and velocity changes occur. This thesis presents an extended method to estimate the dilation factor (α) in such cases. This method can be viewed as a simplified version of time-lapse tomography, but involving fewer unknown parameters, giving more stability to the estimated changes in thickness and velocity. In addition, the presented method is faster and cheaper than a full tomographic method.

In many reservoirs, 30-40% of the oil reserves remain unproduced. To identify undrained areas and detect drainage patterns, it is crucial to monitor the reservoir changes during production. Reservoir monitoring leads to saved costs due to reduced number of misplaced wells and increased production because of optimized well planning. From time-lapse amplitude variation with offset (AVO) analysis, it is possible to estimate reservoir pressure and saturation changes. This thesis introduces a new method which also includes compacting reservoirs. This is initially a three-parameter problem, including pressure and saturation changes and compaction. However, from laboratory measurements, the reservoir compaction is related to the pressure and saturation changes. Using an empirical relation between porosity, saturation, and pressure changes, the problem is reduced to involve only the pressure and saturation changes, which can be solved from time-lapse AVO analysis.

Acknowledgments

I am forever grateful to my supervisor, Professor Martin Landrø, for all help and recommendation. His knowledge and experience has been of great inspiration. Together with good humor, he has encouraged and motivated me during the thesis writing.

Acknowledgments go to TOTAL for financial support, and Jerome Guilbot, Yahui Yin, and Ruben Sanchez for valuable discussions. I also want to thank the people at TOTAL for several pleasant stays at TOTAL, Pau and TOTAL, Stavanger. Alan Burns, Ottar Minsaas, Ole J. Nydal, Hilde Skeie, and Jon Kleppe are acknowledged for interesting meetings between TOTAL and NTNU.

I want to thank Shell, Rijswijk, as well as Paul Hatchell and Peter Wills, for all effort and support spent to make the article given in chapter 4 possible. The help and discussions with the people at Shell, Rijswijk have been very useful, and the collaboration with Paul Hatchell will be remembered.

The Valhall partnership (BP Norge AS, Amerada Hess Norge AS, A/S Norske Shell and Total E&P Norge AS) are acknowledged for permission to publish the articles given in chapters 3 and 4, as well as Ole Jøran Askim, Olav Barkved, and Tron G. Kristiansen for support and discussions.

Thanks to post doc. Alexey Stovas for fruitful discussions and for the collaboration during the work of the article given in chapter 3. Thanks to Øyvind Kvam for advises in the first years of my thesis work and for help regarding finite difference modeling. All my friends and colleagues at the Department of Petroleum Engineering and Applied Geophysics are acknowledged for support and discussions, not only related to this thesis, but also for topics which made life easier through 4 years of hard work. I will particularly mention Ørjan Pedersen, Tor Erik Rabben, Sverre Johnsen, Christian Crescente, Sissel Martinsen, Egil Tjåland, Janniche Nordskag, Andre Strupstad, Alf Lackner, Olve Rasmussen, Amir Ghaderi, Rune Holt, Kenneth Duffaut, and Andreas Evensen.

I acknowledge inspiration from all speed skating friends, especially Arne-Kjell Fold-

vik for his enthusiasm regarding this thesis.

I want to thank my parents for all support and encouragement through many years of study. This work has been impossible without them.

Special thanks go to my girlfriend, Tone, for her patience during my travels abroad and late night working. She always motivated me not to give up, even in the difficult periods where an ending of this thesis seemed impossible.

Contents

Chapter 1

Thesis Introduction

Monitoring reservoir and overburden changes during hydrocarbon production is important to identify undrained areas and for planning placement of wells. Repeated (time-lapse) seismic data is important to obtain this information. The objective of this thesis is to improve the understanding of time-lapse seismic data analysis of compacting hydrocarbon fields. I introduce new methods based on prestack time-lapse seismic data analysis to monitor production-induced reservoir changes and associated overburden changes. Production-induced compaction of reservoir rocks has been observed in several North Sea reservoirs, especially chalk reservoirs like Valhall and Ekofisk (in the southern part of the North Sea). Reservoir compaction leads to changes in porosity and permeabilities which have implications for production and the production performance. In addition, reservoir compaction is often associated with stretching of the overburden rocks. The change in geomechanical stress state for the overburden rocks might lead to damage in existing wells. It is therefore of great interest to the industry to monitor both overburden and reservoir changes during production.

1.1 Motivation for the thesis

Reservoirs producing oil or gas are subjected to pore pressure depletion. This creates changes in the stress and strain fields of the rock material both inside and outside the reservoir. For reservoir rocks with high compressibility, such as chalks and unconsolidated sands, pressure depletion leads to compaction, which has implications for production by changing permeabilities and, hence, the production performance (Hall et al., 2005).

Reservoir compaction due to hydrocarbon production has been observed in several North Sea reservoirs, especially the chalk reservoirs in the southern part. Guilbot and Smith (2002) utilized time isochron differences from 4D seismic data to detect compaction and subsidence at the Ekofisk Field. They observed seismic time shifts

up to 12-16 ms between 1989 and 1999, related to compaction values of up to 6 m for the reservoir chalk formation.

In many reservoirs, compaction of the reservoir rocks represents the major drive mechanism. Significant volumes of produced hydrocarbons may be credited to this effect. However, compaction may also lead to subsidence of the sea bed. At the Valhall Field, Barkved and Kristiansen (2005) report a maximum subsidence of the sea bed larger than 5.4 m (since the field came on production in 1982) and increasing by 0.25 m per year. At the Ekofisk Field, the extensive compaction resulted in sea bed subsidence of nearly 8 m by 2000 (Chin and Nagel, 2004). It is typical for these fields that the sea bed subsidence is less than the corresponding reservoir compaction, meaning that the overburden rocks are stretched. Often the change in geomechanical stress state for the overburden rocks leads to damage in existing wells (especially when significant shear stresses are introduced as a byproduct of the reservoir compaction). It is therefore of importance to map the velocity and thickness changes during production not only for the reservoir itself, but also for the overburden rocks. Time-lapse seismic data can be utilized to obtain this information.

Reservoir compaction may also lead to movements of faults. Several authors (Ewing, 1985; White and Morton, 1997; Morton et al., 2006) discuss the coupling between reservoir compaction and slip along growth faults that become active when sufficiently large volumes of fluid (oil, gas, or formation water) are produced. Reynolds et al. (2003) determined the relative attendant risk of reactivation of faults in the Bight Basin by evaluating the in situ stress field. Mildren et al. (2002) studied reactivation of faults by using the FAST (Fault Analysis Seal Technology) technique. Monitoring fault movements is important for several reasons. Reactivation of faults might lead to leakage of hydrocarbons and affect the reservoir drainage patterns. Fault seal breach in the North Sea (Gaarenstroom et al., 1993), the Penola Through (Jones et al., 2000), and the Gulf of Mexico (Finkbeiner et al., 2001) have been related to faulting and fracturing associated with the in situ stress. Based on seismic data and wellbore information, Allan diagrams (Allan, 1989) are often used to identify potential petroleum leak points along a fault strike. In addition to leakage of hydrocarbons, hazards are associated with wells crossing reactivated faults (Alsos et al., 2002). Barkved et al. (2003) report a strong correlation between overburden faults and drilling problems at the Valhall Field. Maury et al. (1992) discuss further how slipping faults can pose serious problems in the field since it may cause casing failure. Reactivated faults can also have close relationship with earthquakes. Zoback and Zinke (2002) recorded numerous microearthquakes at the Valhall Field during a six week monitoring period. They found the microearthquakes consistent with a normal faulting stress regime.

Monitoring reservoir and overburden layer changes and movements of faults is therefore important, and the combined use of time-lapse seismic data and geomechanical knowledge is expected to be important in future monitoring projects.

1.2 Linking geomechanics and time-lapse seismic

Several authors (Rhett, 1998; Chin et al., 2002; Vikram and Settari, 2005) have created geomechanical and fluid flow models of compacting reservoirs based on laboratory studies of reservoir rocks. Minkoff et al. (2004) try to predict production in compacting reservoirs by linking geomechanics and flow models with time-lapse seismic. Hatchell et al. (2005) and Vidal et al. (2002) try to integrate time-lapse seismic and geomechanics to characterize reservoir changes. Hatchell and Bourne (2005a) constructed forward models of time-lapse time shifts from stress and strain fields using geomechanical models and a stress/strain-dependent seismic velocity. They found that a simple linear model relating seismic velocity with vertical normal strain works well for several locations around the world.

It is important to notice that time-lapse time shifts capture the combined effects of velocity and thickness changes within a given layer. For a layer undergoing thickness changes, the seismic velocity is altered by the changes in the stress and strain fields. For a layer of thickness, z, I express the relative time shift in terms of the relative thickness change and velocity change as (Landrø and Stammeijer, 2004; Hatchell and Bourne, 2005b; Røste et al., 2005)

$$\frac{\Delta T_0}{T_0} \approx \frac{\Delta z}{z} - \frac{\Delta v}{v}, \tag{1.1}$$

where T_0 represents seismic two-way vertical traveltime within the layer and v is the layer velocity. The notations ΔT_0, Δz, and Δv represent changes in vertical two-way traveltime, thickness, and velocity, respectively. (Note that the relative thickness change $\Delta z/z$ is identical to the average vertical strain ϵ_{zz} over the layer.) A major challenge for quantitative time-lapse analysis is to discriminate between thickness changes and velocity changes for both the reservoir section and the overburden. Landrø and Janssen (2002) presented a method utilizing near and far offset traveltime shifts to perform this discrimination procedure.

As a first order approximation for a relation between relative thickness and velocity changes for a given subsurface layer it might be reasonable to assume that the two changes are proportional to each other:

$$\frac{\Delta v}{v} \approx \alpha \frac{\Delta z}{z}, \tag{1.2}$$

where the "dilation factor" $\alpha < 0$ is a parameter dependent on the rock properties of the layer. This is a crucial parameter, since it determines the ratio between velocity and thickness changes. The knowledge of the dilation factor from a rock physics point of view is limited; there are no measurements available to my knowledge. I do not know if the dilation factor is the same for compaction and stretching of a rock. Furthermore, the dilation factor might also be dependent on the magnitude of the relative thickness change. Despite these concerns, I find it fruitful to introduce the dilation factor, since it captures the important relation between velocity and thickness changes. Furthermore, as later shown in section 2.4, the dilation factor can easily be determined from empirical porosity-velocity relations, e.g. given by Mavko et al. (1998).

1.3 Reservoir changes and time-lapse seismic

Hydrocarbon production will cause pore pressure and fluid saturation changes. Both pressure and saturation changes might influence time-lapse seismic data (Landrø, 1999), and it is often difficult to separate the two effects based on stacked PP time-lapse data only. In many time-lapse seismic studies, seismic differences between a baseline and a monitor survey are analyzed as either a pressure effect (Watts et al., 1996) or a fluid effect (Landrø et al., 1999; Gabriels et al., 1999). However, for some fields or segments within the field, both fluid and pressure changes have approximately the same degree of impact on the seismic data. In such cases the use of time-lapse amplitude variation with offset (AVO) analysis (see Tura and Lumley, 1998, 1999a; Landrø, 1999; Landrø, 2001) or time-lapse PP- and PS-reflectivity stacks (see Landrø et al., 2003; Stovas et al., 2003) offer an opportunity to discriminate between the two effects. However, these methods do not include reservoir compaction; that is, porosity changes are neglected. Modifications are therefore needed for reservoirs where production or water injection induces porosity changes.

At first, one might assume that changes in saturation, pressure, and porosity are three independent parameters. However, from laboratory measurements of chalk Sylte et al. (1999) found that porosity changes are related to saturation and pressure changes; that is, the pressure changes might induce fractures and compaction of the weak chalk matrix, while water has a weakening effect on chalk. The relation between porosity changes ($\Delta\phi$), saturation changes (ΔS_w), and effective stress changes ($\Delta\sigma$) can be given as (Sylte et al., 1999)

$$\Delta\phi = \frac{\partial\phi}{\partial\sigma}\Delta\sigma + \frac{\partial\phi}{\partial S_w}\Delta S_w, \tag{1.3}$$

where $\partial\phi/\partial\sigma$ and $\partial\phi/\partial S_w$ are partial differentiations of the porosity with respect to stress and water saturation, respectively.

In addition to reservoir stress and saturation changes, time-lapse seismic data might be influenced by other effects, such as changes in temperature. Variations in reservoir temperature are usually small. However, cases where temperature changes might occur are when steam (temperature around 300°C) is injected in a shallow reservoir with temperature between 10-30°C (e.g. the Duri Field, Jenkins et al., 1997), or when cold sea water (temperature 0-15°C) is injected into deeper reservoirs with temperature 70-90°C (Jack, 1997). Such temperature changes might change both velocity and density (Mavko et al., 1998; Batzle and Wang, 1992).

1.4 The Valhall Field

The methods proposed in this thesis are mainly tested on prestack time-lapse seismic data from the Valhall Field, situated in the southern part of the Norwegian North Sea (see Figure 1.1). The Valhall Field is an over-pressured Late Cretaceous chalk reservoir. The field was discovered in 1975 (after exploration drilling in the

Figure 1.1: Location of the Valhall Field in the Norwegian sector of the North Sea (Barkved et al., 2003).

period 1969-1974) and started producing in October 1982. Daily production is on the order of 100 000 barrels of light oil (Barkved and Kristiansen, 2005). The reservoir layer is at depth 2500 m and ranges in thickness from 0-70 m. Porosity is 35-50% and matrix permeability is generally low, less than 10 mD. Palaeocene shale provides the cap rock. The water depth is 70 m.

The expected recovery rate in 1982 was 14%, a figure which has now increased to 40% (Barkved and Kristiansen, 2005). Time-lapse seismic monitoring with high quality in addition to improved methods to interpret and utilize the seismic might increase the recovery further. The seismic response is very sensitive to production-induced features (such as reservoir compaction, depletion, stretched overburden layers, and seabed subsidence). This was first demonstrated by marine streamer data, acquired in 1992 and 2002. Figure 1.2 shows time-lapse seismic data from the south-east part of the Valhall Field (from 1992 and 2002). Large pull-down effects

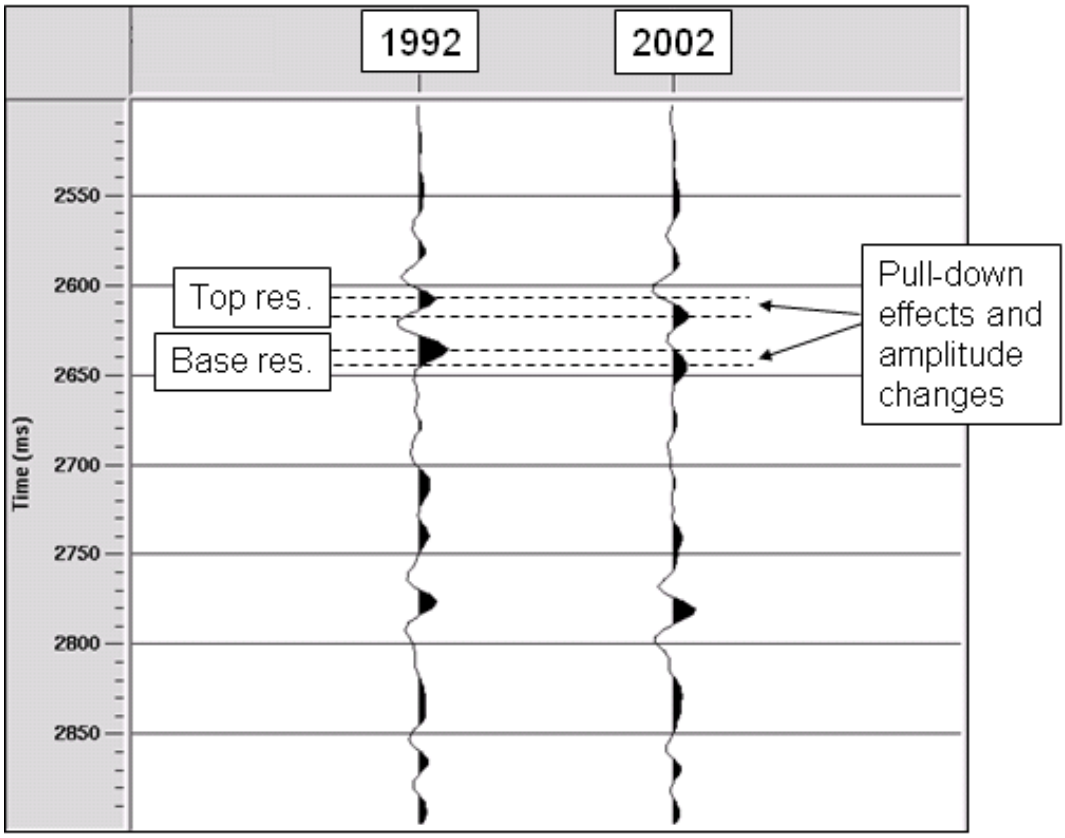

Figure 1.2: Time-lapse seismic data from the south-east part of the Valhall Field, acquired in 1992 and 2002. Large time shifts and amplitude changes are observed near the reservoir zone.

and amplitude changes are observed at the top and base of the reservoir layer. The time-lapse seismic effects are mainly due to compaction of the reservoir (induced by the pore pressure decrease and fluid saturation changes during hydrocarbon production).

In 2003, a permanent ocean bottom cable (OBC) array was installed at the Valhall Field, initiating the "Life of Field Seismic" (LoFS) program which includes a series of 3D OBC surveys. The first survey was acquired from September to November 2003 with subsequent surveys acquired in intervals of approximately 4 months. Results from the earliest surveys confirm that the system can provide high quality data with good repeatability (Kommedal et al., 2004; Barkved, 2004).

In January 2004, water injection started in the center of the field. Field and lab observations indicate that water has a weakening effect on the reservoir chalk. For the Ekofisk chalk field, this water-weakening phenomenon became the primary mechanism for reservoir compaction in 1993, 6 years after the start of water injection (Sylte et al., 1999). Reservoir compaction due to water weakening is also expected at the Valhall Field.

1.5 Thesis content

The thesis contains 7 chapters, including this introduction. The chapters 3, 4, and 6 represent independent papers.

This introductory chapter 1 states the motivation for the thesis. The challenges regarding geomechanical changes during hydrocarbon production are mentioned. Also included is a short description of the Valhall Field.

Chapter 2 contains background theory, including a derivation of the wave equation. Several rock physics models are discussed. By assuming uniaxial stress-strain relations, the dilation factor α is determined based on porosity-velocity relations.

Chapter 3 introduces a new method which discriminates between velocity and thickness changes of stretched or compacted rocks. The method is based on detailed analysis of time-lapse prestack seismic data, and incorporates lateral variations in (relative) velocity changes by utilizing zero-offset and offset-dependent time shifts. The method is tested on a 2D synthetic model that undergoes severe reservoir compaction as well as stretching of the overburden rocks. Finally, the method is utilized to analyze a real 2D prestack time-lapse seismic line from the Valhall Field, acquired in 1992 and 2002. The authors of this paper are T. Røste, A. Stovas, and M. Landrø. The paper was published in the November-December 2006 issue of

Geophysics (Røste et al., 2006). The work has been presented at the 67th EAGE Conference & Exhibition in Madrid, Spain, June 2005, at the ROSE meeting in Trondheim, Norway, June 2005, and at the FORCE seminar in Stavanger, Norway, September 2005.

In chapter 4, time-lapse changes are investigated on prestack time-lapse seismic ocean bottom cable (OBC) data from LoFS survey 1 and survey 3. The OBC recording system provides data with high quality and good repeatability. By utilizing the method introduced in chapter 3, changes in thickness and velocity are estimated for a sequence from the sea bed to the top reservoir horizon. In addition, time-lapse time shift distortion patterns that move systematically with offset are observed. We show that one of the distortion zones (observed between LoFS survey 1 and 3) correlates with buried faults, indicating that a (time-lapse) distortion zone might be produced by a localized slip in a fault zone. An extended method is introduced to describe such positions. The authors of this paper are T. Røste, M. Landrø, and P. Hatchell. The paper was submitted to Geophysical Journal International in May 2006 and accepted for publication in January 2007. In April 2006, the paper was presented at the ROSE meeting in Trondheim, Norway and in January 2007, an expanded abstract was submitted to the 69th EAGE Conference & Exhibition.

The time-lapse discrimination method discussed in chapters 3 and 4 is developed for isotropic cases. However, the earth is most probably anisotropic, and an isotropic case is only a simplified description of the earth. Chapter 5 describes an extended discrimination method which accounts for time-lapse anisotropy changes. Approximations regarding the included anisotropy were necessary to avoid large, complex terms. The method is tested on synthetic anisotropic models undergoing different scenarios of thickness, velocity, and anisotropy changes. Compared with the isotropic method, the proposed method produces better results for the anisotropic time-lapse datasets. For cases with static anisotropy, the derived method becomes identical to the isotropic method.

Chapter 6 introduces a method which discriminates between pressure and fluid saturation changes in compacting reservoirs. The proposed method is based on time-lapse amplitude variation with offset (AVO) analysis. Based on laboratory measurements, the reservoir compaction (or porosity loss) is related to the pressure and saturation changes. By using this empirical relation, explicit expressions for computing pressure- and saturation-related changes from time-lapse seismic data are obtained. The method is tested on synthetic models with different production scenarios. The authors of this paper are T. Røste and M. Landrø. In January 2007, an expanded abstract of this work was submitted to the 69th EAGE Conference & Exhibition.

Finally, chapter 7 completes the thesis with closing remarks.

Chapter 2

Background theory

2.1 The wave equation

Seismic sound waves can be viewed as subsurface disturbances that propagate with velocities given by the elastic stiffness and the density of the rock. Seismic waves induce elastic deformation along the propagation path in the subsurface. The equation of wave propagation in elastic solids is derived by using Hooke's law and Newton's second law of motion. Most rocks have an ability to resist and recover from the deformations produced by forces. This ability is called elasticity. When an elastic material is subjected to stresses, changes in shape and dimensions occur. These changes are referred to as strains. Fjær et al. (1992) evaluate in detail how rock materials respond to a dynamic, time harmonic external stress (or strain).

Strain is defined as the relative change in a dimension or shape of a body. It is common to discriminate between normal strains, shearing strains, and rotations. Normal strains are related to volumetric changes, shearing strains are related to angular deformations, and rotations occur without any deformations. Adding together the normal strains in the x-, y-, and z-direction of a Cartesian coordinate system, gives the relative change in volume, Δ (Sheriff and Geldart, 1995):

$$\Delta = \epsilon_{xx} + \epsilon_{yy} + \epsilon_{zz}, \tag{2.1}$$

where ϵ_{xx}, ϵ_{yy}, and ϵ_{zz} denote the relative change in length in x-, y-, and z-direction (respectively) of the material.

Hooke's law states that for small volumetric changes, a given strain is directly proportional to the stress producing it. The strains involved in seismic waves are usually less than 10^{-8} (except very near the source), which validates the use of Hooke's law. When several stresses exist, each produces strains independently of the others. This means that each strain is a linear function of all of the stresses and vice versa. In general, Hooke's law leads to complicated relations between

strain and stress. But for an isotropic medium, Hooke's law can be expressed in the following relatively simple form (Love, 1944; Timoshenko and Goodier, 1934):

$$\sigma_{ii} = \lambda\Delta + 2\mu\epsilon_{ii}, \quad i = x, y, z, \tag{2.2}$$

$$\sigma_{ij} = 2\mu\epsilon_{ij}, \quad i, j = x, y, z; i \neq j, \tag{2.3}$$

where the parameters λ and μ (Lame's constants) denote elastic stiffness and shear modulus, respectively. Equations (2.2) and (2.3) represent the stress-strain relations for normal components and shear components, respectively, and are often expressed as a matrix equation, $\boldsymbol{\sigma} = \boldsymbol{C\epsilon}$:

$$\begin{bmatrix} \sigma_{xx} \\ \sigma_{yy} \\ \sigma_{zz} \\ \sigma_{xy} \\ \sigma_{yz} \\ \sigma_{zx} \end{bmatrix} = \begin{bmatrix} \lambda+2\mu & \lambda & \lambda & 0 & 0 & 0 \\ \lambda & \lambda+2\mu & \lambda & 0 & 0 & 0 \\ \lambda & \lambda & \lambda+2\mu & 0 & 0 & 0 \\ 0 & 0 & 0 & \mu & 0 & 0 \\ 0 & 0 & 0 & 0 & \mu & 0 \\ 0 & 0 & 0 & 0 & 0 & \mu \end{bmatrix} \begin{bmatrix} \epsilon_{xx} \\ \epsilon_{yy} \\ \epsilon_{zz} \\ \epsilon_{xy} \\ \epsilon_{yz} \\ \epsilon_{zx} \end{bmatrix}. \tag{2.4}$$

Acoustic wave propagation can be described by Newton's second law of motion. The unbalanced force acting on a small volume element of rock equals the mass times the acceleration. In the x-direction, this gives the equation of motion on the following form:

$$\rho\frac{\partial^2 u}{\partial t^2} = \frac{\partial\sigma_{xx}}{\partial x} + \frac{\partial\sigma_{xy}}{\partial y} + \frac{\partial\sigma_{xz}}{\partial z}, \tag{2.5}$$

where u is the particle displacement in the x-direction, ρ is the density, and t denotes time. Substituting Hooke's law into equation (2.5) gives an equation expressing the displacement (in x-direction) in terms of strains (e.g. Sheriff and Geldart, 1995):

$$\rho\frac{\partial^2 u}{\partial t^2} = (\lambda+\mu)\frac{\partial\Delta}{\partial x} + \mu\nabla^2 u, \tag{2.6}$$

where $\nabla^2 u$ is the Laplacian of u; that is, $\nabla^2 u = \partial^2 u/\partial x^2 + \partial^2 u/\partial y^2 + \partial^2 u/\partial z^2$. Similar equations can be found for the motion along the y- and z-axis. Adding together the equations for motion in x-, y-, and z-direction gives the well-known wave equation:

$$\rho\frac{\partial^2\Delta}{\partial t^2} = (\lambda+2\mu)\nabla^2\Delta. \tag{2.7}$$

The Lame constant λ can be related to other elastic constants, e.g. $\lambda = K - \frac{2}{3}\mu$, where K and μ denote bulk and shear moduli, respectively. Using this relation gives the wave equation on following form:

$$\rho\frac{\partial^2\Delta}{\partial t^2} = (K + \frac{4}{3}\mu)\nabla^2\Delta, \tag{2.8}$$

which is the most common representation. If the wave propagation is parallel to the displacement u; that is, a longitudinal (or compressional) wave, equation (2.8) reduces to

$$v_P = \sqrt{\frac{K + \frac{4}{3}\mu}{\rho}}, \tag{2.9}$$

where v_P denotes the velocity of a compressional or primary wave. For a mode of motion in which the particles are displaced only in the x-direction, and the wave propagation is only in the y-direction, equation (2.8) becomes

$$v_S = \sqrt{\frac{\mu}{\rho}}. \tag{2.10}$$

The subscript S denotes that this is a shear wave. The combined particle and wave motion of compressional and shear waves are illustrated in Figure 2.1. Equations (2.9) and (2.10) show that v_P is always larger than v_S. For a fluid media

$$v_P = \sqrt{\frac{K}{\rho}}, \quad v_S = 0, \tag{2.11}$$

since no shear forces exist.

The relation between velocity (v_P or v_S), elastic moduli (K, μ), and density (ρ) appears to be straightforward from equations (2.9) and (2.10). However, this is not the case since K, μ, and ρ are also related to other characteristics of the rock.

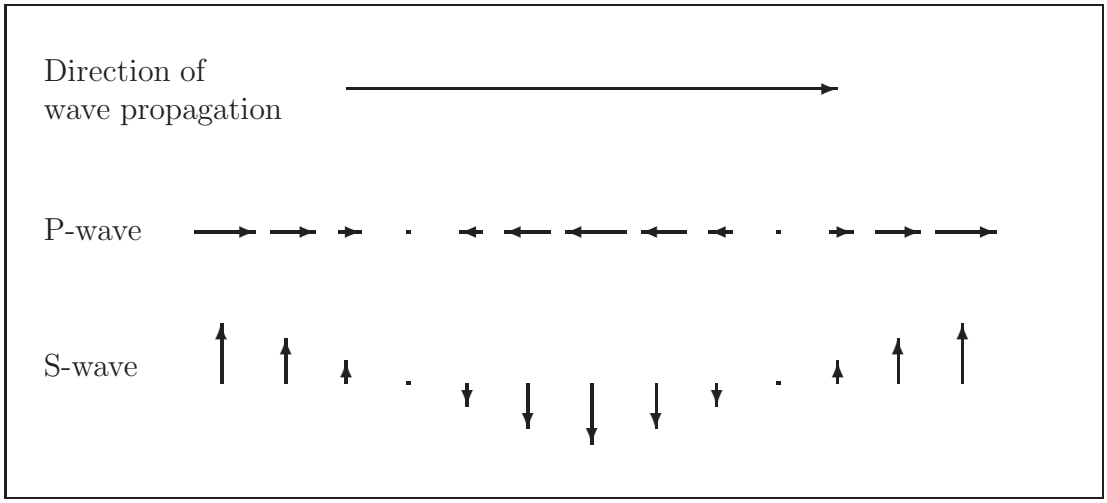

Figure 2.1: Particle motion of P-wave and S-wave propagation (slightly modified from Fjær et al., 1992).

These characteristics may be material and structure of the rock, type or lithology, porosity, degree of fluid saturation, pressure, depth, cementation, degree of compaction, etc. The most notable inhomogeneity of sedimentary rocks is that they are porous and filled with fluid. Wang and Nur (1992) discuss theories relating seismic velocity to the composition of rocks.

2.2 Sedimentary rocks

Sedimentary rocks (sandstones, limestones, shales, etc.) can be considered as packed grains. The space between the grains is called the pore space. This pore space is filled with fluid; that is, oil, water, or gas. Pore pressure is the fluid pressure in the pore space. For a case with perfect communication between the pores, the pore pressure is equal to the hydrostatic pressure caused by the weight of the fluid. The pore pressure at depth z can then be expressed as

$$p_f(z) = \int_{z_0}^{z} \rho_f(z) g z dz + p_f(z_0), \tag{2.12}$$

where $\rho_f(z)$ is the fluid density at depth z and g is the gravitational constant. The pressure at depth z_0, denoted $p_f(z_0)$, is usually the atmospheric pressure. Hydrostatic pressure is often referred to as normal pressure conditions. Rocks that deviate from the hydrostatic pressure are either called overpressured or underpressured, depending on whether the pressure is greater or less than the normal pressure.

The overburden pressure is defined as the combined weight of sediments and fluid overlying a formation:

$$P(z) = \int_{z_0}^{z} \rho(z) g z dz, \tag{2.13}$$

where

$$\rho(z) = \phi(z)\rho_f + (1 - \phi(z))\rho_S. \tag{2.14}$$

The parameters ρ_f and ρ_S denote the fluid and solid densities and ϕ is the porosity. The difference between the pore fluid pressure (p_f) and the overburden pressure (P) is called the effective stress (σ):

$$\sigma = P - \eta p_f, \tag{2.15}$$

where η is the Biot coefficient. For static compression of the rock frame, the Biot coefficient is defined as (Mavko et al., 1998)

$$\eta = 1 - \frac{K_{fr}}{K_S}, \tag{2.16}$$

where K_{fr} and K_S are the bulk and solid moduli of the frame, respectively. For soft materials, $\eta \approx 1$.

2.3 Rock physics models

Rock physics models that relate velocity and impedance to porosity and mineralogy form a critical part of seismic analysis for porosity and lithofacies. Illustrations of velocity-porosity relations are given by Mavko et al. (1998) and Avseth et al. (2005).

2.3.1 A pack of uniform spheres

The simplest rock model consists of identical spheres arranged in a cubic pattern. The porosity of such a model is 0.48 (that is, $1 - \pi/6$) and the average density can be estimated to $\pi/6$ times the density of the material of the spheres. Based on Timoshenko and Goodier (1951), the effective elastic modulus K can be related to the compressive pressure and elastic constants of the spheres.

Gassmann (1951) calculated the velocity for a hexagonal packing of identical spheres under a pressure produced by the overburden spheres. The cubic and hexagonal packed spheres give the same variation of velocity with depth. This velocity variation with depth is also consistent with Faust (1953), which found an empirical formula for velocity in terms of depth of burial and formation resistivity. However, individual measurements of the velocity at a given depth deviate largely between these formulas. This is due to the fact that the porosity estimations are inaccurate (Sheriff and Geldart, 1995).

Random packs of well-sorted particles have porosities in the range of 0.4-0.5, but under pressure, the particles deform at the points of contact, and as a result the density increases and the porosity decreases. Clearly, porosity is an important factor controlling velocities. In addition, the velocity is dependent of fluid in the pores, which affect the density as well as the effective elasticity of the rock.

2.3.2 Velocity-porosity relations with bounds

A useful velocity-porosity relation can be provided by upper and lower bounds on the elastic moduli of rocks. Specifying the volume fractions of the constituents and their elastic moduli, without any geometric details of their arrangement, it is possible to predict the upper and lower bounds on the moduli and velocities of the composite rock.

The simplest bounds are the Voigt (1910) and Reuss (1929) bounds. The Voigt upper bound on the effective elastic modulus M_V of a mixture of N material phases

is given as (Mavko et al., 1998)

$$M_V = \sum_{i=1}^{N} f_i M_i, \tag{2.17}$$

where f_i and M_i are the volume fraction and elastic modulus, respectively, of the i-th constituent. The Voigt upper bound (also called isostrain average) represents the elastically stiffest rock that nature can put together. The Reuss lower bound (also called isostress average) of the effective elastic modulus M_R is

$$\frac{1}{M_R} = \sum_{i=1}^{N} \frac{f_i}{M_i}, \tag{2.18}$$

which represents the elastically softest rock that nature can put together. The variable M in the Voigt and Reuss formulas can represent any modulus. However, it is most common to compute Voigt and Reuss averages of the bulk modulus $M = K$ and shear modulus $M = \mu$. Figure 2.2 shows an illustration of Voigt and Reuss bounds for the bulk modulus K for a mixture of two constituents. The constituents might be two different minerals or a mineral plus fluid (water, oil, or gas). A well-known example where the Reuss model gives a correct prediction is a suspension of particles in a fluid. The undrained bulk modulus K of the suspension is given by

$$\frac{1}{K} = \frac{\phi}{K_{fluid}} + \frac{1-\phi}{K_{solid}}, \tag{2.19}$$

where K_{fluid} and K_{solid} are the bulk moduli of the fluid and the solid mineral material, respectively, and ϕ is the porosity. Equation (2.19) is also known as Wood's (1941) equation.

The best bounds, in the sense of giving the narrowest possible range of elastic moduli without specifying anything about the geometries of the constituents, are the Hashin-Shtrikman bounds (Hashin and Shtrikman, 1963). For a mixture of two constituents, the Hashin and Shtrikman bounds are given by (Mavko et al., 1998)

$$K^{HS\pm} = K_1 + \frac{f_2}{(K_2 - K_1)^{-1} + f_1(K_1 + \frac{4}{3}\mu_1)^{-1}}, \tag{2.20}$$

$$\mu^{HS\pm} = \mu_1 + \frac{f_2}{(\mu_2 - \mu_1)^{-1} + \frac{2f_1(K_1+2\mu_1)}{5\mu_1(K_1+\frac{4}{3}\mu_1)}}, \tag{2.21}$$

where the two individual phases of the bulk modulus K, shear modulus μ, and volume fractions f are denoted with subscripts 1 and 2. Upper and lower bounds are computed by interchanging which material is subscripted 1 and which is subscripted

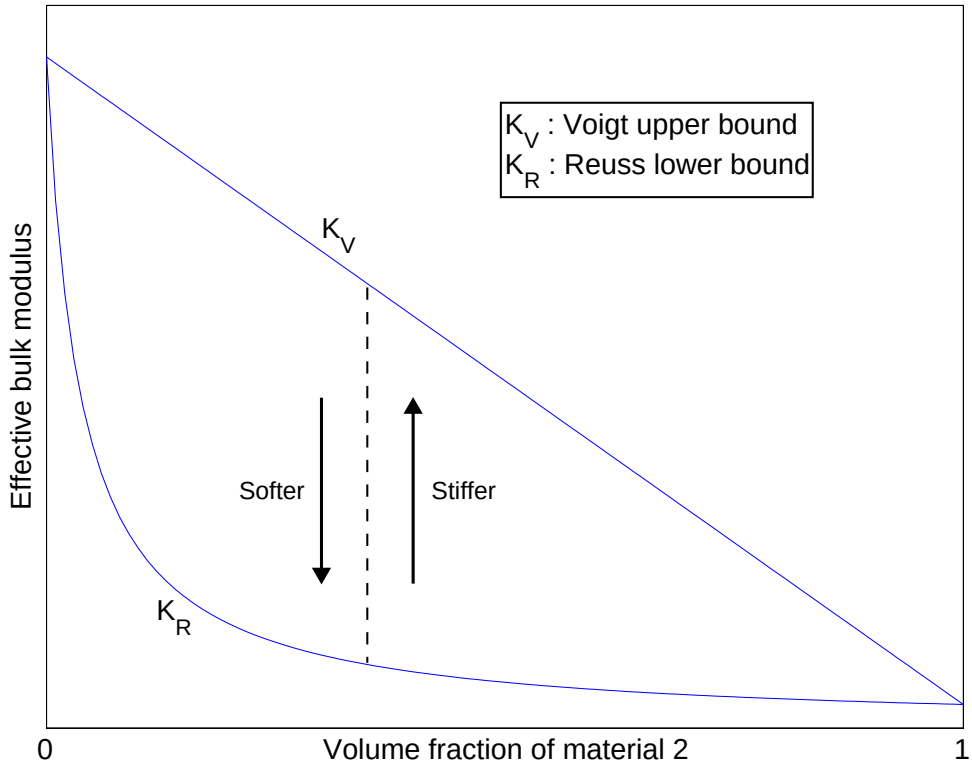

Figure 2.2: Illustration of the Voigt upper and Reuss lower bounds on the effective bulk modulus of a mixture of two constituents (modified from Mavko et al., 1998).

2. Generally, the expressions give the upper bound when the stiffest material is subscripted 1 in the expressions above, and the lower bound when the softest material is subscripted 1.

The physical interpretation of the bounds for bulk modulus is shown schematically in Figure 2.3. The space is filled by an assembly of spheres of material 2, each surrounded by a shell of material 1. Each sphere and its shell has exactly the volume fractions f_1 and f_2. The upper bound is obtained when the stiffer material forms the shell; the lower bound is obtained when it is in the core. A more general form of the Hashin-Shtrikman bounds, which can be applied to more than two phases, is discussed by Mavko et al. (1998).

The separation between the upper and lower bounds of Voigt-Reuss and Hashin-Shtrikman depends on the difference in elasticity of the constituents. For mixed solids that are elastically similar, the bounds are fairly close. In such cases, a simple assumption for predicting the effective medium is the Hill's (1963) average, which is the average of the upper and lower bounds; that is, $K_{Hill} = (K^+ + K^-)/2$.

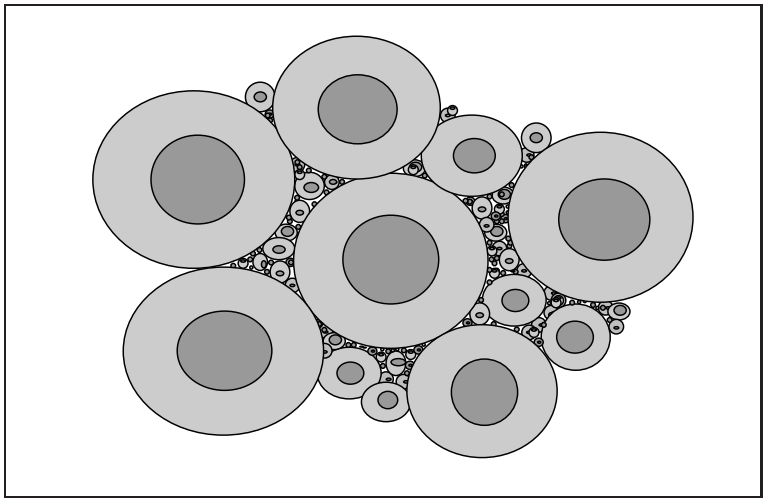

Figure 2.3: Physical interpretation of the Hashin-Shtrikman bounds for bulk modulus of a two-phase material (slightly modified from Mavko et al., 1998): An assembly of spheres of material 2, each surrounded by a shell of material 1.

However, when the constituents are quite different (for example minerals and pore fluids), the bounds become quite separated, and the prediction is more difficult.

2.3.3 Critical porosity model

Sedimentary rocks form initially as unconsolidated deposits of gravels, sand, or mud (see e.g. Boggs, 2001). Before deposition, sediments exist as particles in suspension. Newly deposited sediments are characterized by loosely packed, uncemented fabrics; high porosities; and high interstitial water content. The porosity of newly deposited sediments is referred to as the critical porosity ϕ_c (Nur, 1992). When the porosity gets below the limiting ϕ_c, the grains start to carry load. Porosity may decrease further during diagenesis, which is the final stage of forming conglomerates, sandstones, and shales (Boggs, 2001). Figure 2.4 illustrates the different stages in the process of forming sedimentary rocks.

Nur et al. (1995) presented a simple method that separates the mechanical and acoustic behavior of porous materials into two distinct domains separated by the critical porosity ϕ_c. In the suspension domain; that is, $\phi > \phi_c$, the effective bulk and shear moduli are quite accurately described by the Reuss average given in equation (2.18). In the load-bearing domain; that is, $\phi < \phi_c$, the frame (or dry) bulk and

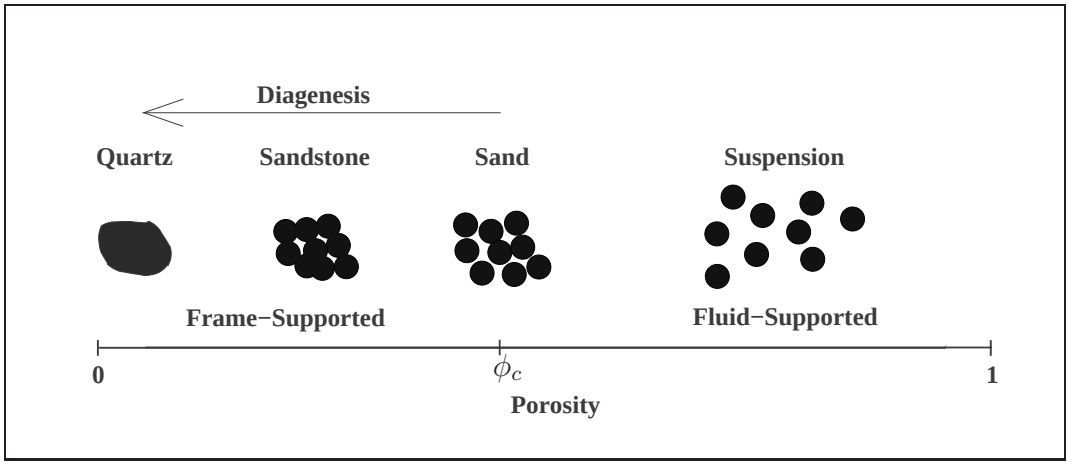

Figure 2.4: Different stages in the process of forming sedimentary rocks (slightly modified from Nur et al., 1998). The critical porosity ϕ_c is defined as the porosity of newly deposited sediments.

shear moduli can be expressed as the linear functions

$$K_{fr} = K_S \left(1 - \frac{\phi}{\phi_c}\right), \tag{2.22}$$

$$\mu_{fr} = \mu_S \left(1 - \frac{\phi}{\phi_c}\right), \tag{2.23}$$

where K_S and μ_S are the solid bulk and shear moduli, respectively. Figure 2.5 shows bulk modulus (K/K_S) versus porosity for a water saturated rock, according to Nur's critical porosity model, Voigt-Reuss bounds, Voigt-Reuss-Hill, and Hashin Shtrikman bounds. An empirical curve (dotted line) for clean sandstones, measured by Murphy et al. (1993), is included for comparison.

The weakness of the critical porosity model is that the critical porosity is not an universal constant (not even for a given class of rock, such as sandstones). The strength is the simplicity: no other assumptions about the microstructure than the knowledge of critical porosity are needed.

The loosest possible packing of spherical, equally sized grains is simple cubic packing which gives a porosity of 0.48, while random loose packing gives porosities between 0.4 and 0.45. For clean, well sorted sands, the critical porosity is near 0.4. Chalk has pores that are most likely spherical in shape, leading to critical porosity as high as 0.6-0.7.

Figure 2.6 shows P-wave velocity versus porosity for a variety of water-saturated

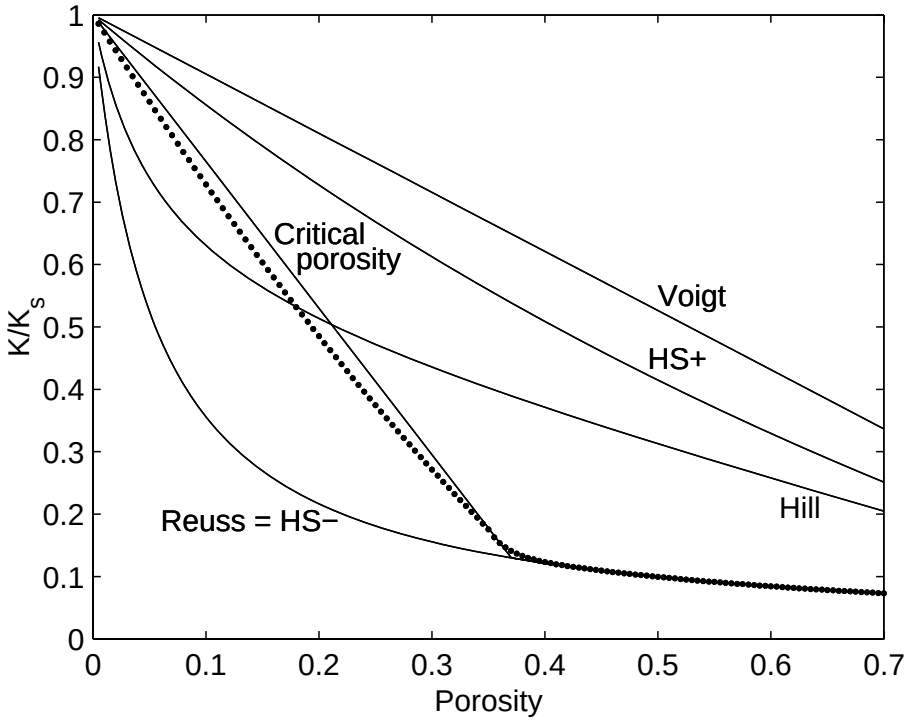

Figure 2.5: Bulk modulus versus porosity for a water-saturated rock, according to various models (solid lines). For comparison, an empirical curve for clean sandstones (Murphy et al., 1993) is included (dotted line).

sediments, ranging from ocean-bottom suspensions to consolidated sandstones. The data is compared with Voigt and Reuss bounds computed for mixtures of quartz and water. In the porosity domain above the critical porosity, sediments follow the Reuss average of mineral and fluid (that is, the undrained bulk modulus K is given by equation (2.19)). Below the critical porosity, the touching grains will induce effective stress, compaction, and cementing, which lead the sediments off the Reuss bound. In this porosity domain, the rock properties follow steep trajectories starting at the critical porosity and ending at the mineral end point at zero porosity (Figure 2.6). These trends are often described by empirical relations.

2.3.4 Empirical velocity-porosity relations

Porosity has an enormous impact on P- and S-wave velocities. Several authors (e.g. Wyllie et al., 1956; Raymer et al., 1980; Tosaya and Nur, 1982; and Han et al., 1986) have derived empirical relations for velocity versus porosity in the porosity domain below critical porosity.

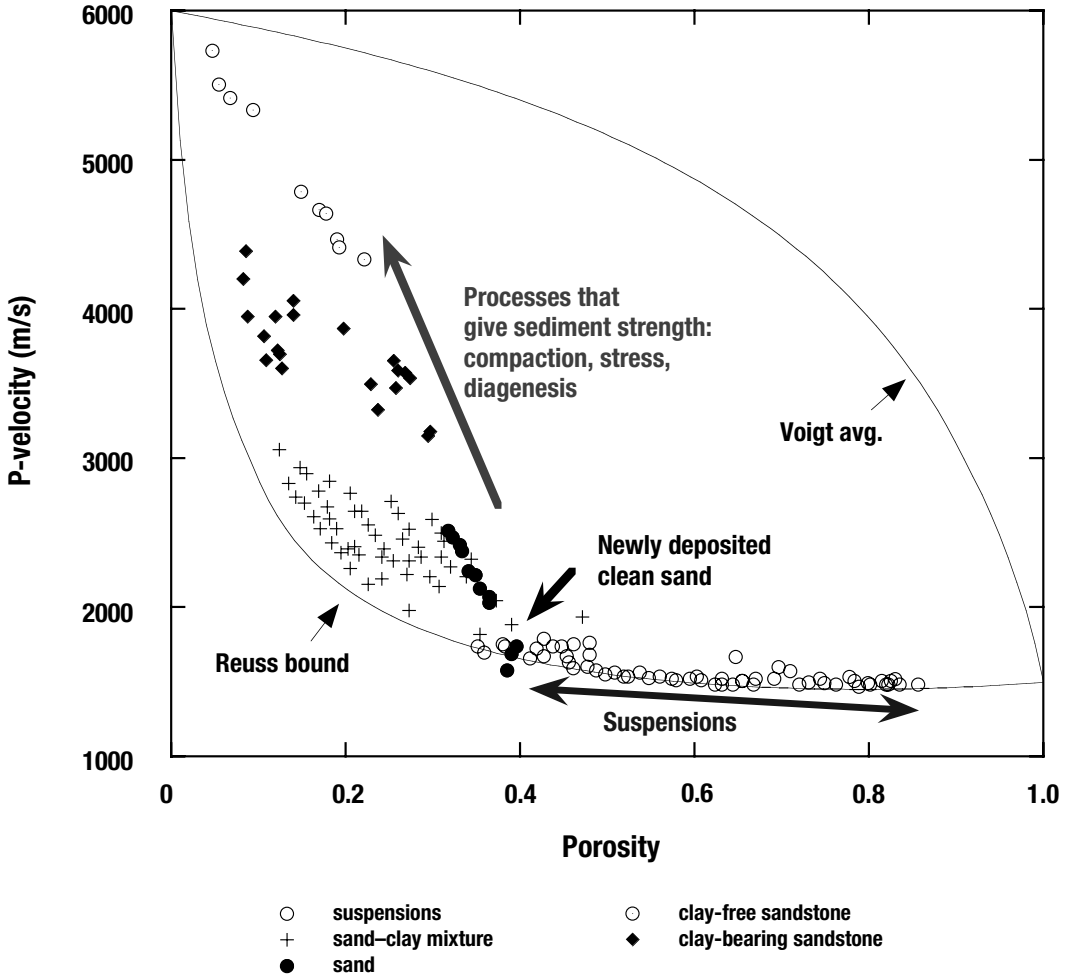

Figure 2.6: P-wave velocity versus porosity for a variety of water-saturated sediments (Avseth et al., 2005). The data is compared with the Voigt-Reuss bounds.

Wyllie et al. (1956) introduced a relation that is still commonly used in the oil industry. For a fluid-saturated rock with high effective pressure, they found the following relation between P-wave velocity v_P and porosity ϕ:

$$\frac{1}{v_P} = \frac{\phi}{v_{P,f}} + \frac{1-\phi}{v_{P,s}}, \tag{2.24}$$

where $v_{P,s}$ and $v_{P,f}$ are the P-wave velocities of the solid and fluid, respectively. The interpretation of equation (2.24) is that the sound wave shares its time passing through the rock in a volumetric portion in the solid and pore fluid. This is strictly valid only if the wavelength is much shorter than the grain and pore size; that is, for high frequencies. Improvements of Wyllie's empirical formula are suggested by

Raymer et al. (1980).

Han et al. (1986) show that velocity-porosity relations are dependent on the clay content. These relations are obtained from ultrasonic measurements of sandstones with porosities, ϕ, ranging from 0.03 to 0.3 and clay volume fractions, C, ranging from 0 to 0.55. For an effective pressure of 40 MPa, Han's velocity-porosity relation for a water-saturated shaley sandstone reads

$$v_P = (5.59 - 2.18C) - 6.93\phi, \tag{2.25}$$
$$v_S = (3.52 - 1.89C) - 4.91\phi, \tag{2.26}$$

where v_P and v_S are given in km/s. Equations (2.25) and (2.26) indicate parallel velocity-porosity trends with zero-porosity intercepts dependent on the clay content.

Tosaya and Nur (1982) determined similar trends based on other ultrasonic measurements of velocity, porosity, and clay content. For water-saturated rocks at an effective pressure of 40 MPa, they obtained the following relation:

$$v_P = (5.8 - 2.4C) - 8.6\phi, \tag{2.27}$$
$$v_S = (3.7 - 2.1C) - 6.3\phi, \tag{2.28}$$

where ϕ is porosity, and C is the clay content. Similar empirical regressions are also found by Castagna et al. (1985). Klimentos (1991) obtained relations between velocity, porosity, clay content, and permeability.

2.4 Determining α from porosity-velocity relations

The dilation factor α (that is, the relative thickness change divided by the relative velocity change within a given layer) can be determined from empirical porosity-velocity relations e.g. given by Mavko et al. (1998). If the seismic velocity is some function of porosity, $v(\phi)$, where $\Delta v/\Delta\phi = v'(\phi)$, the α-value can be found by assuming uniaxial stress-strain relations. For a porous material with uniaxial stress-strain relations (e.g. Guilbot and Smith, 2002), the change in thickness is related to the change in porosity approximately as $\Delta z/z \approx \Delta\phi/(1-\phi)$. This gives the following relation between the velocity change and thickness change (compare with Hatchell and Bourne, 2005a):

$$\frac{\Delta v}{v} = (1-\phi)\frac{v'(\phi)}{v(\phi)}\frac{\Delta z}{z}, \tag{2.29}$$

and, hence,

$$\alpha = (1-\phi)\frac{v'(\phi)}{v(\phi)}. \tag{2.30}$$

For rocks with linear relations between porosity and velocity; that is, $v = a - b\phi$, where a and b are positive constants, α can be given as (Appendix 3.A):

$$\alpha = \frac{a - b}{v} - 1. \tag{2.31}$$

As an example, using Tosaya's empirical porosity-velocity relation, given by equation (2.27), I find the following for clean sandstones:

$$v = 5.8 - 8.6\phi, \tag{2.32}$$

$$\alpha = \frac{5.8 - 8.6}{5.8 - 8.6\phi} - 1, \tag{2.33}$$

giving $\alpha = -1.7$ for a sandstone with porosity 0.20. Figure 2.7 shows estimated α versus porosity for the rock physics models given by Han (equation (2.25)) and Tosaya and Nur (equation (2.27)). The estimations are based on clean sandstones (solid lines) and sandstones with clay content 0.5 (dashed lines). (See Hatchell and Bourne (2005a) for further estimations based on rock-properties trends.) Figure 2.7 shows that the dilation factor α increases in magnitude as the clay content increases. Note, however, that this result gives the same dilation factor for a compacting rock and a stretching rock. In comparison, Hatchell and Bourne (2005a) found that α is larger in absolute value for rock elongation (stretch) than for rock contraction (compaction) for several locations around the world. They estimate α-values around -5 for rocks undergoing elongation strains and α-values ranging from -1 to -3 for rocks undergoing contraction. Different α-values for stretched overburden rocks and compacted reservoir rocks is also predicted by Røste et al. (2006) at the Valhall Field.

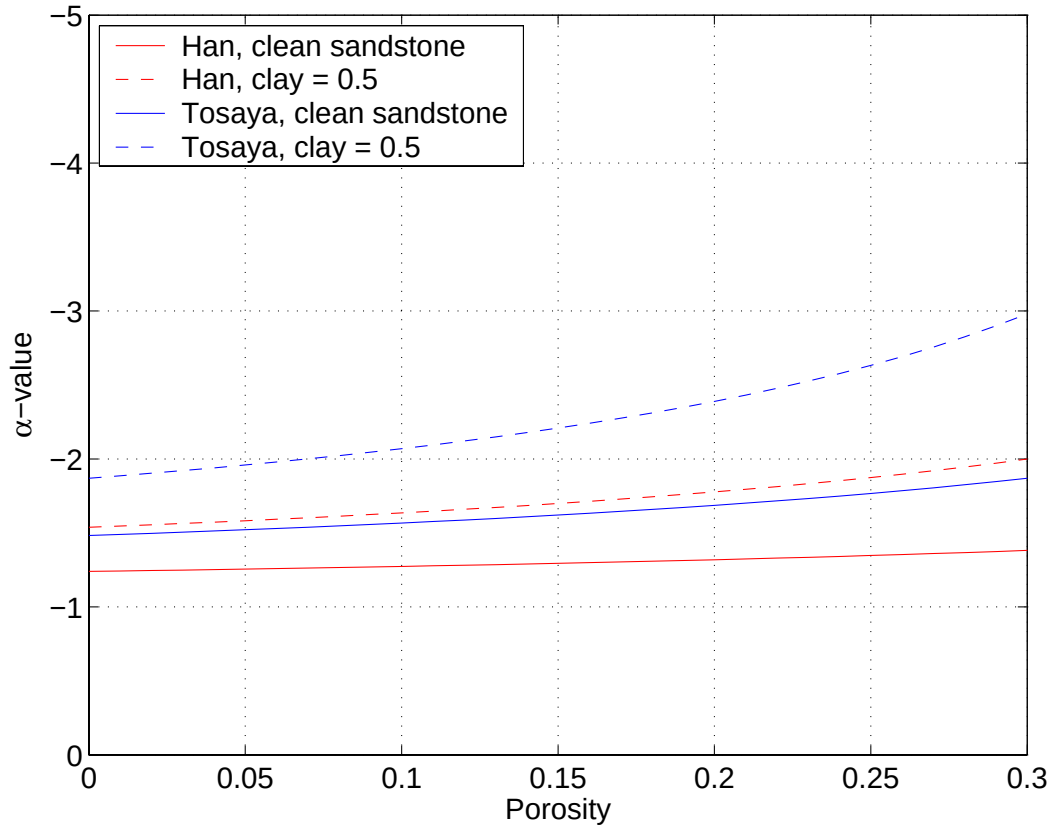

Figure 2.7: Estimated α versus porosity based on Han's and Tosaya's empirical velocity-porosity relations for clean sandstones and sandstones with clay content of 0.5.

Chapter 3

Estimation of layer thickness and velocity changes using 4D prestack seismic data

Thomas Røste*, Alexey Stovas*, and Martin Landrø*

**Norwegian University of Science and Technology,*
Department of Petroleum Engineering and Applied Geophysics,
S.P.Andersens vei 15A, N-7491 Trondheim, Norway.

Published in the November-December 2006 issue of Geophysics. Presented at the 67th EAGE Conference & Exhibition in Madrid, Spain, June 2005, at the ROSE meeting in Trondheim, Norway, June 2005, and at the FORCE seminar in Stavanger, Norway, September 2005.

3.1 Abstract

In some hydrocarbon reservoirs severe compaction of the reservoir rocks is observed. This compaction is caused by production, and is often associated with stretching and arching of the overburden rocks. Time-lapse seismic data can be used to monitor these processes. Since compaction and stretching cause changes in both layer thickness as well as seismic velocities, it is crucial to develop methods to distinguish between the two effects.

We introduce a new method based on detailed analysis of time-lapse prestack seismic data. The equations are derived assuming that the entire model consists of

only one single layer with no vertical velocity variations. The method incorporates lateral variations in (relative) velocity changes by utilizing zero-offset and offset-dependent time shifts. To test the method, we design a 2D synthetic model that undergoes severe reservoir compaction as well as stretching of the overburden rocks. Finally, we utilize the method to analyze a real 2D prestack time-lapse seismic line from the Valhall Field, acquired in 1992 and 2002. For a horizon at a depth of around 2.5 km, which is near the top reservoir horizon, a subsidence of 2.7 m and a velocity decrease of 4.5 m/s for the sequence from the sea surface to the top reservoir horizon are estimated. By assuming that the base of the reservoir remains constant in depth, a reservoir compaction of 3.6 % (corresponding to a subsidence of the top reservoir horizon of 2.7 m), and a corresponding reservoir velocity increase of 6.7 % (corresponding to a velocity increase of 200 m/s), are estimated.

3.2 Introduction

Production-related compaction has been observed in several North Sea reservoirs, especially the chalk reservoirs in the southern part. For example, the compaction of the Valhall Field, at 2.5 km depth, has led to 4.5 m of subsidence at the sea bed since the field came on production in 1982 (Pattillo et al., 1998). Such reservoir compaction will have significant implications for production by changing permeabilities and, hence, the production performance (Hall et al., 2005). It is typical for these fields that the sea bed subsidence is less than the corresponding reservoir compaction, meaning that the overburden rocks are stretched. Often the change in geomechanical stress state for the overburden rocks might lead to damage in existing wells (especially when significant shear stresses are introduced as byproduct of the reservoir compaction). It is therefore of significant importance to map the velocity and thickness changes during production not only for the reservoir itself, but also for the overburden rocks. Between the wells, time-lapse seismic data is a complementary tool for obtaining this information, and the combined use of repeated seismic measurements and geomechanical knowledge is expected to be important in future monitoring projects.

Guilbot and Smith (2002) utilized time-isochron differences from 4D seismic data to detect compaction and subsidence at the Ekofisk Field. They observed seismic time shifts up to 12-16 ms between 1989 and 1999, related to compaction values of up to 6 m for the reservoir chalk formation. They used a 4D tomographic technique where the nonuniqueness between velocity and thickness changes was solved by introducing a velocity-porosity relationship for the reservoir chalk layer. It is important to notice that the 4D time shifts capture the combined effects of velocity and thickness changes within a given layer. For a layer of thickness, z, we express the relative time shift in terms of the relative thickness change and velocity change

as (Landrø and Stammeijer, 2004; Hatchell and Bourne, 2005b; Røste et al., 2005)

$$\frac{\Delta T_0(x_0)}{T_0(x_0)} \approx \frac{\Delta z(x_0)}{z(x_0)} - \frac{\Delta v(x_0)}{v(x_0)}, \tag{3.1}$$

where T_0 represents seismic two-way vertical traveltime within the layer and v is the layer velocity. The parameter x_0 denotes the global x-coordinate for a given CDP-location (position), and ΔT_0, Δz, and Δv represent changes in vertical two-way traveltime, thickness, and velocity, respectively. A major challenge for quantitative time-lapse analysis is to discriminate between thickness changes and velocity changes for both the reservoir section and the overburden. Landrø and Janssen (2002) presented a method utilizing near and far offset traveltime shifts to perform this discrimination procedure. In this paper we introduce a prestack method which utilizes all offsets. As a first order approximation for a relation between relative thickness and velocity changes for a given subsurface layer we will simply assume that the two changes are proportional to each other (Røste et al., 2005):

$$\frac{\Delta v(x_0)}{v(x_0)} \approx \alpha \frac{\Delta z(x_0)}{z(x_0)}, \tag{3.2}$$

where the "dilation factor" α is a parameter dependent on the rock properties of the layer. This is a crucial parameter, since it determines the ratio between velocity and thickness changes. In general, α varies with spatial coordinates. It is important to stress that the knowledge of the dilation factor from a rock physics point of view is limited; there are no measurements available to our knowledge. We do not know if the dilation factor is the same for compaction and stretching of a rock. Furthermore, the dilation factor might also be dependent on the magnitude of the relative thickness change. Despite these concerns, we find it fruitful to introduce the dilation factor, since it captures the important relation between velocity and thickness changes. Furthermore, it can easily be determined if empirical porosity-velocity relations are available. Assuming uniaxial stress-strain relations and a linear relation between porosity (ϕ) and velocity (v); that is, $v = a - b\phi$, it can be shown (Appendix 3.A) that α is given by

$$\alpha = \frac{a-b}{v} - 1. \tag{3.3}$$

Note that $\alpha \leq 0$ because, by equation (3.A-1)), $v \geq a - b$. From equation (3.3) it is clear that α is rock (and lithology) dependent. However, in this paper, we will assume that α is constant for the sequence of layers we study.

Using the empirical relations for the chalk reservoir at Valhall we obtain a value for the dilation factor of -1.5. If we use the empirical porosity-velocity relation published by Tosaya and Nur (1982) we find an α-value of -2.4 for sand and -3.6

for clay. Han's (1986) relation gives an α-value equal to -1.6 for sand and -2.7 for clay. These observations indicate that rocks with high clay content will have dilation factors that are larger in magnitude than clean sands and chalks. (However, note that Han's relation is only based on consolidated sandstones, not unconsolidated sands or shales.)

In the following sections we introduce a method which estimates changes in layer thickness and velocity based on prestack time-lapse seismic data. The developed method is tested on a 2D synthetic model which consists of 7 layers, including an anticline reservoir section. Both the reservoir layer and the overburden layers (of the synthetic model) undergo changes in layer thickness and velocity that vary with lateral position. Finally, we test the method on a 2D prestack time-lapse seismic line from the Valhall Field.

3.3 Methodology

To discriminate between layer thickness and velocity changes, defined by the dilation factor α, both zero-offset and offset-dependent time shifts are utilized. From raypath considerations we include lateral variations in layer changes, which is normally the case for both the reservoir layer and overburden layers when the reservoir undergoes strong compaction.

3.3.1 Estimating α based on time shift analysis

Assume a prestack CDP-gather at position x_0. The seismic two-way traveltime for a raypath with offset $2h$ can be expressed as an integral over the total raypath length S,

$$T(x_0, h) = \int_S \frac{ds}{v(s)}, \tag{3.4}$$

where $v(s)$ denotes the P-wave velocity at the ray position $s(x_0, h)$. Assume a one-layer model with a P-wave velocity field, $v(x)$, that varies along the lateral position x, but is nonvarying with depth (Figure 3.1). By assuming straight raypaths, it can be shown that (similar to assuming average slowness within the offset range $2h$)

$$T(x_0, h) = \sqrt{1 + \frac{z^2(x_0)}{h^2}} \int_{x_0-h}^{x_0+h} \frac{dx}{v(x)}, \tag{3.5}$$

where $z(x_0)$ represents the layer thickness at the CDP-position x_0. The straight raypath assumption used above will lead to inaccuracies, so this equation should be used with care if the variations in velocity are significant and heterogeneous. Equation (3.5) describes the initial (or pre-production) case. For the post-production

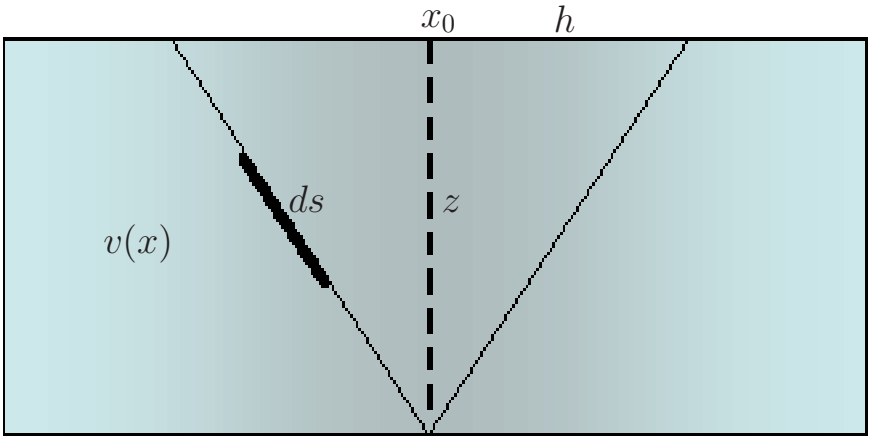

Figure 3.1: Sketch showing that we assume straight raypaths in a model with lateral variations in velocity.

case, we find that it is essential to include the lateral variations in velocity changes, since it is very likely that such changes will occur both within the reservoir layer as well as the overburden layers of a producing hydrocarbon reservoir. It is also possible to include vertical variations in velocity changes. This essentially means that we approach time-lapse tomography (Vesnaver et al., 2003). However, the idea of this paper is to develop something simpler than a full tomographic method, and we therefore assume no vertical variations in velocity changes. From equation (3.5) the two-way prestack traveltime for the monitor case (for a one-layer model) is then given as

$$T'(x_0,h) = \sqrt{1+\frac{z^2(x_0)}{h^2}\left(1+\frac{\Delta z(x_0)}{z(x_0)}\right)^2}\int\limits_{x_0-h}^{x_0+h}\frac{dx}{v(x)\left(1+\frac{\Delta v(x)}{v(x)}\right)}, \tag{3.6}$$

where the relative change in velocity, $\Delta v(x)/v(x)$, might vary laterally but not with depth. (Note that variations in thickness changes only affect the multiplier outside the integral in equation (3.6) when assuming straight raypaths.) Assuming small relative changes in velocity and thickness, the relative change in two-way traveltime becomes (see Appendix 3.B)

$$\frac{\Delta T(x_0,h)}{T(x_0,h)} \approx \frac{\left(1+\frac{z^2(x_0)}{z^2(x_0)+h^2}\frac{\Delta z(x_0)}{z(x_0)}\right)\int\limits_{x_0-h}^{x_0+h}\frac{dx}{v(x)}\left(1-\frac{\Delta v(x)}{v(x)}\right)}{\int\limits_{x_0-h}^{x_0+h}\frac{dx}{v(x)}} - 1. \tag{3.7}$$

From equations (3.1) and (3.2) the relative changes in layer thickness and velocity can be related to the relative change in two-way vertical traveltime T_0:

$$\frac{\Delta z(x_0)}{z(x_0)} \approx \left(\frac{1}{1-\alpha}\right)\frac{\Delta T_0(x_0)}{T_0(x_0)} \quad , \quad \frac{\Delta v(x_0)}{v(x_0)} \approx \left(\frac{\alpha}{1-\alpha}\right)\frac{\Delta T_0(x_0)}{T_0(x_0)}. \tag{3.8}$$

By assuming small lateral variations in initial layer velocity in the vicinity of each position x_0; that is, $v(x) \approx v(x_0)$ for $x_0 - h \leq x \leq x_0 + h$, equation (3.7) can be written in the simple form given by equation (3.9) (see Appendix 3.B). Note, however, that we include the lateral variations in Δv; that is, $\Delta v = \Delta v(x)$.

$$\frac{\Delta T(x_0,h)}{T(x_0,h)} \approx \frac{z^2(x_0)}{z^2(x_0)+h^2}\left(\frac{1}{1-\alpha}\right)\frac{\Delta T_0(x_0)}{T_0(x_0)} - \frac{1}{2h}\left(\frac{\alpha}{1-\alpha}\right)\int_{x_0-h}^{x_0+h} dx \frac{\Delta T_0(x)}{T_0(x)}. \tag{3.9}$$

The relative change in two-way traveltime (for a given half-offset h) is therefore dependent on α and the estimated relative change in vertical traveltime. (Note that the integration sign in equation (3.9) in practice means summation, since time shift estimations only exist for discrete positions (or CDPs).) The parameter α is determined by minimizing the least square error in relative traveltime change (equation (3.9)) over the entire offset range. This α-value is then inserted into equation (3.8) to obtain the changes in layer thickness and velocity.

Equation (3.9) is only valid for one layer. However, equation (3.9) might be applied for a sequence of layers if the relative velocity changes (captured by the relative zero offset time shifts inside the integral sign in equation (3.9)) have no vertical variations. Further, due to the assumption made for equation (3.2), α must be similar for the layers within the investigated sequence. However, choosing a sequence consisting of layers that undergo similar processes, for example, an overburden sequence that only undergoes stretch, we believe that the vertical variations in the relative velocity changes are less important than the lateral variations. For a two-layer model, it is possible to estimate the relative traveltime shift as a function of offset (Appendix 3.C). A comparison between the two-layer traveltime shift and the traveltime shift estimated using equation (3.9) is shown in Figure 3.2. This example shows that the one-layer approximation given by equation (3.9) can be used if the precautions listed above are taken into account. In addition, for stretched overburden rocks, Hatchell and Bourne (2005a) find α to be almost constant (around -5) for several worldwide field examples. Equation (3.9) might therefore be tested on an overburden sequence that only undergoes stretch. When applying equation (3.9) to a sequence of layers, we find that the inaccuracies increase with increased variations in (relative) velocity changes between the layers.

When both vertical and horizontal variations in velocity changes are significant and appear to be heterogeneous, a full 4D tomographic approach is required.

3.3.2 Uncertainty analysis

The method is strongly influenced by how accurately we can measure zero-offset and offset-dependent time shifts from time-lapse seismic data. In addition, large sensitivity in α is needed to be able to discriminate the correct α-value; that is, a test of various values of α (for a given position) should give clearly distinct results (from equation (3.9)). (This is later discussed for results from synthetic and field data). Errors due to the approximations made from equation (3.6) to equation (3.9) are given step by step in Appendix 3.D.

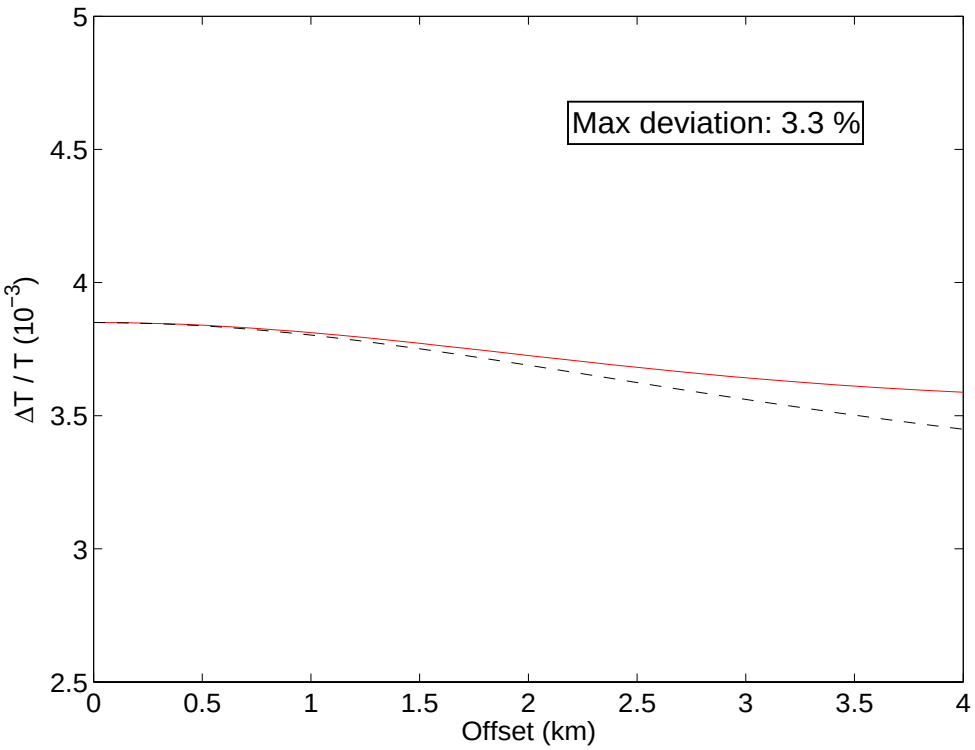

Figure 3.2: Comparison between computed relative traveltime shifts for a two-layer model (solid line) and equation (3.9) (dashed line). A maximum error of 3.3% is observed at 4.0 km offset. Initial thickness of each layer is 1.0 km, velocity of first layer is 1.8 km/s and second layer velocity is 2.5 km/s. The dilation factor α is -4 for both layers, and the stretching of the two layers are 0.6 m and 1.0 m, respectively.

3.4 Synthetic example

3.4.1 The 2D synthetic model

The described method is tested on a 2D synthetic model with a total depth of 3.5 km and a total lateral size of 16 km (Figure 3.3). The model consists of 7 layers including an anticline-shaped reservoir section with thickness (pre-production) given as (all units in km)

$$z_{\text{res}} = -5.600 \times 10^{-3} x^2 + 8.960 \times 10^{-2} x - 0.2184. \tag{3.10}$$

The reservoir thickness (equation (3.10)) varies from zero at position $x = 3$ km to 140 m at the crest ($x = 8$ km) to zero again at $x = 13$ km. P-wave velocity (v_p), S-wave velocity (v_s), and density (ρ) for all 7 layers (pre-production) are given in Table 3.1 (layer 1 is the water layer). The reservoir velocity ($v_p = 2900$ m/s and $v_s = 1500$ m/s) yields a v_p/v_s-ratio similar to oil-bearing chalk (that is, $v_p/v_s = 1.9$ - 2.0).

Inside the compacting area (5.5 km $< x <$ 10.5 km) the thickness change of the reservoir, Δz_{res}, varies from zero at position $x = 5.5$ km to -10 m at the crest ($x = 8$ km) to zero again at $x = 10.5$ km. The polynomial expression (effective only inside the compacting area 5.5 km $< x <$ 10.5 km) reads (all units in km)

$$\Delta z_{\text{res}} = 1.600 \times 10^{-3} x^2 - 2.560 \times 10^{-2} x + 9.240 \times 10^{-2}, \tag{3.11}$$

where negative Δz_{res} corresponds to reservoir compaction. The reservoir thickness changes (equation (3.11)) are shown in bottom of Figure 3.4 together with a plot of the reservoir after compaction (top).

Table 3.1: Initial layer P-wave velocities (v_p), S-wave velocities (v_s), and densities (ρ) used in the synthetic model. Layer 1 denotes the water layer and layer 6 denotes the reservoir layer.

Layer	v_p (m/s)	v_s (m/s)	ρ (g/cm^3)
1	1476	0	1.00
2	1700	800	1.55
3	1800	900	1.60
4	2000	1000	1.70
5	2200	1200	1.75
6	2900	1500	1.80
7	4000	2500	2.30

Changes in reservoir thickness can be linked to changes in other reservoir parameters (such as changes in porosity, velocity, and density). Empirical relationships between reservoir velocity ($v_{p,\mathrm{res}}$, $v_{s,\mathrm{res}}$) and porosity (ϕ_{res}) have previously been used (Guilbot and Smith, 2002) to estimate reservoir compaction. Here we adapt the same technique to establish our *forward* compaction model. For a chalk reservoir it is reasonable to assume

$$v_{p,\mathrm{res}} = a - b\phi_{\mathrm{res}} \quad , \quad v_{s,\mathrm{res}} = a' - b'\phi_{\mathrm{res}}, \tag{3.12}$$

where

$$a = 5500 \text{ m/s} \quad , \quad b = 7000 \text{ m/s} \quad , \quad a' = 2845 \text{ m/s} \quad , \quad b' = 3621 \text{ m/s}. \tag{3.13}$$

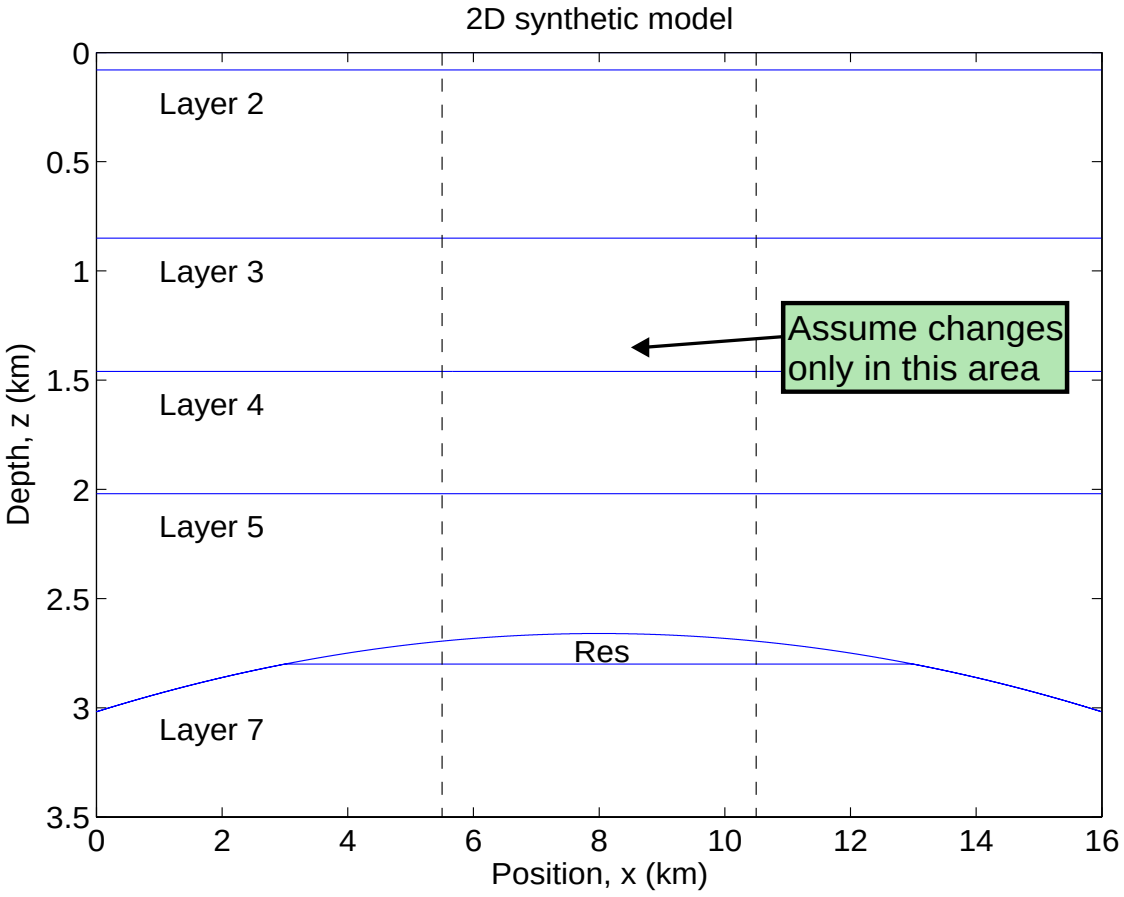

Figure 3.3: The initial (pre-production) 7-layer synthetic model, given in kilometers. Changes are assumed to occur only in the area between the vertical dashed lines; that is, between the positions 5.5 km and 10.5 km.

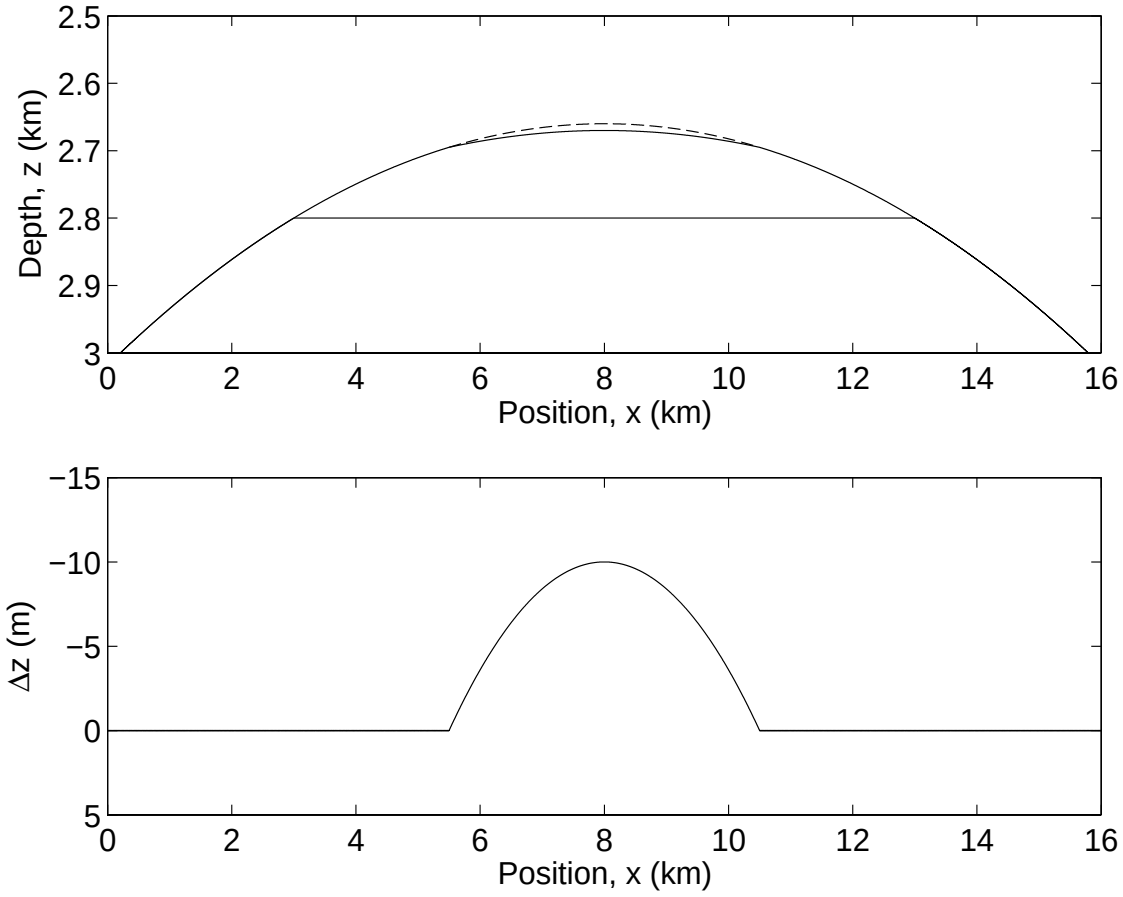

Figure 3.4: The compacted reservoir section of the synthetic model (top) after applying the thickness changes plotted at bottom. Both figures plotted as a function of position.

The above parameters are estimated from well logs. We assume that the reservoir density follows the relation:

$$\rho_{\text{res}} = \phi_{\text{res}}\rho_F + (1 - \phi_{\text{res}})\rho_S, \tag{3.14}$$

where ρ_F and ρ_S are the fluid and solid densities of the reservoir, respectively. By assuming uniaxial strain conditions, differentiation of equations 3.12 and 3.14 reads (see Appendix 3.E)

$$\Delta v_{p,\text{res}} = -b(1 - \phi_{\text{res}})\frac{\Delta z_{\text{res}}}{z_{\text{res}} + \Delta z_{\text{res}}}, \tag{3.15}$$

$$\Delta v_{s,\text{res}} = -b'(1 - \phi_{\text{res}})\frac{\Delta z_{\text{res}}}{z_{\text{res}} + \Delta z_{\text{res}}}, \tag{3.16}$$

$$\Delta\rho_{\text{res}} = -(\rho_{\text{res}} - \rho_F)\frac{\Delta z_{\text{res}}}{z_{\text{res}} + \Delta z_{\text{res}}}, \tag{3.17}$$

where we (still for the forward model) use the following reservoir parameters: porosity $\phi_{\text{res}} = 0.37$, fluid density $\rho_F = 0.8$ g/cm^3, and reservoir density $\rho_{\text{res}} = 1.8$ g/cm^3. Note that $\Delta v_{p,\text{res}}$, $\Delta v_{s,\text{res}}$, and $\Delta\rho_{\text{res}}$ vary laterally since z_{res} and Δz_{res} (given by equations 3.10 and 3.11, respectively) vary laterally. The maximum $\Delta v_{p,\text{res}}$ (at the crest, position $x = 8$ km) is 339 m/s, found from equation (3.15) by substituting the maximum reservoir thickness ($z_{\text{res}} = 140$ m) and thickness change ($\Delta z_{\text{res}} = -10$ m). This gives (equation (3.2))

$$\alpha_{\text{res}} \approx \frac{\Delta v_{p,\text{res}}}{v_{p,\text{res}}}\left(\frac{\Delta z_{\text{res}}}{z_{\text{res}}}\right)^{-1} = \frac{339 \text{ m/s}}{2900 \text{ m/s}}\left(\frac{-10 \text{ m}}{140 \text{ m}}\right)^{-1} = -1.6, \tag{3.18}$$

for the crest. Further estimations by equation (3.2) show that α_{res} varies with position between -1.4 and -1.6. (Note also that α_{res} can be found exactly by equation (3.3), which gives (constant) $\alpha_{\text{res}} = \frac{a-b}{v_{p,\text{res}}} - 1 = -1.5$).

For the forward model the thickness changes (or stretch) of an overburden layer i, denoted Δz_i, are directly linked to the reservoir compaction; see Appendix 3.E. The relative changes in P- and S-wave velocities of an overburden layer i (below the sea bed) are given by

$$\frac{\Delta v_{p,i}}{v_{p,i}} = \frac{\Delta v_{s,i}}{v_{s,i}} = -2 \times \frac{\Delta z_i}{z_i}, \tag{3.19}$$

which means that we assume $\alpha = -2$ within each of the overburden layers (below the sea bed) for the synthetic case. When looking at the total overburden sequence from the sea surface to the top reservoir horizon the modeled α-value is obtained from equation (3.2). For the crest (position $x = 8$ km) we get

$$\alpha_{\text{overb}} \approx \frac{\Delta V_{\text{overb}}}{V_{\text{overb}}}\left(\frac{\Delta z_{\text{overb}}}{z_{\text{overb}}}\right)^{-1} = \frac{-4.95 \text{ m/s}}{1888.4 \text{ m/s}}\left(\frac{10 \text{ m}}{2660 \text{ m}}\right)^{-1} = -0.7, \tag{3.20}$$

where z_{overb} and Δz_{overb} denote the thickness and thickness change (at the crest) of the total overburden sequence, respectively. Note that the estimated $\alpha_{\text{overb}} = -0.7$ (for the total overburden sequence) is independent of the subsidence of the sea bed, meaning that the thickness change, Δz_{overb}, is simply equal to the subsidence of the top reservoir horizon. This leads to the different α-value for the total overburden sequence (-0.7) and the individual overburden layers (-2). The relative change in vertical velocity (at the crest of the given overburden sequence), $\Delta V_{\text{overb}}/V_{\text{overb}}$, are obtained from the Dix interval velocity (Sheriff and Geldart, 1995). Substituting values for other positions in equation (3.20) show that α_{overb} varies with position, between -0.69 and -0.72.

Assuming that the mass within each layer is conserved, and that the stretch only occurs in the z-direction, the relative changes in density can approximately be given as (see Appendix 3.E)

$$\frac{\Delta\rho_i}{\rho_i} \approx -\frac{\Delta z_i}{z_i}. \tag{3.21}$$

Note also that the overburden layer changes $\Delta v_{p,i}$, $\Delta v_{s,i}$, and $\Delta\rho_i$ vary laterally since Δz_i is linked to Δz_{res} (see more details in Appendix 3.E).

3.4.2 Description of the survey

The prestack time-lapse seismic data were modeled by a 2D coarse grid finite difference scheme (Yerneni et al., 2002). A Ricker wavelet with central frequency of 23 Hz was used. The temporal step-length was 1 ms and the grid size was 4 m by 4 m. The receiver cable consisted of 300 receivers with a spacing of 12.5 m. The distance between the source and the first receiver was 150 m, and the shot point interval was 25 m. Based on the synthetic time-lapse seismic data, traveltime shifts for all offsets were estimated.

3.4.3 Synthetic results

Prior to estimating traveltimes of events in a prestack gather we mute all signals above and below the selected events; see Figure 3.5. Traveltimes are then picked for interpolated maximum amplitude. Zero offset traveltimes (T_0) are estimated by assuming that the picked traveltimes (T) follow standard hyperbolic moveout (Dix, 1955); that is,

$$T^2(x_0, h) = T_0^2(x_0) + \frac{4}{V_{rms}^2(x_0)}h^2, \tag{3.22}$$

where h denotes half-offset and V_{rms} denotes rms velocity. For a given position x_0, the picked traveltimes are interpolated along a straight line in the h^2-T^2-domain, according to equation (3.22), to obtain T_0 (and V_{rms}). For the synthetic model we have investigated the overburden sequence from the sea surface to the top reservoir horizon (for both baseline and monitor). Figure 3.6 shows the estimated (crosses) and lateral smoothed (solid line) relative time shifts for zero offset for the investigated sequence (for positions inside the compacting area, 5.5 km - 10.5 km), together with the modeled values (dashed line). The thickness (pre-production) of the investigated sequence, given by

$$z(x_0) \approx \frac{T_0(x_0)V_{rms}(x_0)}{2}, \tag{3.23}$$

is necessary input to equation (3.9), as well as the zero-offset time shift. For an initial guess of α, equation (3.9) gives corresponding (relative) time shifts for different

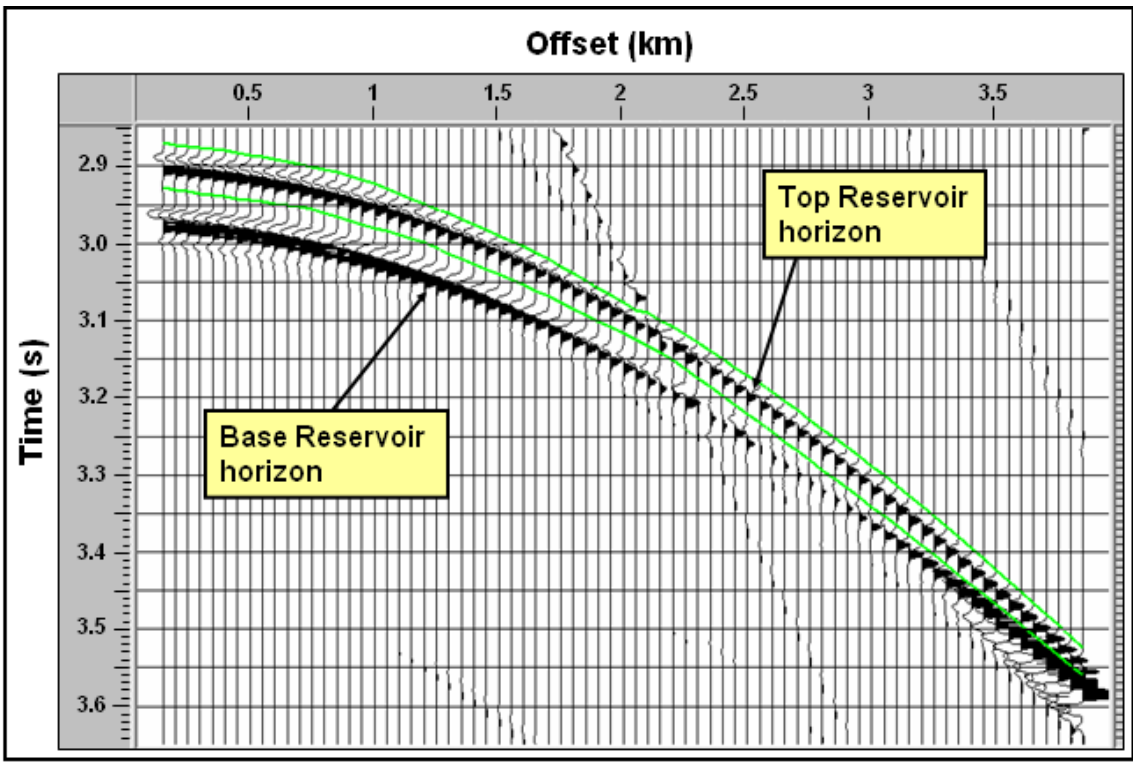

Figure 3.5: Example of event picking in a prestack gather (pre-production). We mute above and below the marked lines prior to time shift analysis. After muting, traveltimes are picked for interpolated maximum amplitudes.

half-offsets (h) which can be compared with the picked time shifts. We search for the α-value that leads to the minimum least square error between the estimated and picked relative time shifts, for all offsets. Figure 3.7 shows how this procedure works for position $x = 5.6$ km: Starting with an initial α-value of 0 in equation (3.9), we search in steps of -0.1 within the span from 0 to -5, until we obtain an optimal α-value (solid line) that gives best fit to the picked relative time shifts (crosses). The dashed lines in Figure 3.7 correspond to the initial and last guess of α. Figure 3.7 shows an example with reasonably good sensitivity in α; that is, inserting various α-values (between 0 and -5) in equation (3.9) gives clearly distinct results making it simpler to determine the correct α-value. The solid line in Figure 3.7 indicates that an optimal α-value of -0.6 correlates best with the picked offset-dependent relative time shifts (crosses). Bad (relative) time shift picks (solid dots in Figure 3.7) are automatically excluded prior to estimating the best fit for α. We interpret picked time shifts as bad (or unphysical) if they correspond to picked traveltimes from either baseline or monitor that fit poorly with the hyperbolic moveout (equation (3.22)). In detail, for a given position (for either baseline

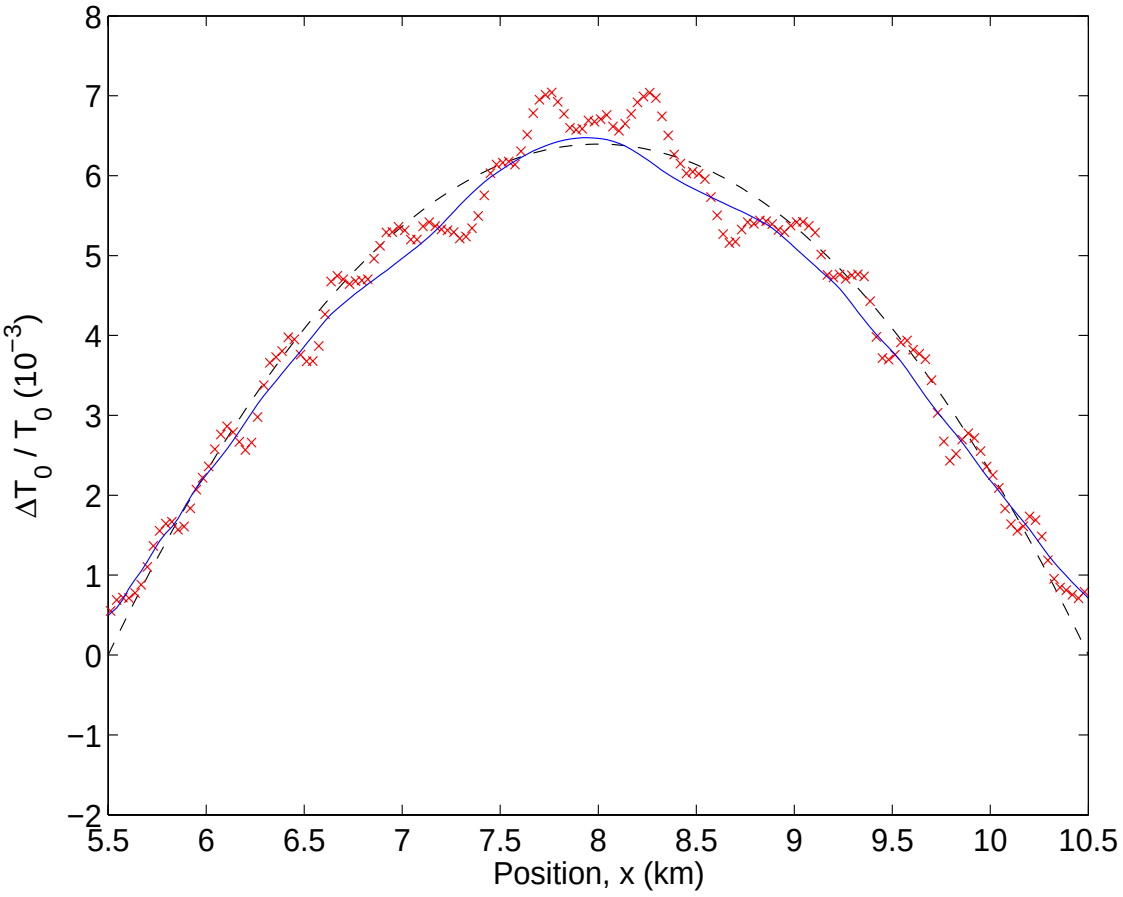

Figure 3.6: Estimated (crosses) and smoothed (solid line) zero-offset relative time shifts as a function of position (inside the compacted area 5.5 km $< x <$ 10.5 km). The modeled values are shown as a dashed line.

or monitor) this automatic procedure starts with excluding traveltimes that are picked far away (typically ±10 ms) from an initial hyperbolic fit (equation (3.22)). The existing picked traveltimes will be fitted to a new hyperbolic moveout curve (equation (3.22)). Again, traveltimes picked far away from this new hyperbolic fit are excluded, but this time the excluding limits are more narrow (typically ±8 ms). This procedure is repeated several times until the excluding limits are narrowed down to around ±2 ms (these limits should be larger for cases where undisturbed prestack seismic reflections are expected to be strongly nonhyperbolic). In this way we are able to exclude time shifts that correspond to picked traveltimes from either baseline or monitor that are (most probably) disturbed (or bad). Investigations show that bad time picks correlate well with noise and/or interference with multiples.

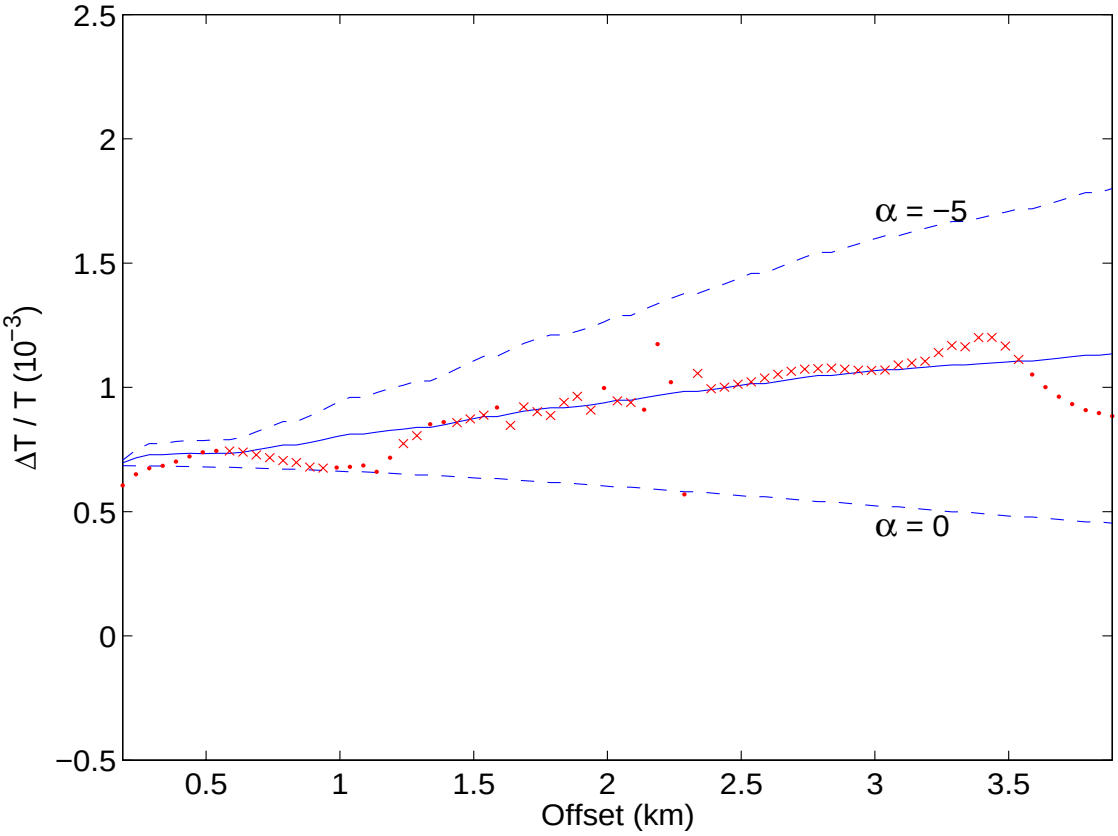

Figure 3.7: Example of finding α for position $x = 5.6$ km: The solid line indicates the best fit ($\alpha = -0.6$) of the picked relative time shifts (crosses) as a function of offset. Bad picked (relative) time shifts (solid dots) are excluded prior to the best fit. The dashed lines correspond to the initial and last guess of α (that is, $\alpha = 0$ and $\alpha = -5$).

Figure 3.8a shows the estimated α-values (for the investigated overburden sequence) for all lateral positions, where positions with acceptable sensitivity in α (crosses) are close to the modeled $\alpha = -0.7$ (indicated with dotted line). Estimated α-values for positions with low sensitivity in α are marked as solid dots. Examples of positions with low sensitivity in α are shown in figures 3.8b and 3.8c for the positions $x = 6.42$ km and $x = 6.45$ km, respectively. The small window between the initial and last guess of α (dashed lines) (that is, $\alpha = 0$ and $\alpha = -5$) makes it difficult to find a trustable α-value. The optimal α-value for all lateral positions is found to be -0.6, with a standard deviation as large as 0.7 when both acceptable and low sensitivity in α are included. However, positions with low sensitivity in α are easy to detect, and by excluding these uncertain α-values (solid dots in Figure 3.8a), we

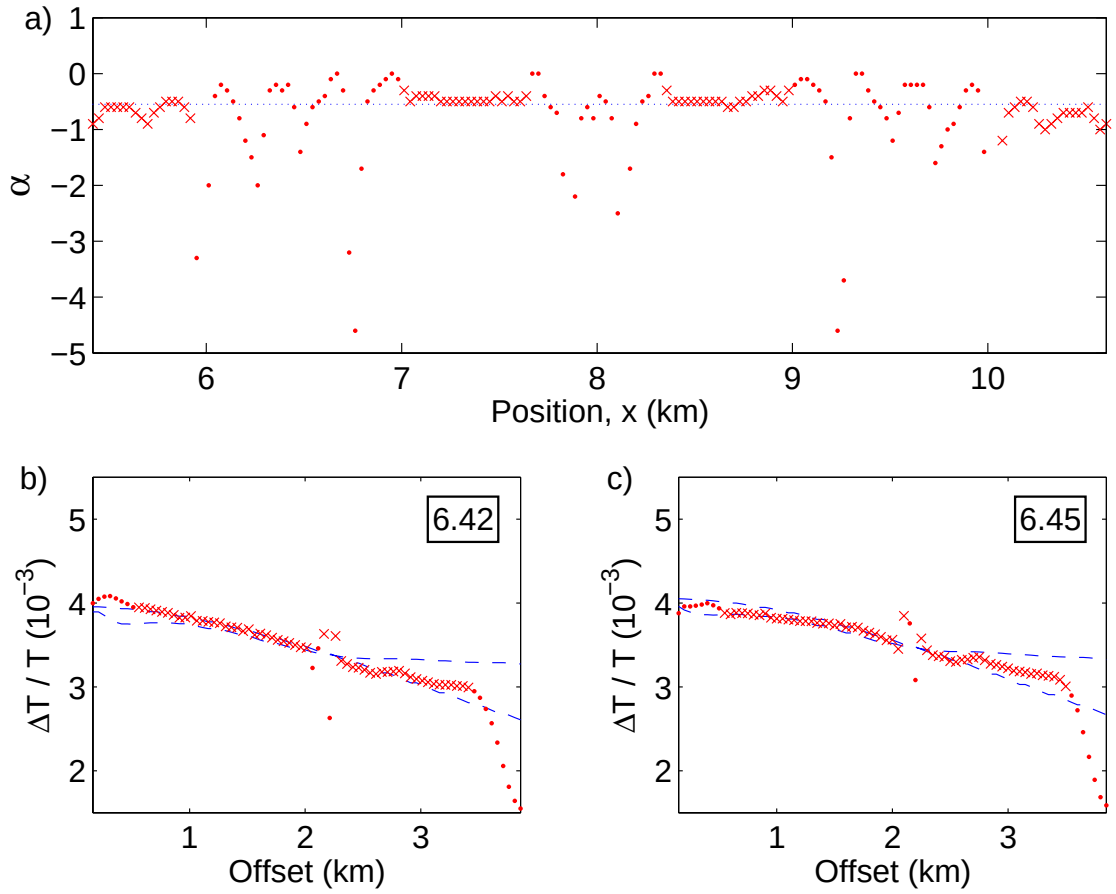

Figure 3.8: Estimated α-values (a) for all lateral positions, showing positions with both acceptable (crosses) and low (solid dots) sensitivity in α. The dotted line indicates the modeled $\alpha = -0.7$. Examples of low sensitivity in α are given for the positions $x = 6.42$ km (b) and $x = 6.45$ km (c). These positions show the difficulties of fitting an accurate α to the picked time shifts (crosses) when the window between the initial and last guess of α (that is, $\alpha = 0$ and $\alpha = -5$) (dashed lines) is small. (The solid dots in (b) and (c) indicate bad picked time shifts.)

estimate a standard deviation of 0.2 for the optimal α-value of -0.6.

Substituting the optimal α-value into equation (3.8) gives changes in thickness and velocity. The results are summarized in Figure 3.9 for the initial guess ($\alpha = 0$), the optimal α-value (-0.6), and the last guess ($\alpha = -5$). The optimal result in thickness and velocity changes (solid line in Figure 3.9) are very close to the modeled changes (dashed line in Figure 3.9). The average error between estimated and modeled changes is 3.5% for Δz and 12.3% for Δv.

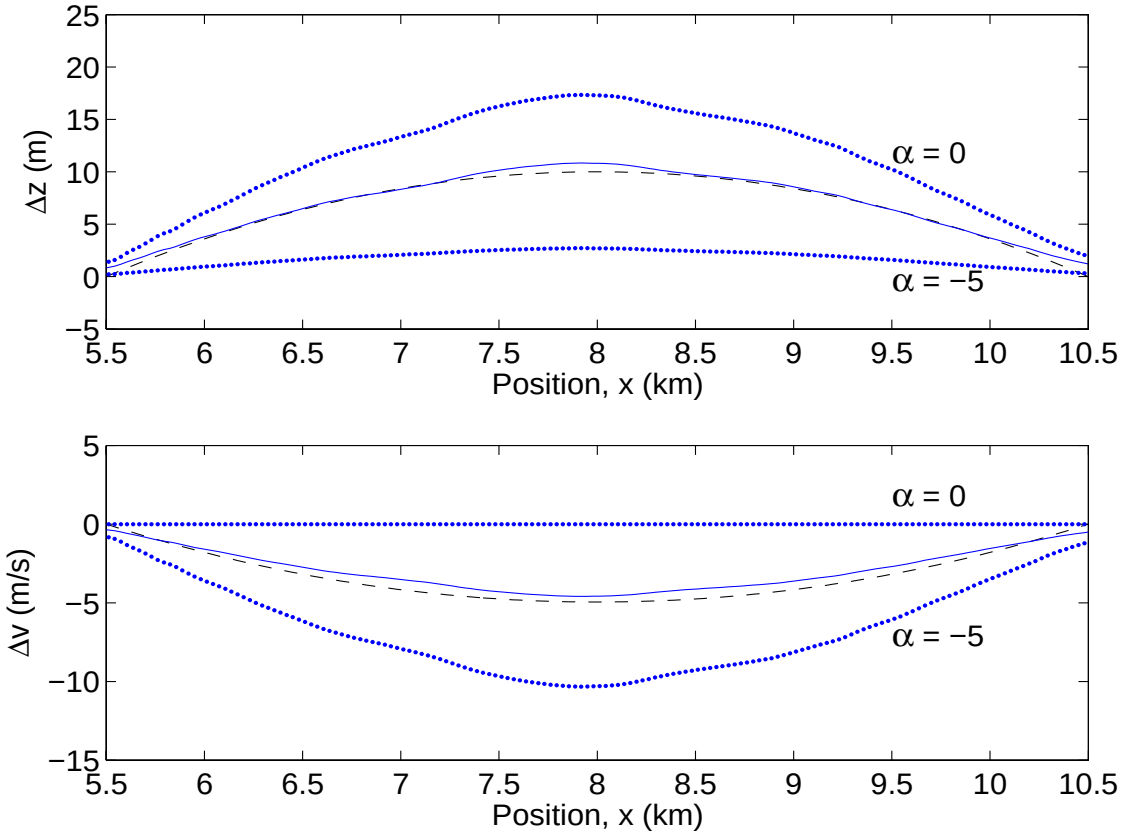

Figure 3.9: Results from the synthetic model. Estimated changes (solid line) in thickness (top) and velocity (bottom), as a function of position (inside 5.5 km $<$ x $<$ 10.5 km), for the sequence from the sea surface to the top reservoir horizon. The modeled values are shown as a dashed line. The solid dots correspond to the initial and last guess of α (that is, $\alpha = 0$ and $\alpha = -5$).

3.5 Field-data example

The method is tested on a prestack time-lapse 2D seismic line from the Valhall Field (around well A30B, see top of Figure 3.10), acquired in 1992 and in 2002. Different sources and source depths were used in the two surveys, causing some frequency and wavelet differences between the two surveys. It was therefore necessary to match the prestack datasets with respect to frequency, amplitudes, and residual traveltimes prior to testing the method. The differences in amplitudes were not entirely global, but were found to be almost constant inside a specific time window for a specific offset range; that is, for a time window between 1.5 s and 3.0 s and offsets between 0.25 km and 2.5 km. The residual time shifts inside this area were found to be constant and therefore easy to correct. A frequency-wavenumber filter

was applied to decrease the multiple energy (Yilmaz, 1987). Bottom of Figure 3.10 shows a poststack section (from 1992) of the selected portion of the 2D line. The total length of the selected portion is 2.5 km and, for simplicity, we define the north-west and south-east ends as positions 0 km and 2.5 km, respectively (see Figure 3.10). The top of the reservoir is around 2.6 s (two-way traveltime), corresponding

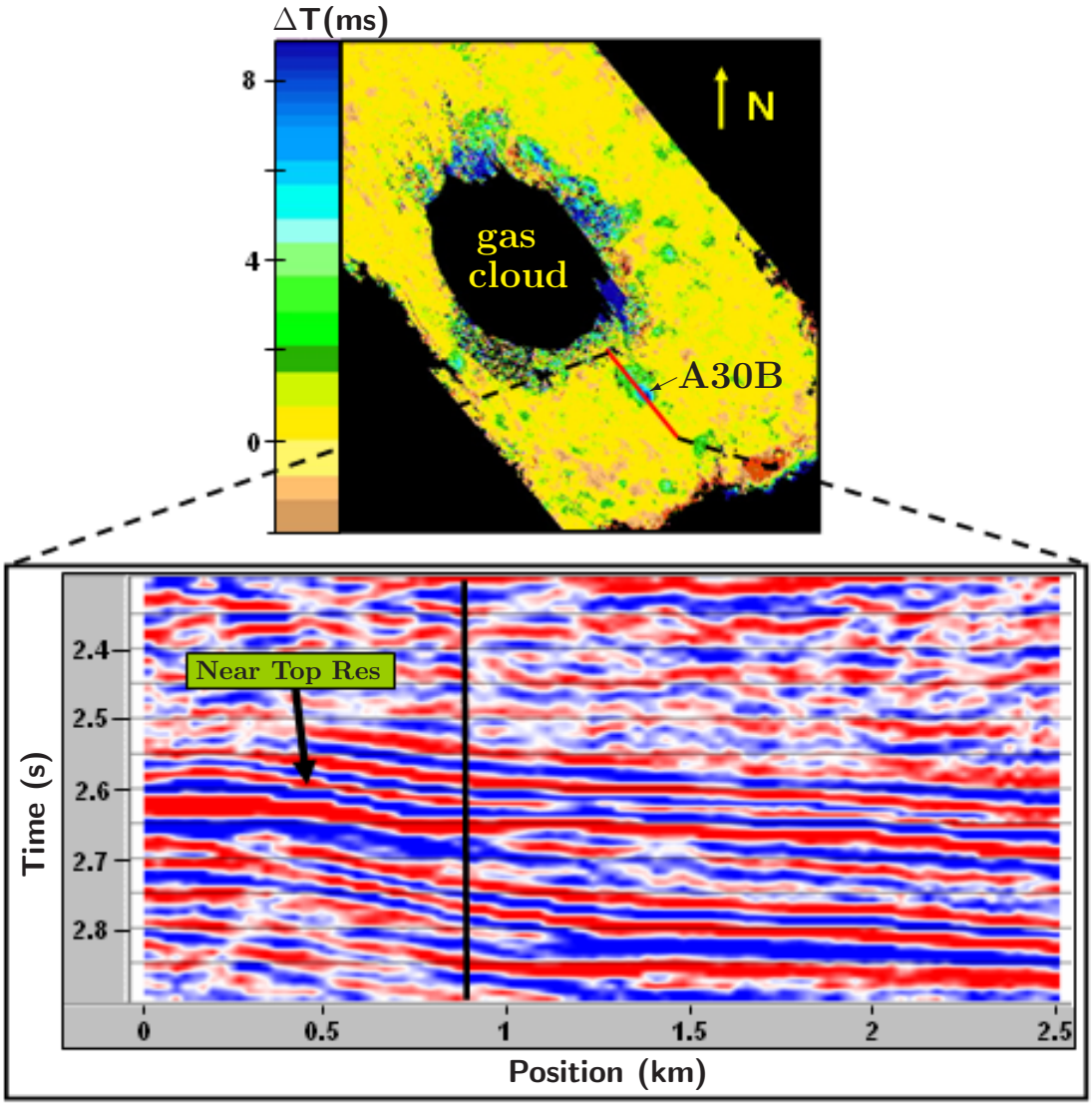

Figure 3.10: Top: Time difference map of the Valhall Field between 1992 and 2002. The selected 2D line (marked) intersects with well A30B. Bottom: Poststack section from 1992 of the selected 2D line focused on the reservoir section. We investigate a horizon around two-way traveltime 2.6 s, which is near the top reservoir horizon. Results from position 0.93 km (marked) are shown in the next figures.

to approximately 2.5 km in depth.

3.5.1 Estimating α for the overburden

We investigate an overburden sequence from the sea surface to a horizon (at 2.6 s) near the top of the reservoir, which will be referred to as the top reservoir horizon. Figure 3.11 shows a prestack gather (from 1992) at lateral position 0.93 km (marked vertical line on the poststack section at the bottom of Figure 3.10). We mute above and below the solid lines (Figure 3.11) to isolate the top reservoir event. After muting, traveltimes are picked for interpolated maximum amplitudes. Similar to the synthetic case, traveltimes for zero offset are estimated from the standard hyperbolic approximation (equation (3.22)). For some positions at the flanks, the events from the top reservoir horizon are weak. (By flanks we mean the areas outside the circular anomaly around well A30B; see Figure 3.10.) Figure 3.12 shows the estimated (crosses) and laterally smoothed (solid line) relative time shifts for

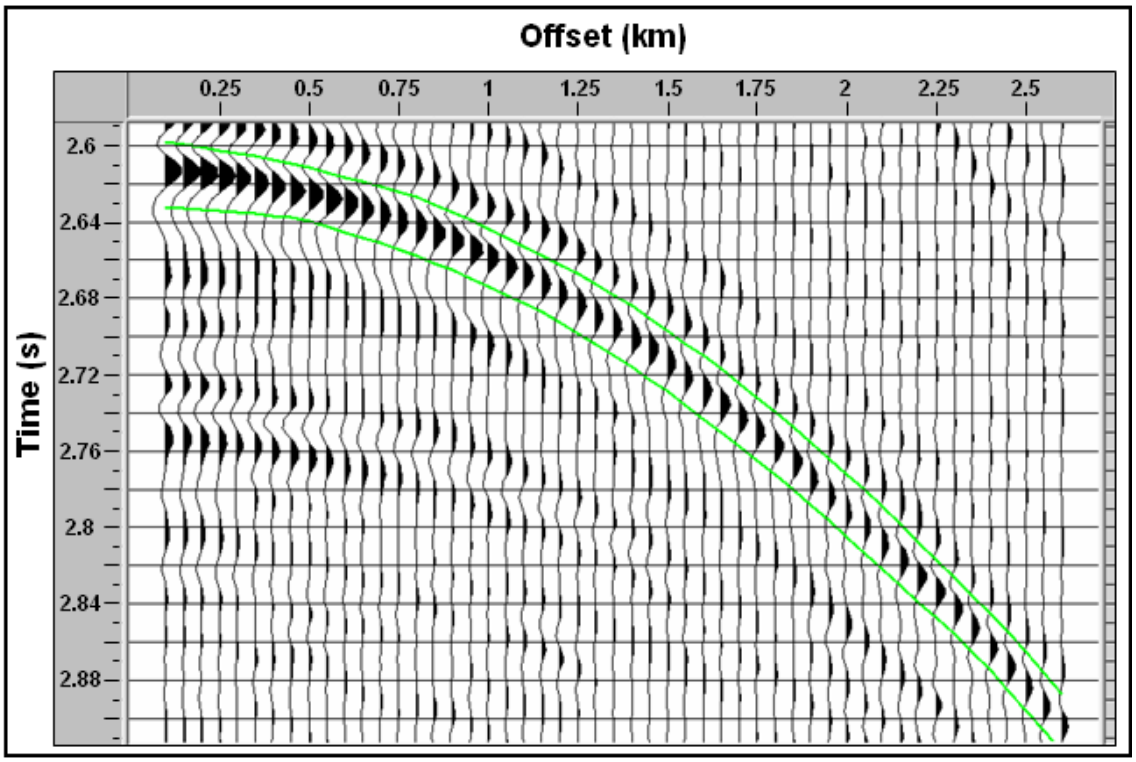

Figure 3.11: Example of event picking in a prestack gather from the Valhall Field baseline (1992) at position 0.93 km. We mute above and below the top reservoir horizon (marked with solid lines) prior to time shift analysis. After muting, traveltimes are picked for interpolated maximum amplitudes.

zero offset for the top reservoir horizon, where we force unphysical time shifts at the flanks to be zero prior to smoothing. This zeroing of time shifts at the flanks can be supported by the trend of the time shifts before reaching the flanks, and, in addition, to the fact that no production effects are expected at the flanks.

Again, using equation (3.9), we search for the α-value which leads to the minimum least square error between the estimated and picked relative time shifts. Figure 3.13 shows the picked time shifts (crosses) together with the best-fitting α (solid line) for position 0.93 km from the investigated sequence. Bad picked time shifts (solid dots in Figure 3.13) are automatically excluded prior to finding the optimal α. The dashed lines in Figure 3.13 correspond to the initial and last guess of α; that is, $\alpha = 0$ and $\alpha = -5$.

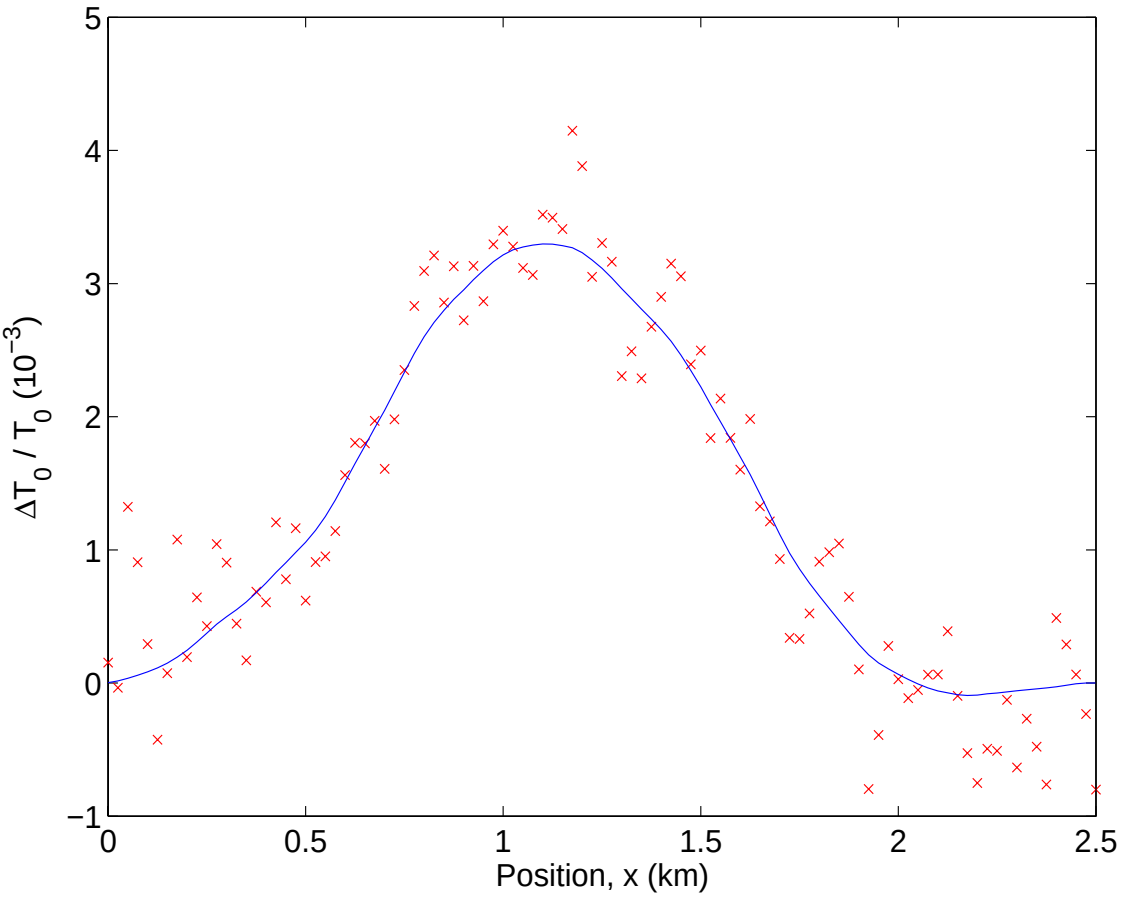

Figure 3.12: Estimated (crosses) and smoothed (solid line) zero-offset relative time shifts (field data) for the top reservoir horizon. Unphysical estimates at the (anomaly) flanks are set to zero prior to smoothing.

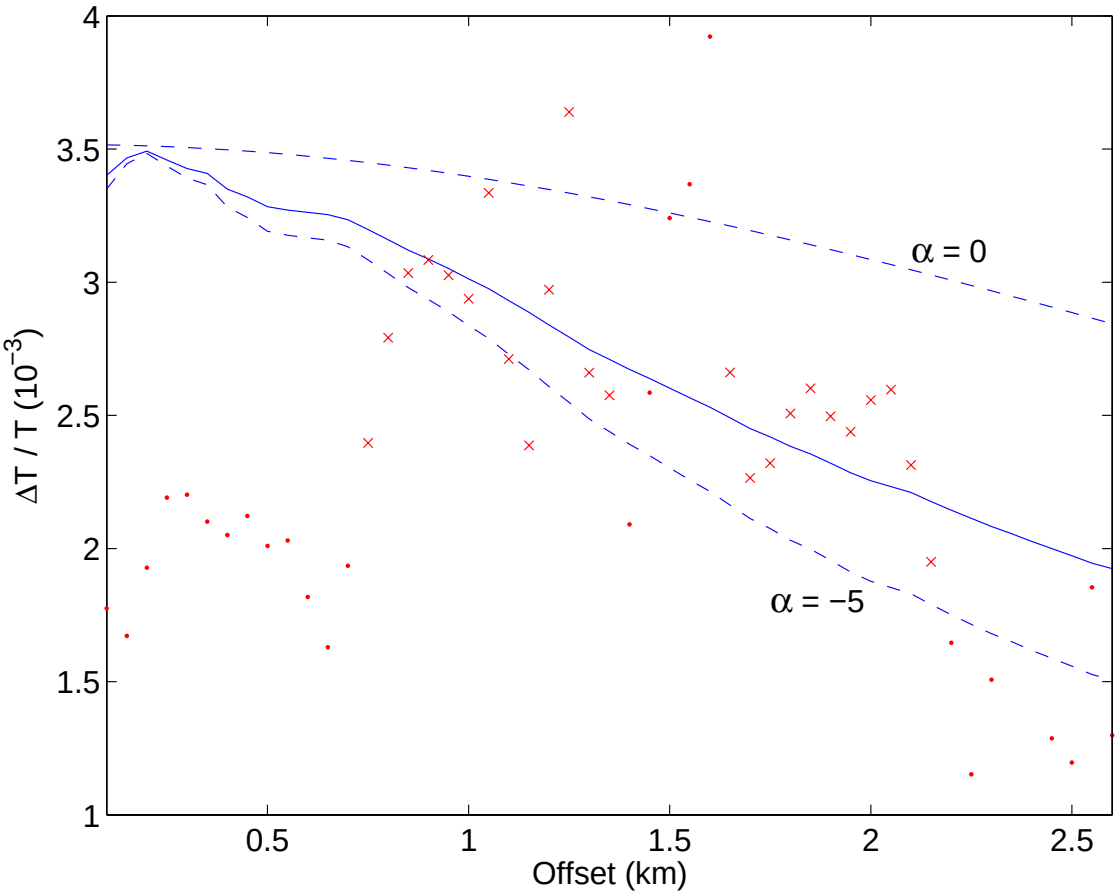

Figure 3.13: Example of finding α for the top reservoir horizon for position 0.93 km. The solid line indicates the best fit of the picked relative time shifts (crosses) as a function of offset. Bad picked time shifts (solid dots) are automatically excluded prior to finding the best fit (solid line). The dashed lines correspond to the initial and last guess of α (that is, $\alpha = 0$ and $\alpha = -5$).

If too many bad time-shift picks are observed for a given position, we simply exclude this position when searching for the optimal α-value. An example of such a position is at 0.10 km (see Figure 3.14), where more than 70% of the picked time shifts are bad (solid dots), and hence it is excluded from further analysis. (The bad picks for position 0.10 km might also be predicted by investigating the estimated zero-offset time shifts (Figure 3.12). Estimations around position 0.10 km have a larger deviation from the smooth curve.) Furthermore, notice that the sensitivity for α is low for position 0.10 km; that is, as mentioned in the last section, the window between the initial and last guessed α-values (dashed lines in Figure 3.14) is small, which makes

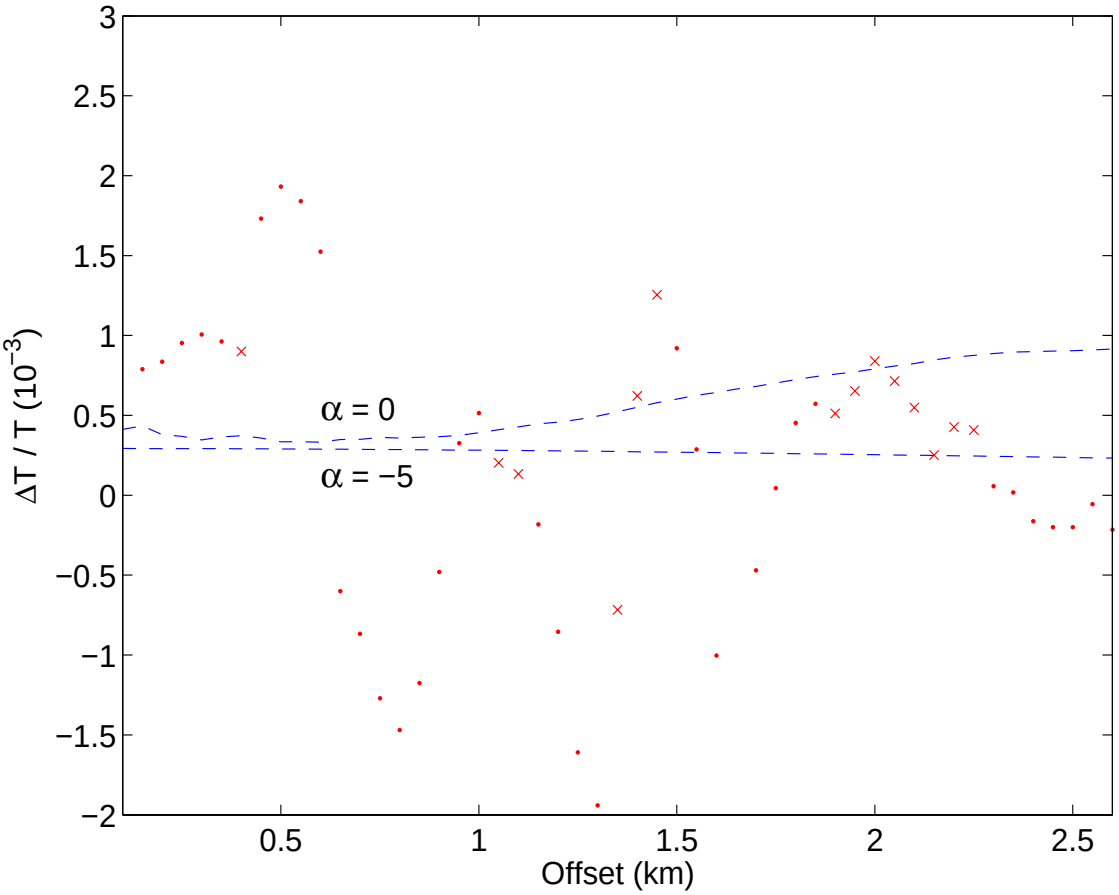

Figure 3.14: Example of a position (0.10 km) with poor picked time shifts; that is, over 70% of the picked relative time shifts are (automatically) found to be bad (solid dots). The existing picked time shifts (crosses) cannot be fitted to an optimal α-value between the initial and last guess of α (that is, $\alpha = 0$ and $\alpha = -5$) (dashed lines).

it difficult to determine an optimal α-value with high accuracy. Investigations show that low sensitivity in α occurs especially at the anomaly flanks (for this dataset), while the middle of the anomaly has higher α sensitivity and generally a smaller number of bad time shift picks. We therefore decided to estimate an α only based on a few positions in the middle (that is, the positions from 0.80 km to 1.13 km). All estimated α-values for the sequence from the sea surface to the top reservoir horizon are shown in Figure 3.15, where the chosen α-values are encircled. The chosen estimates indicate an average α-value of -2.1, with a standard deviation of 0.5. A more detailed uncertainty estimation method is discussed in Appendix 3.F. Assuming an uncertainty of 0.3×10^{-3} for both zero-offset and offset-dependent relative

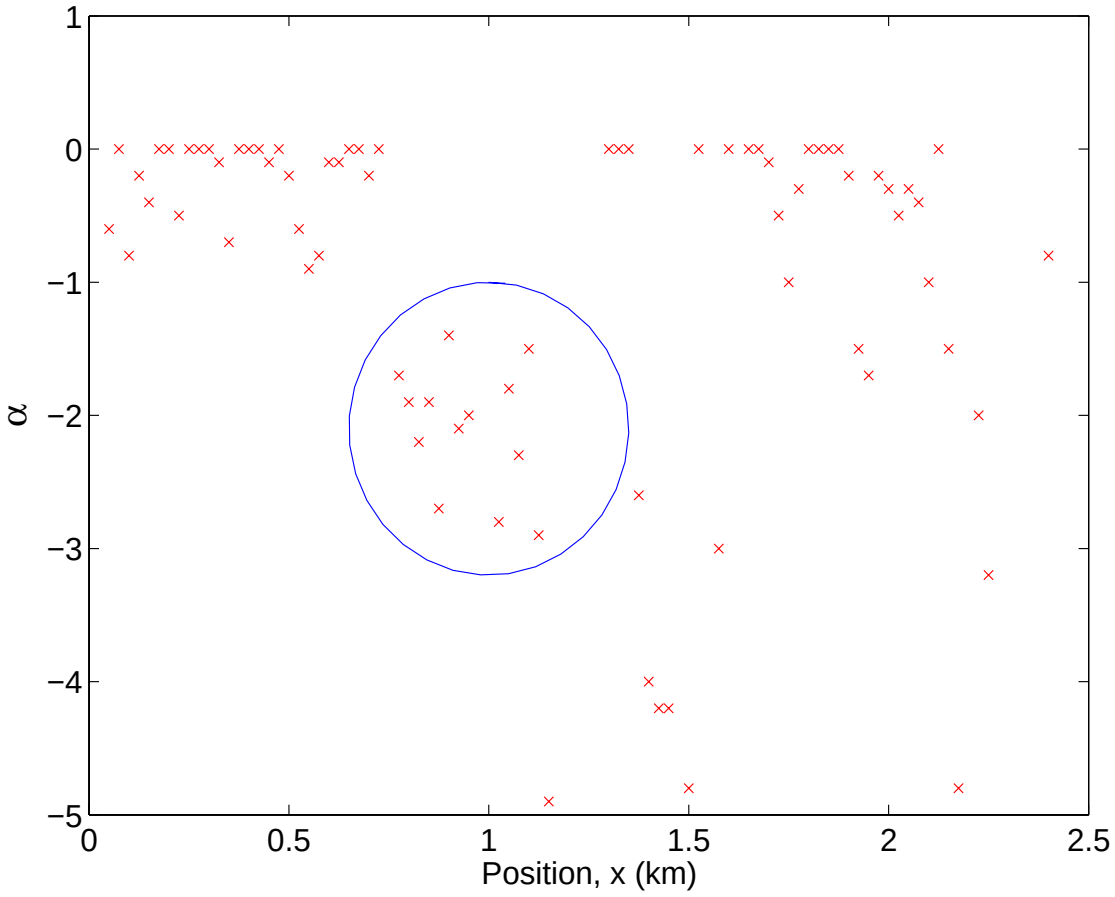

Figure 3.15: Estimated α-values (crosses) for the sequence from the sea surface to the top reservoir horizon for all positions. From investigations we decided to trust only the estimates in the middle (encircled). This gives an average α-value of -2.1 (with a standard deviation of 0.5).

time shifts gives an uncertainty of 1.7 in the estimated α of -2.1 (see Appendix 3.F).

Figure 3.16 shows estimated thickness and velocity changes (solid line) using the estimated α-value of -2.1, together with initial ($\alpha = 0$) and last guess ($\alpha = -5$) of α (solid dots). The estimated optimal result in Figure 3.16 indicates a maximum subsidence of the top reservoir horizon of 2.7 m and a maximum velocity decrease for the overburden sequence of 4.5 m/s. Using the estimated uncertainty in α of 1.7 yields corresponding uncertainties in thickness and velocity changes of 1.6 m and 1.3 m/s, respectively (indicated with dashed lines in Figure 3.16).

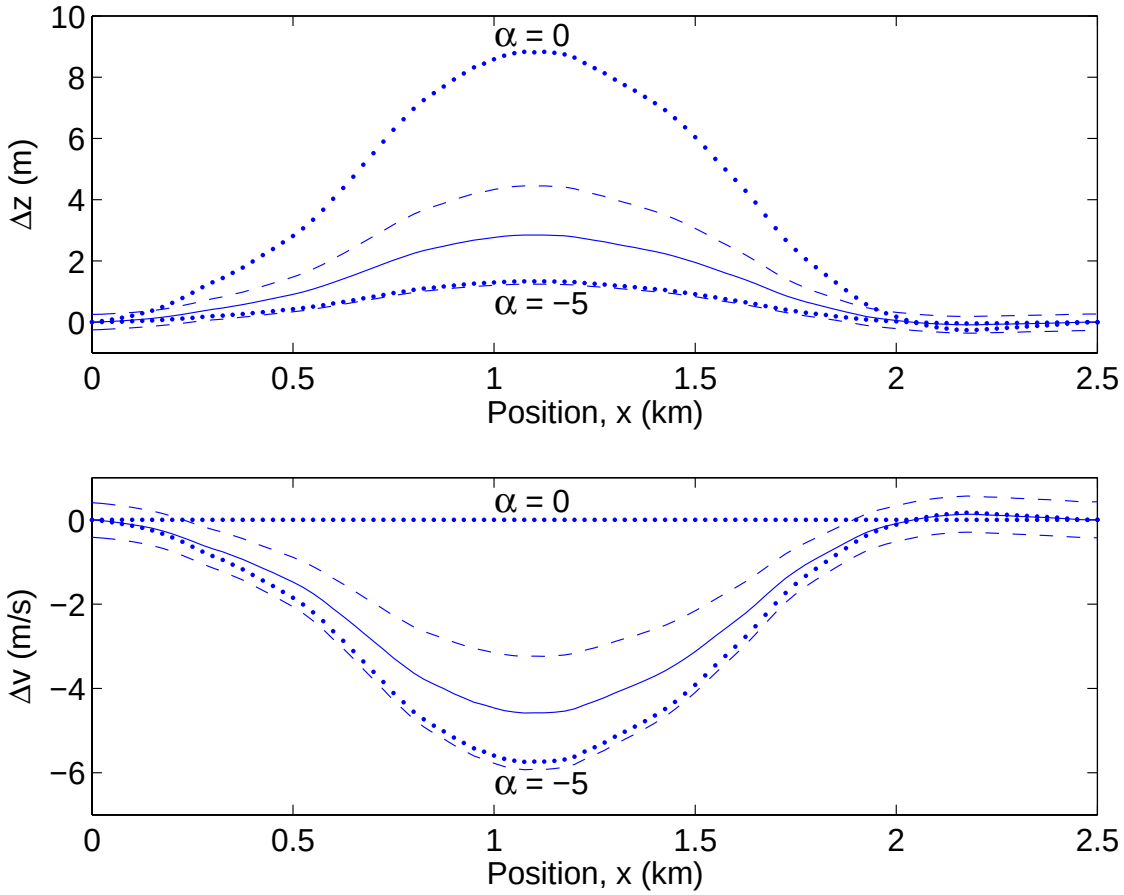

Figure 3.16: Results from the Valhall data. Estimated changes (solid line) in thickness (top) and velocity (bottom) together with indicated uncertainties (dashed lines), as a function of position, for the sequence from the sea surface to the top reservoir horizon. The solid dots correspond to the initial and last guess of α (that is, $\alpha = 0$ and $\alpha = -5$).

3.5.2 Estimating α for the reservoir layer and overburden rocks

In addition to the top reservoir horizon, traveltimes are picked for the base reservoir horizon to find the zero-offset time shifts within the reservoir layer. We assume that the base reservoir horizon is constant in depth during production, which means that the compaction of the reservoir layer is equal to the subsidence of the top reservoir horizon (that is, 2.7 m at maximum). Rearranging equation (3.8) gives

$$\alpha_{\text{res}} \approx 1 - \frac{\Delta T_{0,\text{res}}}{T_{0,\text{res}}} \left(\frac{\Delta z_{\text{res}}}{z_{\text{res}}} \right)^{-1}, \tag{3.24}$$

where z_{res} is the reservoir thickness and $T_{0,\text{res}}$ is the zero-offset traveltime within the reservoir layer. Figure 3.17 shows the estimated α-values for the reservoir using equation (3.24). For areas with small time-lapse changes, typically at the anomaly flanks, equation (3.24) becomes inaccurate (see Figure 3.17). However, estimates at the (anomaly) crest (that is, for positions from 0.68 km to 1.68 km (see Figure 3.17)), indicate an optimal α close to -1.5, with a standard deviation of 0.35. This value is identical to the value estimated from equation (3.3) using the empirical velocity-porosity relation for chalk. Figure 3.18 shows the thickness and velocity changes (solid line) of the reservoir layer when using the optimal α-value of -1.5, indicating a maximum velocity increase of 200 m/s (and a maximum compaction of 2.7 m, as expected). The uncertainty in zero-offset relative time shifts for the

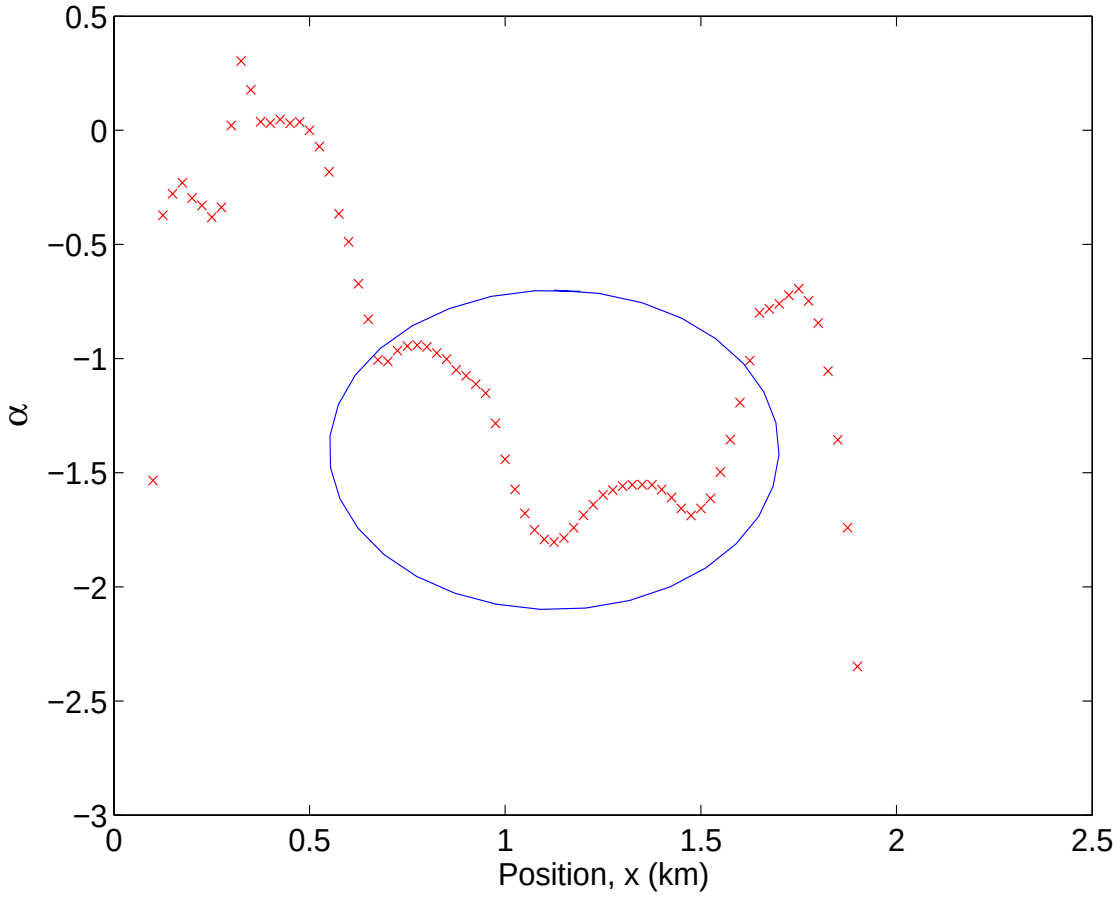

Figure 3.17: Estimated α-values (crosses) for the reservoir layer for all positions. Estimations of α become difficult at the (anomaly) flanks (that is, for small zero-offset time shifts). However, the estimates between positions 0.68 km and 1.68 km (encircled) indicate an optimal (average) α of -1.5.

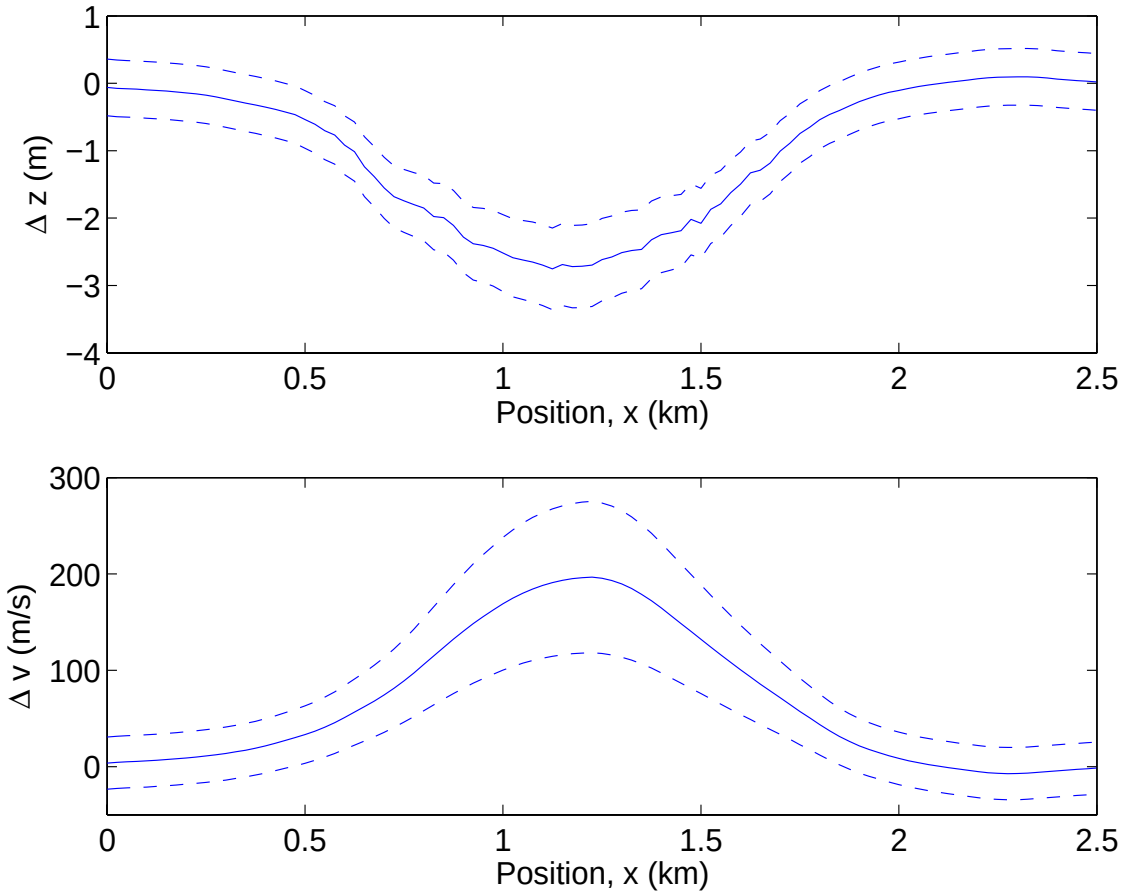

Figure 3.18: Estimated changes (solid line) in thickness (top) and velocity (bottom) for the reservoir layer (as a function of position) when using an optimal α-value of -1.5. The dashed lines indicate the uncertainties.

reservoir layer is estimated to be 15×10^{-3} by assuming a deviation in zero-offset relative time shifts for both top and base reservoir of 0.3×10^{-3}. This gives an uncertainty (marked as dashed lines in Figure 3.18) in the maximum estimated reservoir velocity change (+200 m/s) of 85 m/s, when assuming an uncertainty of 0.35 in the estimated α (of -1.5) for the reservoir.

We estimated an average α from the sea surface to the top reservoir horizon of -2.1. If we know the sea bed subsidence, this α-value can be used to estimate the α-value for overburden rocks only, using equation (3.24). Bathymetry surveys (Hall et al., 2005) show a maximum sea bed subsidence of approximately 0.5 m in our area, corresponding to a maximum stretch of the overburden rocks of 2.2 m. This gives an α-value of -2.6 for the overburden rocks, which is very close to the

rock physics estimate based on equation (3.3) and Han's (1986) empirical relation for clay, which is -2.7. Tosaya and Nur's (1982) relation for clay give a slightly different value (-3.6).

3.5.3 Anisotropy

In cases with overburden thickness and velocity changes, we might expect changes in anisotropy. For simplicity we have chosen not to incorporate anisotropy in the developed method. Investigations show that static anisotropy has almost no effect on the method (equation (3.9)). However, large time-lapse anisotropy *changes* must be included. We test the method on a synthetic model that consists of one overburden layer with thickness 2500 m and velocity 2100 m/s, and a second layer which simulates a reservoir. The overburden layer has initially anisotropic parameters similar to Valhall; that is, Thomsen's (1986) anisotropic parameters $\delta = 0.05$ and $\epsilon = 0.05$ (see Le Rousseau and De Hoop, 2001; Guerrero et al., 2002). For the monitor case, the overburden layer undergoes a stretch of 2.0 m, and a vertical velocity decrease of 4.5 m/s. Corresponding changes in the anisotropic parameters δ and ϵ are tested for two cases; that is, 1) 0.5% change in both ϵ and δ and 2) 1.0% change in both ϵ and δ.

The choices of change in anisotropic parameters (for the two given cases) are based on Yongyi (2004). He links the anisotropic parameter ϵ to vertical (P-wave) velocities and clay volume (based on laboratory measurements) as follows:

$$\epsilon = \frac{0.7V_{\text{clay}}(v_p - v_{p,\text{water}})}{v_{p,\text{quartz}} - v_{p,\text{water}} - 2.29V_{\text{clay}}}, \tag{3.25}$$

where v_p denotes the vertical velocity and V_{clay} denotes the clay volume. The parameters $v_{p,\text{quartz}} = 6050$ m/s and $v_{p,\text{water}} = 1500$ m/s are velocities for quartz and water, respectively. Assuming an average clay volume of 50% for the overburden layer gives $\epsilon \approx 0.06$ from equation (3.25), when using the initial vertical velocity of 2100 m/s. Substituting the vertical velocity for the monitor case (that is, 2095.5 m/s) in equation (3.25) gives a change in ϵ of 0.75% (when assuming constant clay volume). For simplicity, we assume that δ and ϵ have changes of the same order; that is, around 0.75%.

For the overburden layer, we found the optimal α to be -2.1 for case 1 (that is, when $\Delta\epsilon/\epsilon = \Delta\delta/\delta = 0.5\%$) and -1.5 for case 2 (that is, when $\Delta\epsilon/\epsilon = \Delta\delta/\delta = 1.0\%$). The modeled $\alpha = -2.6$, which equals a deviation in the estimated α of 19% for case 1 and 42% for case 2. The estimated values of α give $\Delta z = 2.5$ m and $\Delta v = -4.4$ m/s for case 1 and $\Delta z = 3.1$ m and $\Delta v = -3.9$ m/s for case 2. The modeled values are $\Delta z = 2.0$ m and $\Delta v = -4.5$ m/s, which equals a deviation in the estimated Δz and Δv of 25% and 2% (respectively) for case 1, and 55% and 13% (respectively) for case 2. This shows that the uncertainty in estimated thickness and velocity

changes becomes severe when the changes in anisotropic parameters exceed 1%.

3.6 Discussion

Static anisotropy is found to be much less of a problem than time-lapse changes in anisotropy. We find that changes of only 1% in the anisotropic parameters need to be taken into account.

For the estimated α of -1.5 for the reservoir layer (field data), we assume that the base of the reservoir is constant in depth during reservoir compaction. This is not the case for a layer that consists of the same type of material as the surroundings, in which case the base of the layer tends to move upward during layer compaction (see Tura et al., 2005). At Valhall, hard chalk underlies the reservoir chalk, and we believe that this hard chalk is less affected by reservoir changes. However, a sequence of 0.4 km right below the reservoir layer shows time shifts (maximum 1-2 ms) that indicate stretch. An uplift of the base reservoir horizon at Valhall is also predicted by Hatchell and Bourne (2005b). This means (equation (3.8)) that the magnitude of the estimated α is overestimated, and correspondingly the velocity increase is also overestimated.

Our estimates of the dilation factor (α) is in good agreement with empirical rock physics relations. However, it should be noted that these empirical relations are based on ultrasonic measurements relating velocity to porosity. We do not know to what extent such empirical relationships can be used for a dynamic case, where velocity changes are introduced by for instance stretching of the rock.

The proposed method can be further improved by utilizing data with larger offsets. In addition, new rock physics models can be used to constrain the α-parameter estimation. Geomechanical modeling and reservoir simulation can give additional information (Hatchell et al., 2005; Vidal et al., 2002). Improved results can also be achieved by including ray-bending and by accounting for vertical variations in (relative) velocity changes.

The proposed method was tested on a sequence from the sea surface to the top reservoir horizon, and then, indirectly, the thickness and velocity changes for the reservoir layer and overburden rocks (for the Valhall Field) were estimated. It may also be possible to apply the method directly on one single layer (for example, the reservoir layer). However, investigations show that picked offset-dependent relative time shifts become more uncertain when based on picks from both top and base

horizons of a layer, rather than a sequence from the sea surface to one (base) horizon only. In addition, correction terms are needed if the top of the layer is changing in depth, since our method was derived assuming that the top of the layer is constant (zero) in depth.

The proposed method is almost unaffected by velocity-depth ambiguities and errors in stacking velocity (see Bickel, 1990; Bube et al., 2004) which are well-known phenomena in seismic exploration. This is due to the fact that we utilize offset-dependent time shifts (rather than time-lapse changes in stacking velocity). However, it should be noted that stacking velocity is used to estimate the thickness (z), which is needed in equation (3.9). Nevertheless, investigations (of the overburden estimated $\alpha = -2.1$) show that the deviation in α is almost unaffected by uncertainties in z as large as 20%.

In all time-lapse monitoring, repeatability is crucial. Different sources and source depths were used in the time-lapse surveys (1992-2002) from Valhall. This might introduce nonrepeatability (Landrø, 1999b) even though a good match is found. Further examples of nonrepeatability problems in time-lapse seismic are differences in the source-receiver positions, changes in the water temperature, tidal differences, random noise in the recording units, and coherent noise such as free surface multiples. In addition, for cases with reservoir compaction and corresponding overburden changes, the elastic wavefield parameters and, further, the quality factor Q (damping), change. Stewart et al. (1984) derived an equation that estimates the delay in traveltimes based on traveltimes, frequency ratios, and quality factor Q. The quality factor Q can be estimated from a constant-Q model (Kjartansson, 1979). Combining the two models, assuming a constant Q equal to 70 for the baseline and 75 for the monitor, gives a difference in traveltime delay of 0.1 ms between baseline and monitor. Another example, using Q equal to 70 and 90 for the baseline and monitor, respectively, gives a time-lapse difference in traveltime delay of 0.5 ms.

3.7 Conclusions

Prestack analysis of time-lapse seismic traveltime shifts gives an opportunity to discriminate between layer thickness and velocity changes, for both the reservoir layer and the overburden layers. We find that the introduction of the dilation factor (ratio between relative velocity changes and relative thickness changes) is both practical and a useful concept for the prestack time lapse analysis. The developed method links the relative change in traveltime (for a given offset) with the dilation factor and the relative change in zero-offset traveltime, where lateral variations in relative velocity changes are incorporated. Basic assumptions in the derivation of the equations are the assumption of one single horizontal layer, straight raypaths

and neglecting vertical changes in the velocity field. If the method is applied to a multilayer case we find that the errors increase if the velocity changes between the layers are significant. For a synthetic model consisting of 5 overburden layers that are stretched and a compacting reservoir layer, we find that our method can be applied successfully to estimate the average dilation factor for the overburden layers.

For the top reservoir horizon at the Valhall Field we estimate a maximum subsidence of 2.7 m $\pm$ 1.6 m and a corresponding velocity decrease for the sequence from the sea surface to the top reservoir of 4.5 m/s $\pm$ 1.3 m/s. For the reservoir section a maximum velocity increase of 200 m/s $\pm$ 85 m/s is calculated when related to the maximum top reservoir subsidence (of 2.7 m).

The method does not require any information or model for the mechanism creating the velocity change. Discrimination between pressure, fluid, or compaction changes should be performed in a preceding analysis step. Compared to measured compaction rates in other areas of this field, the estimated values are reasonable.

3.8 Acknowledgments

Thomas Røste acknowledges TOTAL for financial support, and Jerome Guilbot, Yahui Yin, and Ruben Sanchez for valuable discussions. We thank the Valhall partnership (BP Norge AS, Amerada Hess Norge AS, A/S Norske Shell, and Total E&P Norge AS) for providing data from the Valhall Field and permission to publish this work, as well as Ole Jøran Askim, Olav Barkved, and Tron G. Kristiansen for support and discussions. We also acknowledge constructive comments from several reviewers and Yonghe Sun for discussions in finalizing this paper. Martin Landrø and Alexey Stovas acknowledge the Norwegian Research Council for financial support to the ROSE project at NTNU. Finally, we thank Øyvind Kvam for advice on making the synthetic model. The results and opinions presented in this paper do not necessarily reflect the view of the Valhall partnership.

3.A Rock physics

Well log observations show empirical relationships between velocity (v) and porosity(ϕ) given as (Han, 1986; Rafavich et al., 1984)

$$v = a - b\phi, \tag{3.A-1}$$

where a and b are positive constants. Differentiation of equation (3.A-1) and substitution of b gives

$$\frac{dv}{v} = \left(1 - \frac{a}{v}\right)\frac{d\phi}{\phi}. \tag{3.A-2}$$

The uniaxial strain relationship reads (Guilbot and Smith, 2002)

$$\frac{d\phi}{1-\phi} = \frac{dz}{z+dz}, \tag{3.A-3}$$

where z and dz denote thickness and thickness changes, respectively. By assuming small changes and substituting for ϕ (given by rearranging equation (3.A-1)), equation (3.A-3) reads

$$\frac{d\phi}{\phi} = \frac{dz}{z}\left(\frac{b}{a-v} - 1\right). \tag{3.A-4}$$

Substituting equation (3.A-4) into equation (3.A-2) gives

$$\frac{dv}{v} = \left(\frac{a-b}{v} - 1\right)\frac{dz}{z}. \tag{3.A-5}$$

Equation (3.A-5) shows that relative thickness and velocity changes are linked by the factor:

$$\alpha = \frac{a-b}{v} - 1, \tag{3.A-6}$$

which is spatially dependent since a, b, and v are expected to vary spatially.

3.B Detailed derivation of the method

Assuming a one-layer model with straight raypaths, seismic two-way traveltime for a ray with CDP-position x_0 and offset $2h$ can be expressed as

$$T(x_0,h)=\sqrt{1+\frac{z^2(x_0)}{h^2}}\int\limits_{x_0-h}^{x_0+h}\frac{dx}{v(x)}. \tag{3.B-1}$$

For the post-production (or monitor) case, the two-way traveltime is

$$T'(x_0,h)=\sqrt{1+\frac{z^2(x_0)}{h^2}\left(1+\frac{\Delta z(x_0)}{z(x_0)}\right)^2}\int\limits_{x_0-h}^{x_0+h}\frac{dx}{v(x)\left(1+\frac{\Delta v(x)}{v(x)}\right)}, \tag{3.B-2}$$

where $\Delta v(x)/v(x)$ is assumed to vary with lateral position x, but not with depth. The square root and functions $(1+\Delta z(x_0)/z(x_0))^2$ and $(1+\Delta v(x)/v(x))^{-1}$ in equation (3.B-2) can be expanded in Taylor series. Assuming small relative changes in velocity and thickness; that is, keeping only the first expanded term, equation (3.B-2) becomes

$$\begin{aligned}
T'(x_0,h) &\approx \sqrt{1+\frac{z^2(x_0)}{h^2}\left(1+2\frac{\Delta z(x_0)}{z(x_0)}\right)}\int\limits_{x_0-h}^{x_0+h}\frac{dx}{v(x)}\left(1-\frac{\Delta v(x)}{v(x)}\right)\\
T'(x_0,h) &= \sqrt{1+\frac{z^2(x_0)}{h^2}+2\frac{z^2(x_0)}{h^2}\frac{\Delta z(x_0)}{z(x_0)}}\int\limits_{x_0-h}^{x_0+h}\frac{dx}{v(x)}\left(1-\frac{\Delta v(x)}{v(x)}\right)\\
T'(x_0,h) &= \sqrt{1+\frac{z^2(x_0)}{h^2}}\sqrt{1+\frac{2\frac{z^2(x_0)}{h^2}\frac{\Delta z(x_0)}{z(x_0)}}{1+\frac{z^2(x_0)}{h^2}}}\int\limits_{x_0-h}^{x_0+h}\frac{dx}{v(x)}\left(1-\frac{\Delta v(x)}{v(x)}\right)\\
T'(x_0,h) &\approx \sqrt{1+\frac{z^2(x_0)}{h^2}}\left(1+\frac{\frac{z^2(x_0)}{h^2}\frac{\Delta z(x_0)}{z(x_0)}}{1+\frac{z^2(x_0)}{h^2}}\right)\int\limits_{x_0-h}^{x_0+h}\frac{dx}{v(x)}\left(1-\frac{\Delta v(x)}{v(x)}\right)\\
T'(x_0,h) &= \sqrt{1+\frac{z^2(x_0)}{h^2}}\left(1+\frac{z^2(x_0)}{h^2+z^2(x_0)}\frac{\Delta z(x_0)}{z(x_0)}\right)\\
&\quad\times\int\limits_{x_0-h}^{x_0+h}\frac{dx}{v(x)}\left(1-\frac{\Delta v(x)}{v(x)}\right).
\end{aligned} \tag{3.B-3}$$

From equations (3.B-1) and (3.B-3) the relative change in two-way traveltime becomes

$$\frac{\Delta T(x_0,h)}{T(x_0,h)} = \frac{\left(1+\frac{z^2(x_0)}{h^2+z^2(x_0)}\frac{\Delta z(x_0)}{z(x_0)}\right)\int\limits_{x_0-h}^{x_0+h}\frac{dx}{v(x)}\left(1-\frac{\Delta v(x)}{v(x)}\right)}{\int\limits_{x_0-h}^{x_0+h}\frac{dx}{v(x)}}-1. \qquad (3.B\text{-}4)$$

By assuming small lateral variations in initial layer velocity in the vicinity of each position x_0; that is, $v(x)\approx v(x_0)$ for $x_0-h\le x\le x_0+h$, the term $1/v(x)$ can be put outside the integration signs (given in both the numerator and denominator of equation (3.B-4)) and be cancelled out. Note, however, that the lateral variations in Δv are included; that is, $\Delta v=\Delta v(x)$:

$$\frac{\Delta T(x_0,h)}{T(x_0,h)} \approx \frac{\left(1+\frac{z^2(x_0)}{h^2+z^2(x_0)}\frac{\Delta z(x_0)}{z(x_0)}\right)\frac{1}{v(x_0)}\int\limits_{x_0-h}^{x_0+h}dx\left(1-\frac{\Delta v(x)}{v(x)}\right)}{\frac{1}{v(x_0)}\int\limits_{x_0-h}^{x_0+h}dx}-1$$

$$\frac{\Delta T(x_0,h)}{T(x_0,h)} = \frac{\left(1+\frac{z^2(x_0)}{h^2+z^2(x_0)}\frac{\Delta z(x_0)}{z(x_0)}\right)\int\limits_{x_0-h}^{x_0+h}dx\left(1-\frac{\Delta v(x)}{v(x)}\right)}{2h}-1. \qquad (3.B\text{-}5)$$

Rearranging equation (3.B-5) gives

$$\begin{aligned}
\frac{\Delta T(x_0,h)}{T(x_0,h)} &= \frac{1}{2h}\int_{x_0-h}^{x_0+h} dx\left(1-\frac{\Delta v(x)}{v(x)}\right) \\
&\quad +\frac{z^2(x_0)}{h^2+z^2(x_0)}\frac{\Delta z(x_0)}{z(x_0)}\frac{1}{2h}\int_{x_0-h}^{x_0+h} dx\left(1-\frac{\Delta v(x)}{v(x)}\right)-1 \\
\frac{\Delta T(x_0,h)}{T(x_0,h)} &= 1-\frac{1}{2h}\int_{x_0-h}^{x_0+h} dx\frac{\Delta v(x)}{v(x)}+\frac{z^2(x_0)}{h^2+z^2(x_0)}\frac{\Delta z(x_0)}{z(x_0)} \\
&\quad -\frac{z^2(x_0)}{h^2+z^2(x_0)}\frac{\Delta z(x_0)}{z(x_0)}\frac{1}{2h}\int_{x_0-h}^{x_0+h} dx\frac{\Delta v(x)}{v(x)}-1 \\
\frac{\Delta T(x_0,h)}{T(x_0,h)} &= -\frac{1}{2h}\int_{x_0-h}^{x_0+h} dx\frac{\Delta v(x)}{v(x)}+\frac{z^2(x_0)}{h^2+z^2(x_0)}\frac{\Delta z(x_0)}{z(x_0)} \\
&\quad -\frac{z^2(x_0)}{h^2+z^2(x_0)}\frac{\Delta z(x_0)}{z(x_0)}\frac{1}{2h}\int_{x_0-h}^{x_0+h} dx\frac{\Delta v(x)}{v(x)}, \qquad (3.B\text{-}6)
\end{aligned}$$

where the last term in equation (3.B-6) can be neglected for small changes in relative velocity and thickness changes. This gives

$$\frac{\Delta T(x_0,h)}{T(x_0,h)} \approx -\frac{1}{2h}\int_{x_0-h}^{x_0+h} dx\frac{\Delta v(x)}{v(x)}+\frac{z^2(x_0)}{h^2+z^2(x_0)}\frac{\Delta z(x_0)}{z(x_0)}. \qquad (3.B\text{-}7)$$

The relative changes in thickness and velocity can be related to the relative change in vertical traveltime as

$$\frac{\Delta z(x)}{z(x)} \approx \left(\frac{1}{1-\alpha}\right)\frac{\Delta T_0(x)}{T_0(x)} \quad , \quad \frac{\Delta v(x)}{v(x)} \approx \left(\frac{\alpha}{1-\alpha}\right)\frac{\Delta T_0(x)}{T_0(x)}, \qquad (3.B\text{-}8)$$

which gives equation (3.B-7) on the following form:

$$\frac{\Delta T(x_0,h)}{T(x_0,h)} \approx \frac{z^2(x_0)}{z^2(x_0)+h^2}\left(\frac{1}{1-\alpha}\right)\frac{\Delta T_0(x_0)}{T_0(x_0)}-\frac{1}{2h}\left(\frac{\alpha}{1-\alpha}\right)\int_{x_0-h}^{x_0+h} dx\frac{\Delta T_0(x)}{T_0(x)}. \qquad (3.B\text{-}9)$$

Equation (3.B-9) shows that there exists a relationship between the parameter α, the relative change in traveltime for zero offset, and the relative change in traveltime for a given half-offset h.

3.C Testing equation (3.9) for a two-layer model

In order to test the accuracy of using the straight-ray approximation used in equation (3.9) and test how accurate it can be when applied to a stack of several layers, we consider a two layer model, with initial layer thicknesses z_1 and z_2, respectively. Let the incidence angle in the first layer be θ_1 and the ray angle in the second layer be θ_2. Then the two-way traveltime for the pre-stretch situation is given as

$$T = 2\left[\frac{z_1}{v_1\cos\theta_1} + \frac{z_2}{v_2\cos\theta_2}\right]. \tag{3.C-1}$$

The half-offset is given as

$$h = z_1\tan\theta_1 + z_2\tan\theta_2. \tag{3.C-2}$$

After stretching (monitor survey), the offset is conserved; that is,

$$h = (z_1+\Delta z_1)\tan(\theta_1+\Delta\theta_1) + (z_2+\Delta z_2)\tan(\theta_2+\Delta\theta_2), \tag{3.C-3}$$

where $\Delta\theta$ represents change in ray angle due to stretching. Combining equations (3.C-2) and (3.C-3) and assuming that the changes in ray angles are small due to the stretching of the layers, lead to

$$\Delta z_1\tan\theta_1 + \Delta z_2\tan\theta_2 = -z_1\Delta\theta_1(1+\tan^2\theta_1) - z_2\Delta\theta_2(1+\tan^2\theta_2). \tag{3.C-4}$$

Now we apply Snell's law for initial and monitor cases:

$$\frac{\sin\theta_1}{v_1} = \frac{\sin\theta_2}{v_2}, \tag{3.C-5}$$

$$\frac{\sin(\theta_1+\Delta\theta_1)}{(v_1+\Delta v_1)} = \frac{\sin(\theta_2+\Delta\theta_2)}{(v_2+\Delta v_2)}. \tag{3.C-6}$$

Combining equations (3.C-5) and (3.C-6) and assuming small changes in ray angles gives

$$\Delta\theta_1 = \tan\theta_1\left(\frac{\Delta v_1}{v_1} - \frac{\Delta v_2}{v_2}\right) + \Delta\theta_2\frac{v_1\cos\theta_2}{v_2\cos\theta_1}. \tag{3.C-7}$$

Inserting equation (3.C-7) into equation (3.C-4) gives an explicit expression for the change in ray angle in layer 2:

$$\Delta\theta_2 = -\frac{z_1\tan\theta_1\left(\frac{\Delta v_1}{v_1} - \frac{\Delta v_2}{v_2}\right)(1+\tan^2\theta_1) + \Delta z_1\tan\theta_1 + \Delta z_2\tan\theta_2}{z_1\frac{v_1\cos\theta_2}{v_2\cos\theta_1}(1+\tan^2\theta_1) + z_2(1+\tan^2\theta_2)}. \tag{3.C-8}$$

The traveltime after stretching for the two-layer model is given as

$$T' = 2\left[\frac{z_1+\Delta z_1}{(v_1+\Delta v_1)\cos(\theta_1+\Delta\theta_1)} + \frac{z_2+\Delta z_2}{(v_2+\Delta v_2)\cos(\theta_2+\Delta\theta_2)}\right]. \tag{3.C-9}$$

From equations (3.C-1) and (3.C-9) the relative traveltime shift can be computed, and compared to the one-layer approximation given in equation (3.9). An example of such a comparison is shown in Figure 3.2.

3.D Uncertainty estimates

Errors due to the approximations made from equation (3.6) to equation (3.9) can be investigated step by step. The approximations made from equation (3.6) to equation (3.7) are summarized by equation (3.D-1) (for small thickness changes) and equation (3.D-2) (for small velocity changes).

$$\sqrt{1+\frac{z^2(x_0)}{h^2}\left(1+\frac{\Delta z(x_0)}{z(x_0)}\right)^2} \approx \sqrt{1+\frac{z^2(x_0)}{h^2}}\left(1+\frac{z^2(x_0)}{h^2+z^2(x_0)}\frac{\Delta z(x_0)}{z(x_0)}\right) \quad (3.D\text{-}1)$$

$$\int_{x_0-h}^{x_0+h}\frac{dx}{v(x)\left(1+\frac{\Delta v(x)}{v(x)}\right)} \approx \int_{x_0-h}^{x_0+h}\frac{dx}{v(x)}\left(1-\frac{\Delta v(x)}{v(x)}\right). \quad (3.D\text{-}2)$$

These approximation steps lead to negligible error for general cases. As an example for equation (3.D-1), assuming $h = 0.5$ km, $z = 2.5$ km, and $\Delta z = 2.5$ m (that is, $\Delta z/z = 0.001$) gives the left hand side (LHS) of equation (3.D-1) equal to 5.1039225 and the right hand side (RHS) equal to 5.1039224, which corresponds to 0.000002 % relative error. Using $\Delta z/z = 0.01$ in equation (3.D-1) gives LHS = 5.1480579 and RHS = 5.1480485 corresponding to 0.0002 % relative error. A similar example for equation (3.D-2), assuming $h = 0.5$ km, $v = 2.0$ km/s, and $\Delta v = -5$ m/s (that is, $\Delta v/v = -0.0025$, where we for simplicity assume $\Delta v(x)$ and $v(x)$ laterally constant) gives the LHS in equation (3.D-2) equal to 0.501253 and the RHS equal to 0.501250, which corresponds to 0.0006% relative error. Using $\Delta v/v = -0.01$ in equation (3.D-2) gives LHS = 0.505051 and RHS = 0.505000 corresponding to 0.010 % relative error.

The approximations from equation (3.7) to equation (3.9) can be summarized in three steps:

$$\int_{x_0-h}^{x_0+h}\frac{dx}{v(x)}\frac{\Delta v(x)}{v(x)} \approx \frac{1}{v(x_0)}\int_{x_0-h}^{x_0+h}dx\frac{\Delta v(x)}{v(x)}, \quad (3.D\text{-}3)$$

$$\frac{1}{v(x_0)}\int_{x_0-h}^{x_0+h}dx\frac{\Delta v(x)}{v(x)} \approx \frac{1}{v(x_0)}\left(\frac{\alpha}{1-\alpha}\right)\int_{x_0-h}^{x_0+h}dx\frac{\Delta T_0(x)}{T_0(x)}, \quad (3.D\text{-}4)$$

$$\frac{z^2(x_0)}{h^2+z^2(x_0)}\frac{\Delta z(x_0)}{z(x_0)}\frac{1}{2h}\int_{x_0-h}^{x_0+h}dx\frac{\Delta v(x)}{v(x)} \approx 0, \quad (3.D\text{-}5)$$

where the approximation step given by equation (3.D-4) is only a substitution of the relative velocity changes; that is, $\Delta v(x)/v(x) \approx (\alpha/(1-\alpha))\,\Delta T_0(x)/T_0(x)$. The approximation given in equation (3.D-3) is the critical step. As an example, we

assume linear lateral variations in the layer velocity and velocity changes, and that position x is defined from zero to h; that is,

$$v(x) = v(0) + A\frac{x}{h}, \tag{3.D-6}$$

$$\Delta v(x) = \Delta v(0) + B\frac{x}{h}. \tag{3.D-7}$$

Inserting equations (3.D-6) and (3.D-7) into equation (3.D-3), we obtain (skipping the symmetric part of the integral)

$$\int_0^h \frac{dx(\Delta v(0) + B\frac{x}{h})}{(v(0) + A\frac{x}{h})^2} \approx \frac{1}{v(0)} \int_0^h \frac{dx(\Delta v(0) + B\frac{x}{h})}{(v(0) + A\frac{x}{h})}. \tag{3.D-8}$$

The integral on the LHS of equation (3.D-8) is equal to

$$\frac{-Ah\Delta v(0) + Bhv(0)}{A^2(A + v(0))} - \frac{-Ah\Delta v(0) + Bhv(0)}{A^2 v(0)} + \frac{B}{A^2} h \ln(\frac{A}{v(0)} + 1). \tag{3.D-9}$$

The RHS of equation (3.D-8) is equal to

$$\frac{h}{v(0)} \left[\frac{B}{A} - \left(\frac{Bv(0)}{A^2} - \frac{\Delta v(0)}{A} \right) \ln(\frac{A}{v(0)} + 1) \right]. \tag{3.D-10}$$

As an example, we assume $\Delta v(0) = 0$ (note, however, that the lateral variations in $\Delta v(x)$ are still included by parameter B). This gives the LHS of equation (3.D-8) on the following form:

$$\frac{h}{v(0)} \left[\frac{Bv^2(0)}{A^2(A + v(0))} - \frac{Bv(0)}{A^2} + \frac{Bv(0)}{A^2} \ln(\frac{A}{v(0)} + 1) \right], \tag{3.D-11}$$

and the RHS of equation (3.D-8) on the following form:

$$\frac{h}{v(0)} \left[\frac{B}{A} - \frac{Bv(0)}{A^2} \ln(\frac{A}{v(0)} + 1) \right]. \tag{3.D-12}$$

By assuming $A = B = 0.01v(0)$, the LHS of equation (3.D-8) is equal to $0.0049341\frac{h}{v(0)}$ (from equation (3.D-11)), and the RHS of equation (3.D-8) is equal to $0.0049669\frac{h}{v(0)}$ (from equation (3.D-12)) corresponding to 0.66% relative error. Using $A = B = 0.1v(0)$ in equation (3.D-8) gives LHS = $0.0440109\frac{h}{v(0)}$ and RHS = $0.0468982\frac{h}{v(0)}$ corresponding to 6.56 % relative error. This means that the approximation given by equation (3.D-3) holds as long as the lateral variations in the layer velocity and velocity changes are small (inside the offset range $2h$).

The third approximation step from equation (3.7) to equation (3.9), given by equation (3.D-5), leads normally to small errors. As an example, assuming $h = 0.5$ km, $z = 2.5$ km, $\Delta v/v = -0.0025$ (laterally constant), and $\Delta z/z = 0.001$ gives the LHS in equation (3.D-5) equal to -2.4×10^{-6}. Since RHS $= 0$, this approximation leads to an error of -2.4×10^{-6} in $\Delta T/T$, where $\Delta T/T \approx 0.0035$ (from the given $\Delta v/v$ and $\Delta z/z$); that is, an error of 0.069% in $\Delta T/T$.

3.E Synthetic model parameters

For the forward model of the reservoir layer we express the P- and S-wave velocities as a function of porosity (ϕ_{res}); that is,

$$v_{p,\text{res}} = a - b\phi_{\text{res}} \quad , \quad v_{s,\text{res}} = a' - b'\phi_{\text{res}}, \tag{3.E-1}$$

where

$$a = 5500 \text{ m/s} \quad , \quad b = 7000 \text{ m/s} \quad , \quad a' = 2845 \text{ m/s} \quad , \quad b' = 3621 \text{ m/s}. \tag{3.E-2}$$

The above given parameters are based on well logs. Differentiation of equation (3.E-1) yields

$$\Delta v_{p,\text{res}} = -b\Delta\phi_{\text{res}}, \tag{3.E-3}$$

$$\Delta v_{s,\text{res}} = -b'\Delta\phi_{\text{res}}, \tag{3.E-4}$$

where $\Delta\phi_{\text{res}}$ denotes porosity changes in the reservoir. The reservoir density is assumed to follow the relation:

$$\rho_{\text{res}} = \phi_{\text{res}}\rho_F + (1 - \phi_{\text{res}})\rho_S, \tag{3.E-5}$$

where ρ_F and ρ_S denote fluid and solid densities of the reservoir, respectively. Assuming that the fluid density is constant during compaction gives

$$\Delta\rho_{\text{res}} = (\rho_F - \rho_S)\Delta\phi_{\text{res}} = \frac{\rho_F - \rho_{\text{res}}}{(1 - \phi_{\text{res}})}\Delta\phi_{\text{res}}, \tag{3.E-6}$$

by substituting ρ_S (obtained from equation (3.E-5)).

The uniaxial strain condition reads (Guilbot and Smith, 2002)

$$\Delta\phi_{\text{res}} = (1 - \phi_{\text{res}})\frac{\Delta z_{\text{res}}}{z_{\text{res}} + \Delta z_{\text{res}}}, \tag{3.E-7}$$

where z_{res} and Δz_{res} denote the reservoir thickness and thickness changes, respectively. Substituting $\Delta\phi_{\text{res}}$ from equation (3.E-7) into the equations (3.E-3), (3.E-4), and (3.E-6) gives the following changes in the reservoir parameters:

$$\Delta v_{p,\text{res}} = -b(1 - \phi_{\text{res}})\frac{\Delta z_{\text{res}}}{z_{\text{res}} + \Delta z_{\text{res}}}, \tag{3.E-8}$$

$$\Delta v_{s,\text{res}} = -b'(1 - \phi_{\text{res}})\frac{\Delta z_{\text{res}}}{z_{\text{res}} + \Delta z_{\text{res}}}, \tag{3.E-9}$$

$$\Delta\rho_{\text{res}} = -(\rho_{\text{res}} - \rho_F)\frac{\Delta z_{\text{res}}}{z_{\text{res}} + \Delta z_{\text{res}}}. \tag{3.E-10}$$

Associated with the reservoir compaction we define overburden changes (for the forward model). For the overburden, Z_i denotes the depth (from the sea surface) down to the base interface of layer i and the change in this depth denotes ΔZ_i (where positive ΔZ_i corresponds to subsidence). The subsidence of the sea bed interface is set to

$$\Delta Z_1 = 0.8 \times \Delta z_{\text{res}}. \tag{3.E-11}$$

We assume that the subsidence of the overburden interfaces increases linearly with depth (down to the top reservoir interface); that is,

$$\Delta Z_i = F_i \times \Delta z_{\text{res}}, \tag{3.E-12}$$

where F_i is a depth dependent factor given as (only valid for the overburden layers below the sea bed; that is, $1 \leq i \leq 5$)

$$F_i = 7.634 \times 10^{-5} Z_i + 0.7939, \tag{3.E-13}$$

where Z_i (the depth down to the base interface of layer i) is given in meters. The thickness change of an overburden layer i, $\Delta z_i = \Delta Z_i - \Delta Z_{i-1}$, is given by equations (3.E-12) and (3.E-13); that is,

$$\Delta z_i \;\; = \;\; 7.634 \times 10^{-5} (Z_i - Z_{i-1}) \Delta z_{\text{res}}. \tag{3.E-14}$$

Assuming mass conservation and layer expansion only in the z-direction, the relation between changes in thickness (Δz_i) and density ($\Delta \rho_i$) for an overburden layer i is given as

$$\frac{\rho_i + \Delta \rho_i}{\rho_i} = \frac{z_i}{z_i + \Delta z_i}, \tag{3.E-15}$$

where z_i and ρ_i denote the thickness and density of layer i, respectively. For small thickness changes, equation (3.E-15) can be written

$$\frac{\Delta \rho_i}{\rho_i} = -\frac{\Delta z_i}{z_i}. \tag{3.E-16}$$

3.F Uncertainty in estimated α

The standard deviation of a function $S = S(a, b, c, ...)$, where $a, b, c, ...$ are parameters assumed to be independent of each other, is given by (Landrø, 2002)

$$\delta S = \sqrt{\left(\frac{\partial S}{\partial a}\delta a\right)^2 + \left(\frac{\partial S}{\partial b}\delta b\right)^2 + \left(\frac{\partial S}{\partial c}\delta c\right)^2 + ...}\,, \tag{3.F-1}$$

where δa denotes the standard deviation or uncertainty in parameter a, etc.

An expression for α is found by rearranging equation (3.9):

$$\alpha = \frac{\frac{z^2(x_0)}{z^2(x_0)+h^2}\frac{\Delta T_0(x_0)}{T_0(x_0)} - \frac{\Delta T(x_0,h)}{T(x_0,h)}}{\frac{1}{2h}\int\limits_{x_0-h}^{x_0+h} dx \frac{\Delta T_0(x)}{T_0(x)} - \frac{\Delta T(x_0,h)}{T(x_0,h)}}. \tag{3.F-2}$$

Using the notations

$$f_1 = \frac{z^2(x_0)}{z^2(x_0)+h^2}, \tag{3.F-3}$$

$$f_2 = \frac{1}{2h}\int\limits_{x_0-h}^{x_0+h} dx \frac{\Delta T_0(x)}{T_0(x)}, \tag{3.F-4}$$

$$f_3 = \frac{\Delta T_0(x_0)}{T_0(x_0)}, \tag{3.F-5}$$

$$f_4 = \frac{\Delta T(x_0,h)}{T(x_0,h)}, \tag{3.F-6}$$

the standard deviation in α can be written as

$$\delta\alpha = \sqrt{\left(\frac{\partial\alpha}{\partial f_1}\delta f_1\right)^2 + \left(\frac{\partial\alpha}{\partial f_2}\delta f_2\right)^2 + \left(\frac{\partial\alpha}{\partial f_3}\delta f_3\right)^2 + \left(\frac{\partial\alpha}{\partial f_4}\delta f_4\right)^2}, \tag{3.F-7}$$

where

$$\frac{\partial\alpha}{\partial f_1} = \frac{f_3}{f_2 - f_4}, \tag{3.F-8}$$

$$\frac{\partial\alpha}{\partial f_2} = \frac{f_4 - f_1 f_3}{(f_2 - f_4)^2}, \tag{3.F-9}$$

$$\frac{\partial\alpha}{\partial f_3} = \frac{f_1}{f_2 - f_4}, \tag{3.F-10}$$

$$\frac{\partial\alpha}{\partial f_4} = \frac{f_1 f_3 - f_2}{(f_2 - f_4)^2}. \tag{3.F-11}$$

Normal values for f_1 are between 0.5 and 1.0, while f_2, f_3, and f_4 are normally of the order 10^{-3}. All equations (3.F-8) to (3.F-11) are highly dependent of the difference between f_2 and f_4 which is normally of the order 10^{-3} to 10^{-4}. Investigations show that it is crucial to have differences between f_2 and f_4 larger than 1.0×10^{-4}. In addition, any uncertainties in f_1, f_2, f_3, and f_4 must be small in order to estimate α accurately.

As an example, we investigate the uncertainty in an estimated α of -2.1 for a sequence with thickness $z = 2.5$ km and half-offset $h = 1.0$ km. The uncertainty in f_1 is assumed to be 3.9% (which is obtained from equation (3.F-1) by assuming an uncertainty in both z and h of 10%). The difference between f_2 and f_4 is set to 0.66×10^{-3}. The standard deviation in zero-offset relative time shifts is estimated to be 0.33×10^{-3} for the positions 0.80 km to 1.13 km (see Figure 3.12). The standard deviation in far offset relative time shifts is estimated to 0.32×10^{-3} for position 0.93 km (see Figure 3.13), when excluding the bad picked time shifts. Assuming an uncertainty of 0.3×10^{-3} for both zero-offset and offset-dependent relative time shifts gives an uncertainty of 1.7 in the estimated α (of -2.1).

Chapter 4

Monitoring overburden layer changes and fault movements from time-lapse seismic data on the Valhall Field

Thomas Røste*, Martin Landrø*, and Paul Hatchell‡

*Norwegian University of Science and Technology,
Department of Petroleum Engineering and Applied Geophysics,
S.P.Andersens vei 15A, N-7491 Trondheim, Norway .
‡Shell International Exploration and Production, Rijswijk, The Netherlands.

Accepted for publication in Geophysical Journal International in January 2007. Presented at the ROSE meeting in Trondheim, Norway, April 2006. Expanded abstract submitted to the 69th EAGE Conference & Exhibition, London, England, June 2007.

4.1 Abstract

A method developed by Røste et al. (2005), which discriminates between layer thickness and velocity changes, is tested on prestack time-lapse seismic ocean bottom cable (OBC) data from the Valhall Field. A key parameter in this discrimination process is the dilation factor, α, which is the relative velocity change divided by the relative thickness change within a given layer. The high quality and good repeatability of the OBC data enables us to estimate α with a reasonable accuracy

for α-values between 0 and -5. For α-values below -5, complementary information, like for instance geomechanics is required. For the top reservoir horizon we estimate a maximum subsidence of 0.50 m $\pm$ 0.29 m and a corresponding velocity decrease for the sequence from the sea bed to the top reservoir of 2.0 m/s $\pm$ 0.40 m/s.

Time-lapse distortion patterns with characteristic time shift versus offset signatures are observed. The positions and vertical extents of the distortion zones are determined from raypath considerations and modeling. The distortion zones correlate with buried faults, indicating that a (time-lapse) distortion zone might be produced by a localized slip in a fault zone. We present an extended method which allows for vertical (in addition to lateral) variations in the relative thickness and velocity changes. This method can be viewed as a simplified version of time-lapse tomography, but involving less number of unknown parameters, giving more stability to the estimated changes in thickness and velocity. Using this technique, we are able to estimate α for positions with localized time-lapse distortions.

4.2 Introduction

Production-induced compaction is a significant drive mechanism for production in several North Sea reservoirs, especially the chalk reservoirs in the south. Guilbot and Smith (2002) utilized time isochron differences from 4D seismic data to detect compaction and subsidence at the Ekofisk Field. They observed seismic time shifts up to 12-16 ms between 1989 and 1999, related to compaction values of up to 6 m for the reservoir chalk formation. Røste et al. (2005) developed a method, based on prestack time-lapse seismic data, which discriminates between changes in layer thickness and velocity. They estimated a subsidence up to 2.7 m for the top reservoir horizon at the Valhall Field (in the southern part of the field) from 1992 to 2002. Reservoir compaction might have implications for production by changing permeabilities and, hence, the production performance (Hall et al., 2005). In addition, compaction might lead to subsidence of the sea bed. At the Valhall Field, Barkved and Kristiansen (2005) report a maximum subsidence of the sea bed larger than 5.4 m (since the field came on production in 1982) and increasing at 0.25 m per year. It is typical for these fields that the sea bed subsidence is less than the corresponding reservoir compaction, meaning that the overburden rocks are stretched. Often the change in geomechanical stress state for the overburden rocks leads to damage in existing wells (especially when significant shear stresses are introduced as a byproduct of the reservoir compaction). It is therefore of importance to map the velocity and thickness changes during production not only for the reservoir itself, but also for the overburden rocks. Between the wells, time-lapse seismic data is a complementary tool for obtaining this information, and the combined use of repeated seismic measurements and geomechanical knowledge is expected to be im-

portant in future monitoring projects.

Several authors (Ewing, 1985; White and Morton, 1997; Morton et al., 2006) show that there is a coupling between reservoir compaction and slip along growth faults that become active when sufficiently large volumes of fluid (oil, gas, or formation water) are produced. Fluid extraction may cause pore pressure decrease within the rocks and alter the state of stress near the faults (Geertsma, 1973). At the Valhall and Ekofisk fields, Zoback and Zinke (2002) demonstrate that as a result of production-induced pore pressure and stress changes, normal faulting appears to have spread out from the crests of the structures on to the flanks. Reynolds et al. (2003) determined the relative attendant risk of reactivation of faults in the Bight Basin by evaluating the in situ stress field. Mildren et al. (2002) tried to predict reactivation of faults by using the FAST (Fault Analysis Seal Technology) technique. Monitoring fault movements is important for several reasons. Most important, hazards are associated with wells crossing reactivated faults (Alsos et al., 2002). Maury et al. (1992) discuss how slipping faults can pose serious problems since it may cause casing failure. Kristiansen (2004) reviews the drilling history at Valhall with main focus on the increasing problems in the late 90's where several very expensive wells were lost. He concludes that wells (particularly high angle wells) are vulnerable for changes in stress changes and cavings from fault zones (see also Kristiansen, 1998). Barkved et al. (2003) report a strong correlation between overburden faults and drilling problems at the Valhall Field. Casing deformations are expected to be part of the operational cost at Valhall (Kristiansen et al., 2000). In the reservoir zone, reactivation of faults might lead to leakage of hydrocarbons and affect the reservoir drainage patterns. Fault seal breach in the North Sea (Gaarenstroom et al., 1993), the Penola Through (Jones et al., 2000), and the Gulf of Mexico (Finkbeiner et al., 2001) has been related to faulting and fracturing associated with the in situ stress. A fault can be a transmitter of or barrier to fluid and pressure communication. Cerveny et al. (2004) discuss several fault-seal analysis methods which evaluate the flow potential across a fault. Revil and Cathles (2002) show an example from the Gulf of Mexico where fluids migrate into active growing faults. Based on seismic data and wellbore information, Allan (1989) diagrams are often used to identify potential petroleum leak points along a fault strike. Reactivated faults can also have close relationship with earthquakes. Zoback and Zinke (2002) recorded numerous microearthquakes at the Valhall Field during a six week monitoring period. They found the microearthquakes consistent with a normal faulting stress regime. Chen and Bai (2006) built a model which relates the growth of microcracks with the occurrence of earthquakes.

The Valhall Field, situated in the southern part of the Norwegian North Sea, is a high-porosity Late Cretaceous chalk (porosities between 35-50%). The daily production is on the order of 100 000 barrels of light oil. The expected recovery rate

in 1982 was 14%, a figure which has now increased to 40%. Time-lapse seismic monitoring with high quality in addition to improved methods to interpret and utilize the seismic might increase the recovery further. In 2003, a permanent ocean bottom cable (OBC) array was installed at the Valhall Field, initiating the "Life of Field Seismic" (LoFS) program which includes a series of 3D OBC surveys. The first survey was acquired from September to November 2003 with subsequent surveys acquired in intervals of approximately 4 months. Results from the earliest surveys confirm that the system can provide high quality data with good repeatability (Kommedal et al., 2004; Barkved, 2004).

In the present paper we investigate time-lapse changes on 2D prestack time-lapse seismic OBC lines from the LoFS survey 1 and survey 3. The 2D lines are situated in the south-east part of the Valhall Field. By utilizing a method developed by Røste et al. (2005), changes in thickness and velocity are estimated for a sequence from the sea bed to the top reservoir horizon for one of the 2D lines. This method utilizes time-lapse traveltime shifts for all offsets to find the dilation factor α which discriminates between layer thickness changes and velocity changes. An advantage of this method is that no information or model is required for the mechanism creating the velocity and thickness changes.

The LoFS data shows time shift patterns (between surveys 1 and 3) that move systematically with offset. Analogous signatures have earlier been observed for single prestack surveys (e.g. Allen and Bruso, 1989; Fagin, 1996; Hatchell, 2000) and are associated with shallow distortion zones. As far as we know, such distortions in time-lapse seismic are not so common. The location of the distortion zones are determined from geometry and raypath considerations. At least one of the distortions for the time-lapse time shifts observed between LoFS survey 1 and 3 is located in the vicinity of an existing fault. The distortions can be produced by a localized slip in this observed fault zone creating changes in the rock properties framework. A time-lapse synthetic model is created to match the observed time shifts. To find the dilation factor α for positions with time-lapse distortions we must account for vertical variations (in addition to lateral variations) in the relative velocity and thickness changes. An extended method is introduced to describe such positions.

4.3 Discrimination between layer thickness and velocity changes

It is important to notice that time-lapse seismic time shifts capture the combined effects of velocity and thickness changes within a given layer. The relative time shift for zero offset can be expressed in terms of the relative thickness change and velocity change as (Landrø and Stammeijer, 2004; Røste et al., 2005; Hatchell and Bourne, 2005b)

$$\frac{\Delta T_0(x_0)}{T_0(x_0)} \approx \frac{\Delta z(x_0)}{z(x_0)} - \frac{\Delta v(x_0)}{v(x_0)}, \tag{4.1}$$

where T_0 represents two-way traveltime for zero offset, z is the layer thickness, and v is the layer velocity. The parameter x_0 denotes the global x-coordinate for a given CDP-location (position), and ΔT_0, Δz, and Δv represent changes in vertical two-way traveltime, thickness, and velocity, respectively. The basic assumption in equation (4.1) is that all relative changes are small; that is, $\frac{\Delta z}{z} << 1$ and $\frac{\Delta v}{v} << 1$. As a first order approximation for a relation between relative thickness and velocity changes for a given subsurface layer we assume that the two changes are proportional to each other (Røste et al., 2005):

$$\frac{\Delta v(x_0)}{v(x_0)} \approx \alpha \frac{\Delta z(x_0)}{z(x_0)}, \tag{4.2}$$

where the dilation factor $\alpha < 0$ is a parameter dependent on the rock properties of the layer. This is a crucial parameter, since it determines the ratio between velocity and thickness changes. In general, α varies with spatial coordinates. However, similar to Røste et al. (2005, 2006), we assume that α is constant for the sequence of layers we study.

The dilation factor α can be estimated based on time shift analysis. For a prestack CDP gather at position x_0, the seismic two-way traveltime for a raypath with offset $2h$ can be expressed as an integral over the total raypath length S,

$$T(x_0, h) = \int_S \frac{ds}{v(s)}, \tag{4.3}$$

where $v(s)$ denotes the P-wave velocity at the ray position $s(x_0, h)$. Assume a one-layer model with a P-wave velocity field, $v(x)$, that varies along the lateral position x, but is nonvarying with depth. By assuming straight raypaths, it can be shown that (similar to assuming average slowness within the offset range $2h$)

$$T(x_0, h) = \sqrt{1 + \frac{z^2(x_0)}{h^2}} \int_{x_0-h}^{x_0+h} \frac{dx}{v(x)}, \tag{4.4}$$

where $z(x_0)$ represents the layer thickness at the CDP-position x_0. Equation (4.4) describes the initial (or pre-production) case. For the post-production case, we find that it is essential to include the lateral variations in velocity changes, since it is very likely that such changes will occur both within the reservoir layer as well as the overburden layers of a producing hydrocarbon reservoir (see also Røste et al., 2006). From equation (4.4), the two-way prestack traveltime for the monitor case (for a one-layer model) is then given as

$$T^{'}(x_0,h) = \sqrt{1+\frac{z^2(x_0)}{h^2}\left(1+\frac{\Delta z(x_0)}{z(x_0)}\right)^2}\int\limits_{x_0-h}^{x_0+h}\frac{dx}{v(x)\left(1+\frac{\Delta v(x)}{v(x)}\right)}, \tag{4.5}$$

where the relative change in velocity, $\frac{\Delta v(x)}{v(x)}$, might vary laterally but not with depth. (Note that variations in thickness changes only affect the multiplier outside the integral in equation (4.5) when assuming straight raypaths.) Assuming small relative changes in velocity and thickness, the relative change in two-way traveltime becomes (see Appendix 4.A)

$$\frac{\Delta T(x_0,h)}{T(x_0,h)} \approx \frac{\left(1+\frac{z^2(x_0)}{z^2(x_0)+h^2}\frac{\Delta z(x_0)}{z(x_0)}\right)\int\limits_{x_0-h}^{x_0+h}\frac{dx}{v(x)}\left(1-\frac{\Delta v(x)}{v(x)}\right)}{\int\limits_{x_0-h}^{x_0+h}\frac{dx}{v(x)}} - 1. \tag{4.6}$$

From equations (4.1) and (4.2), the relative changes in layer thickness and velocity can be related to the relative change in two-way vertical traveltime T_0:

$$\frac{\Delta z(x_0)}{z(x_0)} \approx \left(\frac{1}{1-\alpha}\right)\frac{\Delta T_0(x_0)}{T_0(x_0)} \quad , \quad \frac{\Delta v(x_0)}{v(x_0)} \approx \left(\frac{\alpha}{1-\alpha}\right)\frac{\Delta T_0(x_0)}{T_0(x_0)}. \tag{4.7}$$

By assuming small lateral variations in initial layer velocity in the vicinity of each position x_0; that is, $v(x) \approx v(x_0)$ for $x_0 - h \leq x \leq x_0 + h$, equation (4.6) can be written in the simple form given by equation (4.8) (see Appendix 4.A). Note, however, that we include the lateral variations in Δv; that is, $\Delta v = \Delta v(x)$.

$$\frac{\Delta T(x_0,h)}{T(x_0,h)} \approx \frac{z^2(x_0)}{z^2(x_0)+h^2}\left(\frac{1}{1-\alpha}\right)\frac{\Delta T_0(x_0)}{T_0(x_0)} - \frac{1}{2h}\left(\frac{\alpha}{1-\alpha}\right)\int\limits_{x_0-h}^{x_0+h} dx\frac{\Delta T_0(x)}{T_0(x)}. \tag{4.8}$$

The relative change in two-way traveltime (for a given half-offset h) is therefore dependent on α and the estimated relative change in vertical traveltime. (Note that the integration sign in equation (4.8) in practice means summation, since time shift estimations only exist for discrete positions (or CDPs).) The parameter α is determined by minimizing the least square error in relative traveltime change (equation (4.8)) over the entire offset range. This α-value is then inserted into equation (4.7) to obtain the changes in layer thickness and velocity. Røste et al., 2006 discuss in detail the approximations made for equation (4.8).

4.4 Estimate α from permanent OBC data

The method (given by equation (4.8)) is tested on a prestack time-lapse 2D OBC line situated in the south-east part of the Valhall Field (denoted l in Figure 4.1), acquired from survey 1 and survey 3 in the LoFS project. The selected 2D line

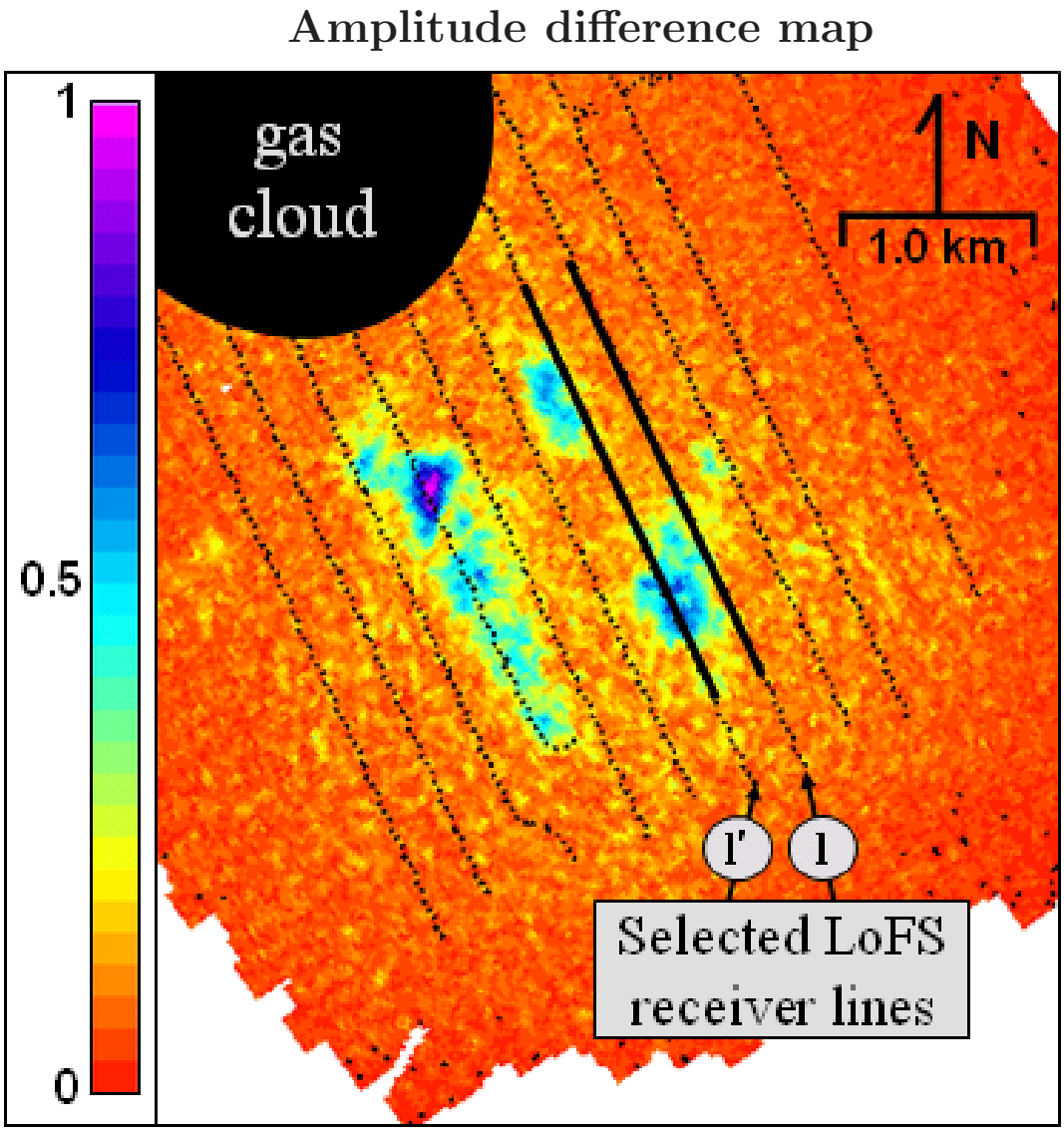

Figure 4.1: Amplitude difference map of the top reservoir horizon in the south part of the Valhall Field (between LoFS survey 1 and survey 3). The two selected LoFS 2D lines (marked) follow buried cables. (The buried cables are given as dotted lines.)

follows a buried receiver cable, leading to excellent inline distribution of offsets. The data is corrected for tidal statics and a frequency-wavenumber filter was applied to decrease multiple energy (Yilmaz, 1987). In addition, the signal to noise ratio and repeatability was increased by stacking 5 shots to each receiver, leading to normalized root-mean-square (NRMS) of 0.41 for a 1.0 s time gate centered at 2.0 s. Further, a 5x5 mixing operation of traces improved the NRMS to 0.19 for the same time gate (of 1.0 s). This operation resulted in an effective offset spacing of 200 m between the traces. The original offset spacing was 50 m. The total length of the selected 2D line is 2.3 km and, for simplicity, we define the north-west and south-east ends of this selection as positions $x = 0$ km and $x = 2.3$ km, respectively. Figure 4.2 shows the quality and repeatability of the LoFS data. Here the data from LoFS survey 1 for zero offset is shown inside the letters "NTNU" together with survey 3 given in the background. The top of the reservoir is around 2.6 s (two-way

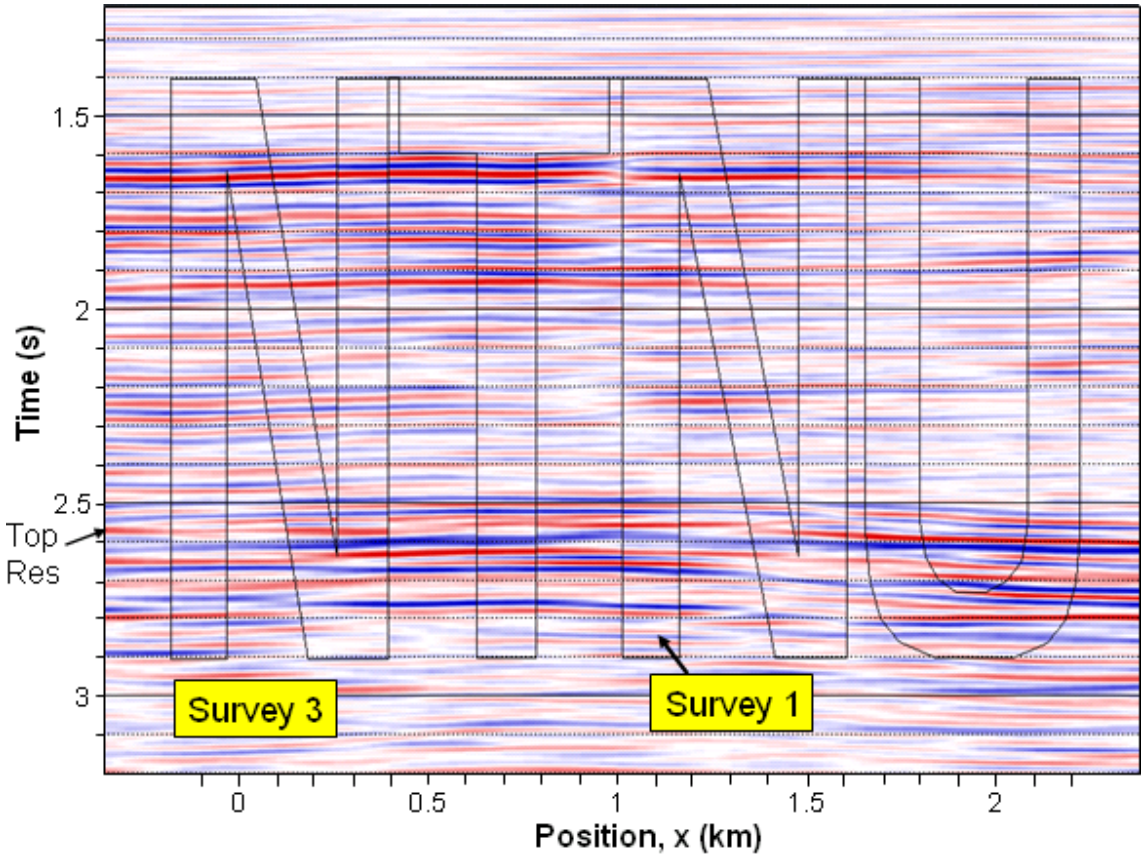

Figure 4.2: LoFS survey 1 (inside the letters "NTNU") shown together with survey 3 (in the background) for zero offset, as a function of position. Note the good quality and high repeatability of the data.

traveltime), corresponding to approximately 2.5 km in depth. We investigate an overburden sequence from the sea bed to this top reservoir horizon.

The prestack events from the top reservoir horizon are picked for interpolated maximum amplitudes. To increase the accuracy of the picked zero-offset traveltime (T_0) (for a given position x_0), it is normal to stack the picked offset-dependent traveltimes (T) by assuming standard hyperbolic moveout (Dix, 1955); that is,

$$T^2(x_0, h) = T_0^2(x_0) + \frac{4}{V_{rms}^2(x_0)} h^2, \tag{4.9}$$

where h denotes half-offset and V_{rms} denotes rms velocity. Due to the high quality of the LoFS data, zero-offset traveltimes are estimated by stacking only the near offsets (that is, offsets below 1 km). Figure 4.3 shows the estimated (crosses) and laterally smoothed (solid line) relative time shifts for zero offset for the top reservoir horizon.

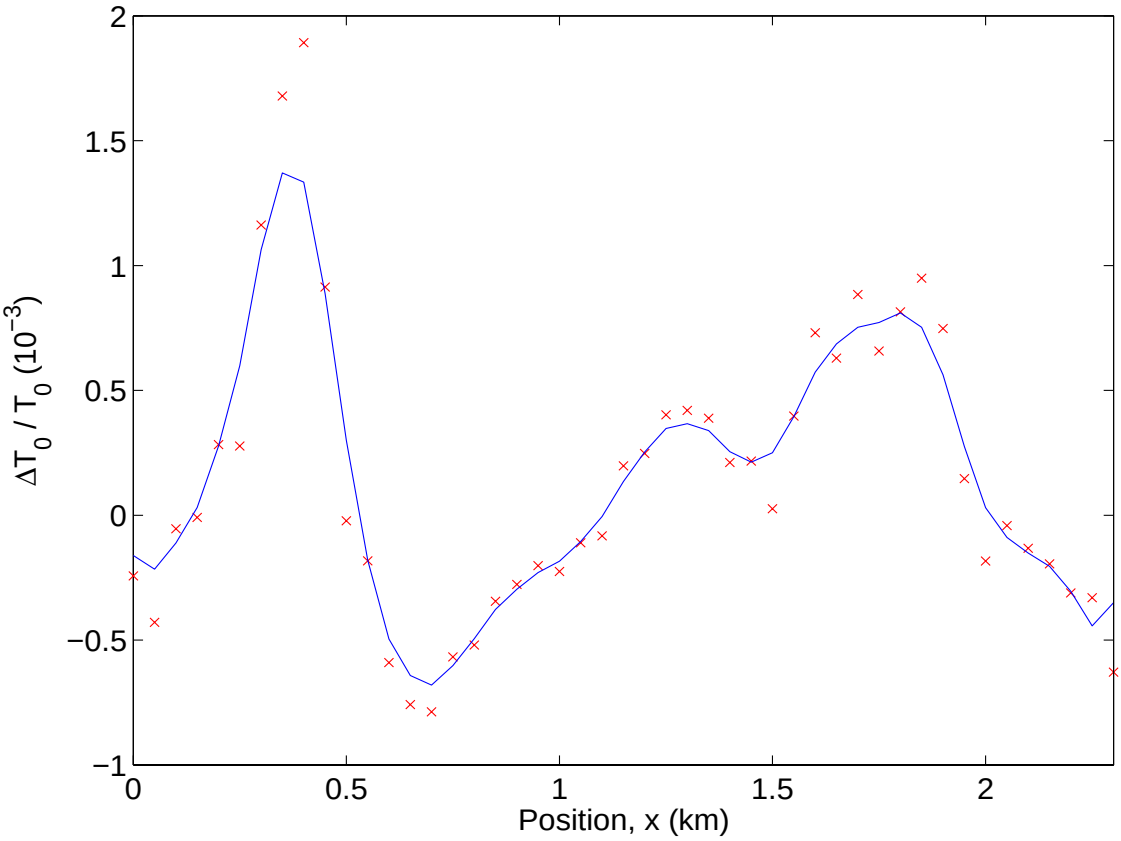

Figure 4.3: Estimated (crosses) and smoothed (solid line) relative zero-offset time shifts for the top reservoir horizon.

The LoFS data shows high degree of repeatability, making it possible to detect subtle traveltime changes. This is shown in Fig. 4.4, where LoFS data from survey 1 (solid black line) is shown together with survey 3 (solid blue line) for position 1.6 km at 1.0 km offset. For the reservoir section, solid black line is survey 1 and solid red line is survey 3 (top right). By interpolating the seismic we are able to detect a traveltime shift (measured at the maximum amplitude) of around 1.5 ms (bottom right). The repeatability is maintained for increasing offsets. Fig. 4.5 shows LoFS data from survey 1 (solid black line) together with survey 3 (solid blue line) at 2.0 km offset (for same position 1.6 km). For the reservoir section, solid black line is survey 1 and solid red line is survey 3 (top right). A traveltime shift of 1.0 ms is detected for interpolated maximum amplitude (bottom left).

Our analysis follows the method of Røste et al. (2005): For an initial guess of α, equation (4.8) gives corresponding (relative) time shifts for different half-offsets (h) which can be compared with the picked time shifts. We search for the α-value that leads to minimum least square error between the estimated and picked relative time shifts, for all offsets. Figure 4.6 shows this procedure (for the sequence from the sea bed to the top reservoir horizon) for the 4 positions $x = 0.3$ km, $x = 0.35$ km, $x = 0.4$ km, and $x = 0.45$ km: Starting with an initial α-value of 0 in equation (4.8), we search in steps of -0.1 within the span from 0 to -5, until we obtain an optimal α-value (solid line), for each position, that gives the best fit to the picked relative time shifts (crosses). (Multiple picked time shifts for a given offset occur due to opposite shooting directions.) The dashed lines in Figure 4.6 correspond to the initial and last guess of α; that is, $\alpha = 0$ and $\alpha = -5$. The positions shown in Figure 4.6 (especially position $x = 0.35$ km) indicate an optimal α-value around -5. For position $x = 0.3$ km, picked relative time shifts seem to be uncertain for offsets around 0.5 km, which might explain why the optimal α is slightly above -5 for this position. The picked relative time shifts for positions $x = 0.4$ km and $x = 0.45$ km indicate an optimal α-value slightly below -5. This might be correct; however, it is difficult to discriminate optimal α-values below -5, and we therefore choose to stop our search at $\alpha = -5$.

The difficulty of distinguishing α for decreasing values is shown in Figure 4.7 for position $x = 0.35$ km. Here α-values ranging from 0 to -20 are inserted in equation (4.8) to estimate relative time shifts as a function of offset. When the absolute magnitude of α is large, changes in α of the order 1 have negligible influence on the factors $(\frac{1}{1-\alpha})$ and $(\frac{\alpha}{1-\alpha})$ in equation (4.8), and, consequently, the relative time shifts are almost unchanged. This is obtained in Figure 4.7 for α-values below -5.

Figure 4.6 shows the positions from the investigated 2D line that have the best sensitivity in α; that is, various values of α (within the range 0 to -5) give clearly distinct results from equation (4.8). Acceptable sensitivity in α is also observed for

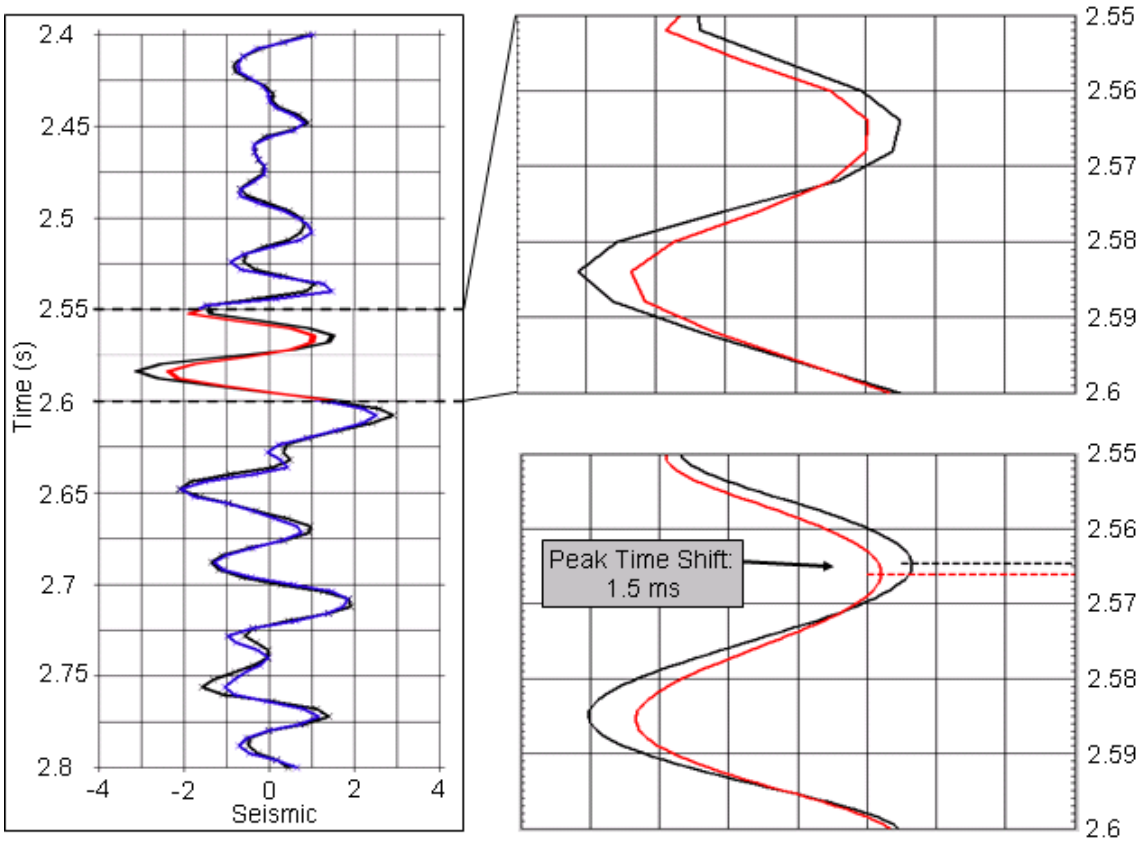

Figure 4.4: Left: LoFS data from survey 1 (solid black line) together with survey 3 (solid blue line) at 1.0 km offset for position 1.6 km. For the reservoir section, black solid line is survey 1 and red solid is survey 3 (top right). Due to the high degree of repeatability we are able to detect subtle traveltime changes. Interpolating the seismic and picking for maximum amplitude gives a time shift (measured at the maximum amplitude) of 1.5 ms (bottom left).

the 4 positions $x = 2.15$ km, $x = 2.2$ km, $x = 2.25$ km, and $x = 2.3$ km. These positions are shown in Figure 4.8, where the optimal fitted α-values (solid lines) of the picked relative time shifts (crosses) again indicate an α-value close to -5. (The dashed lines indicate the initial and last guess of α; that is, $\alpha = 0$ and $\alpha = -5$.)

For the chosen 2D line we found locations characterized by both low sensitivity in α as well as good sensitivity in α. Note that the sensitivity in α is not dependent on the noise-level. Low sensitivity in α seems to occur for positions with small time shifts, especially observed for the positions from $x = 0.9$ km to $x = 1.4$ km. Figure 4.9 shows 4 of these positions; that is, positions $x = 1.05$ km, $x = 1.1$ km, $x = 1.15$ km, and $x = 1.2$ km. Here the small size of the window between the initial and last

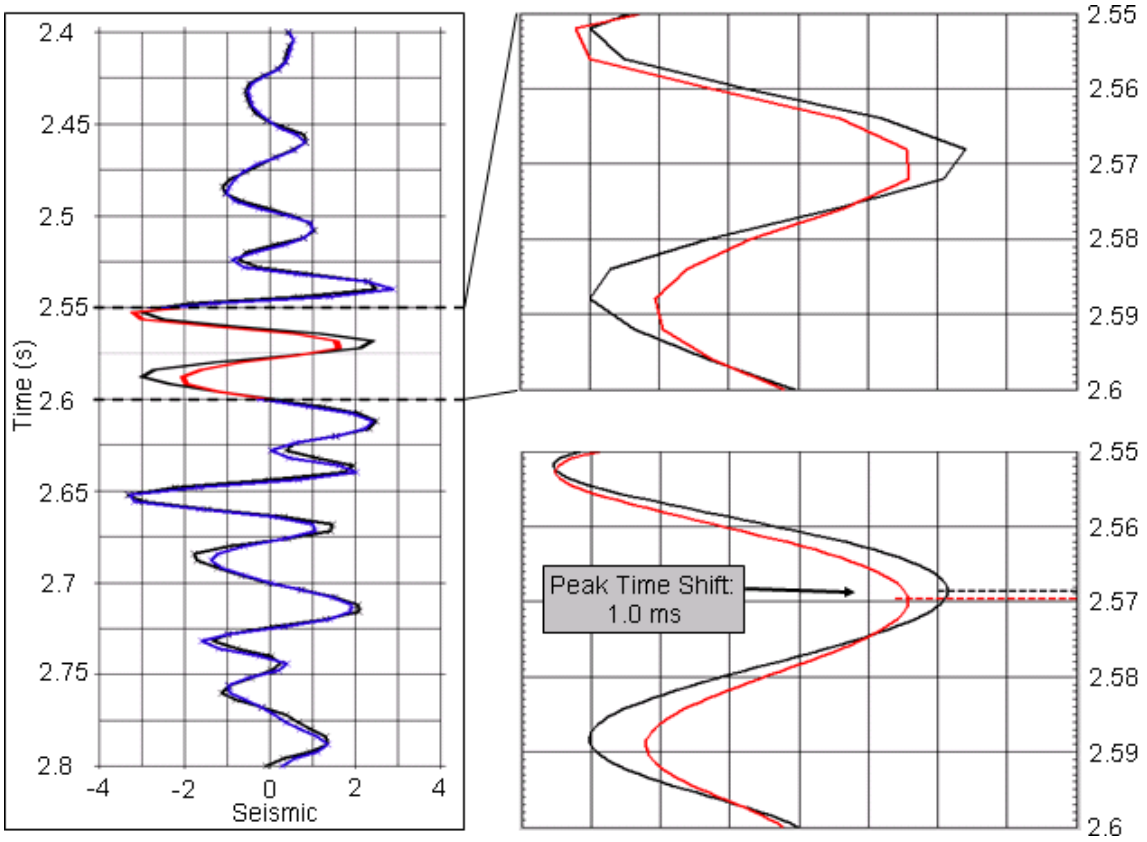

Figure 4.5: Repeatability is maintained for higher offsets. At the left, LoFS data from survey 1 (solid black line) is shown together with survey 3 (solid blue line) at 2.0 km offset (for position 1.6 km). For the reservoir section, black solid line is survey 1 and red solid is survey 3 (top right). A subtle time shift of 1.0 ms is detected for interpolated maximum amplitude (bottom left).

guess of α (that is, $\alpha = 0$ and $\alpha = -5$) (dashed lines) makes it impossible to find a trustable α-value. However, such positions are easy to detect and can be excluded when determining the optimal α-value for all positions.

Results and uncertainties

The method, given by equation (4.8), is highly dependent on the accuracy of the picked zero-offset and offset-dependent time shifts. Obviously, data quality has a significant impact on our ability to estimate α from time-lapse prestack seismic data. Values of α down to -5 can be determined; however, below this limit, the uncertainties are large (as underlined in Figure 4.7). The standard deviation (denoted

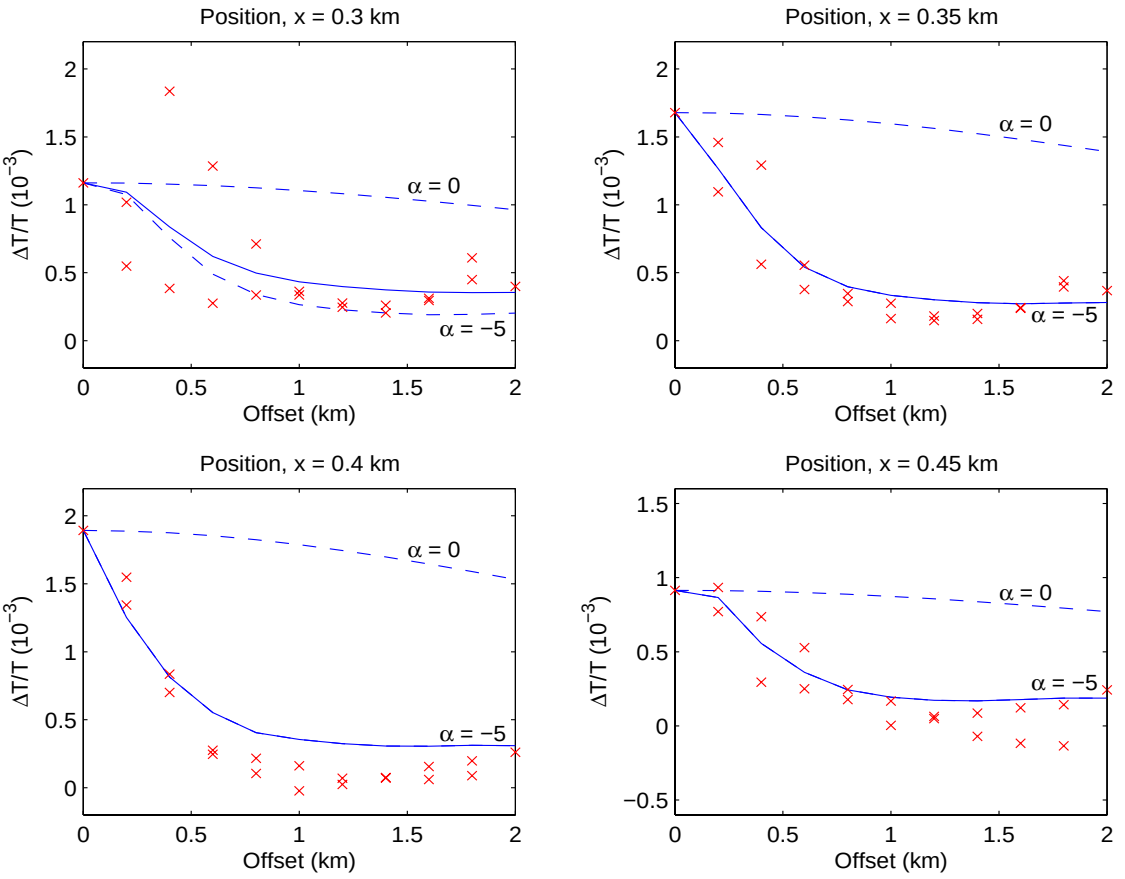

Figure 4.6: Example of finding α (for the sequence from the sea bed to the top reservoir horizon) for the 4 positions $x = 0.3$ km, $x = 0.35$ km, $x = 0.4$ km, and $x = 0.45$ km. For each position, the solid line indicates the best fit of the picked relative time shifts (crosses) as a function of offset. The dashed lines correspond to the initial and last guess of α; that is, $\alpha = 0$ and $\alpha = -5$. These 4 positions indicate an α around -5.

δ) in α can be given as (Røste et al., 2006)

$$\delta\alpha = \sqrt{\left(\frac{\partial\alpha}{\partial f_1}\delta f_1\right)^2 + \left(\frac{\partial\alpha}{\partial f_2}\delta f_2\right)^2 + \left(\frac{\partial\alpha}{\partial f_3}\delta f_3\right)^2 + \left(\frac{\partial\alpha}{\partial f_4}\delta f_4\right)^2}, \tag{4.10}$$

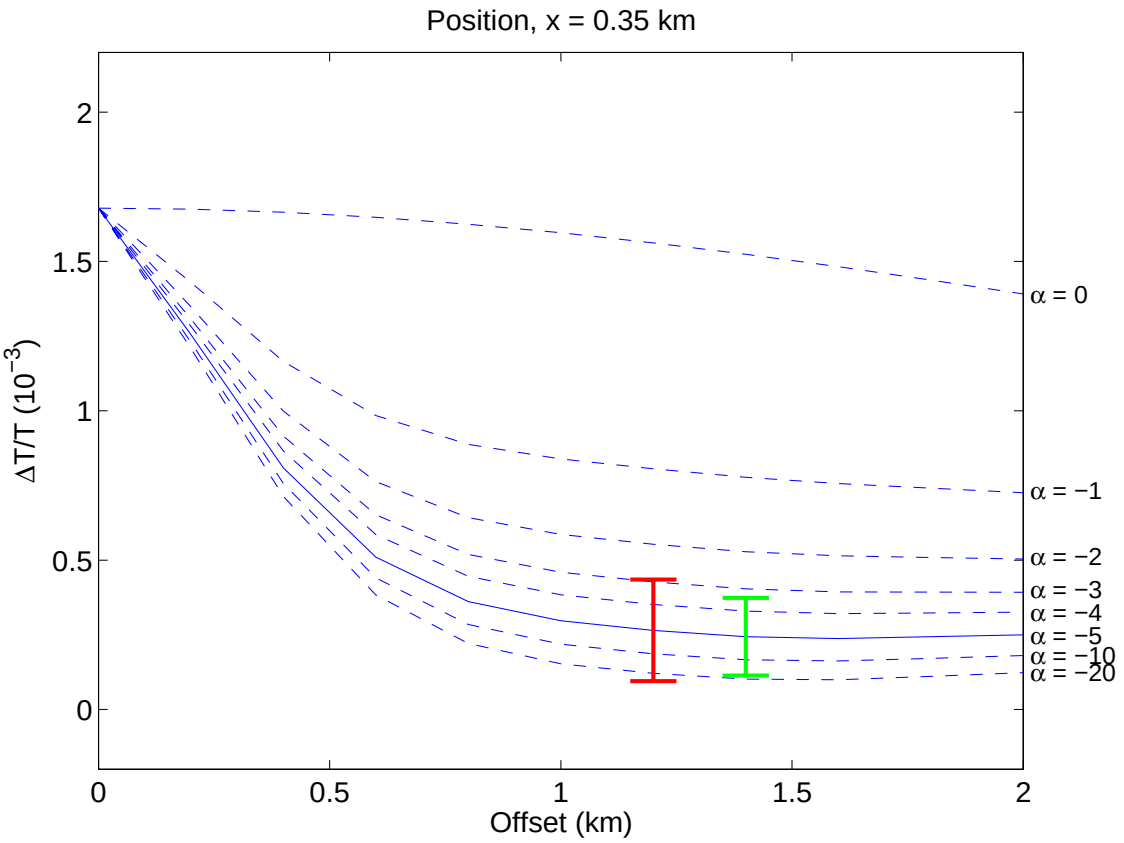

Figure 4.7: Estimated relative time shifts (as a function of offset) for several values of α for position $x = 0.35$ km. The solid line indicates the optimal $\alpha = -5$. Note the increased difficulty of distinguishing α-values as α decreases. The red and green vertical bars indicate the standard and mean deviations (respectively) in picked relative time shifts.

where

$$\frac{\partial \alpha}{\partial f_1} = \frac{f_3}{f_2 - f_4}, \tag{4.11}$$

$$\frac{\partial \alpha}{\partial f_2} = \frac{f_4 - f_1 f_3}{(f_2 - f_4)^2}, \tag{4.12}$$

$$\frac{\partial \alpha}{\partial f_3} = \frac{f_1}{f_2 - f_4}, \tag{4.13}$$

$$\frac{\partial \alpha}{\partial f_4} = \frac{f_1 f_3 - f_2}{(f_2 - f_4)^2}, \tag{4.14}$$

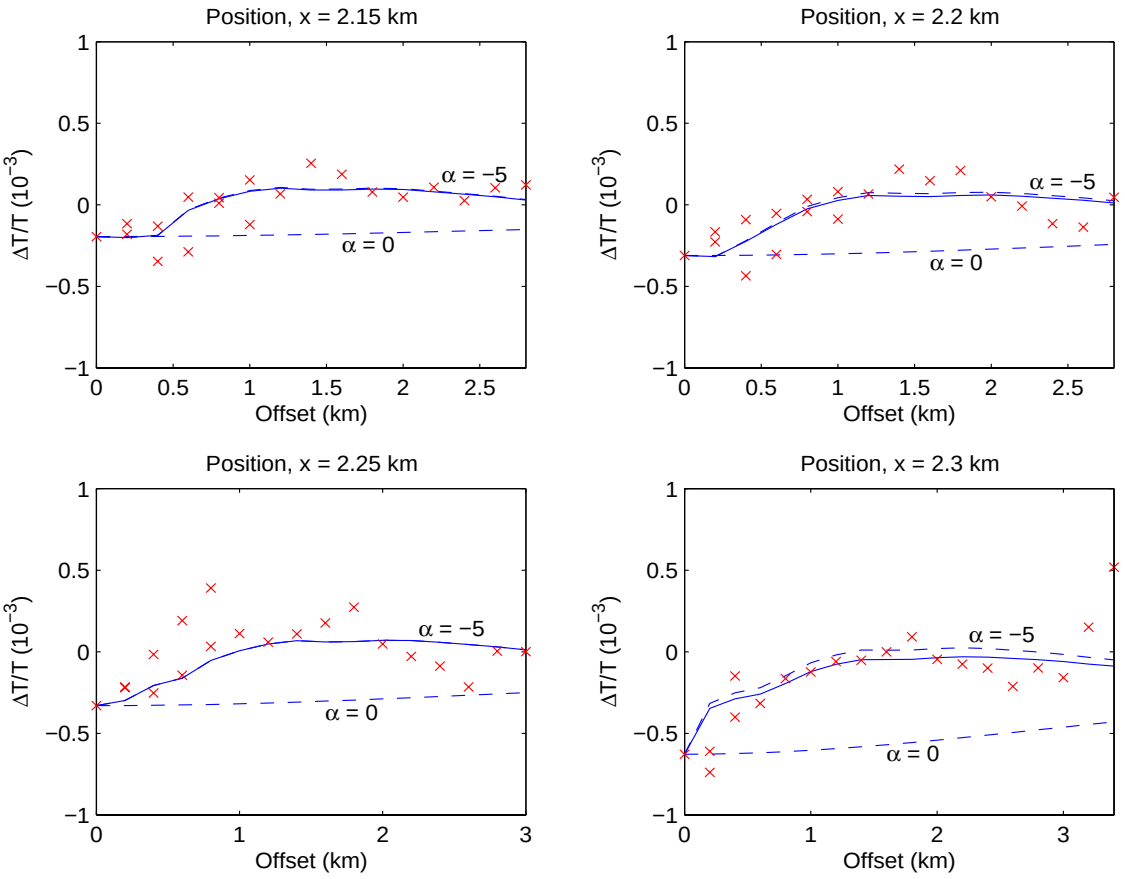

Figure 4.8: Example of finding α (for the sequence from the sea bed to the top reservoir horizon) for the 4 positions $x = 2.15$ km, $x = 2.2$ km, $x = 2.25$ km, and $x = 2.3$ km. For each position, the solid line indicates the best fit of the picked relative time shifts (crosses) as a function of offset. The dashed lines correspond to the initial and last guess of α; that is, $\alpha = 0$ and $\alpha = -5$. Similar to Figure 4.6, the above positions indicate an α close to -5.

and

$$f_1 = \frac{z^2(x_0)}{z^2(x_0) + h^2}, \tag{4.15}$$

$$f_2 = \frac{1}{2h} \int_{x_0-h}^{x_0+h} dx \frac{\Delta T_0(x)}{T_0(x)}, \tag{4.16}$$

$$f_3 = \frac{\Delta T_0(x_0)}{T_0(x_0)}, \tag{4.17}$$

$$f_4 = \frac{\Delta T(x_0, h)}{T(x_0, h)}. \tag{4.18}$$

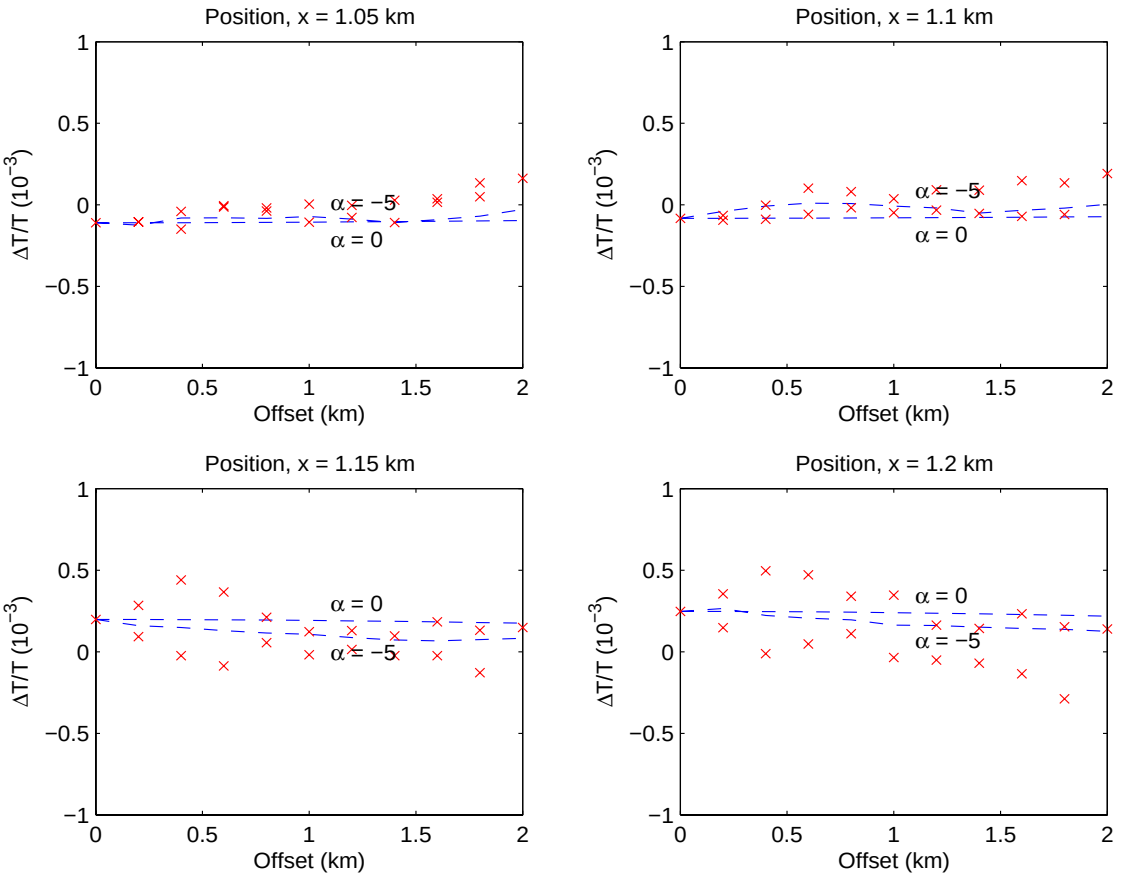

Figure 4.9: Example of 4 positions ($x = 1.05$ km, $x = 1.1$ km, $x = 1.15$ km, and $x = 1.2$ km) with low sensitivity in α. The small size of the window between the initial and last guess of α (that is, $\alpha = 0$ and $\alpha = -5$) (dashed lines) makes it impossible to find a trustable α-value.

Relative time shifts (also denoted f_4) can be related to α according to equation (4.8); that is,

$$\frac{\Delta T(x_0,h)}{T(x_0,h)} \approx \frac{z^2(x_0)}{z^2(x_0)+h^2}\left(\frac{1}{1-\alpha}\right)\frac{\Delta T_0(x_0)}{T_0(x_0)} - \frac{1}{2h}\left(\frac{\alpha}{1-\alpha}\right)\int_{x_0-h}^{x_0+h} dx \frac{\Delta T_0(x)}{T_0(x)}. \quad (4.19)$$

Equations (4.10) to (4.19) make it possible to find the standard deviation in α versus two key parameters: α itself and the uncertainty in the picked time shifts. An example is shown in Figure 4.10 for a picked time shift with offset 1.0 km (that is, $h = 0.5$ km). Here a layer with initial thickness $z = 2.5$ km undergoes changes corresponding to relative zero-offset time shifts ($\frac{\Delta T_0}{T_0}$) (laterally constant) equal to $2.0 \cdot 10^{-3}$. The uncertainty in $\frac{z^2}{z^2+h^2}$ (denoted δf_1 in equation (4.10)) is assumed

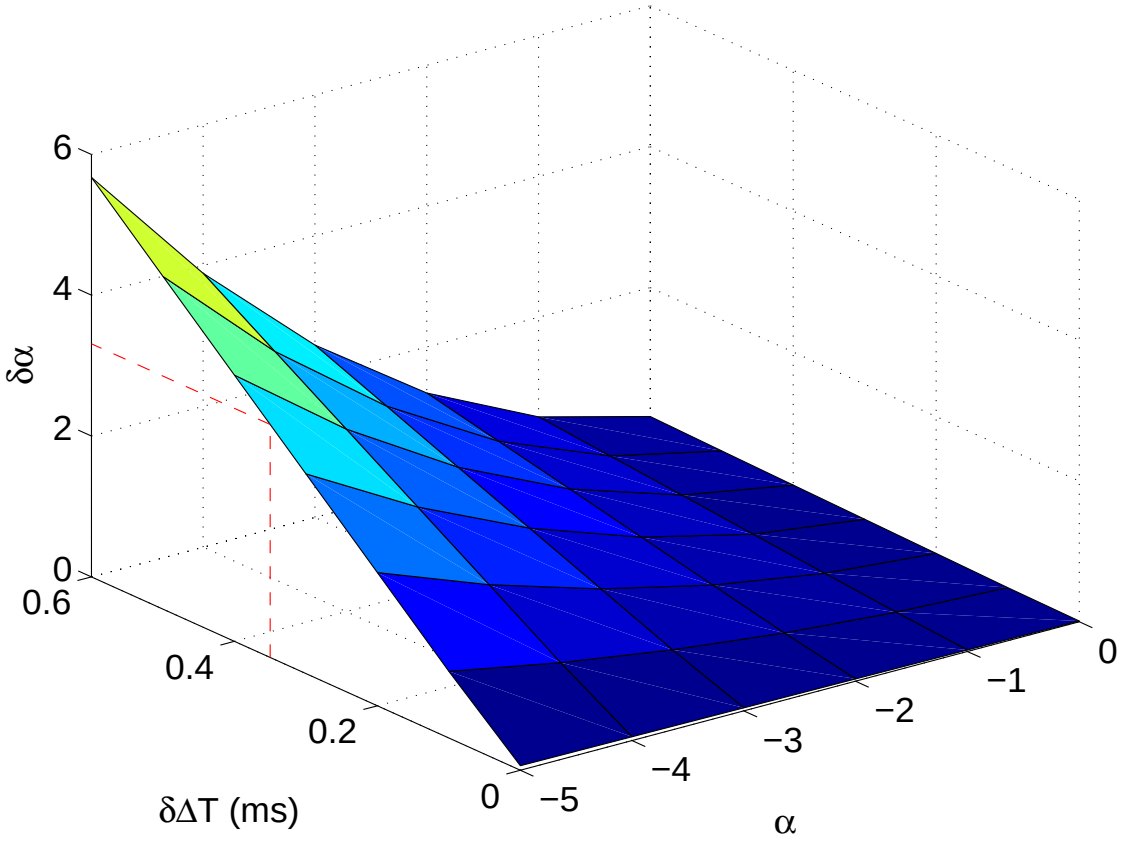

Figure 4.10: Standard deviation in α versus α itself and standard deviation in a picked time shift with offset 1.0 km. The example is based on a layer with thickness 2.5 km that undergoes changes corresponding to relative zero-offset time shifts of $2.0 \cdot 10^{-3}$. A standard deviation of 3.3 is obtained for an α-value of -5 (indicated with dashed line), when the standard deviation in picked time shifts is assumed to be 0.35 ms.

to be 1.1 % (which can be obtained by assuming an uncertainty in both z and h of 10 %, see Landrø, 2002) and we assume equal uncertainty in $\frac{\Delta T_0}{T_0}$ and $\frac{\Delta T}{T}$ (that is, $\delta f_2 = \delta f_3 = \delta f_4$ in equation (4.10)). As Figure 4.10 shows, the uncertainty in α increases significantly with increasing deviation in time shifts and decreasing α-values. The standard and mean deviations in picked relative time shifts are estimated to be $0.17 \cdot 10^{-3}$ and $0.13 \cdot 10^{-3}$, respectively (based on the misfit between picked relative time shifts and their best fit, see e.g. Figure 4.6) meaning that the deviation in time shifts is around 0.3-0.4 ms. Assuming 0.35 ms deviation in time shifts gives a standard deviation of 3.3 in the optimal estimated α of -5 for the investigated overburden sequence on Valhall (marked with dashed line in Figure 4.10). Note, however, that the total uncertainty range is not symmetric around

the optimal α-value of -5, since the distribution of α is non-linear (Figure 4.7). The standard deviation in picked relative time shifts of $0.17 \cdot 10^{-3}$ indicates that α lies within the range $-3 < \alpha < -25$ (marked as vertical red bar in Figure 4.7), while the mean deviation in relative time shifts (of $0.13 \cdot 10^{-3}$) indicates a narrower range for α; that is, $-3.4 < \alpha < -17$ (marked as vertical green bar in Figure 4.7). Both results show that we are able to exclude α-values between 0 and -3 for the investigated overburden rocks.

Figure 4.11 shows the estimated changes in thickness and velocity (solid line) for the investigated sequence when using the optimal α-value of -5, together with uncertainties (dashed lines) correlated to an uncertainty of 3.3 in the optimal α (of -5). The solid dots indicate the initial guess of α; that is, $\alpha = 0$. The estimated

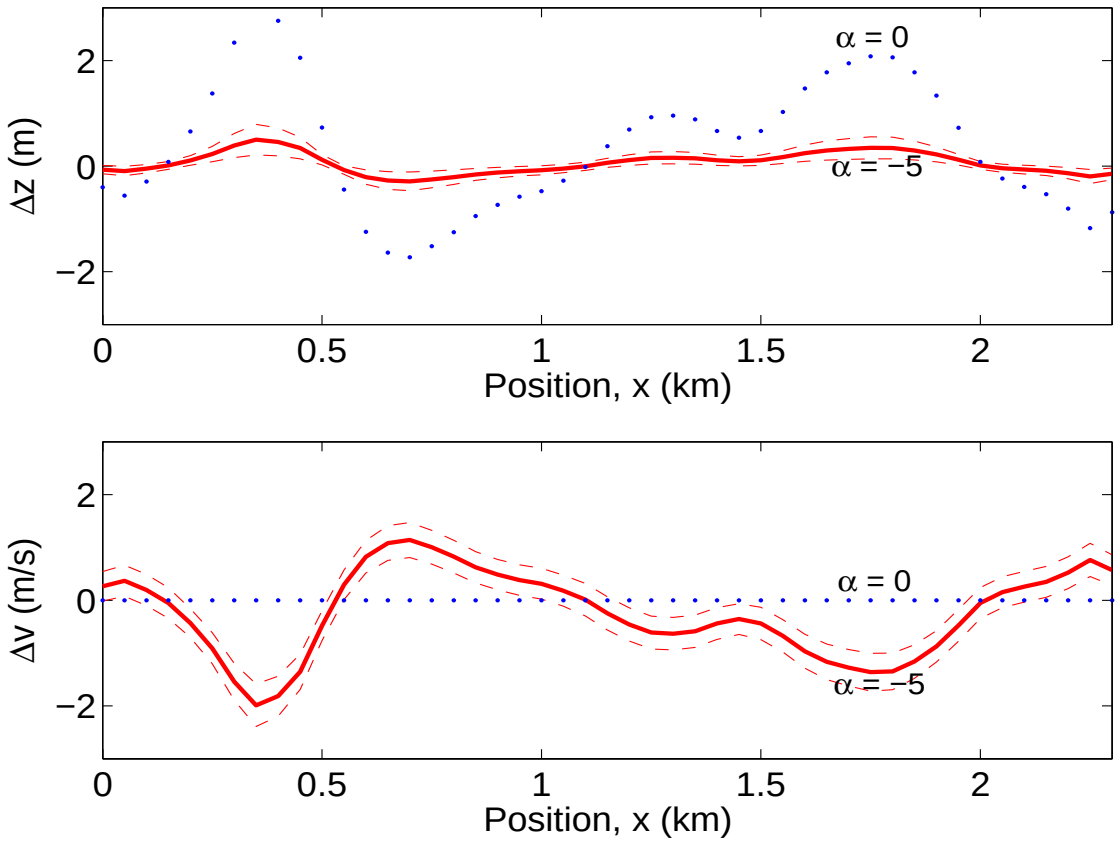

Figure 4.11: Estimated changes (solid line) in thickness (top) and velocity (bottom), together with indicated uncertainties (dashed lines) as a function of position (for the sequence from the sea bed to the top reservoir horizon) when using the optimal α-value of -5. The solid dots correspond to the initial guess of α; that is, $\alpha = 0$.

optimal result in Figure 4.11 indicates a maximum subsidence of the top reservoir horizon of 0.50 m (with deviation 0.29 m) and a maximum velocity decrease for the overburden sequence of 2.0 m/s (with deviation 0.40 m/s).

4.5 Time-lapse distortions

In the second 2D line shown in Figure 4.1 (denoted l′) we observe time shift patterns that move systematically with offset. The positions on line l′ are denoted x' and range from $x' = 0$ km (north-west) to $x' = 2.3$ km (south-east). Figure 4.12 shows the picked relative time shifts (crosses) for the top reservoir horizon as a function of offset for the positions $x' = 1.55$ km to $x' = 1.8$ km. Note the marked positive time shifts around zero offset for position $x' = 1.55$ km (shown by arrow in Figure 4.12a). These time shifts move systematically with offset as the position increases (Figure 4.12b-4.12f), as shown by the arrow. In top of Figure 4.13, the same picked time shifts are displayed in the offset versus position domain (where the positive and negative offsets only indicate opposite shooting directions). Here the time shift pattern from the previous figure is clearly visible as a diagonal feature, moving from zero offset at position $x' = 1.55$ km towards increasing offset distance as the position increases. In addition, a similar feature, starting at position $x' = 0.4$ km for zero offset, is observed with marked negative time shifts. Both features are indicated with solid lines in top of Figure 4.13.

Similar patterns as shown in Figure 4.13 (top) have been previously observed on 3D prestack datasets and are attributable to shallow velocity distortion zones. Hatchell (2000) observed transmission distortions that produce anomalous amplitude versus offset (AVO) signatures on 3D seismic data at two locations in the Gulf of Mexico. He explains the distortion zones by velocity changes across faults and unconformity surfaces. Fagin (1996) presents an example of seismic distortions (that is, time sags and time pull-ups) resulting from extensional faults in the Wilcox trend of south Texas. His analysis shows that these distortions are produced by faults related to the stratigraphic-velocity alternations in the Wilcox Formation. Time anomalies attributable to growth faults are also discussed by Allen and Bruso (1989). Further discussions on transmission distortions are given by Kjartansson (1979) and Harlan (1994). As far as we know, distortions (or anomalies) are not as common in *time-lapse* seismic.

Interpretation of time-lapse distortion zones

The location of an observed distortion zone, that produces anomalous time-lapse time shift versus offset, can be determined by using geometry and ray tracing. Bottom of Figure 4.13 illustrates a buried anomaly (marked as star) at depth Z_A that distorts a ray at position x_0 for zero offset and a ray at position x_h for offset $2h$.

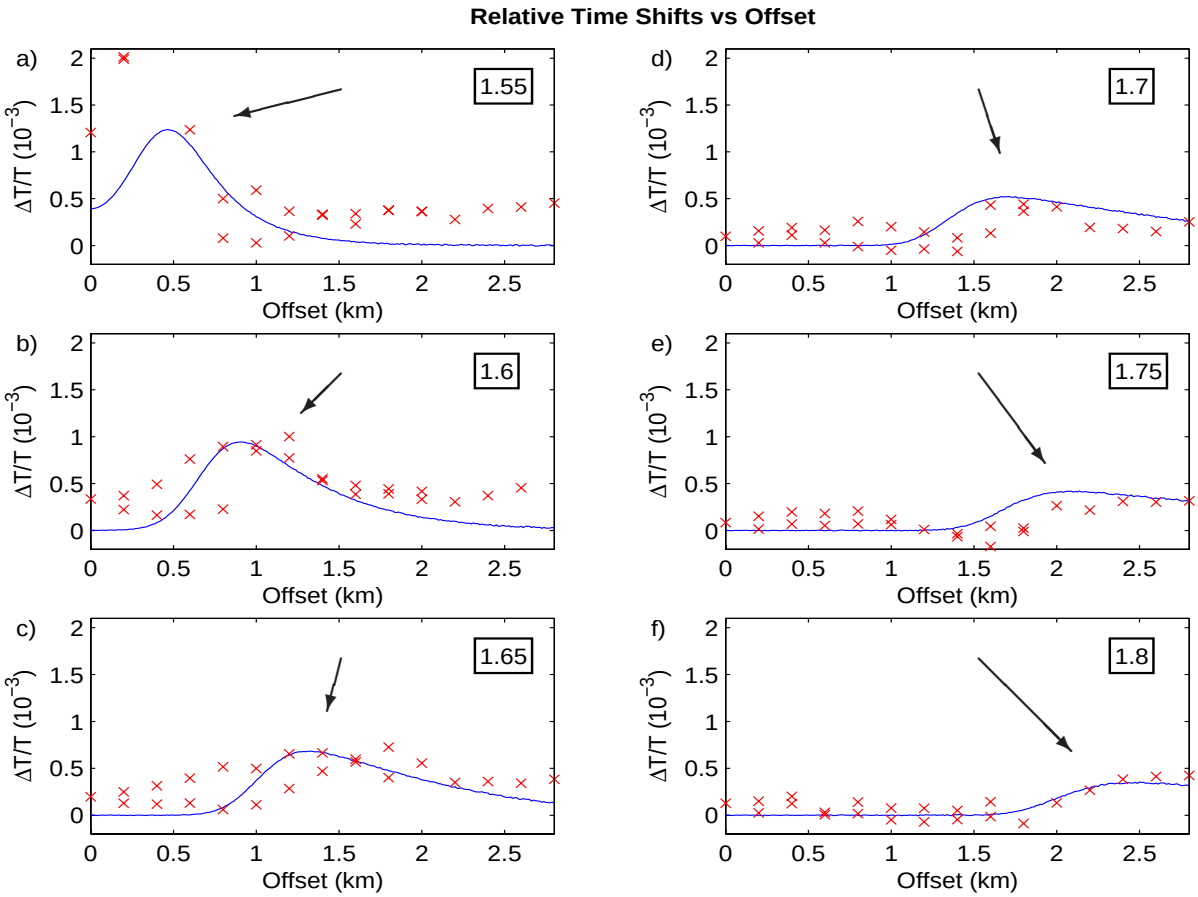

Figure 4.12: Picked time shifts (crosses), as a function of offset, for the top reservoir horizon for the 6 positions from $x' = 1.55$ km to $x' = 1.8$ km (from line l' in Figure 4.1). Marked positive time shifts (shown by an arrow) starts at position $x' = 1.55$ km (a) around zero offset and moves systematically with increasing offset as the position increases (b-f). The solid line represents time shifts from a synthetic time-lapse model.

By assuming straight raypaths and horizontal reflectors, the following expression for the anomaly depth can be obtained:

$$Z_A = Z(1 - \frac{|x_0 - x_h|}{h}), \tag{4.20}$$

where Z is the depth of the reflector and $|x_0 - x_h|$ is the absolute value of $x_0 - x_h$ (which includes both possibilities $x_0 < x_h$ and $x_0 > x_h$). From equation (4.20), we see that the slope of the distortion pattern observed in the offset versus position domain determines the anomaly depth (Z_A). This leads to anomaly depths around

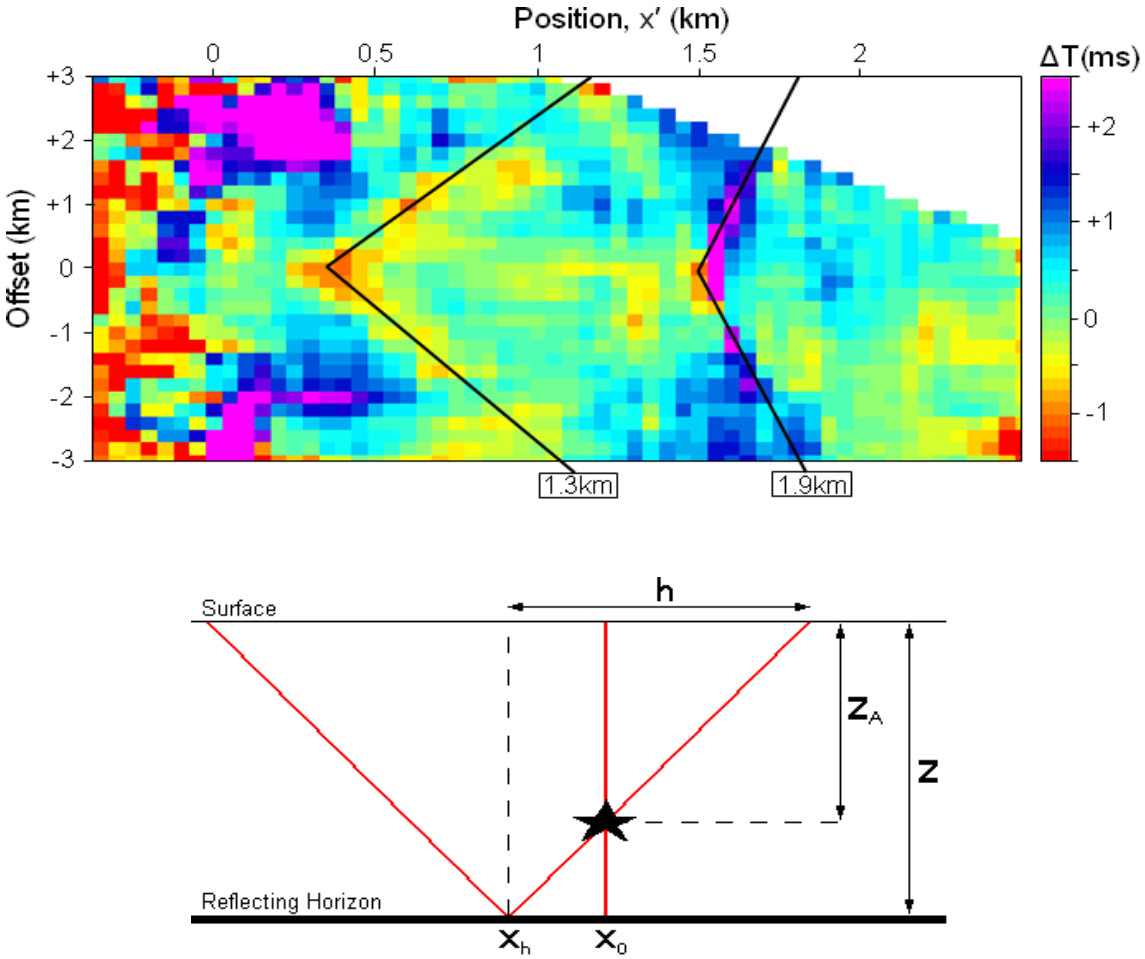

Figure 4.13: Picked time shifts for the top reservoir horizon displayed in the offset versus position domain (top). Note the diagonal features (indicated with solid lines) starting at positions $x' = 0.4$ km and $x' = 1.55$ km. The bottom figure shows the relationship between a buried anomaly (marked as a star) and the distortion of straight raypaths at position x_0 for zero offset and position x_h for offset $2h$. This relationship correlates the distortion zones shown in the top figure with buried anomalies at depths around 1.3 km and 1.9 km.

1.3 km and 1.9 km for the observed distortion patterns (Figure 4.13 (top)) starting at positions $x' = 0.4$ km and $x' = 1.55$ km, respectively.

We tried to match the observed time shift pattern starting at position $x' = 1.55$ by creating a synthetic model with a time-lapse anomaly. Since we only want to capture time-lapse time shifts, the synthetic baseline is a constant velocity-model with velocity 1.95 km/s. The monitor case is shown in Figure 4.14, where we have

assumed changes only inside an anomaly with depth 1.9 km and position close to $x' = 1.55$ km. The maximum velocity decrease is 25 m/s and occurs at the center of the anomaly. The thickness of the model is 2.45 km, which is representative for the Valhall overburden layers. Note that the anomaly is tilted and has larger extent in vertical direction than lateral direction, which is found necessary to match the distorted time shifts in the real data. The time shifts from the synthetic model are given as solid line in Figure 4.12 and show good match with the real time shifts (crosses in Figure 4.12).

Since the distortion patterns are observed in *time-lapse* seismic (and not for a single dataset) the distortion zones should be connected to *changes* in buried faults (or anomalies). The offset-dependent time shifts might therefore be produced by

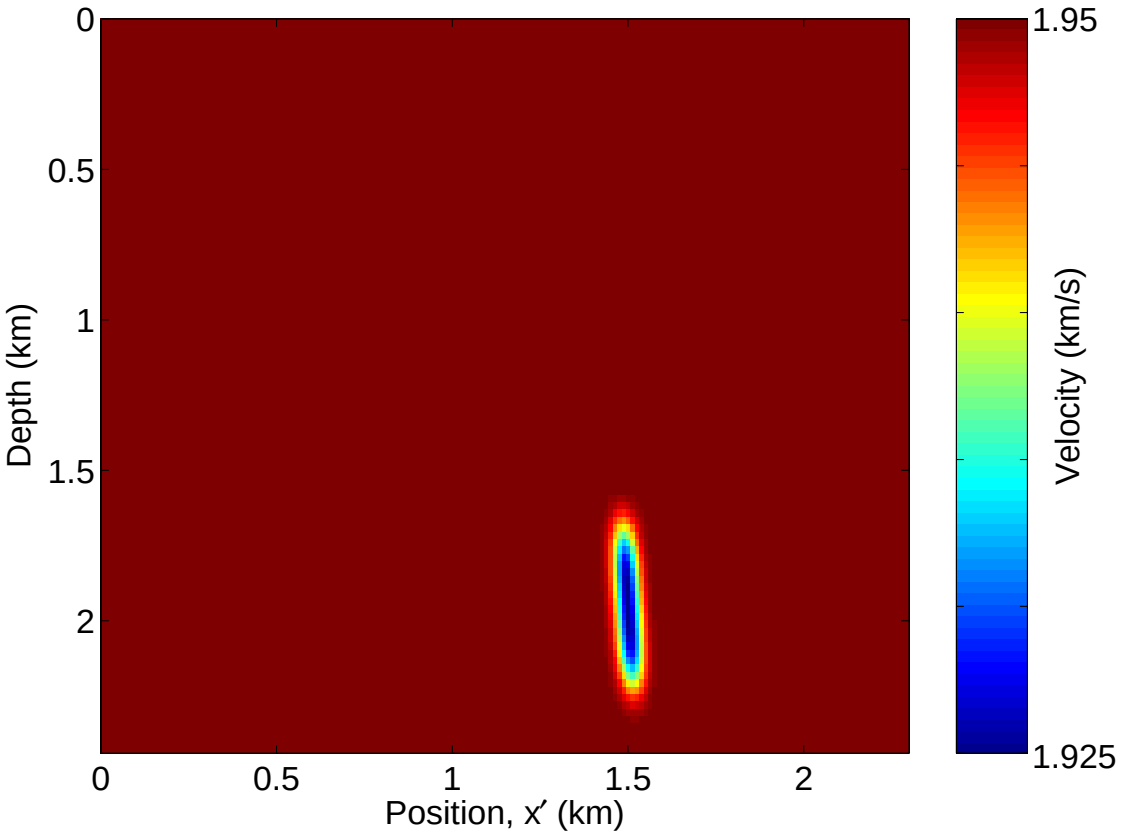

Figure 4.14: Synthetic model representing the observed anomaly at position $x' = 1.55$ km in the monitor case. The initial case is a constant velocity-model with velocity 1.95 km/s, which means that the model remains unchanged outside the anomaly. A velocity decrease of 25 m/s occurs at the center of the anomaly.

a localized slip in this observed fault zone creating changes in the rock properties framework. To strengthen this theory we have investigated the anomaly at position $x' = 1.55$ km. The observations are summarized in Figures 4.15 and 4.16. Top of Figure 4.15 shows a time-slice coherency map at 1960 ms of the Valhall poststack streamer data (from 2002). Time 1960 ms is close to depth 1.9 km which is the estimated depth for the anomaly at position $x' = 1.55$ km. In bottom of Figure 4.15 we show the coherency time-slice with two interpreted faults (given in yellow and red). The yellow fault is clearly older because it is cut by the red fault. The red fault is a left-lateral strike probably caused by late structural tectonics. The location of the time-lapse distortion anomaly (encircled) occurs at the south-west tip of the red fault. In top of Figure 4.16, the interpreted faults and the anomaly location (encircled) are shown together with the amplitude changes occurring at the top reservoir horizon. Here we see large amplitude changes for the positions around the tip of the fault, indicating that the reservoir level (700 m below the fault tip) is compacting. These observations are significant for several reasons: 1) If any fault were going to slip, the more recent faults are most expected. 2) The shear stresses at the fault tip will be large and 3) given that a compacting zone exists directly beneath the fault tip, we could expect changes in the overburden stress fields that might cause this fault to grow at the tip. Sure enough, this is exactly where the anomaly appears.

Extended method

Time-lapse distortions indicate locations that undergo relative velocity and thickness changes that differ largely from the surrounding changes. This means that the relative velocity and thickness changes are irregular in both vertical and lateral directions. The method of Røste et al. (2005) (as given by equation (4.8)) captures irregularities (or variations) in the lateral direction, but not in the vertical direction, because relative velocity and thickness changes are assumed to be constant in vertical direction. Therefore, we need to extend our method to handle vertical variations.

We divide the investigated sequence (that is, from the sea bed to the top reservoir horizon) into smaller horizontally sequences that undergo relative velocity and thickness changes assumed to be vertically constant within each sub-sequence. In Appendix 4.A we show an example with 3 divided sub-sequences. Figure 4.17 shows the sub-sequences and the intersection points between the interfaces and a ray reflected at position x_0. Note that the defined interfaces (that separates the sub-sequences) do not necessarily correlate to any geological features. By assuming straight raypath lines, the method of Røste et al. (2005), given by equation (4.8), can be rewritten as (see Appendix 4.A and Figure 4.17)

$$\frac{\Delta T(x_0,h)}{T(x_0,h)} \approx \frac{z^2(x_0)}{z^2(x_0)+h^2}\left(\frac{1}{1-\alpha}\right)\frac{\Delta T_0(x_0)}{T_0(x_0)} - \frac{1}{2h}\left(\frac{\alpha}{1-\alpha}\right)A(x_0,h), \qquad (4.21)$$

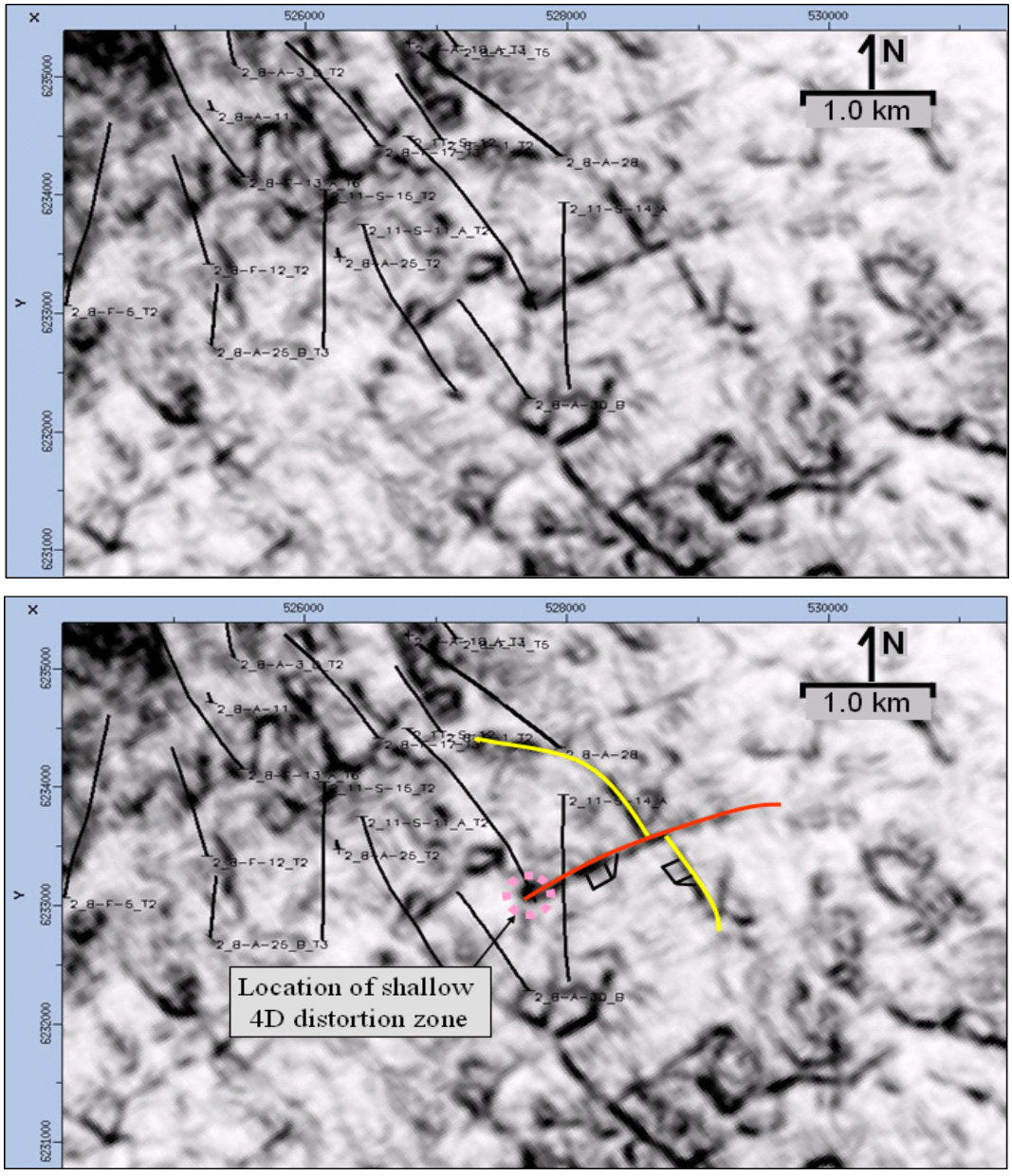

Figure 4.15: Top: Coherency slice at time 1960 ms of Valhall poststack streamer data (from 2002). Bottom: Same coherency slice with two interpreted faults (marked red and yellow). The younger red fault (strike slip) cuts the older yellow fault. The location of the time-lapse distortion zone (encircled) is at the south-west tip of the red fault.

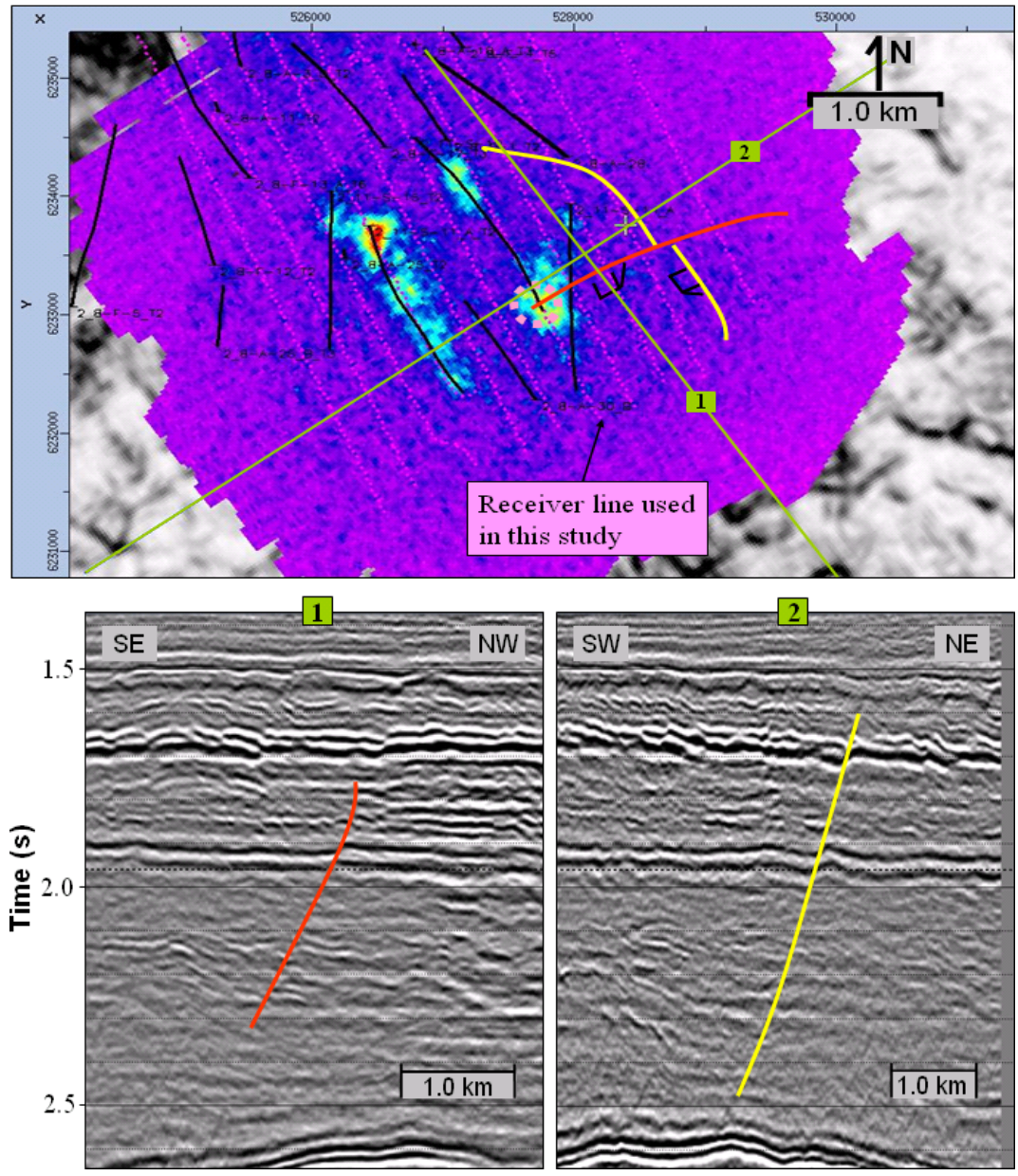

Figure 4.16: The time-slice (at 1960 ms) from last figure shown together with RMS amplitude changes at the top reservoir horizon (top). Marked amplitude changes occur directly beneath the location of the 4D anomaly (encircled). One inline (marked as 1) and one xline (marked as 2) crossing the red and yellow faults are shown at bottom left and right, respectively.

where

$$
\begin{aligned}
A(x_0,h) \;=\; & F_1\left[\int_{x_0-h}^{x_0-h_{p1}} dx\frac{\Delta T_0(x)}{T_0(x)} + \int_{x_0+h_{p1}}^{x_0+h} dx\frac{\Delta T_0(x)}{T_0(x)}\right] \\
& +F_2\left[\int_{x_0-h_{p1}}^{x_0-h_{p2}} dx\frac{\Delta T_0(x)}{T_0(x)} + \int_{x_0+h_{p2}}^{x_0+h_{p1}} dx\frac{\Delta T_0(x)}{T_0(x)}\right] \\
& +F_3\left[\int_{x_0-h_{p2}}^{x_0+h_{p2}} dx\frac{\Delta T_0(x)}{T_0(x)}\right], \qquad (4.22)
\end{aligned}
$$

where h_{p1} and h_{p2} denote the horizontal distances from position x_0 to the ray intersections at the base interface of the sub-sequences 1 and 2, respectively, and h denotes the half-offset. The factors F_1, F_2, and F_3 define the vertical variations in the relative velocity (and thickness) changes, where the case $F_1 = F_2 = F_3 = 1$ leads to no vertical variations (giving equation (4.21) on the same form as equation

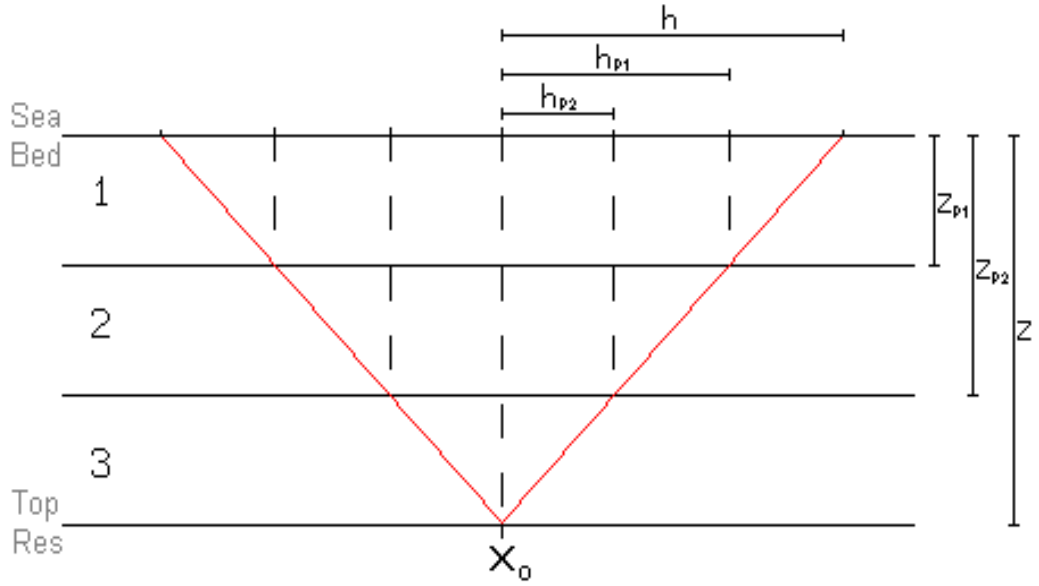

Figure 4.17: The investigated sequence (from the sea bed to the top reservoir horizon) can be divided into 3 smaller horizontal sequences. For simplicity we assume straight raypaths. The points where the ray intersects with the (fictitious) interfaces are given by the depths z_{p1}, z_{p2}, and z, and the horizontal distances from position x_0, denoted h_{p1}, h_{p2}, and h.

(4.8)). The factors must always follow the relation (Appendix 4.A):

$$F_1\left[\int_{x_0-h}^{x_0-h_{p1}} dx + \int_{x_0+h_{p1}}^{x_0+h} dx\right] + F_2\left[\int_{x_0-h_{p1}}^{x_0-h_{p2}} dx + \int_{x_0+h_{p2}}^{x_0+h_{p1}} dx\right] + F_3\left[\int_{x_0-h_{p2}}^{x_0+h_{p2}} dx\right] = \int_{x_0-h}^{x_0+h} dx, \tag{4.23}$$

where the integration signs mean summation over discrete positions (or CDPs).

Note that the extended method is similar to time-lapse tomography (Vesnaver et al., 2003); however, the advantage of our method is that we typically assume 3-4 different factors F_i and that the lateral velocity function is simple (based on zero-offset time shifts).

Examples with the extended method

The extended method is tested on positions around the buried anomaly that creates the distortion pattern observed from positions $x' = 1.55$ km to $x' = 1.8$ km (see Figure 4.12 or Figure 4.13 (top)). The synthetic model in Figure 4.14 shows that this anomaly has position close to $x' = 1.55$ km and vertical extent ranging from depth 1.6 km to 2.3 km. No changes occur above this anomaly. This is also indicated by the real data for a horizon at depth 1.4 km, where no positive time-lapse changes can be found in the area around position $x' = 1.55$ km. This means that approximately 2/3 of the sequence from the sea bed to the top reservoir horizon has no influence on the marked time shifts observed from positions $x' = 1.55$ km to $x' = 1.8$ km. In this case, we might use the extended method (given by equation (4.21)), and assume equal thickness for the 3 sub-sequences with values for the factors F_1 and F_2 close to zero, giving F_3 approximately equal to 3 (from equation (4.23)). These defined factors indicate that time shifts for the top reservoir horizon contribute only from the third sub-sequence (defined between depth 1.7 km and the top reservoir horizon at depth 2.5 km), which might be realistic in this case. Figure 4.18 illustrates the necessity of including these vertical variations for position $x' = 1.7$ km to explain the picked relative offset-dependent time shifts (crosses) for the top reservoir horizon. Figure 4.18(a) shows that the picked (relative) time shifts are poorly described when *no* vertical variations are included; that is, when $F_1 = F_2 = F_3 = 1$ in equation (4.22): Neither the initial nor the last guess of α (that is, $\alpha = 0$ and $\alpha = -5$), given as dashed lines, reproduce the time shifts in the distorted area around offset 1.8 km (shown by an arrow). In comparison, Figure 4.18(b) shows the same position ($x' = 1.7$ km) when using the extended method with $F_1 = 0$ and $F_2 = 0$ (leading to $F_3 \approx 3.0$). The extended method captures the picked time shifts (crosses) better in the distorted area around offset 1.8 km (shown by an arrow). The solid line in Figure 4.18(b) indicates that the best fit of α is close to -5. Even though the

size of the window between the initial and last guess of α (dashed lines in Figure 4.18) is fairly small for the given position, this example confirms that the extended method is applicable for cases with strong vertical variations in relative velocity and thickness changes.

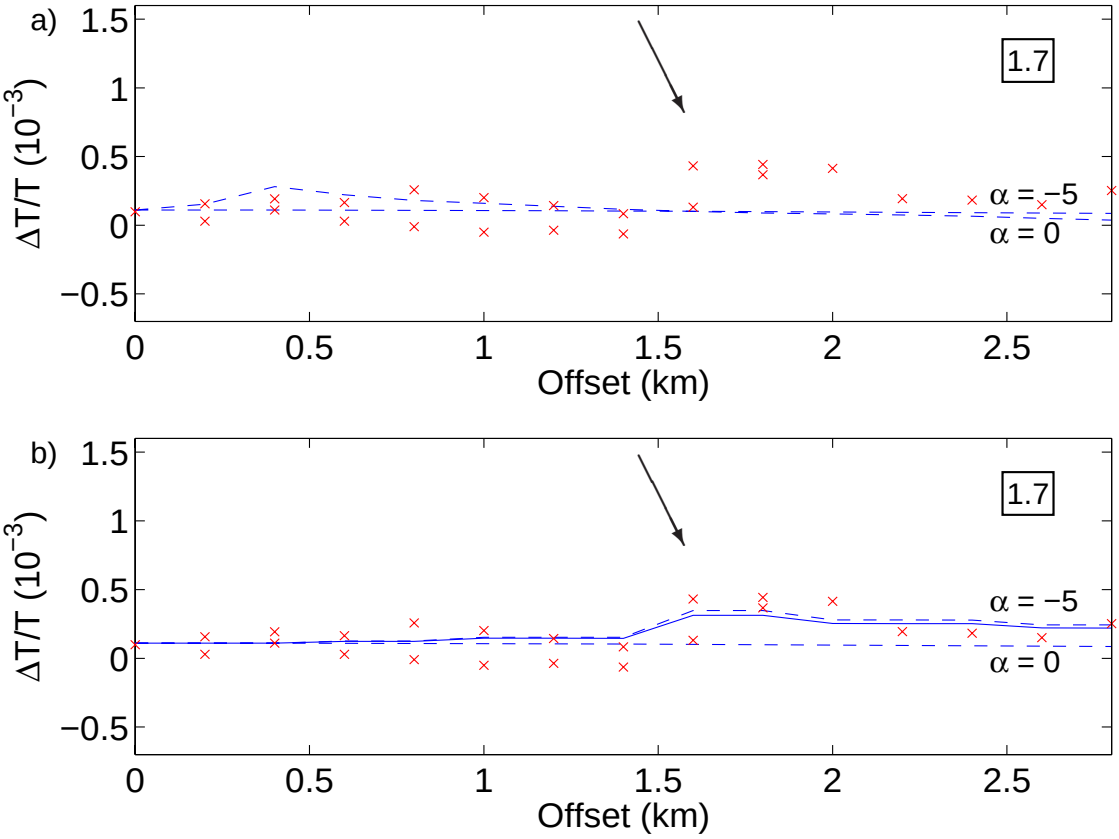

Figure 4.18: Picked time shifts (crosses), as a function of offset, for the top reservoir horizon for position $x' = 1.7$ km (also shown in Figure 4.12d). The dashed lines indicate the initial and last guess of α (that is, $\alpha = 0$ and $\alpha = -5$) when no vertical variations are included (a) and when vertical variations are included with $F_1 = 0$, $F_2 = 0$, and $F_3 \approx 3$ (b). The distorted time shifts around offset 1.8 km (shown by an arrow) are better described in the latter case. The solid line indicates an optimal α-value close to -5.

4.6 Discussion

The quality of the LoFS data appears to be very good, and the permanent installed OBC array offers a high degree of repeatability (NRMS=0.19). Investigations show

an uncertainty in picked relative time shifts of around $0.17 \cdot 10^{-3}$; that is, an uncertainty in time shifts of around 0.4 ms. For the estimated optimal α of -5 for the overburden layers we find a standard deviation ranging from -3 to -25. This uncertainty in α is expected to decrease for time-lapse data with larger time shifts, given that the accuracy of the picked time shifts remains at 0.4 ms.

The α-values estimated in this study correspond well with previous work based on other techniques. Hatchell et al. (2005) determine α to be -5 by matching observed poststack time shift magnitudes for overburden rocks at the Valhall Field. Hatchell and Bourne (2005a) constructed forward models from stress and strain fields using geomechanical models and a stress/strain-dependent seismic velocity. They compared various stress/strain models with observed time shifts for several worldwide field examples, all leading to good match when using α equal to -5 for overburden rocks. A rock physics based study by Carcione et al. (2006) give α-predictions around -5. Future research will hopefully make this picture clearer: Why is the α-value different for overburden rocks compared to reservoir rocks? Is it the difference between compaction and stretching that is the key issue, or is it a lithological effect? Or maybe a combination of the two effects. It might also be that one effect is more dominant for shallow depths.

The accuracy of the present method is dependent on the degree of sensitivity in α (that is, on the size of the window between the initial and last guess of α). However, positions with low sensitivity in α are easy to detect, and therefore easily excluded when estimating the optimal α-value (of -5) for all lateral positions. The method is dependent of small time-lapse changes in anisotropy (less than 1%) and small time-lapse changes in layer thickness and velocity (less than 10%). Further discussions on uncertainties and suggestions for improvements of the method are given by Røste et al. (2006).

The estimated results in this paper are based on receivers (or OBC) assumed to be constant in depth during reservoir compaction (between LoFS surveys 1 and 3). This means that negligible subsidence of the sea bed is assumed, and this is realistic for the investigated 2D lines since the sea bed subsidence during LoFS 1 and 3 is much less than the top reservoir subsidence of the compacting zone studied here. For cases with non-negligible sea bed subsidence, corrections should be made for the subsided receiver-cables.

Observed anomalous time-lapse time shifts systematically moving with offset can be interpreted as slipping faults. Further investigations should be made to decide if such features are common in time-lapse data. It is important to note that such anomalies cannot be detected from poststack time-lapse analysis. In addition, time shift versus offset signatures might lead to uncertainties in stacked zero-offset time

shifts.

Permanent OBC surveys lead to high repeatability. However, non-repeatability problems might still occur. Examples are differences in the source signature and source positions, changes in the water temperature, random noise in the recording units, coherent noise such as free surface multiples, and changes in the quality factor (damping). Saunders et al. (2004) studied differences in source signature from shot to shot and survey to survey at Valhall and concluded that the source signature is sufficiently stable. This is also mentioned by Kommedal et al. (2004), which further discuss the non-repeatability sources of noise, such as noise from rig activity, vessels and other seismic activities on the field. Different traveltime delays for baseline and monitor might occur due to changes in elastic wavefield parameters and quality factor. Stewart et al. (1984) derived an equation that estimates the delay in traveltimes based on traveltimes, frequency ratios, and quality factor Q.

4.7 Conclusions

For reservoir and overburden rocks undergoing compaction and stretching due to reservoir production, it is a challenge to discriminate between velocity and thickness changes. By exploiting differences in zero-offset and offset-dependent time-lapse time shifts, we find that it is possible to estimate thickness and velocity changes simultaneously using high repeatable time-lapse sea bed seismic data from the Valhall Field. For this field data example, we find that we can reliably estimate the ratio between relative velocity and thickness changes, α, for values between 0 and -5. However, for α-values below -5, the uncertainty becomes significant, and other methods, like for instance geomechanical modeling, are needed to constrain the discrimination process. For the top reservoir horizon we estimate a maximum subsidence of 0.50 m $\pm$ 0.29 m and a corresponding velocity decrease for the sequence from the sea bed to the top reservoir of 2.0 m/s $\pm$ 0.40 m/s.

Two localized time-lapse anomalies with characteristic time shift versus offset patterns are observed. The depths and positions of the time shift distortions are determined from geometry and ray tracing. The location of at least one of the time-lapse distortion zones correlates with the tip of a fault. A compacting zone exists directly beneath this fault tip, indicating that a growing fault might be producing the observed anomalies. Detection of fault movements might decrease drilling problems and indicate where fluids have migrated. A semi-tomographic approach which allows vertical (in addition to lateral) variations in the relative thickness and velocity changes is introduced and tested on a position with time shift anomalies.

A major conclusion from this work is that given the high repeatability provided

by a stationary 4D recording system, prestack time-lapse analysis will be an important tool to obtain more precise and quantitative 4D results.

4.8 Acknowledgments

Thomas Røste acknowledges TOTAL for financial support. Special thanks go to Shell for all effort and support spent to make this article possible, as well as Peter Wills for valuable help and discussions. Alexey Stovas is acknowledged for help on making the synthetic model. We thank the Valhall partnership (BP Norge AS, Amerada Hess Norge AS, A/S Norske Shell and Total E&P Norge AS) for permission to publish this work. The results and opinions presented in this paper do not necessarily reflect the view of the Valhall partnership.

4.A Detailed derivation of the method

Assuming a one-layer model with straight raypaths, seismic two-way traveltime for a ray with CDP-position x_0 and offset $2h$ can be expressed as

$$T(x_0,h)=\sqrt{1+\frac{z^2(x_0)}{h^2}}\int\limits_{x_0-h}^{x_0+h}\frac{dx}{v(x)}. \tag{4.A-1}$$

For the post-production (or monitor) case, the two-way traveltime is

$$T'(x_0,h)=\sqrt{1+\frac{z^2(x_0)}{h^2}\left(1+\frac{\Delta z(x_0)}{z(x_0)}\right)^2}\int\limits_{x_0-h}^{x_0+h}\frac{dx}{v(x)\left(1+\frac{\Delta v(x)}{v(x)}\right)}, \tag{4.A-2}$$

where $\frac{\Delta v(x)}{v(x)}$ is assumed to vary with lateral position x, but not with depth. The square root and functions $(1+\frac{\Delta z(x_0)}{z(x_0)})^2$ and $(1+\frac{\Delta v(x)}{v(x)})^{-1}$ in equation (4.A-2) can be expanded in Taylor series. Assuming small relative changes in velocity and thickness; that is, keeping only the first expanded term, equation (4.A-2) becomes

$$\begin{aligned}
T'(x_0,h) &\approx \sqrt{1+\frac{z^2(x_0)}{h^2}\left(1+2\frac{\Delta z(x_0)}{z(x_0)}\right)}\int\limits_{x_0-h}^{x_0+h}\frac{dx}{v(x)}\left(1-\frac{\Delta v(x)}{v(x)}\right)\\
T'(x_0,h) &= \sqrt{1+\frac{z^2(x_0)}{h^2}+2\frac{z^2(x_0)}{h^2}\frac{\Delta z(x_0)}{z(x_0)}}\int\limits_{x_0-h}^{x_0+h}\frac{dx}{v(x)}\left(1-\frac{\Delta v(x)}{v(x)}\right)\\
T'(x_0,h) &= \sqrt{1+\frac{z^2(x_0)}{h^2}}\sqrt{1+\frac{2\frac{z^2(x_0)}{h^2}\frac{\Delta z(x_0)}{z(x_0)}}{1+\frac{z^2(x_0)}{h^2}}}\int\limits_{x_0-h}^{x_0+h}\frac{dx}{v(x)}\left(1-\frac{\Delta v(x)}{v(x)}\right)\\
T'(x_0,h) &\approx \sqrt{1+\frac{z^2(x_0)}{h^2}}\left(1+\frac{\frac{z^2(x_0)}{h^2}\frac{\Delta z(x_0)}{z(x_0)}}{1+\frac{z^2(x_0)}{h^2}}\right)\int\limits_{x_0-h}^{x_0+h}\frac{dx}{v(x)}\left(1-\frac{\Delta v(x)}{v(x)}\right)\\
T'(x_0,h) &= \sqrt{1+\frac{z^2(x_0)}{h^2}}\left(1+\frac{z^2(x_0)}{h^2+z^2(x_0)}\frac{\Delta z(x_0)}{z(x_0)}\right)\\
&\quad\times\int\limits_{x_0-h}^{x_0+h}\frac{dx}{v(x)}\left(1-\frac{\Delta v(x)}{v(x)}\right).
\end{aligned} \tag{4.A-3}$$

From equations (4.A-1) and (4.A-3), the relative change in two-way traveltime becomes

$$\frac{\Delta T(x_0,h)}{T(x_0,h)} = \frac{\left(1+\frac{z^2(x_0)}{h^2+z^2(x_0)}\frac{\Delta z(x_0)}{z(x_0)}\right)\int\limits_{x_0-h}^{x_0+h}\frac{dx}{v(x)}\left(1-\frac{\Delta v(x)}{v(x)}\right)}{\int\limits_{x_0-h}^{x_0+h}\frac{dx}{v(x)}}-1. \quad (4.A\text{-}4)$$

By assuming small lateral variations in initial layer velocity in the vicinity of each position x_0; that is, $v(x)\approx v(x_0)$ for $x_0-h\le x\le x_0+h$, the term $\frac{1}{v(x)}$ can be put outside the integration signs (given in both the numerator and denominator of equation (4.A-4)) and be canceled out. Note, however, that the lateral variations in Δv are included; that is, $\Delta v=\Delta v(x)$:

$$\frac{\Delta T(x_0,h)}{T(x_0,h)} \approx \frac{\left(1+\frac{z^2(x_0)}{h^2+z^2(x_0)}\frac{\Delta z(x_0)}{z(x_0)}\right)\frac{1}{v(x_0)}\int\limits_{x_0-h}^{x_0+h}dx\left(1-\frac{\Delta v(x)}{v(x)}\right)}{\frac{1}{v(x_0)}\int\limits_{x_0-h}^{x_0+h}dx}-1$$

$$\frac{\Delta T(x_0,h)}{T(x_0,h)} = \frac{\left(1+\frac{z^2(x_0)}{h^2+z^2(x_0)}\frac{\Delta z(x_0)}{z(x_0)}\right)\int\limits_{x_0-h}^{x_0+h}dx\left(1-\frac{\Delta v(x)}{v(x)}\right)}{2h}-1. \quad (4.A\text{-}5)$$

Rearranging equation (4.A-5) gives

$$\begin{aligned}
\frac{\Delta T(x_0,h)}{T(x_0,h)} &= \frac{1}{2h}\int_{x_0-h}^{x_0+h} dx\left(1-\frac{\Delta v(x)}{v(x)}\right) \\
&\quad +\frac{z^2(x_0)}{h^2+z^2(x_0)}\frac{\Delta z(x_0)}{z(x_0)}\frac{1}{2h}\int_{x_0-h}^{x_0+h} dx\left(1-\frac{\Delta v(x)}{v(x)}\right)-1 \\
\frac{\Delta T(x_0,h)}{T(x_0,h)} &= 1-\frac{1}{2h}\int_{x_0-h}^{x_0+h} dx\frac{\Delta v(x)}{v(x)}+\frac{z^2(x_0)}{h^2+z^2(x_0)}\frac{\Delta z(x_0)}{z(x_0)} \\
&\quad -\frac{z^2(x_0)}{h^2+z^2(x_0)}\frac{\Delta z(x_0)}{z(x_0)}\frac{1}{2h}\int_{x_0-h}^{x_0+h} dx\frac{\Delta v(x)}{v(x)}-1 \\
\frac{\Delta T(x_0,h)}{T(x_0,h)} &= -\frac{1}{2h}\int_{x_0-h}^{x_0+h} dx\frac{\Delta v(x)}{v(x)}+\frac{z^2(x_0)}{h^2+z^2(x_0)}\frac{\Delta z(x_0)}{z(x_0)} \\
&\quad -\frac{z^2(x_0)}{h^2+z^2(x_0)}\frac{\Delta z(x_0)}{z(x_0)}\frac{1}{2h}\int_{x_0-h}^{x_0+h} dx\frac{\Delta v(x)}{v(x)}, \qquad (4.\text{A-6})
\end{aligned}$$

where the term $\frac{z^2(x_0)}{h^2+z^2(x_0)}\frac{\Delta z(x_0)}{z(x_0)}\frac{1}{2h}\int_{x_0-h}^{x_0+h} dx\frac{\Delta v(x)}{v(x)}$ can be neglected for small changes in relative velocity and thickness changes. This gives

$$\frac{\Delta T(x_0,h)}{T(x_0,h)} \approx -\frac{1}{2h}\int_{x_0-h}^{x_0+h} dx\frac{\Delta v(x)}{v(x)}+\frac{z^2(x_0)}{h^2+z^2(x_0)}\frac{\Delta z(x_0)}{z(x_0)}. \qquad (4.\text{A-7})$$

The relative changes in thickness and velocity can be related to the relative change in vertical traveltime as

$$\frac{\Delta z(x)}{z(x)} \approx \left(\frac{1}{1-\alpha}\right)\frac{\Delta T_0(x)}{T_0(x)} \quad , \quad \frac{\Delta v(x)}{v(x)} \approx \left(\frac{\alpha}{1-\alpha}\right)\frac{\Delta T_0(x)}{T_0(x)}, \qquad (4.\text{A-8})$$

which gives equation (4.A-7) on the following form:

$$\frac{\Delta T(x_0,h)}{T(x_0,h)} \approx \frac{z^2(x_0)}{z^2(x_0)+h^2}\left(\frac{1}{1-\alpha}\right)\frac{\Delta T_0(x_0)}{T_0(x_0)}-\frac{1}{2h}\left(\frac{\alpha}{1-\alpha}\right)\int_{x_0-h}^{x_0+h} dx\frac{\Delta T_0(x)}{T_0(x)}. \qquad (4.\text{A-9})$$

Equation 4.A-9 shows that there exists a relationship between the parameter α, the relative change in traveltime for zero offset, and the relative change in traveltime for a given half-offset h.

4.B Extended method

It is possible to extend the method of Røste et al. (2005) to handle vertical (in addition to lateral) variations in the relative velocity and thickness changes. This can be done by dividing the investigated (overburden) sequence into several smaller horizontal sequences, where the relative velocity and thickness changes are vertically constant within each sub-sequence. By assuming straight raypaths, the method of Røste et al. (2005), given by equation (4.8), can be rewritten:

$$\frac{\Delta T(x_0,h)}{T(x_0,h)} \approx \frac{z^2(x_0)}{h^2+z^2(x_0)}\frac{\Delta z(x_0)}{z(x_0)} - \frac{1}{2h}\left(\int_{L1} dx \frac{\Delta v_1(x)}{v_1(x)} + \int_{L2} dx \frac{\Delta v_2(x)}{v_2(x)} + ... + \int_{Li} dx \frac{\Delta v_i(x)}{v_i(x)}\right) \quad (4.\text{A-}1)$$

where $L1$, $L2$, and Li denote the lengths of the lateral components of the ray inside the sub-sequences 1, 2, and i, respectively, and $\frac{\Delta v_1}{v_1}$, $\frac{\Delta v_2}{v_2}$, and $\frac{\Delta v_i}{v_i}$ denote the relative (vertical) velocity changes for the sub-sequences 1, 2, and i, respectively. Note that the first term on the right side of equation (4.A-1) is unchanged from equation (4.8) since the ray is not influenced by the thickness changes inside each sub-sequence (when assuming straight raypaths), but only by the thickness change for the total investigated sequence at position x_0.

In this paper we will (for simplicity) divide the total sequence into 3 smaller sequences; that is,

$$\frac{\Delta T(x_0,h)}{T(x_0,h)} \approx \frac{z^2(x_0)}{h^2+z^2(x_0)}\frac{\Delta z(x_0)}{z(x_0)} - \frac{1}{2h}\left(\int_{L1} dx \frac{\Delta v_1(x)}{v_1(x)} + \int_{L2} dx \frac{\Delta v_2(x)}{v_2(x)} + \int_{L3} dx \frac{\Delta v_3(x)}{v_3(x)}\right) \quad (4.\text{A-}2)$$

Utilizing equation (4.7) and assuming constant α for all the 3 sub-sequences, equation (4.A-2) may be given as

$$\frac{\Delta T(x_0,h)}{T(x_0,h)} \approx \frac{z^2(x_0)}{z^2(x_0)+h^2}\left(\frac{1}{1-\alpha}\right)\frac{\Delta T_0(x_0)}{T_0(x_0)} - \frac{1}{2h}\left(\frac{\alpha}{1-\alpha}\right)A(x_0,h), \quad (4.\text{A-}3)$$

where

$$\begin{aligned} A(x_0,h) &= F_1\left[\int_{x_0-h}^{x_0-h_{p1}} dx\frac{\Delta T_0(x)}{T_0(x)} + \int_{x_0+h_{p1}}^{x_0+h} dx\frac{\Delta T_0(x)}{T_0(x)}\right] \\ &\quad +F_2\left[\int_{x_0-h_{p1}}^{x_0-h_{p2}} dx\frac{\Delta T_0(x)}{T_0(x)} + \int_{x_0+h_{p2}}^{x_0+h_{p1}} dx\frac{\Delta T_0(x)}{T_0(x)}\right] \\ &\quad +F_3\left[\int_{x_0-h_{p2}}^{x_0+h_{p2}} dx\frac{\Delta T_0(x)}{T_0(x)}\right], \end{aligned} \tag{4.A-4}$$

where h_{p1} and h_{p2} denote the lateral distances from position x_0 to the ray intersections at the base interface of the sub-sequences 1 and 2, respectively, and h denotes the half-offset (see Figure 4.17). The factors F_1, F_2, and F_3 define the vertical variations in relative velocity and thickness changes (where $F_1 = F_2 = F_3 = 1$ give no vertical variations). By defining two of the factors, the last factor is constrained, since the factors need a valid relation; that is,

$$F_1\left[\int_{x_0-h}^{x_0-h_{p1}} dx + \int_{x_0+h_{p1}}^{x_0+h} dx\right] + F_2\left[\int_{x_0-h_{p1}}^{x_0-h_{p2}} dx + \int_{x_0+h_{p2}}^{x_0+h_{p1}} dx\right] + F_3\left[\int_{x_0-h_{p2}}^{x_0+h_{p2}} dx\right] = \int_{x_0-h}^{x_0+h} dx, \tag{4.A-5}$$

where the integration signs mean summation over discrete positions (or CDPs).

Chapter 5

Estimation of layer thickness and velocity changes in anisotropic rocks

5.1 Abstract

A method developed by Røste et al. (2005), which estimates the dilation factor, α, to discriminate between changes in layer thickness and velocity, is here further extended to handle weak anisotropic cases. The dilation factor is the relative velocity change divided by the relative thickness change for a rock undergoing either stretch or compaction. Based on prestack time-lapse seismic data and information about the time-lapse anisotropy changes, the dilation factor α is obtained. The method is tested on synthetic anisotropic models undergoing changes in layer thickness, velocity, and anisotropy. The results are compared with Røste et al.'s (2005) isotropic method.

5.2 Introduction

Based on time-lapse seismic data, Røste et al. (2005, 2006) have tried to monitor thickness and velocity changes of compacting reservoir layers and stretched overburden layers. Since 4D time shifts capture the combined effects of velocity and thickness changes within a given layer, it is a challenge to discriminate the two effects. The relative time shift for zero offset can be expressed in terms of the relative thickness change and velocity change as (Landrø and Stammeijer, 2004; Røste et

al., 2005; Hatchell and Bourne, 2005b)

$$\frac{\Delta T_0(x_0)}{T_0(x_0)} \approx \frac{\Delta z(x_0)}{z(x_0)} - \frac{\Delta v(x_0)}{v(x_0)}, \tag{5.1}$$

where T_0 represents two-way traveltime for zero offset, z is the layer thickness, and v is the layer P-wave velocity. The parameter x_0 denotes the global x-coordinate for a given CDP-location (position), and ΔT_0, Δz, and Δv represent changes in vertical two-way traveltime, thickness, and P-wave velocity, respectively. The basic assumption in equation (5.1) is that all relative changes are small; that is, $\Delta z/z << 1$ and $\Delta v/v << 1$. The relation between relative thickness and velocity changes for a given subsurface layer is approximately proportional to each other (Røste et al., 2005):

$$\frac{\Delta v(x_0)}{v(x_0)} \approx \alpha \frac{\Delta z(x_0)}{z(x_0)}, \tag{5.2}$$

where the dilation factor $\alpha < 0$ is a parameter dependent on the rock properties of the layer. This is a crucial parameter, since it determines the ratio between velocity and thickness changes.

By assuming straight raypaths and small relative changes in velocity and thickness, Røste et al. (2006) obtained a relation between the relative change in two-way traveltime (for a given half-offset h), the dilation factor (α), and relative change in zero-offset traveltime as follows:

$$\frac{\Delta T(x_0,h)}{T(x_0,h)} \approx \frac{z^2(x_0)}{z^2(x_0)+h^2}\left(\frac{1}{1-\alpha}\right)\frac{\Delta T_0(x_0)}{T_0(x_0)} - \frac{1}{2h}\left(\frac{\alpha}{1-\alpha}\right)\int_{x_0-h}^{x_0+h} dx \frac{\Delta T_0(x)}{T_0(x)}. \tag{5.3}$$

Equation (5.3) is only valid for isotropic cases. However, the earth is most likely anisotropic, so the isotropic equation (5.3) is a simplification.

Investigations show that static anisotropy has almost no effect on equation (5.3). However, large time-lapse anisotropy changes must be included. Røste et al. (2006) find that changes of only 1% in Thomsen's (1986) anisotropic parameters δ and ϵ need to be taken into account. In this paper, I try to extend equation (5.3) to handle time-lapse anisotropy changes. By introducing velocities valid for weak anisotropic layers, it is possible to discriminate between velocity and thickness changes for cases with anisotropy changes. Simple synthetic models are made to test the method. As a comparison, the isotropic method of Røste et al. (2005, 2006) (given by equation (5.3)) is tested on the same synthetic time-lapse dataset.

5.3 Estimating α for rocks undergoing time-lapse changes in anisotropy

For layers with weak anisotropy, the P-wave phase velocity can be given as (Thomsen, 1986)

$$v(\theta) = v_0 \left(1 + \delta \sin^2\theta \cos^2\theta + \epsilon \sin^4\theta\right), \tag{5.4}$$

where v_0 denotes the vertical P-wave velocity and δ and ϵ are Thomsen's anisotropic parameters. The parameter θ denotes the phase (wavefront) angle. For small angles θ, equation (5.4) can be given as

$$v(\theta) = v_0 \left(1 + \delta \sin^2\theta\right). \tag{5.5}$$

Note that the approximation (5.5) does not include the anisotropic parameter ϵ. For weak anisotropy, the phase velocity is approximately equal to the group velocity, which means that the phase angle θ is approximately equal to the ray angle.

Assume a one-layer model with vertical P-wave velocity, $v_0(x)$, and weak anisotropy, characterized by $\delta(x)$, that vary along the lateral position x, but are nonvarying with depth (Figure 5.1). By assuming straight raypaths, it can be shown that

$$v(x,h) = v_0(x)\left(1 + \delta(x)\frac{h^2}{h^2 + z^2(x_0)}\right), \tag{5.6}$$

where h denotes half offset and z is depth.

For a prestack CDP gather at position x_0, the seismic two-way traveltime for a raypath with offset $2h$ can be given as an integral over the total raypath length S,

$$T(x_0,h) = \int_S \frac{ds}{v(s)}, \tag{5.7}$$

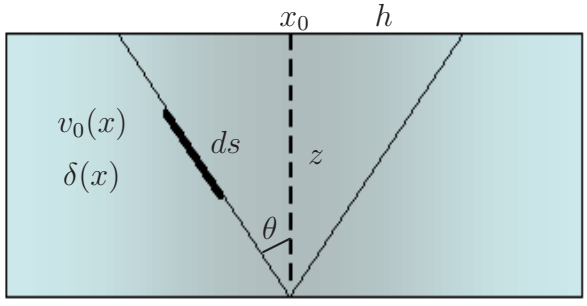

Figure 5.1: Sketch showing that straight raypaths is assumed in an anisotropic model with horizontal variations in vertical velocity and anisotropy. For weak anisotropy, the phase angle θ is approximately equal to the ray angle.

where $v(s)$ denotes the P-wave velocity at the ray position $s(x_0, h)$. For straight raypaths, equation (5.7) can be written as (similar to assuming average slowness within the offset range $2h$)

$$T(x_0,h) \;=\; \sqrt{1+\frac{z^2(x_0)}{h^2}}\int\limits_{x_0-h}^{x_0+h}\frac{dx}{v(x)}, \tag{5.8}$$

where $z(x_0)$ represents the layer thickness at the CDP-position x_0. Inserting the velocity given by equation (5.6) for weak anisotropic cases into equation (5.8), gives the following expression for two-way prestack traveltime:

$$T(x_0,h) \;=\; \sqrt{1+\frac{z^2(x_0)}{h^2}}\int\limits_{x_0-h}^{x_0+h}\frac{dx}{v_0(x)\left(1+\delta(x)\frac{h^2}{h^2+z^2(x_0)}\right)}. \tag{5.9}$$

Equation (5.9) describes the initial (or preproduction) case for weak anisotropic layers. Similar to Røste et al. (2006), I find it essential to include the lateral variations in velocity changes, since it is very likely that such changes will occur both within the reservoir layer as well as the overburden layers of a producing reservoir. For this anisotropic case, I capture the lateral variations in anisotropy changes as well. From equation (5.9), the two-way prestack traveltime for the monitor case is then given as

$$\begin{aligned} T'(x_0,h) \;=\; & \sqrt{1+\frac{z^2(x_0)}{h^2}\left(1+\frac{\Delta z(x_0)}{z(x_0)}\right)^2} \\ & \times\int\limits_{x_0-h}^{x_0+h}\frac{dx}{v_0(x)\left(1+\frac{\Delta v_0(x)}{v_0(x)}\right)\left(1+(\delta(x)+\Delta\delta(x))\left(\frac{h^2}{h^2+z^2(x_0)(1+\frac{\Delta z(x_0)}{z(x_0)})^2}\right)\right)}, \end{aligned} \tag{5.10}$$

where the relative change in vertical velocity, $\Delta v_0(x)/v_0(x)$, and change in anisotropy, $\Delta\delta(x)$, might vary laterally but not with depth. (Note that variations in thickness changes only affect the multiplier outside the integral in equation (5.10) when assuming straight raypaths.) Assuming small relative changes in vertical velocity and thickness, and small change in anisotropy, the relative change in two-way traveltime becomes (Appendix 5.A)

$$\begin{aligned} \tfrac{\Delta T(x_0,h)}{T(x_0,h)} \;=\; & \left(1+\tfrac{z^2(x_0)}{h^2+z^2(x_0)}\tfrac{\Delta z(x_0)}{z(x_0)}\right) \\ & \times\frac{\int_{x_0-h}^{x_0+h}\frac{dx\left(1-\frac{\Delta v_0(x)}{v_0(x)}-\frac{h^2}{h^2(1+\delta(x))+z^2(x_0)}\left(\Delta\delta(x)-\delta(x)\frac{2z^2(x_0)}{z^2(x_0)+h^2}\frac{\Delta z(x_0)}{z(x_0)}\right)\right)}{v_0(x)\left(1+\delta(x)\frac{h^2}{h^2+z^2(x_0)}\right)}}{\int_{x_0-h}^{x_0+h}\frac{dx}{v_0(x)\left(1+\delta(x)\frac{h^2}{h^2+z^2(x_0)}\right)}}-1. \end{aligned} \tag{5.11}$$

From equations (5.1) and (5.2), the relative changes in layer thickness and velocity can be related to the relative change in two-way vertical traveltime T_0:

$$\frac{\Delta z(x_0)}{z(x_0)} \approx \left(\frac{1}{1-\alpha}\right)\frac{\Delta T_0(x_0)}{T_0(x_0)} \quad , \quad \frac{\Delta v(x_0)}{v(x_0)} \approx \left(\frac{\alpha}{1-\alpha}\right)\frac{\Delta T_0(x_0)}{T_0(x_0)}. \tag{5.12}$$

I assume that the initial anisotropy is small; that is, $\delta(x) \ll 1$. In addition, I assume small lateral variations in initial vertical velocity and anisotropy in the vicinity of each position x_0; that is, $v_0(x) \approx v_0(x_0)$ and $\delta(x) \approx \delta(x_0)$ for $x_0 - h \leq x \leq x_0 + h$. This gives equation (5.11) on the simpler form given by equation (5.13). Note, however, that I include the lateral variations in Δv_0 and $\Delta\delta$; that is, $\Delta v_0 = \Delta v_0(x)$ and $\Delta\delta = \Delta\delta(x)$ (Appendix 5.A).

$$\begin{aligned}\frac{\Delta T(x_0,h)}{T(x_0,h)} \quad \approx \quad & \frac{z^2(x_0)}{z^2(x_0)+h^2}\left(\frac{1}{1-\alpha}\right)\frac{\Delta T_0(x_0)}{T_0(x_0)} \\ & -\frac{1}{2h}\left(\frac{\alpha}{1-\alpha}\right)\int_{x_0-h}^{x_0+h} dx \frac{\Delta T_0(x)}{T_0(x)} + A_\delta(x_0,h),\end{aligned} \tag{5.13}$$

Thus, compared to the isotropic case (Røste et al, 2006), an additional term is added:

$$A_\delta(x_0,h) \approx -\frac{h^2}{h^2+z^2(x_0)}\frac{1}{2h}\int_{x_0-h}^{x_0+h} dx \Delta\delta(x), \tag{5.14}$$

where the anisotropy change $\Delta\delta$ is normally unknown. Equation (5.13) shows that the relative change in two-way traveltime (for a given half-offset h) for a medium with time-lapse anisotropy changes is dependent on the anisotropy change ($\Delta\delta$), the estimated relative zero-offset time shifts ($\Delta T_0/T_0$), and the dilation factor (α). This means that the anisotropy change $\Delta\delta$ is needed as input in equation (5.13) as well as the estimated relative zero-offset time shifts. The parameter α is determined by minimizing the least square error in relative traveltime change (equation (5.13)) over the entire offset range.

Note that the anisotropic term $A_\delta(x_0,h)$ is not influenced by static anisotropy. For cases with no time-lapse anisotropy changes; that is, $\Delta\delta(x) = 0$, the anisotropic term $A_\delta(x_0,h)$ becomes zero, giving equation (5.13) on the isotropic form given by equation (5.3).

5.3.1 Synthetic examples for time-lapse anisotropy changes

To test the described anisotropic method, simple synthetic two-layer models (representing one overburden layer and one reservoir layer) are created. The overburden layer models are initially anisotropic and undergo different scenarios of time-lapse

anisotropy changes. The rock physical properties of the layer below the reservoir zone (including the base reservoir horizon) are kept constant. The reservoir layer model preproduction has thickness $z_{\text{res}} = 100$ m and undergoes a compaction of $\Delta z_{\text{res}} = 2$ m. The initial thickness of the overburden layer is $z_{\text{overb}} = 2500$ m and the top horizon of the overburden layer is kept constant in depth, meaning that the thickness change of the overburden layer is equal to the reservoir compaction; that is, $\Delta z_{\text{res}} = \Delta z_{\text{overb}} = 2$ m. The corresponding relative changes in P- and S-wave velocities for the overburden layer model are found by using a dilation factor $\alpha = -2.7$; that is,

$$\frac{\Delta v_{p,\text{overb}}}{v_{p,\text{overb}}} = \frac{\Delta v_{s,\text{overb}}}{v_{s,\text{overb}}} = -2.7\frac{\Delta z_{\text{overb}}}{z_{\text{overb}}}, \tag{5.15}$$

where $v_{p,\text{overb}}$ and $v_{s,\text{overb}}$ denote the initial overburden P- and S-wave velocities, respectively. Assuming mass conservation, the relative change in density is given as

$$\frac{\Delta \rho_{\text{overb}}}{\rho_{\text{overb}}} = \frac{\Delta z_{\text{overb}}}{z_{\text{overb}}}, \tag{5.16}$$

where ρ_{overb} denotes the initial overburden density. Different scenarios for the corresponding time-lapse anisotropy changes for the overburden are created. In all models, the initial overburden anisotropic parameters δ and ϵ are both set to 0.05. Only the overburden layer is investigated, so, for simplicity, the reservoir layer model is isotropic both pre- and postproduction. The reservoir layer model has a dilation factor of -1.5 and mass conservation is assumed.

Figure 5.2 shows the baseline (top) and monitor (bottom) prestack synthetic seismograms for a scenario with initial anisotropic parameters $\delta = 0.05$ and $\epsilon = 0.05$ and time-lapse changes of 1% in both δ and ϵ. The modeled overburden changes in P- and S-wave velocities and density are given by equations (5.15) and (5.16) for a case with $\Delta z_{\text{overb}} = 2$ m and $z_{\text{overb}} = 2500$ m. Prestack traveltimes for the top reservoir horizon are picked for interpolated maximum amplitudes. Zero-offset traveltime (T_0), for a given position x_0, is estimated by stacking the picked offset-dependent traveltimes (T) according to standard hyperbolic moveout (Dix, 1955):

$$T^2(x_0, h) = T_0^2(x_0) + \frac{4}{V_{rms}^2(x_0)}h^2, \tag{5.17}$$

where h denotes half-offset and V_{rms} is rms velocity. For an anisotropic layer, the relation between rms and vertical P-wave velocities for position x_0 is given by (Thomsen, 1986)

$$V_{rms}(x_0) = v_0(x_0)\sqrt{1 + 2\delta(x_0)}. \tag{5.18}$$

The thickness (preproduction) of the investigated sequence is given by

$$z(x_0) = \frac{T_0(x_0)v_0(x_0)}{2}. \tag{5.19}$$

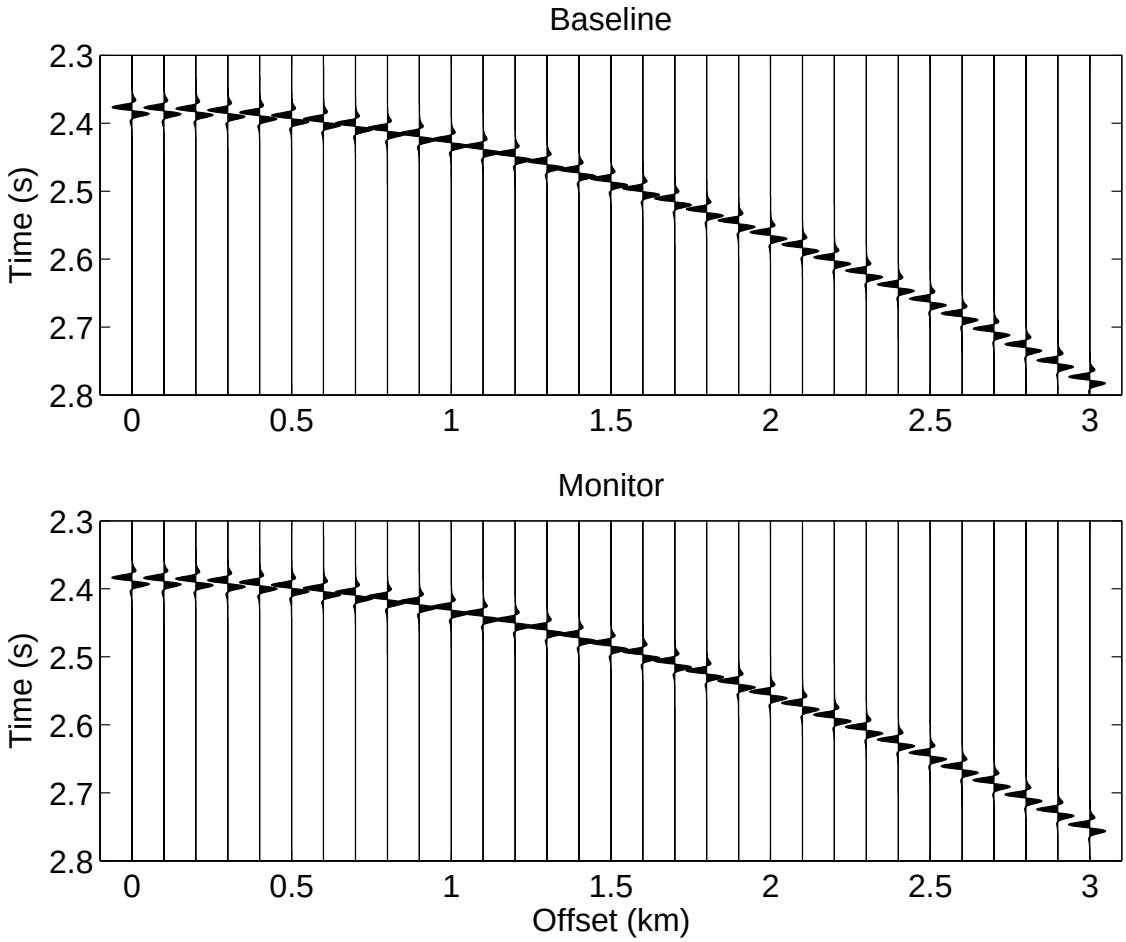

Figure 5.2: Synthetic seismograms (offset gathers) for baseline (top) and monitor (bottom) for an overburden layer model with initial anisotropy $\delta = 0.05$ and $\epsilon = 0.05$ and 1% change in both δ and ϵ. The overburden dilation factor $\alpha = -2.7$.

In contrast to the method of Røste et al. (2005), information about the anisotropy change $\Delta\delta$ is needed as input in equation (5.13). For all analysis given here, I assume that the anisotropy change $\Delta\delta$ is known (however, in practice, estimating $\Delta\delta$ is difficult). When the input parameters are set, the discrimination procedure can start: For an initial guess of α, equation (5.13) gives corresponding (relative) time shifts for different half offsets (h) which can be compared with the picked time shifts. I search for the α-value that leads to the minimum least square error between the estimated and picked relative time shifts, for all offsets.

Figure 5.3 shows this procedure for an overburden layer model with $\alpha = -2.7$ and where the anisotropic parameters $\delta = 0.05$ and $\epsilon = 0.05$ are kept constant;

that is, no time-lapse anisotropy changes occur. The solid line indicates the best fit of the picked relative time shifts (crosses) as a function of offset based on the anisotropic equation (5.13). In this static anisotropic case, the optimal α-value is found to be equal to the modeled value; that is, -2.7. The dashed lines correspond to the initial and last guess of α; that is, $\alpha = 0$ and $\alpha = -5$. Note that the result shown in Figure 5.3 can also be obtained by using the isotropic equation (5.3), since the anisotropic equation (5.13) becomes identical to the isotropic equation (5.3) for cases with static anisotropy (that is, when $\Delta\delta = 0$).

Figure 5.4 shows an example of finding α for an overburden layer model with 1%

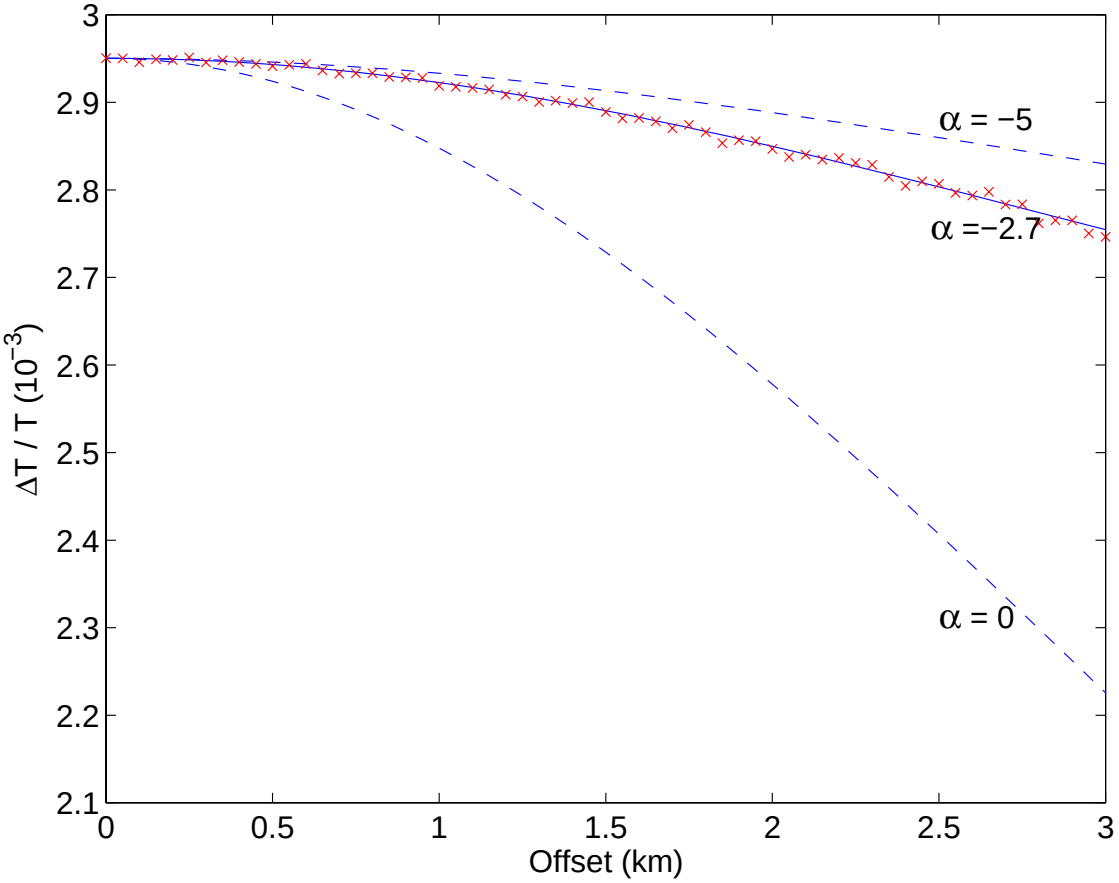

Figure 5.3: Example of finding α for a stretched overburden layer model with $\alpha = -2.7$ and static anisotropy parameters $\delta = 0.05$ and $\epsilon = 0.05$. The solid line indicates the best fit ($\alpha = -2.7$) of the picked relative time shifts (crosses) as a function of offset. The dashed lines correspond to the initial and last guess of α (that is, $\alpha = 0$ and $\alpha = -5$).

time-lapse changes in both δ and ϵ and a dilation factor α of -2.7. The initial overburden parameters δ and ϵ are both set to 0.05. The top of Figure 5.4 shows the result of using the anisotropic equation (5.13), where an optimal α-value of -3.1 (solid line) fits best with the relative picked time shifts (crosses). As a comparison, bottom of Figure 5.4 shows the result of using the isotropic equation (5.3) on the same synthetic dataset. With the isotropic method, an optimal α-value of -1.5 (solid line) fits best with the picked relative time shifts (crosses).

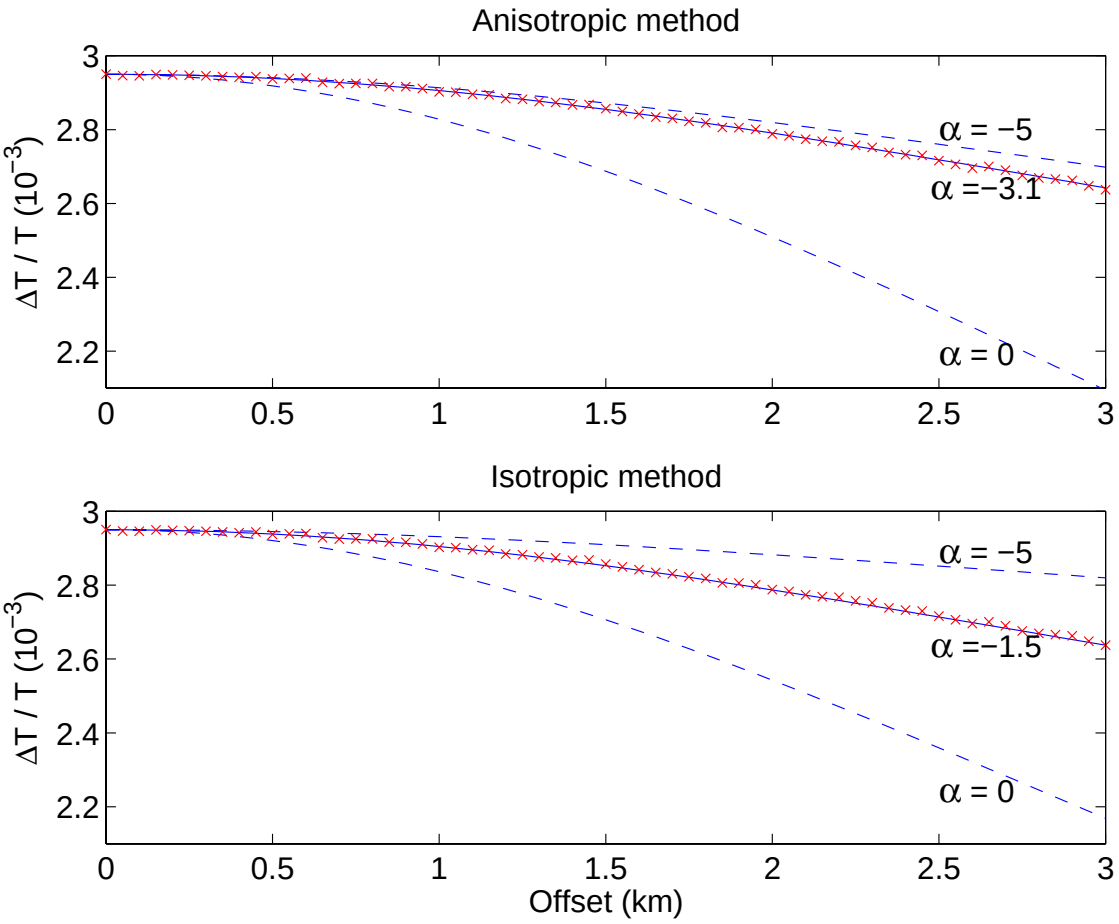

Figure 5.4: Comparing α-estimations by using the anisotropic method (top) and the isotropic method (bottom) on an overburden layer model with 1% change in both the anisotropic parameters δ and ϵ. The initial modeled $\delta = 0.05$ and $\epsilon = 0.05$ and the modeled $\alpha = -2.7$. The solid line indicates the best fit of the picked relative time shifts (crosses) as a function of offset. The dashed lines correspond to the initial and last guess of α (that is, $\alpha = 0$ and $\alpha = -5$).

Figure 5.5 shows an example of finding α for an overburden layer model that undergoes 2% change in both the anisotropic parameters δ and ϵ. The modeled α is -2.7 and the initial δ and ϵ are both set to 0.05. The optimal fitted α (solid line) of the picked relative time shifts (crosses) is -3.6 when using the anisotropic method (top) and -0.9 when using the isotropic method (bottom). By increasing the modeled change in both anisotropic parameters δ and ϵ to 3%, shown in Figure 5.6, the optimal fitted α (solid line) of the picked relative time shifts (crosses) is -4.2 when using the anisotropic method (top) and -0.5 when using the isotropic

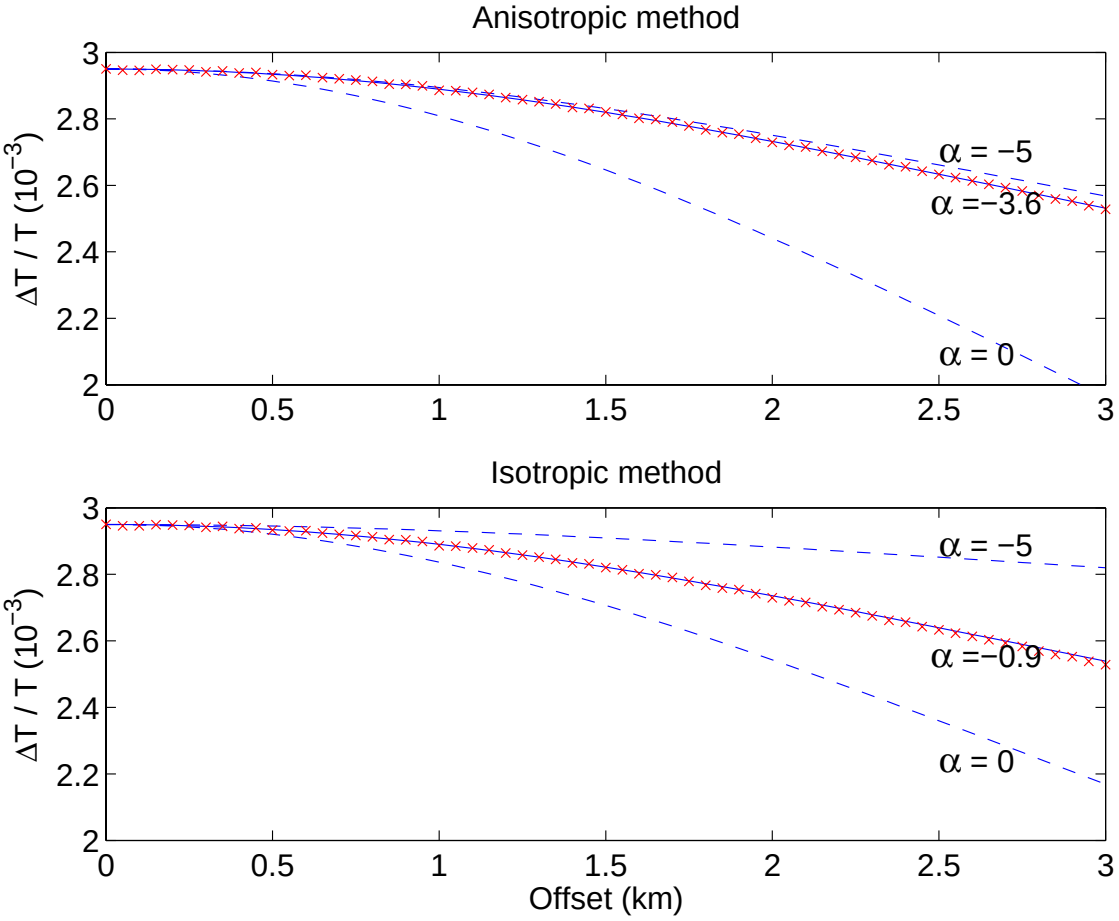

Figure 5.5: Comparing α-estimations by using the anisotropic method (top) and the isotropic method (bottom) on an overburden layer model with 2% change in both the anisotropic parameters δ and ϵ. The initial modeled $\delta = 0.05$ and $\epsilon = 0.05$ and the modeled $\alpha = -2.7$. The solid line indicates the best fit of the picked relative time shifts (crosses) as a function of offset. The dashed lines correspond to the initial and last guess of α (that is, $\alpha = 0$ and $\alpha = -5$).

method (bottom).

Figures 5.4-5.6 show that in anisotropic cases (with time-lapse anisotropy changes), the anisotropic method is better than the isotropic method. However, even the anisotropic method gives inaccurate estimates of α when the changes in anisotropic parameters exceed 3%.

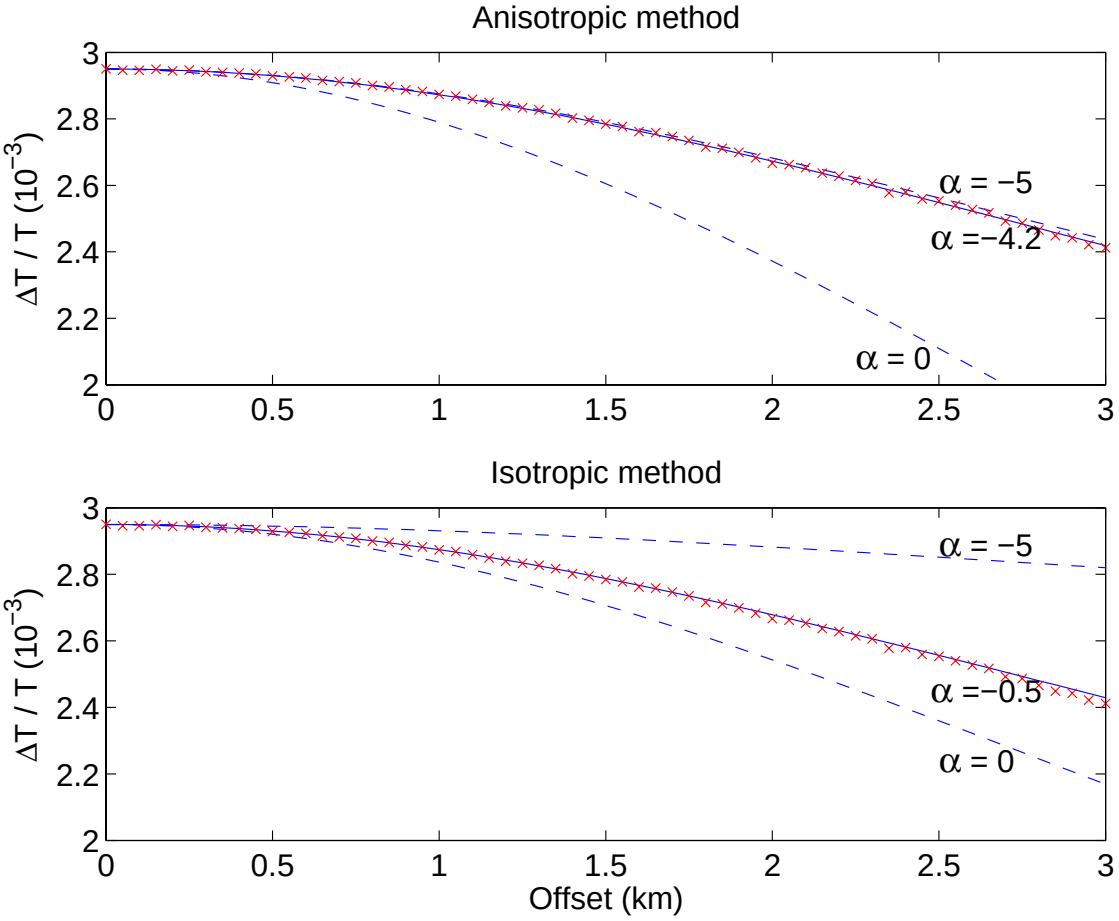

Figure 5.6: Comparing α-estimations by using the anisotropic method (top) and the isotropic method (bottom) on an overburden layer model with 3% change in both the anisotropic parameters δ and ϵ. The initial modeled $\delta = 0.05$ and $\epsilon = 0.05$ and the modeled $\alpha = -2.7$. The solid line indicates the best fit of the picked relative time shifts (crosses) as a function of offset. The dashed lines correspond to the initial and last guess of α (that is, $\alpha = 0$ and $\alpha = -5$).

5.4 Discussion

The proposed method makes it possible to estimate the dilation factor (α) in anisotropic cases with time-lapse anisotropy changes. No information about the initial anisotropic parameters δ and ϵ is needed. However, the anisotropy change $\Delta\delta$ is necessary input to estimate the dilation factor α. In the analysis given here, I have assumed that $\Delta\delta$ is known; however, in practice, it is difficult to estimate $\Delta\delta$.

Attempts to estimate time-lapse anisotropy changes have been proposed by Angerer et al. (2000). Angerer et al. (2002) analyze and identify anisotropic time-lapse effects for a model incorporating saturation and pressure changes in a fractured reservoir. They observe that changes in crack aspect ratios (due to pore-fluid pressure changes) influence the shear-wave splitting. This might indicate that shear-wave splitting can be used to estimate anisotropy changes also for overburden layers. Other ways to estimate $\Delta\delta$ may be to utilize changes in amplitudes or changes in critical reflection angles. It may also be possible to utilize the anisotropic method given in this chapter; that is, assuming that the dilation factor α is known, $\Delta\delta$ can approximately be estimated by use of equation (5.13) (for changes in $\Delta\delta$ less than 3%). However, to determine anisotropy changes was not the objective of this chapter.

The derived anisotropic method is based on Thomsen's (1986) expression for P-wave velocity for layers with weak anisotropy. Further, I have assumed a one-layer model and straight raypaths with small incidence angles, and that the phase velocity is approximately equal to the group velocity. Due to these approximations, the anisotropic parameter ϵ is excluded, and changes in ϵ is not captured by the proposed method. It is possible to develop a method that describes the anisotropy more exact. However, this gives the anisotropic equation (5.13) on a more complex form. In addition, more input parameters, such as $\Delta\epsilon$ and maybe even δ and ϵ (dependent on the accuracy of the method) become necessary.

If no time-lapse anisotropy changes exist, the derived equation (5.13) becomes identical to the isotropic case given by Røste et al. (2005).

5.5 Conclusions

Based on prestack time-lapse seismic traveltime shifts and information about the anisotropy change, I propose a method to estimate the dilation factor (ratio between layer thickness and velocity changes) in anisotropic cases with time-lapse anisotropy changes. The developed method links the relative change in traveltime (for a given offset) with the dilation factor, the change in anisotropy, and the relative change in zero-offset traveltime.

The main conclusion from this study is that if there exist time-lapse anisotropy changes, it is important to account for them when determining the dilation factor α. Synthetic results show that the given anisotropic method produces better results compared to an isotropic method for an anisotropic time-lapse dataset. However, due to approximations, the proposed method becomes inaccurate when the changes in anisotropic parameters exceed 3%. For a synthetic case with static anisotropy; that is, no time-lapse anisotropy changes, it is possible to estimate α accurately. However, in this static anisotropic case, the proposed method becomes identical to the isotropic method.

5.A Detailed derivation of the method

Assume a one-layer model with weak anisotropy defined by the Thomsen parameter δ. Assuming straight raypaths, seismic two-way traveltime for a ray with CDP position x_0 and offset $2h$ can be expressed as

$$T(x_0,h) = \sqrt{1+\frac{z^2(x_0)}{h^2}}\int_{x_0-h}^{x_0+h}\frac{dx}{v_0(x)\left(1+\delta(x)\frac{h^2}{h^2+z^2(x_0)}\right)}. \qquad (5.A\text{-}1)$$

For the postproduction (or monitor) case, the two-way traveltime is

$$T'(x_0,h) = \sqrt{1+\frac{z^2(x_0)}{h^2}\left(1+\frac{\Delta z(x_0)}{z(x_0)}\right)^2} \times\int_{x_0-h}^{x_0+h}\frac{dx}{v_0(x)\left(1+\frac{\Delta v_0(x)}{v_0(x)}\right)\left(1+(\delta(x)+\Delta\delta(x))\left(\frac{h^2}{h^2+z^2(x_0)(1+\frac{\Delta z(x_0)}{z(x_0)})^2}\right)\right)}, \qquad (5.A\text{-}2)$$

where $\Delta v_0(x)/v_0(x)$ and $\Delta\delta(x)$ might vary with lateral position x but not with depth. The functions $(1+\frac{\Delta z(x_0)}{z(x_0)})^2$ and $(1+\frac{\Delta v(x)}{v(x)})^{-1}$ in equation (5.A-2) can be expanded in Taylor series. Assuming small relative changes in velocity and thickness, and small changes in anisotropy; that is, keeping only the first expanded term, the

integral in equation (5.A-2) becomes

$$
\begin{aligned}
&\int_{x_0-h}^{x_0+h} \frac{dx}{v_0(x)\left(1+\frac{\Delta v_0(x)}{v_0(x)}\right)\left(1+(\delta(x)+\Delta\delta(x))\left(\frac{h^2}{h^2+z^2(x_0)(1+\frac{\Delta z(x_0)}{z(x_0)})^2}\right)\right)} \\
\approx &\int_{x_0-h}^{x_0+h} \frac{dx\left(1-\frac{\Delta v_0(x)}{v_0(x)}\right)}{v_0(x)\left(1+(\delta(x)+\Delta\delta(x))\left(\frac{h^2}{h^2+z^2(x_0)(1+2\frac{\Delta z(x_0)}{z(x_0)})}\right)\right)} \\
= &\int_{x_0-h}^{x_0+h} \frac{dx\left(1-\frac{\Delta v_0(x)}{v_0(x)}\right)}{v_0(x)\left(1+(\delta(x)+\Delta\delta(x))\frac{1}{z^2(x_0)}\left(\frac{h^2}{\frac{h^2}{z^2(x_0)}+1+2\frac{\Delta z(x_0)}{z(x_0)}}\right)\right)} \\
= &\int_{x_0-h}^{x_0+h} \frac{dx\left(1-\frac{\Delta v_0(x)}{v_0(x)}\right)}{v_0(x)\left(1+(\delta(x)+\Delta\delta(x))\frac{h^2}{h^2+z^2(x_0)}\left(1-\frac{z^2(x_0)}{2z^2(x_0)+h^2}\frac{\Delta z(x_0)}{z(x_0)}\right)\right)} \\
\approx &\int_{x_0-h}^{x_0+h} \frac{dx\left(1-\frac{\Delta v_0(x)}{v_0(x)}\right)}{v_0(x)\left(1+\delta(x)\frac{h^2}{h^2+z^2(x_0)}\left(1-\frac{z^2(x_0)}{2z^2(x_0)+h^2}\frac{\Delta z(x_0)}{z(x_0)}\right)+\Delta\delta(x)\frac{h^2}{h^2+z^2(x_0)}\right)} \\
= &\int_{x_0-h}^{x_0+h} \frac{dx\left(1-\frac{\Delta v_0(x)}{v_0(x)}\right)}{v_0(x)\left(1+\delta(x)\frac{h^2}{h^2+z^2(x_0)}+\frac{h^2}{h^2+z^2(x_0)}\left(\Delta\delta(x)-\delta(x)\frac{2z^2(x_0)}{z^2(x_0)+h^2}\frac{\Delta z(x_0)}{z(x_0)}\right)\right)} \\
\approx &\int_{x_0-h}^{x_0+h} \frac{dx\left(1-\frac{\Delta v_0(x)}{v_0(x)}\right)}{v_0(x)\left(1+\delta(x)\frac{h^2}{h^2+z^2(x_0)}\right)} \\
&\times\left(1-\frac{\frac{h^2}{h^2+z^2(x_0)}\left(\Delta\delta(x)-\delta(x)\frac{2z^2(x_0)}{z^2(x_0)+h^2}\frac{\Delta z(x_0)}{z(x_0)}\right)}{1+\delta(x)\frac{h^2}{h^2+z^2(x_0)}}\right) \\
= &\int_{x_0-h}^{x_0+h} \frac{dx\left(1-\frac{\Delta v_0(x)}{v_0(x)}\right)\left(1-\frac{h^2\left(\Delta\delta(x)-\delta(x)\frac{2z^2(x_0)}{z^2(x_0)+h^2}\frac{\Delta z(x_0)}{z(x_0)}\right)}{h^2+z^2(x_0)+\delta(x)h^2}\right)}{v_0(x)\left(1+\delta(x)\frac{h^2}{h^2+z^2(x_0)}\right)} \\
\approx &\int_{x_0-h}^{x_0+h} \frac{dx\left(1-\frac{\Delta v_0(x)}{v_0(x)}-\frac{h^2}{h^2(1+\delta(x))+z^2(x_0)}\left(\Delta\delta(x)-\delta(x)\frac{2z^2(x_0)}{z^2(x_0)+h^2}\frac{\Delta z(x_0)}{z(x_0)}\right)\right)}{v_0(x)\left(1+\delta(x)\frac{h^2}{h^2+z^2(x_0)}\right)}.
\end{aligned}
\tag{5.A-3}
$$

For small relative change in thickness, the square root term in equation (5.A-2) can

be expanded in Taylor series. This gives

$$\begin{aligned}
& \sqrt{1+\frac{z^2(x_0)}{h^2}\left(1+\frac{\Delta z(x_0)}{z(x_0)}\right)^2} \\
\approx\ & \sqrt{1+\frac{z^2(x_0)}{h^2}\left(1+2\frac{\Delta z(x_0)}{z(x_0)}\right)} \\
=\ & \sqrt{1+\frac{z^2(x_0)}{h^2}+2\frac{z^2(x_0)}{h^2}\frac{\Delta z(x_0)}{z(x_0)}} \\
=\ & \sqrt{1+\frac{z^2(x_0)}{h^2}}\sqrt{1+\frac{2\frac{z^2(x_0)}{h^2}\frac{\Delta z(x_0)}{z(x_0)}}{1+\frac{z^2(x_0)}{h^2}}} \\
\approx\ & \sqrt{1+\frac{z^2(x_0)}{h^2}}\left(1+\frac{\frac{z^2(x_0)}{h^2}\frac{\Delta z(x_0)}{z(x_0)}}{1+\frac{z^2(x_0)}{h^2}}\right) \\
=\ & \sqrt{1+\frac{z^2(x_0)}{h^2}}\left(1+\frac{z^2(x_0)}{h^2+z^2(x_0)}\frac{\Delta z(x_0)}{z(x_0)}\right). \qquad \text{(5.A-4)}
\end{aligned}$$

Collecting the results from equations (5.A-3) and (5.A-4) gives equation (5.A-2) on the following form:

$$\begin{aligned}
T'(x_0,h) =\ & \sqrt{1+\frac{z^2(x_0)}{h^2}}\left(1+\frac{z^2(x_0)}{h^2+z^2(x_0)}\frac{\Delta z(x_0)}{z(x_0)}\right) \\
& \times \int_{x_0-h}^{x_0+h} \frac{dx\left(1-\frac{\Delta v_0(x)}{v_0(x)}-\frac{h^2}{h^2(1+\delta(x))+z^2(x_0)}\left(\Delta\delta(x)-\delta(x)\frac{2z^2(x_0)}{z^2(x_0)+h^2}\frac{\Delta z(x_0)}{z(x_0)}\right)\right)}{v_0(x)\left(1+\delta(x)\frac{h^2}{h^2+z^2(x_0)}\right)}.
\end{aligned} \qquad \text{(5.A-5)}$$

From equations (5.A-1) and (5.A-5) the relative change in two-way traveltime becomes

$$\begin{aligned}
\frac{\Delta T(x_0,h)}{T(x_0,h)} =\ & \left(1+\frac{z^2(x_0)}{h^2+z^2(x_0)}\frac{\Delta z(x_0)}{z(x_0)}\right) \\
& \times \frac{\int_{x_0-h}^{x_0+h} \frac{dx\left(1-\frac{\Delta v_0(x)}{v_0(x)}-\frac{h^2}{h^2(1+\delta(x))+z^2(x_0)}\left(\Delta\delta(x)-\delta(x)\frac{2z^2(x_0)}{z^2(x_0)+h^2}\frac{\Delta z(x_0)}{z(x_0)}\right)\right)}{v_0(x)\left(1+\delta(x)\frac{h^2}{h^2+z^2(x_0)}\right)}}{\int_{x_0-h}^{x_0+h}\frac{dx}{v_0(x)\left(1+\delta(x)\frac{h^2}{h^2+z^2(x_0)}\right)}} - 1.
\end{aligned} \qquad \text{(5.A-6)}$$

Assuming small lateral variations in initial vertical velocity and anisotropy in the vicinity of each position x_0; that is, $v_0(x) \approx v_0(x_0)$ and $\delta(x) \approx \delta(x_0)$ for $x_0 - h \leq$

$x \leq x_0 + h$, equation (5.A-6) can be written in the simpler form given by equation (5.A-7). Note, however, that I include the lateral variations in Δv_0 and $\Delta\delta$, that is, $\Delta v_0 = \Delta v_0(x)$ and $\Delta\delta = \Delta\delta(x)$).

$$
\begin{aligned}
\tfrac{\Delta T(x_0,h)}{T(x_0,h)} &\approx \left(1+\tfrac{z^2(x_0)}{h^2+z^2(x_0)}\tfrac{\Delta z(x_0)}{z(x_0)}\right) \\
&\quad \times \frac{\int_{x_0-h}^{x_0+h} dx \left(1-\frac{\Delta v_0(x)}{v_0(x)}-\frac{h^2}{h^2(1+\delta(x_0))+z^2(x_0)}\left(\Delta\delta(x)-\delta(x_0)\frac{2z^2(x_0)}{z^2(x_0)+h^2}\frac{\Delta z(x_0)}{z(x_0)}\right)\right)}{v_0(x_0)\left(1+\delta(x_0)\frac{h^2}{h^2+z^2(x_0)}\right)} \\
&\quad \times \frac{}{\int_{x_0-h}^{x_0+h} \frac{dx}{v_0(x_0)\left(1+\delta(x_0)\frac{h^2}{h^2+z^2(x_0)}\right)}} - 1 \\
&= \left(1+\tfrac{z^2(x_0)}{h^2+z^2(x_0)}\tfrac{\Delta z(x_0)}{z(x_0)}\right) \\
&\quad \times \frac{\int_{x_0-h}^{x_0+h} dx \left(1-\frac{\Delta v_0(x)}{v_0(x)}-\frac{h^2}{h^2(1+\delta(x_0))+z^2(x_0)}\left(\Delta\delta(x)-\delta(x_0)\frac{2z^2(x_0)}{z^2(x_0)+h^2}\frac{\Delta z(x_0)}{z(x_0)}\right)\right)}{\int_{x_0-h}^{x_0+h} dx} - 1 \\
&= \left(1+\tfrac{z^2(x_0)}{h^2+z^2(x_0)}\tfrac{\Delta z(x_0)}{z(x_0)}\right) \\
&\quad \times \left(1-\tfrac{1}{2h}\int_{x_0-h}^{x_0+h} dx \tfrac{\Delta v_0(x)}{v_0(x)}-\tfrac{h^2}{h^2(1+\delta(x_0))+z^2(x_0)}\left(\tfrac{1}{2h}\int_{x_0-h}^{x_0+h} dx\Delta\delta(x)-\delta(x_0)\tfrac{2z^2(x_0)}{z^2(x_0)+h^2}\tfrac{\Delta z(x_0)}{z(x_0)}\right)\right) - 1.
\end{aligned}
\tag{5.A-7}
$$

Rearranging equation (5.A-7) and assuming small relative changes in thickness and velocity, and small changes in anisotropy gives

$$
\begin{aligned}
\tfrac{\Delta T(x_0,h)}{T(x_0,h)} &= \left(1+\tfrac{z^2(x_0)}{h^2+z^2(x_0)}\tfrac{\Delta z(x_0)}{z(x_0)}\right) \\
&\quad -\left(1+\tfrac{z^2(x_0)}{h^2+z^2(x_0)}\tfrac{\Delta z(x_0)}{z(x_0)}\right)\tfrac{1}{2h}\int_{x_0-h}^{x_0+h} dx \tfrac{v_0(x)}{v_0(x)} \\
&\quad -\left(1+\tfrac{z^2(x_0)}{h^2+z^2(x_0)}\tfrac{\Delta z(x_0)}{z(x_0)}\right)\tfrac{h^2}{h^2(1+\delta(x_0))+z^2(x_0)}\tfrac{1}{2h}\int_{x_0-h}^{x_0+h} dx\Delta\delta(x) \\
&\quad +\left(1+\tfrac{z^2(x_0)}{h^2+z^2(x_0)}\tfrac{\Delta z(x_0)}{z(x_0)}\right)\tfrac{h^2}{h^2(1+\delta(x_0))+z^2(x_0)}\delta(x_0)\tfrac{2z^2(x_0)}{h^2+z^2(x_0)}\tfrac{\Delta z(x_0)}{z(x_0)} \\
&\quad -1 \\
&\approx \tfrac{z^2(x_0)}{h^2+z^2(x_0)}\tfrac{\Delta z(x_0)}{z(x_0)}-\tfrac{1}{2h}\int_{x_0-h}^{x_0+h} dx \tfrac{\Delta v_0(x)}{v_0(x)} \\
&\quad -\tfrac{h^2}{h^2(1+\delta(x_0))+z^2(x_0)}\left(\tfrac{1}{2h}\int_{x_0-h}^{x_0+h} dx\Delta\delta(x)-\delta(x_0)\tfrac{2z^2(x_0)}{h^2+z^2(x_0)}\tfrac{\Delta z(x_0)}{z(x_0)}\right).
\end{aligned}
\tag{5.A-8}
$$

Assuming small $\delta(x_0)$ (in addition to small $\Delta z(x_0)/z(x_0)$ and $\Delta\delta(x)$), equation (5.A-8) becomes

$$\begin{aligned}\frac{\Delta T(x_0,h)}{T(x_0,h)} &\approx \frac{z^2(x_0)}{h^2+z^2(x_0)}\frac{\Delta z(x_0)}{z(x_0)} - \frac{1}{2h}\int_{x_0-h}^{x_0+h} dx \frac{\Delta v_0(x)}{v_0(x)} \\ &\quad - \frac{h^2}{h^2+z^2(x_0)}\left(1-\frac{\delta(x_0)}{1+\frac{h^2}{z^2(x_0)}}\right)\left(\frac{1}{2h}\int_{x_0-h}^{x_0+h} dx\Delta\delta(x)\right) \\ &\approx \frac{z^2(x_0)}{h^2+z^2(x_0)}\frac{\Delta z(x_0)}{z(x_0)} - \frac{1}{2h}\int_{x_0-h}^{x_0+h} dx \frac{\Delta v_0(x)}{v_0(x)} \\ &\quad - \frac{h^2}{h^2+z^2(x_0)}\frac{1}{2h}\int_{x_0-h}^{x_0+h} dx\Delta\delta(x). \end{aligned} \tag{5.A-9}$$

The two first terms on the right hand side of equation (5.A-9) describe the isotropic case, while the last term includes anisotropic cases. Simplified, the relative change in traveltime can be given as

$$\frac{\Delta T(x_0,h)}{T(x_0,h)} \approx \frac{z^2(x_0)}{h^2+z^2(x_0)}\frac{\Delta z(x_0)}{z(x_0)} - \frac{1}{2h}\int_{x_0-h}^{x_0+h} dx \frac{\Delta v_0(x)}{v_0(x)} + A_\delta(x_0,h), \tag{5.A-10}$$

where the anisotropic term $A_\delta(x_0,h)$ is only dependent on the anisotropy change; that is,

$$A_\delta(x_0,h) \approx -\frac{h^2}{h^2+z^2(x_0)}\frac{1}{2h}\int_{x_0-h}^{x_0+h} dx\Delta\delta(x). \tag{5.A-11}$$

The relative changes in thickness and velocity can be related to the relative change in vertical traveltime as

$$\frac{\Delta z(x)}{z(x)} \approx \left(\frac{1}{1-\alpha}\right)\frac{\Delta T_0(x)}{T_0(x)} \quad , \quad \frac{\Delta v(x)}{v(x)} \approx \left(\frac{\alpha}{1-\alpha}\right)\frac{\Delta T_0(x)}{T_0(x)}, \tag{5.A-12}$$

which gives equation (5.A-10) on the following form:

$$\begin{aligned}\frac{\Delta T(x_0,h)}{T(x_0,h)} &\approx \frac{z^2(x_0)}{z^2(x_0)+h^2}\left(\frac{1}{1-\alpha}\right)\frac{\Delta T_0(x_0)}{T_0(x_0)} \\ &\quad -\frac{1}{2h}\left(\frac{\alpha}{1-\alpha}\right)\int_{x_0-h}^{x_0+h} dx\frac{\Delta T_0(x)}{T_0(x)} + A_\delta(x_0,h). \end{aligned} \tag{5.A-13}$$

Chapter 6

Discrimination between pressure and fluid saturation changes in compacting reservoirs from time-lapse seismic data

Thomas Røste*, and Martin Landrø*

**Norwegian University of Science and Technology,*
Department of Petroleum Engineering and Applied Geophysics,
S.P.Andersens vei 15A, N-7491 Trondheim, Norway.

Expanded abstract submitted to the 69th EAGE Conference & Exhibition, London, England, June 2007.

6.1 Abstract

A method based on time-lapse amplitude variation with offset (AVO) analysis is presented to discriminate between pressure and saturation changes in compacting reservoirs. This might be a three-parameter problem, including pressure, saturation, and porosity changes. However, laboratory measurements show that the porosity changes are related to pressure and saturation changes, which reduces the problem to two parameters.

Due to pressure and saturation changes, the reservoir rocks might undergo changes in porosity, rock framework moduli, fluid density, and fluid bulk modulus. These

processes occur simultaneously; however, we assume that they can be treated independently. Based on this assumption, explicit expressions for computing pressure- and saturation-related changes from time-lapse seismic data are presented. The expressions are tested on 10 synthetic models for different reservoir scenarios. The fit between estimated and "real" changes in pressure and water saturation is good, except for cases where the pressure change becomes larger than 2 kpsi (13.8 MPa).

6.2 Introduction

Several researches (Dutta et al., 2002; Carcione et al., 2003) have tried to predict overpressured zones from seismic data. The basic tool in such studies has been velocity analysis. For most reservoirs, pore pressure changes and fluid saturation changes create abnormal seismic responses. It is difficult to separate the effects based on stacked PP seismic data only. In most time-lapse seismic studies, seismic differences between a baseline and a monitor survey are analyzed and interpreted as either a pressure effect or a fluid effect. In the Magnus study (Watts et al., 1996), the main seismic changes were attributed to pore pressure changes, while in the Gullfaks (Landrø et al., 1999) and the Draugen (Gabriels et al., 1999) 4D seismic studies, most of the seismic changes were interpreted as fluid related.

For some fields or segments within the field, both fluid and pressure changes have approximately the same degree of impact on the seismic data. In such cases the use of time-lapse amplitude variation with offset (AVO) analysis (see Tura and Lumley, 1998, 1999a; Landrø, 1999a; Landrø, 2001) or time-lapse PP- and PS-reflectivity stacks (see Landrø et al., 2003; Stovas et al., 2003) offer an opportunity to discriminate the two effects. However, these methods do not include reservoir compaction; that is, porosity changes during hydrocarbon production and water injection are neglected. Modifications are therefore needed for reservoirs where pressure and water saturation changes induce porosity changes.

At first, one might assume that changes in pressure, saturation, and porosity are three independent parameters. However, from laboratory measurements Sylte et al. (1999) found that porosity changes are related to pressure and saturation changes. By using this empirical relation, we reduce our three parameter estimation problem to a two-parameter problem. We therefore need two equations to determine these two parameters (for instance pressure and saturation changes), and our approach is to assume that time-lapse amplitude changes versus offset can be used.

Examples of reservoirs compacting due to pressure and saturation changes are the Ekofisk and Valhall chalk fields. At the Ekofisk Field, pressure depletion and water injection have induced significant compaction of the reservoir, and, as a result, the

sea bed has subsided up to 7.8 meters (Sylte et al., 1999). At the Valhall Field, the compaction of the chalk reservoir has led to a maximum subsidence of the sea bed of the order of 5-6 meters (Barkved and Kristiansen, 2005). So far, the compaction at Valhall has been primarily due to pressure depletion, but a recent (January 2004) water injection program is expected to induce additional reservoir compaction. Although compaction effects are most significant for chalk fields, it is also expected that sandstone reservoirs will compact. Tura et al. (2005) show an example from a turbidite field in the deepwater Gulf of Mexico, where production-induced compaction is the main drive mechanism.

A difficult task for compacting reservoirs is that changes in the solid framework and pore-fluid density occur simultaneously with porosity changes. However, in this paper we assume that the framework and fluid density changes can be treated independently of the porosity changes. We describe a method which estimates changes in fluid saturation and pore pressure in a compacting reservoir based on time-lapse PP AVO seismic data. The developed method is based on parameters similar to the Ekofisk Field. A suggestion on how to use two-way traveltime shifts for PP- and PS-waves is given in Appendix 6.C.

6.3 Saturation and stress versus seismic parameters

Distinguishing between fluid saturation and pore pressure changes from seismic data requires knowledge about how seismic parameters are influenced by such changes. Landrø (2001) and Landrø et al. (1999, 2003) used a rock physics model calibrated with well-log measurements from the Gullfaks Field to predict the seismic effect of substituting oil with water. Other methods are proposed by Tura and Lumley (1998, 1999a, 1999b) and Brevik (1999). The basic equation in this rock physics modeling is the Gassmann equation (Gassmann, 1951). It is assumed that the Gullfaks reservoir sand layers do not compact during production, meaning that there are no porosity changes. For compacting reservoirs such as Valhall and Ekofisk, additional terms for porosity loss are therefore needed in the rock physics modeling.

In this paper the initial (or preproduction) P-wave velocity, S-wave velocity, and density for the cap rock layer are α_1, β_1, and ρ_1, respectively. In layer 2 (which is assumed to be the reservoir layer), the corresponding preproduction parameters are denoted α_2, β_2, and ρ_2. For chalk reservoir rocks, we might discriminate between the processes that lead to porosity changes, and the processes that lead to reservoir changes independently of the porosity changes. Simplified, the change in P-wave

velocity for the reservoir can be given as a function of these parameters; that is,

$$\Delta\alpha_2 = \frac{\partial\alpha_2}{\partial\phi_2}\Delta\phi_2 + \frac{\partial\alpha_2}{\partial S_w}\Delta S_w + \frac{\partial\alpha_2}{\partial\sigma}\Delta\sigma. \tag{6.1}$$

where $\Delta\phi_2$, ΔS_w, and $\Delta\sigma$ denote changes in porosity, water saturation, and effective stress, respectively. According to equation (6.1), we assume that the velocity change is a function of three independent parameters. However, according to Sylte et al. (1999) there is a relation between the porosity changes and the saturation and stress changes; that is,

$$\Delta\phi_2 = \frac{\partial\phi_2}{\partial\sigma}\Delta\sigma + \frac{\partial\phi_2}{\partial S_w}\Delta S_w. \tag{6.2}$$

Combining equations (6.1) and (6.2), we reduce the number of parameters from three to two. Equation (6.2) is based on rock physics laboratory measurements. However, based on simple physical considerations, it is reasonable to assume that porosity might change as stress and saturation changes. The important, remaining question is if there are other reservoir parameters that might influence the porosity, which should be included in equation (6.2). One such parameter might be temperature, since we know that the rock framework (solid rock) and the pore fluids will expand at different rates as the temperature changes. Despite these concerns, we choose to disregard other parameters in equation (6.2), and assume that other terms in this equation can be neglected.

For weak reservoir chalk, porosity changes (or compaction) may occur as a result of pressure depletion or water injection. Pressure depletion is normally the main contribution to compaction in the early phases of a chalk field's life. Later, water injection becomes a large additional drive mechanism to reservoir compaction. The strong compaction of chalk when reacting with water is confirmed by laboratory experiments. Sylte et al. (1999) found a quantitative model of Ekofisk chalk behavior, where porosity loss is a function of initial porosity, effective stress, and water saturation. From extensive rock mechanics testing they found that a good approximation for chalk is that the porosity is a linear function of water saturation over the range of stresses encountered during production from the Ekofisk reservoir. Based on the result of Sylte et al. (1999) for a chalk sample with initial porosity 42% (Figure 6.1), we find the following relation between porosity (ϕ), water saturation (S_w), and effective stress (σ):

$$\phi_2 = A_{\phi S}S_w + A_{\phi\sigma}\sigma + A_{\phi S\sigma}S_w\sigma + A_\phi, \tag{6.3}$$

where $A_{\phi S} = 0.128$, $A_{\phi\sigma} = -0.00283\ \frac{1}{\text{kpsi}}$, $A_{\phi S\sigma} = -0.064\ \frac{1}{\text{kpsi}}$, and $A_\phi = 0.426$ when the effective stress is given in kpsi and the water saturation is given as a number between 0 and 1. Partial differentiations of equation (6.3) with respect to

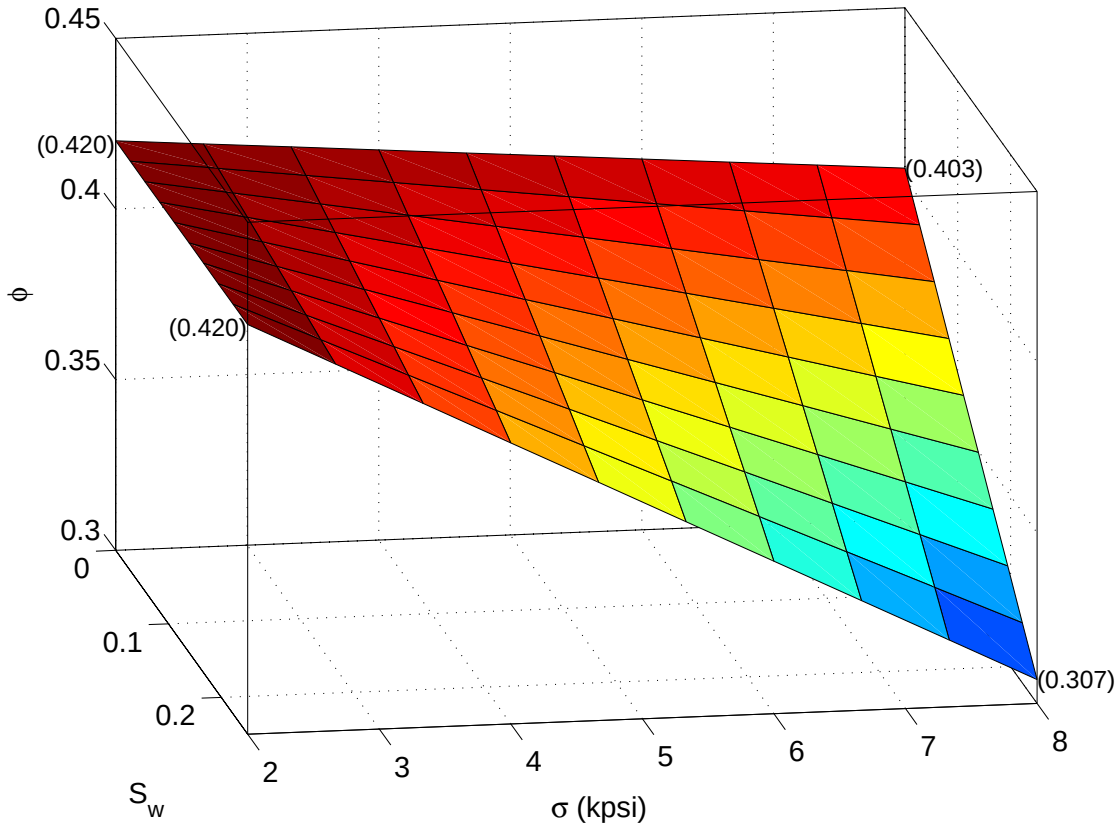

Figure 6.1: Porosity as a function of effective stress (given in kpsi) and water saturation for chalk (as given by equation (6.7)) with initial water saturation of 5% and 2 kpsi initial stress. The model is based on laboratory data from Sylte et al. (1999) for a 42% porosity chalk sample.

saturation and stress give

$$\frac{\partial \phi_2}{\partial S_w} = A_{\phi S} + A_{\phi S\sigma}\sigma, \tag{6.4}$$

$$\frac{\partial \phi_2}{\partial \sigma} = A_{\phi\sigma} + A_{\phi S\sigma}S_w. \tag{6.5}$$

The expression for porosity changes can then be written as

$$\Delta\phi_2 = (A_{\phi S} + A_{\phi S\sigma}\sigma)\Delta S_w + (A_{\phi\sigma} + A_{\phi S\sigma}S_w)\Delta\sigma. \tag{6.6}$$

Substituting initial values for S_w and σ in equation (6.6) gives a first order approximation for $\Delta\phi_2$. This means that $\Delta\phi_2$ versus ΔS_w and $\Delta\sigma$ become a plane surface,

which will not capture the curved surface shape of $\Delta\phi_2$, originating from the cross term ($A_{\phi S\sigma}S_w\sigma$) in equation (6.3) (Figure 6.1). Since porosity changes have large influence on the seismic parameter changes, we choose to capture this cross term. This can be done by inserting the initial value for water saturation (S_{wi}) and the postproduction value for stress ($\sigma_i + \Delta\sigma$) in equation (6.6):

$$\Delta\phi_2 = (A_{\phi S} + A_{\phi S\sigma}\sigma_i)\Delta S_w + (A_{\phi\sigma} + A_{\phi S\sigma}S_{wi})\Delta\sigma + A_{\phi S\sigma}\Delta S_w\Delta\sigma, \quad (6.7)$$

where S_{wi} and σ_i denote the initial states of water saturation and stress, respectively. Figure 6.2 shows the change in porosity versus water saturation and effective stress (equation (6.7)) for initial water saturation of 5% and 2 kpsi initial stress, which is similar to the initial reservoir state at Ekofisk (Gauer et al., 2002; Sylte et al., 1999).

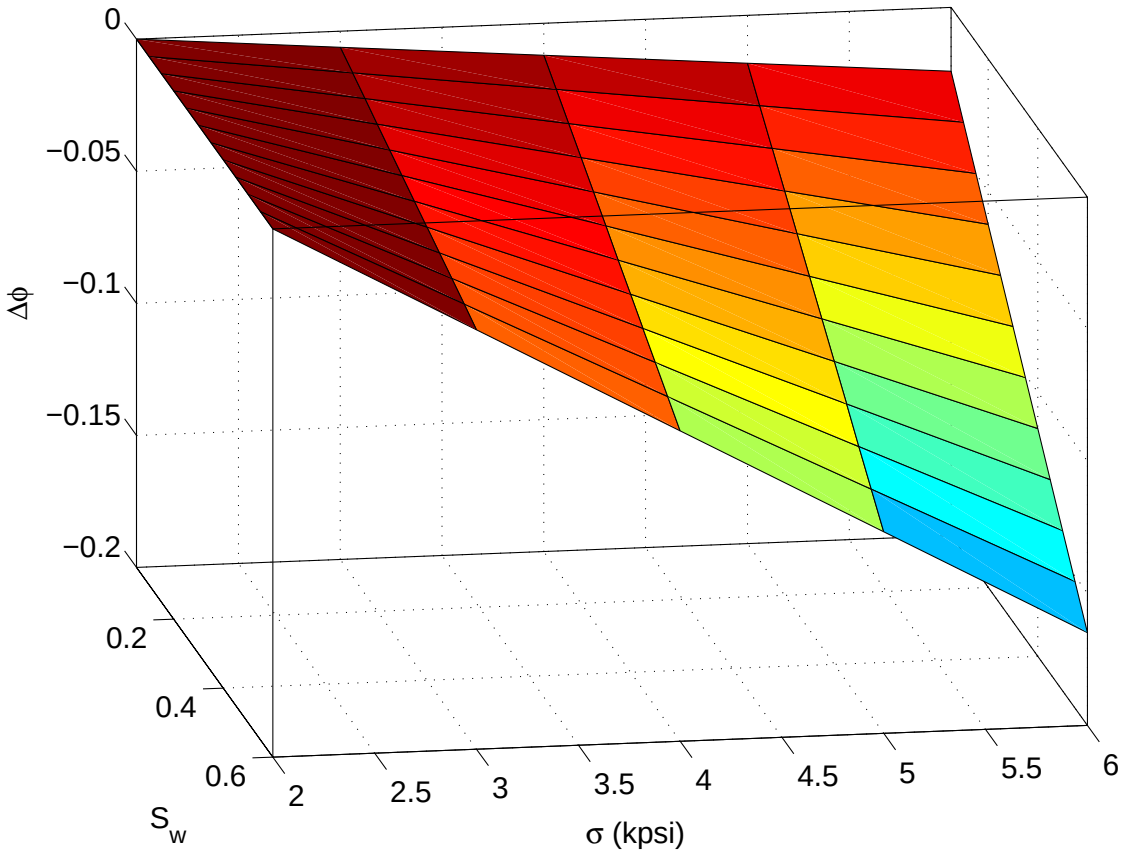

Figure 6.2: Change in porosity as a function of water saturation S_w and effective stress σ based on laboratory data for a 42% porosity chalk sample. Initial water saturation of 5% and 2 kpsi initial effective stress are assumed.

Changes in reservoir P-wave velocity, S-wave velocity, and density, due to porosity changes only, can be written as

$$[\Delta\alpha_2]_{\Delta\phi} = \frac{\partial\alpha_2}{\partial\phi_2}\Delta\phi_2, \tag{6.8}$$

$$[\Delta\beta_2]_{\Delta\phi} = \frac{\partial\beta_2}{\partial\phi_2}\Delta\phi_2, \tag{6.9}$$

$$[\Delta\rho_2]_{\Delta\phi} = \frac{\partial\rho_2}{\partial\phi_2}\Delta\phi_2, \tag{6.10}$$

where the porosity changes $\Delta\phi_2$ are given by equation (6.7). The partial derivatives $\frac{\partial\alpha_2}{\partial\phi_2}$ and $\frac{\partial\beta_2}{\partial\phi_2}$ (given in equations (6.8) and (6.9), respectively) can be estimated from well logs. Based on ultrasonic measurements on core samples, Han (1986) found the following empirical relationships between velocity and porosity:

$$\alpha_2 = B_\alpha + B_{\alpha\phi}\phi_2, \tag{6.11}$$
$$\beta_2 = B_\beta + B_{\beta\phi}\phi_2, \tag{6.12}$$

where B_α, $B_{\alpha\phi}$, B_β, and $B_{\beta\phi}$ are positive constants. Differentiation of equations (6.11) and (6.12) gives

$$\frac{\partial\alpha_2}{\partial\phi_2} = B_{\alpha\phi}, \tag{6.13}$$

$$\frac{\partial\beta_2}{\partial\phi_2} = B_{\beta\phi}. \tag{6.14}$$

For a chalk reservoir, we find from well logs that $B_{\alpha\phi} = -5500$ m/s and $B_{\beta\phi} = -3000$ m/s. The partial derivative $\frac{\partial\rho_2}{\partial\phi_2}$ (given in equation (6.10)) can be found by using the following density relation for the reservoir chalk:

$$\rho_2 = \phi_2\left(\rho_w S_w + \rho_o(1 - S_w)\right) + (1 - \phi_2)\rho_S, \tag{6.15}$$

where ρ_w, ρ_o, and ρ_S are the water, oil, and solid densities of the reservoir, respectively, and S_w is the water saturation. The density change due to porosity changes can then be given as

$$\frac{\partial\rho_2}{\partial\phi_2} = B_{\rho\phi}, \tag{6.16}$$

where $B_{\rho\phi} = \rho_w S_w - \rho_o(1 - S_w) - \rho_S$. We assume oil density $\rho_o = 0.75$ g/cm^3, water density $\rho_w = 1.02$ g/cm^3, solid density $\rho_S = 2.70$ g/cm^3 (for chalk), and water saturation $S_w = 0.05$ (similar to initial saturation state of Ekofisk).

Equations (6.8), (6.9), and (6.10) describe changes in reservoir seismic parameters only influenced by porosity changes. However, compacting reservoirs might also undergo changes in the solid framework due to stress changes and changes in density due to pore fluid changes. In practice, these changes occur simultaneously with the porosity changes in a compacting reservoir. However, we will assume that the framework changes (that is, changes in bulk and shear moduli) and pore fluid density changes can be treated independently of the porosity changes. It is important to stress that this stepwise view is idealized. Changes in reservoir P-wave velocity, S-wave velocity, and density can be given as (assuming constant porosity)

$$[\Delta\alpha_2]_{\phi_c} = \left[\frac{\partial\alpha_2}{\partial S_w}\Delta S_w + \left(\frac{\partial\alpha_2}{\partial K_{fr}}\frac{\partial K_{fr}}{\partial\sigma} + \frac{\partial\alpha_2}{\partial G_{fr}}\frac{\partial G_{fr}}{\partial\sigma}\right)\Delta\sigma\right]_{\phi_c}, \tag{6.17}$$

$$[\Delta\beta_2]_{\phi_c} = \left[\frac{\partial\beta_2}{\partial S_w}\Delta S_w + \frac{\partial\beta_2}{\partial G_{fr}}\frac{\partial G_{fr}}{\partial\sigma}\Delta\sigma\right]_{\phi_c}, \tag{6.18}$$

$$[\Delta\rho_2]_{\phi_c} = \left[\frac{\partial\rho_2}{\partial S_w}\Delta S_w\right]_{\phi_c}, \tag{6.19}$$

where ϕ_c denotes constant porosity, indicating that the seismic parameter changes given by equations (6.17) to (6.19) occur independently of the porosity changes. (Note that the density changes given by equation (6.19) are not influenced by stress changes under the assumption of constant porosity.) We will use the following notations:

$$\begin{gathered}\left[\frac{\frac{\partial\alpha_2}{\alpha_2}}{\partial S_w}\right]_{\phi_c} = L_{\alpha S}, \quad \left[\frac{\frac{\partial\beta_2}{\beta_2}}{\partial S_w}\right]_{\phi_c} = L_{\beta S}, \quad \left[\frac{\frac{\partial\rho_2}{\rho_2}}{\partial S_w}\right]_{\phi_c} = L_{\rho S}, \\ \left[\frac{\frac{\partial\alpha_2}{\alpha_2}}{\partial K_{fr}}\right]_{\phi_c} = M_{\alpha K}, \quad \left[\frac{\frac{\partial\alpha_2}{\alpha_2}}{\partial G_{fr}}\right]_{\phi_c} = M_{\alpha G}, \quad \left[\frac{\frac{\partial\beta_2}{\beta_2}}{\partial G_{fr}}\right]_{\phi_c} = M_{\beta G}, \\ \left[\frac{\partial K_{fr}}{\partial\sigma}\right]_{\phi_c} = N_{K\sigma}, \quad \left[\frac{\partial G_{fr}}{\partial\sigma}\right]_{\phi_c} = N_{G\sigma},\end{gathered} \tag{6.20}$$

where the first 6 parameters in equation (6.20); that is, $L_{\alpha S}$, $L_{\beta S}$, $L_{\rho S}$, $M_{\alpha K}$, $M_{\alpha G}$, and $M_{\beta G}$, are estimated by calibrating the Gassmann model to parameters valid for the field under consideration. In general, the Gassmann equation should be used with care for compacting reservoirs, since the equation is only valid for static cases. The validity of the Gassmann equation for chalk may also be discussed (see e.g. Røgen et al., 2005). However, we assume that the Gassmann equation is valid for the static case described by equations (6.17) to (6.19). Figure 6.3 shows the change in P-wave velocity versus saturation for calibrated Gassmann model valid for the Ekofisk Field (see Table 6.1). The initial (preproduction) water saturation is set

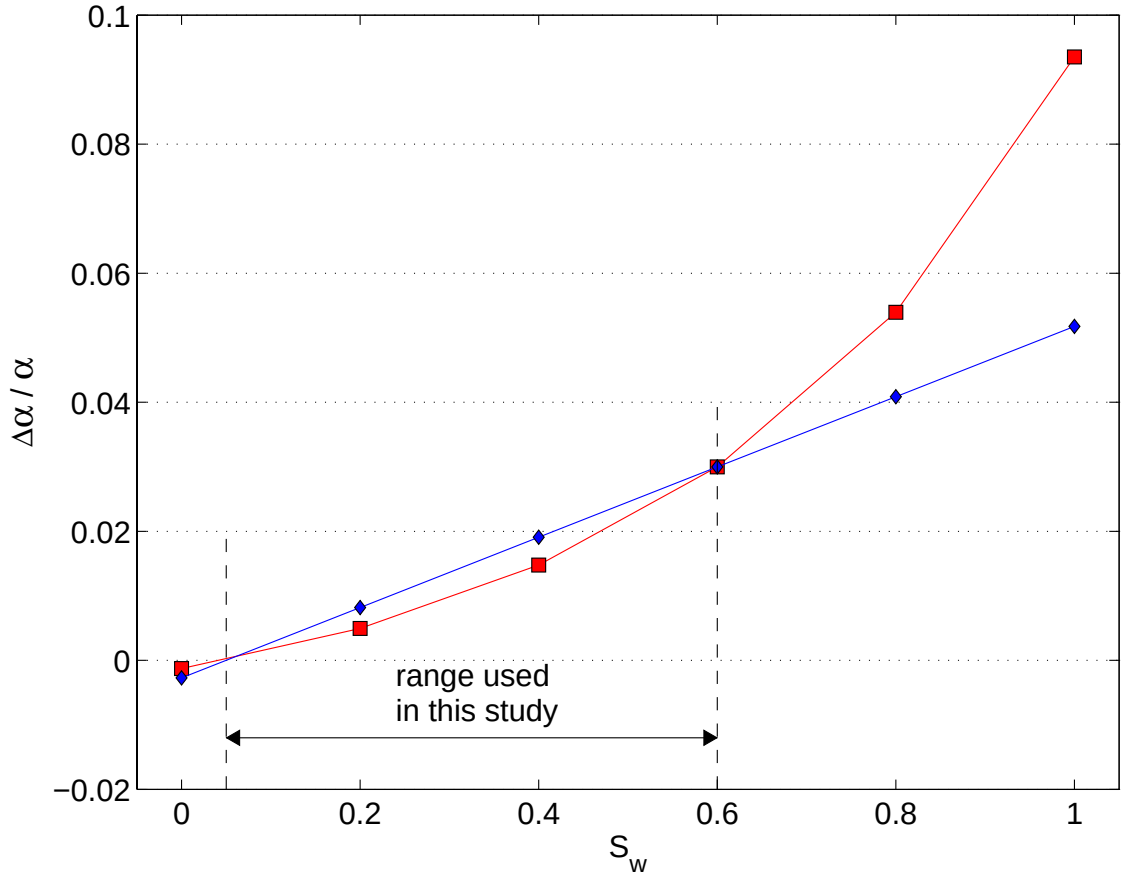

Figure 6.3: Relationship between relative change in P-wave velocity and water saturation based on a calibrated Gassmann model (line with squares). Initial water saturation is set to 5% (which is similar to Ekofisk) and we assume a maximum water saturation of 60%. The line with diamonds shows the straight-line approximation used in this study.

to 5% and we assume a maximum water saturation of 60%. Within this span, the slightly nonlinear relationship between seismic parameters and saturation changes are approximated by linear functions (however, we assume uniform saturation distribution). The relationship between change in P-wave velocity and bulk modulus (when assuming constant porosity) for a calibrated Gassmann model is shown in Figure 6.4. The relation is linear and the initial bulk modulus is assumed to be 4.55 GPa (similar to Ekofisk).

Dvorkin and Nur (1996) presented a Hertz-Mindlin model (Mindlin, 1949) to describe the stress effect on sandstones. Here we calibrate a Hertz-Mindlin model to ultrasonic measurements of a dry chalk sample (with porosity 40%) to obtain the

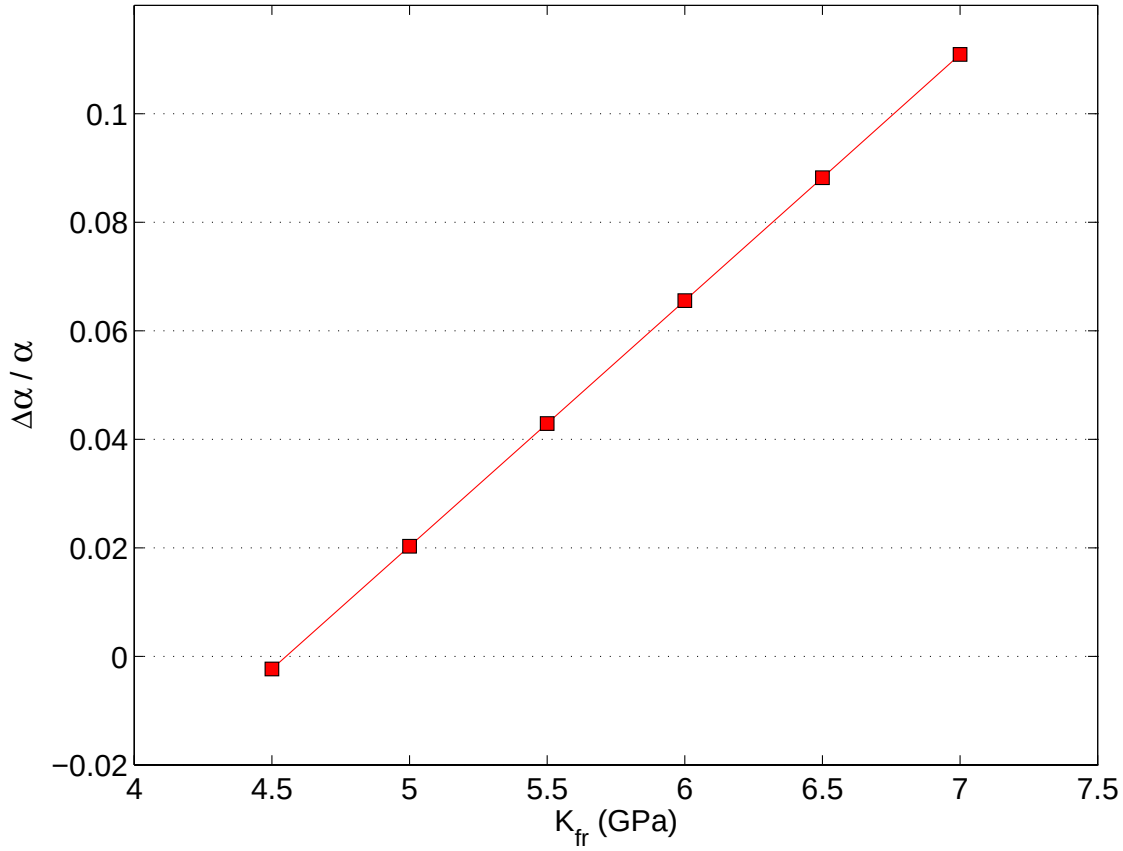

Figure 6.4: Relative change in P-wave velocity versus bulk modulus based on a calibrated Gassmann model. The relation is linear. Initial bulk modulus is assumed to be 4.55 GPa (similar to Ekofisk).

two last parameters, $N_{K\sigma}$ and $N_{G\sigma}$, in equation (6.20). Figure 6.5 shows the bulk (left) and shear (right) moduli versus effective stress using the Hertz-Mindlin model (dashed line with diamonds) together with the laboratory measurements (solid line with squares). The calibrated Hertz-Mindlin model is given by (Yin, 2002)

$$K_{fr} = a_K \times \sqrt[3]{\frac{C^2(1-\phi)^2 G_S^2}{18\pi^2(1-\nu_S)^2}\,\sigma^{d_K}}, \tag{6.21}$$

$$G_{fr} = a_G \times \frac{5-4\nu_S}{5(2-\nu_S)} \sqrt[3]{\frac{3C^2(1-\phi)^2 G_S^2}{2\pi^2(1-\nu_S)^2}\,\sigma^{d_G}}, \tag{6.22}$$

where our calibration gives $a_K = 16$, $a_G = 13$, $d_K = 0.705$, and $d_G = 0.601$. The coordination number C denotes the average number of contacts per sphere. We assume $C = 9$, which is the case for random packed identical spherical grains. The

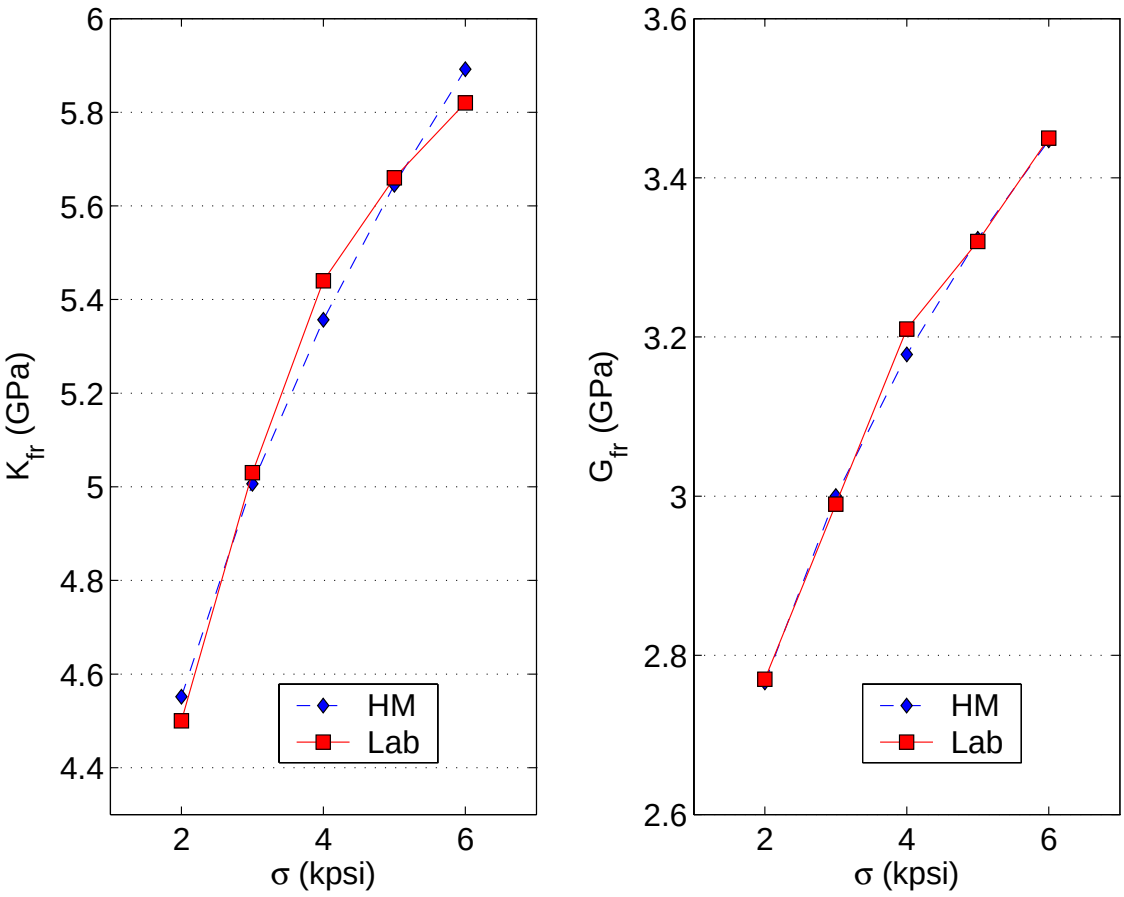

Figure 6.5: Bulk (left) and shear (right) moduli of the solid framework versus effective stress for a chalk sample with 40% porosity. The dashed lines are estimated using a calibrated Hertz-Mindlin model, while the solid lines are obtained from laboratory measurements taken from Yin (2002).

Poisson's ratio ν_s is given by

$$\nu_S = \frac{3K_S - 2G_S}{2(3K_S + G_S)}. \tag{6.23}$$

Values for K_S, G_S, and ϕ are given in Table 6.1. Differentiation of equations (6.21) and (6.22) give relationships between moduli changes (ΔK_{fr} and ΔG_{fr}) and stress changes. Figure 6.6 shows the change in bulk modulus versus effective stress. Expected values of effective stress might range from 2 kpsi to maximum around 6 kpsi (similar to Ekofisk). We approximate the relationships between moduli changes (ΔK_{fr} and ΔG_{fr}) and stress by linear functions.

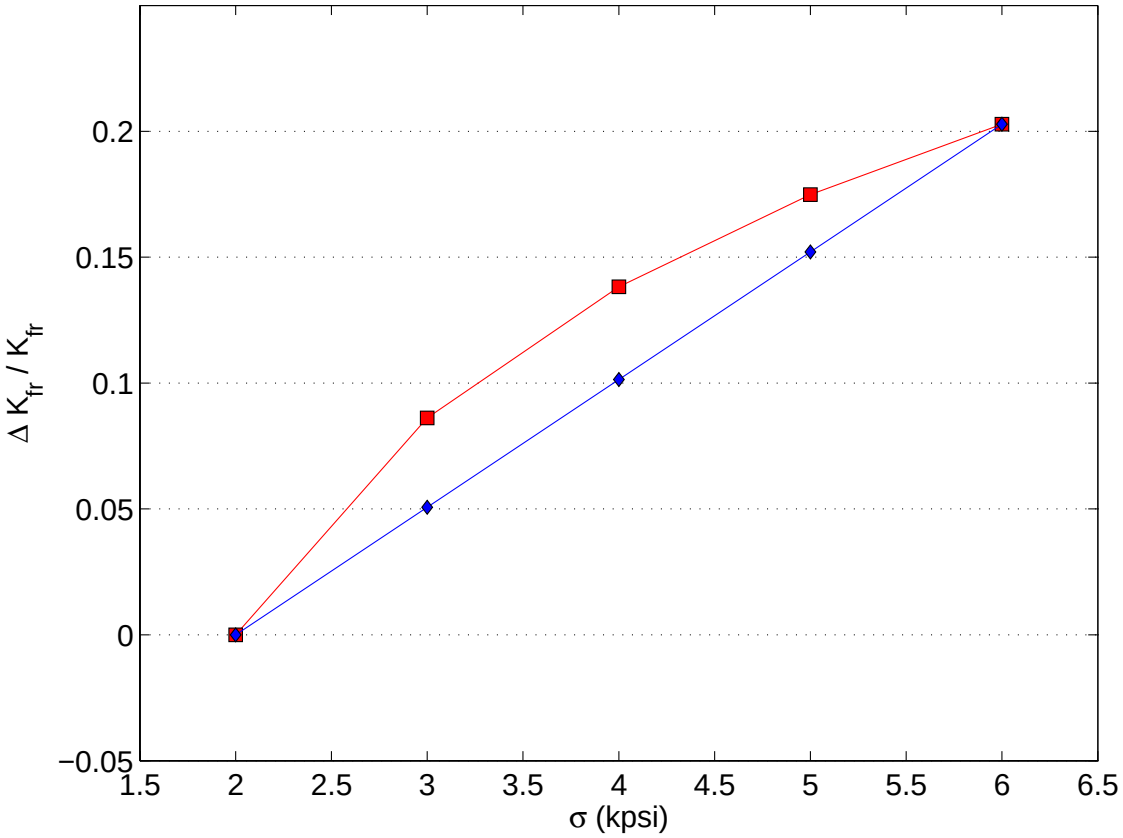

Figure 6.6: Relationship between relative change in bulk modulus and effective stress (line with squares). The curve is based on a calibrated Hertz-Mindlin model (shown on left side of Figure 6.5). Expected values of effective stress might range from 2 kpsi to maximum around 6 kpsi (similar to Ekofisk). The line with diamonds shows the straight-line approximation used in this study.

The total changes in seismic parameters for a compacting reservoir are found by adding together the changes in seismic parameters due to porosity changes ($\Delta\phi$) and due to moduli and pore-fluid changes independent of porosity changes (ϕ_c); that is,

$$\Delta\alpha_2 = [\Delta\alpha_2]_{\Delta\phi} + [\Delta\alpha_2]_{\phi_c}\,, \tag{6.24}$$

$$\Delta\beta_2 = [\Delta\beta_2]_{\Delta\phi} + [\Delta\beta_2]_{\phi_c}\,, \tag{6.25}$$

$$\Delta\rho_2 = [\Delta\rho_2]_{\Delta\phi} + [\Delta\rho_2]_{\phi_c}\,. \tag{6.26}$$

Expressions for $[\Delta\alpha_2]_{\Delta\phi}$, $[\Delta\beta_2]_{\Delta\phi}$, and $[\Delta\rho_2]_{\Delta\phi}$ are obtained by substituting equations (6.7), (6.13), (6.14), and (6.16) into equations (6.8), (6.9), and (6.10), and expressions for $[\Delta\alpha_2]_{\phi_c}$, $[\Delta\beta_2]_{\phi_c}$, and $[\Delta\rho_2]_{\phi_c}$ are obtained by substituting equa-

Table 6.1: Initial reservoir rock and fluid parameters.

P-wave velocity, α	2339 m/s
S-wave velocity, β	1211 m/s
Density, ρ	1.887 g/cm^3
Water Saturation, S_w	0.05
Stress, σ	2.0 kpsi
Porosity, ϕ	0.42
Bulk modulus of dry frame, K_{fr}	4.55 GPa
Shear modulus of dry frame, G_{fr}	2.77 GPa
Bulk modulus of solid grain, K_S	65 GPa
Shear modulus of solid grain, G_S	25 GPa
Bulk modulus of water, K_w	2.3 GPa
Bulk modulus of oil, K_o	1.0 GPa
Density of oil, ρ_o	0.75 g/cm^3
Density of water, ρ_w	1.02 g/cm^3
Density of rock matrix, ρ_S	2.7 g/cm^3

tion (6.20) into equations (6.17), (6.18), and (6.19). Adding the results together gives the following for the total relative changes in reservoir P-wave velocity, S-wave velocity, and density:

$$\frac{\Delta\alpha_2}{\alpha_2} = P_\alpha \Delta S_w + Q_\alpha \Delta\sigma + Z_\alpha \Delta S_w \Delta\sigma, \tag{6.27}$$

$$\frac{\Delta\beta_2}{\beta_2} = P_\beta \Delta S_w + Q_\beta \Delta\sigma + Z_\beta \Delta S_w \Delta\sigma, \tag{6.28}$$

$$\frac{\Delta\rho_2}{\rho_2} = P_\rho \Delta S_w + Q_\rho \Delta\sigma + Z_\rho \Delta S_w \Delta\sigma, \tag{6.29}$$

where P_α, Q_α, Z_α, P_β, Q_β, Z_β, P_ρ, Q_ρ, and Z_ρ are given in Appendix 6.A for a compacting reservoir with parameters similar to Ekofisk Field. For other fields with different reservoir properties, other expressions should be used. The unknown reservoir parameters $\Delta\sigma$ and ΔS_w can be found in several ways from time-lapse seismic data. We will focus in detail on a method which utilizes the variation in PP-reflectivity changes versus offset. However, an example using stacked PP- and PS-reflectivity changes can be found in Landrø et al. (2003) for the Gullfaks Field. The parameters $\Delta\sigma$ and ΔS_w can also be found by using traveltime shifts (Appendix 6.C).

6.3.1 Using PP-reflectivity changes

For a two-layer model (1 = cap rock, 2 = reservoir rock), let the contrast in P-wave velocity, S-wave velocity, and density be denoted by $\Delta\alpha = \alpha_2 - \alpha_1$, $\Delta\beta = \beta_2 - \beta_1$,

and $\Delta\rho = \rho_2 - \rho_1$, respectively. We choose to neglect P-wave velocity changes in layer 1 ($\Delta\alpha_1$) as well as S-wave velocity changes ($\Delta\beta_1$) and density changes ($\Delta\rho_1$), since these changes are expected to be small compared to the changes in the reservoir layer (2). Following the same procedure as outlined in Landrø (2001), we use the Smith and Gidlow (1987) approximation for the PP-reflection coefficient. The PP-reflection coefficient prior to production is (Smith and Gidlow, 1987)

$$R^{PP}(\theta) = \frac{1}{2}\left(\frac{\Delta\alpha}{\alpha} + \frac{\Delta\rho}{\rho}\right) - 2\frac{\beta^2}{\alpha^2}\left(2\frac{\Delta\beta}{\beta} + \frac{\Delta\rho}{\rho}\right)\sin^2\theta + \frac{1}{2}\frac{\Delta\alpha}{\alpha}\tan^2\theta, \qquad (6.30)$$

where $\alpha = (\alpha_1+\alpha_2)/2$, $\beta = (\beta_1+\beta_2)/2$, and $\rho = (\rho_1+\rho_2)/2$. For the postproduction case, the reflection coefficient becomes

$$R'^{PP}(\theta) = \frac{1}{2}\left(\frac{\Delta\alpha'}{\alpha'} + \frac{\Delta\rho'}{\rho'}\right) - 2\frac{\beta'^2}{\alpha'^2}\left(2\frac{\Delta\beta'}{\beta'} + \frac{\Delta\rho'}{\rho'}\right)\sin^2\theta + \frac{1}{2}\frac{\Delta\alpha'}{\alpha'}\tan^2\theta. \quad (6.31)$$

where $\Delta\alpha' = \alpha_2' - \alpha_1 = \alpha_2 + \Delta\alpha_2 - \alpha_1$, $\alpha' = (\alpha_1 + \alpha_2 + \Delta\alpha_2)/2$, etc. Assuming $\frac{\Delta\alpha}{\alpha} \ll 1$, $\frac{\Delta\beta}{\beta} \ll 1$, and $\frac{\Delta\rho}{\rho} \ll 1$, and $\frac{\Delta\alpha_2}{\alpha} \ll 1$, etc., we find

$$\begin{aligned} R'^{PP}(\theta) \;\approx\; & R^{PP}(\theta) + \frac{1}{2}\left(\frac{\Delta\alpha_2}{\alpha_2} + \frac{\Delta\rho_2}{\rho_2}\right) \\ & -2\frac{\beta^2}{\alpha^2}\left(2\frac{\Delta\beta_2}{\beta_2} + \frac{\Delta\rho_2}{\rho_2}\right)\sin^2\theta + \frac{1}{2}\frac{\Delta\alpha_2}{\alpha_2}\tan^2\theta. \end{aligned} \qquad (6.32)$$

The change in PP-reflectivity is then given as

$$\begin{aligned} \Delta R^{PP}(\theta) \;=\; & \frac{1}{2}\left(\frac{\Delta\alpha_2}{\alpha_2} + \frac{\Delta\rho_2}{\rho_2}\right) \\ & -2Y^2\left(\frac{2\Delta\beta_2}{\beta_2} + \frac{\Delta\rho_2}{\rho_2}\right)\sin^2\theta + \frac{\Delta\alpha_2}{2\alpha_2}\tan^2\theta, \end{aligned} \qquad (6.33)$$

where $Y = \beta/\alpha$. Assuming $\tan^2\theta \approx \sin^2\theta$, equation (6.33) can be split into one intercept and one gradient term (similar to Landrø, 2001); that is, $\Delta R^{PP}(\theta) \approx \Delta R_0^{PP} + \Delta G^{PP}\sin^2\theta$, where

$$\Delta R_0^{PP} \;=\; \frac{1}{2}\left(\frac{\Delta\alpha_2}{\alpha_2} + \frac{\Delta\rho_2}{\rho_2}\right), \qquad (6.34)$$

$$\Delta G^{PP} \;=\; -2Y^2\left(\frac{2\Delta\beta_2}{\beta_2} + \frac{\Delta\rho_2}{\rho_2}\right) + \frac{\Delta\alpha_2}{2\alpha_2}. \qquad (6.35)$$

Substituting equations (6.27), (6.28), and (6.29) into equations (6.34) and (6.35), the intercept and gradient terms become functions of pressure and water saturation changes; that is, $\Delta R_0 = f_1(\Delta\sigma, \Delta S_w)$ and $\Delta G = f_2(\Delta\sigma, \Delta S_w)$. By direct inversion,

we are then able to find explicit expressions for changes in stress and saturation. The solutions for the estimated saturation change can be written

$$\Delta S_w = \frac{-b + \sqrt{b^2 - 4ac}}{2a}, \tag{6.36}$$

where the constants a, b, and c are given in Appendix 6.A. The corresponding expression for change in stress (given in kpsi) can be written as

$$\Delta\sigma = \frac{2\Delta R_0 - \Delta S_w(P_\alpha + P_\rho)}{\Delta S_w(Z_\alpha + Z_\rho) + Q_\alpha + Q_\rho}. \tag{6.37}$$

The parameters P_α, P_β, P_ρ, Q_α, Q_β, Q_ρ, Z_α, Z_β, and Z_ρ, valid for the Ekofisk Field, are given in Appendix 6.A. The corresponding porosity change is given by equation (6.7):

$$\Delta\phi_2 = (A_{\phi S} + A_{\phi S\sigma}\sigma_i)\Delta S_w + (A_{\phi\sigma} + A_{\phi S\sigma}S_{wi})\Delta\sigma + A_{\phi S\sigma}\Delta S_w\Delta\sigma, \tag{6.38}$$

where $A_{\phi S}$, $A_{\phi\sigma}$, and $A_{\phi S\sigma}$ are given in appendix C.

6.4 Synthetic data example

Simple synthetic models with two layers are generated to test the validity of the methodology for time-lapse PP AVO seismic data. In all synthetic models, the rock physical properties of the layer below the reservoir zone are kept constant and only the reservoir rock is changed. The reservoir rock is assumed to be buried at 3000 m depth, and the initial properties are similar to the Ekofisk chalk field (see e.g. Gauer et al., 2002; Sylte et al., 1999; Yin, 2002), given in Table 6.1. For the overburden rocks, different scenarios are modeled: In 10 of the models, the rock physical properties of the overburden undergo changes dependent of the reservoir compaction (Appendix 6.A), while in the remaining 10 models the overburden rock physical properties are kept constant.

For the reservoir layer models, we assume that framework and pore-fluid density changes occur independently of porosity changes. The relationship between framework moduli and stress is found through calibrating a Hertz-Mindlin model to laboratory measurements (Figure 6.5). The framework moduli are related to P- and S-wave velocities through Gassmann's equation (Figure 6.4). The relationship between seismic parameters and saturated reservoir rock (independent of porosity changes) is calculated using Gassmann's equation (Figure 6.3). The porosity changes are related to stress, and saturation according to laboratory data for a 42% porosity chalk sample (Figure 6.2). The porosity is related to P- and S-wave velocities through empirical relationships (given by equations (6.11) and (6.12)). The

relation between density and porosity is found from equation (6.15).

Different scenarios of stress and water saturation changes are made. All models have the same initial (preproduction) scenario with a water saturation of 5%, effective stress equal to 2 kpsi, and porosity of 42%. For a scenario with given saturation and stress changes, the modeled porosity change is given by equation (6.7). Assuming uniaxial strain relations (e.g. Guilbot and Smith, 2002), the modeled relative change in reservoir thickness can be expressed in terms of the porosity changes; that is,

$$\frac{\Delta z_2}{z_2} \approx \frac{\Delta \phi_2}{1-\phi_2}. \tag{6.39}$$

Figure 6.7 shows PP prestack synthetic seismograms (angle gathers) for baseline (a) and monitor (b) for a model undergoing a water saturation change of 20% and 1.5 kpsi change in stress. This means (from equation (6.7)) that the porosity decrease is 2.8% and the corresponding relative compaction is 4.8% (from equation (6.39)). Amplitude changes (versus angle) between baseline and monitor are picked for maximum amplitude. Figure 6.7 shows the picked amplitude changes (c) and relative amplitude changes (d). Reflection coefficients are calculated using Zoeppritz' equations for offsets from 0 m to 3000 m (that is, for angles θ from 0° to 27°), for the different models. By plotting the change in calculated reflection coefficients as a function of $\sin^2\theta$, the change in intercept (ΔR_0) and gradient (ΔG) terms are found. In the final step, the intercept and gradient changes are substituted into the derived equations (6.36) and (6.37) to obtain changes in saturation and stress. The results are given in Table 6.2 together with the modeled values for saturation and stress changes. Here the modeled rock physical properties of the overburden rocks are kept constant. As an example, the first row in Table 6.2 indicates a reservoir model with $\Delta S_w = 0.2$ and $\Delta\sigma = 1.5$ kpsi (which means $\Delta\phi = -0.028$ from equation (6.7)). For a test with no noise, we estimate $\Delta S_w = 0.287$ and $\Delta\sigma = 1.04$, which corresponds to relative errors of 44% in ΔS_w and 31% in $\Delta\sigma$.

Figure 6.8 shows a plot of the same initial and monitor parameters with random noise added. The signal to noise ratio (SNR) is approximately 0.4 for baseline (a) and monitor (b). Amplitude changes (c) and relative amplitude changes (d) are obtained by picking interpolated maximum amplitudes. With this noise level, we estimate the saturation change to be 0.281 and the stress change to be 1.07. This gives a relative error of 41% for the saturation change estimate and 29% for the stress change estimate. (Note that random noise might sometimes lead to decreased error in the estimated saturation and stress changes.)

Tests of synthetic models including overburden changes are given in Table 6.3. The modeled overburden changes are dependent on the modeled porosity change in the reservoir (see Appendix 6.B). The reservoir models in Table 6.3 are identical to

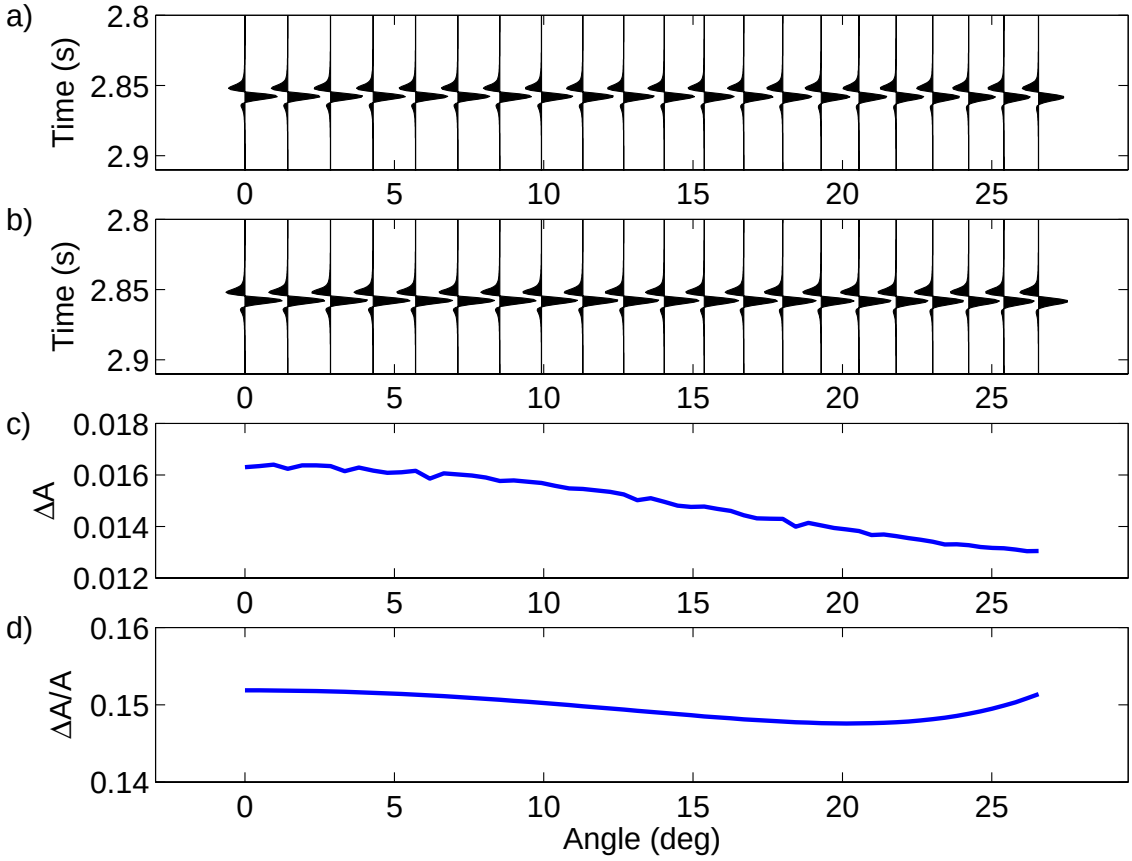

Figure 6.7: Synthetic seismograms for PP reflections (angle gathers) for baseline (a) and monitor (b). For the baseline model, the stress is 2 kpsi and water saturation is 5%. The monitor changes are 1.5 kpsi in stress and 20% in water saturation. By picking maximum amplitude for the baseline and monitor seismograms, we obtain amplitude changes (c) and relative amplitude changes (d).

the reservoir models in Table 6.2.

6.5 Discussion

In the methodology we have assumed no overburden changes during reservoir compaction. However, the method is tested on synthetic models which include overburden changes (Table 6.3). For the given tests, we conclude that overburden changes might be neglected. (Note, however, that the influence of overburden changes might be different when using time-lapse time shifts (Appendix 6.C) instead of amplitudes.)

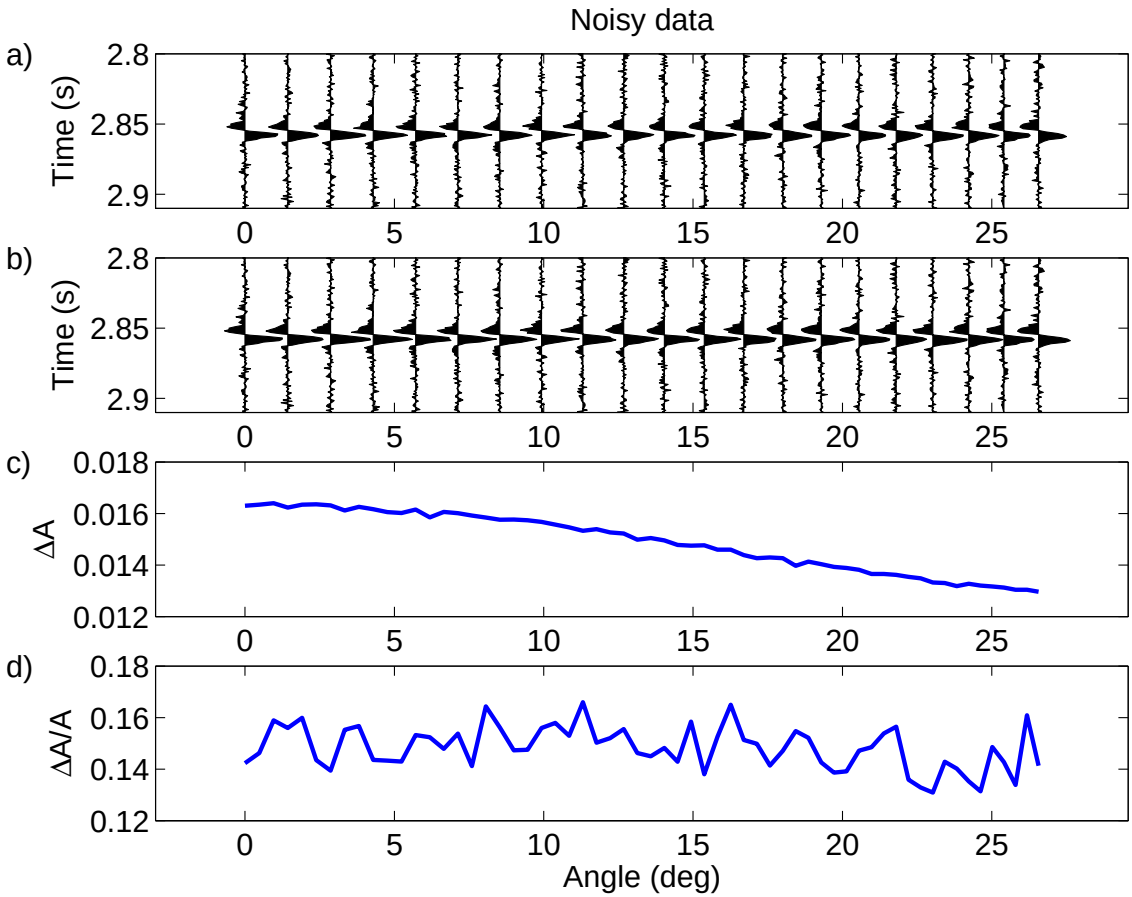

Figure 6.8: Synthetic seismograms for PP reflections (angle gathers) with noise for baseline (a) and monitor (b) for the same model parameters as used in Figure 6.7. By picking maximum amplitude for the baseline and monitor seismograms, we obtain amplitude changes (c) and relative amplitude changes (d).

In this study we predict the reservoir porosity change by assuming that porosity is a linear function of initial porosity, water saturation, and effective stress. This linear relationship is consistent with laboratory measurements from Sylte et al. (1999) for small, intact rock samples. However, nonlinear behavior is often seen in the field due to the impact of fractures and other properties of large rock masses (Sylte et al., 1999).

In addition to porosity changes, we have calibrated the Gassmann equation and Hertz-Mindlin model with well log measurements (from the Ekofisk Field) to predict the seismic effect of changing the saturation and stress. Results from Landrø

Table 6.2: Estimation of saturation and effective stress changes from time-lapse PP AVO seismic data. S_{w1} and S_{w2} are the saturation before and after production, and σ_1 and σ_2 are the effective stress before and after production.

S_{w1}/S_{w2}	Real S_w change	Est. S_w change	with noise SNR = 0.4	σ_1/σ_2 (kpsi)	Real σ change	Est. σ change	with noise SNR = 0.4
0.05/0.25	0.2	0.287	0.281	2/3.5	1.5	1.04	1.07
0.05/0.1	0.05	0.117	0.107	2/4	2	1.40	1.39
0.05/0.35	0.3	0.376	0.435	2/3	1	0.73	0.57
0.05/0.3	0.25	0.354	0.390	2/2.5	1.5	1.01	0.86
0.05/0.45	0.4	0.403	0.389	2/2	0	-0.05	-0.05
0.05/0.40	0.35	0.723	0.409	2/5	3	1.22	2.09
0.05/0.05	0	0.014	0.024	2/2.5	0.5	0.64	0.48
0.05/0.35	0.3	0.322	0.289	2/2.5	0.5	0.42	0.46
0.05/0.15	0.1	0.117	0.070	2/2.75	075	0.71	0.92
0.05/0.40	0.35	0.360	0.295	2/2.25	0.25	0.20	0.27

Table 6.3: Estimation of saturation and effective stress changes from time-lapse PP AVO seismic data. Here the forward models include time-lapse overburden changes. S_{w1} and S_{w2} are the saturation before and after production, and σ_1 and σ_2 are the effective stress before and after production.

S_{w1}/S_{w2}	Real S_w change	Est. S_w change	with noise SNR = 0.4	σ_1/σ_2 (kpsi)	Real σ change	Est. σ change	with noise SNR = 0.4
0.05/0.25	0.2	0.287	0.193	2/3.5	1.5	1.04	1.35
0.05/0.1	0.05	0.118	0.181	2/4	2	1.40	1.01
0.05/0.35	0.3	0.366	0.378	2/3	1	0.77	0.69
0.05/0.3	0.25	0.354	0.310	2/2.5	1.5	1.02	1.13
0.05/0.45	0.4	0.403	0.389	2/2	0	-0.05	-0.06
0.05/0.40	0.35	0.726	0.623	2/5	3	1.24	1.42
0.05/0.05	0	0.014	0.009	2/2.5	0.5	0.64	0.56
0.05/0.35	0.3	0.318	0.275	2/2.5	0.5	0.43	0.50
0.05/0.15	0.1	0.114	0.191	2/2.75	0.75	0.73	0.41
0.05/0.40	0.35	0.358	0.480	2/2.25	0.25	0.20	0.07

(2001), show that the Gassmann equation successfully describes the relation between change in seismic parameters and water saturation for the static Gullfaks sandstone reservoir. Dvorkin and Nur (1996) presented Hertz-Mindlin theory to

describe the relationship between stress and moduli for high porosity sandstones. The validity of the Gassmann and Hertz-Mindlin models may be different for compacting chalk reservoirs. However, as an attempt, we assume that these models can describe processes occurring independently of the porosity changes in a compacting reservoir.

The proposed method does not account for tuning effects between the seismic events from the top and base of the reservoir layer. Tuning effects might influence the amplitude change and lead to incorrect estimations of the saturation and stress changes. However, for the presented numerical example, we have used data relevant the Ekofisk Field, which is a relatively thick reservoir. Vertical resolution of two horizontal reflectors with distance z is gained when the seismic wavelength is larger than $z/4$ (Sheriff and Geldart, 1995).

In this paper we have assumed that changes in saturation and stress are the only production-related changes that lead to porosity changes. However, porosity changes might also be induced by for instance temperature changes and bacterial changes. It is possible to extend the proposed method to include more than saturation and stress changes, by using PS reflectivity (stacked or AVO) data, in addition to the PP reflectivity AVO data used here. (Another way might be to utilize both reflectivity and traveltime data (Landrø and Stammeijer, 2004).) However, porosity changes of compacting reservoirs are mainly due to saturation and stress changes (Sylte et al., 1999). Other production-related changes are therefore neglected in this paper.

The uncertainty in estimated changes in saturation and stress is strongly dependent on the accuracy of the measured seismic amplitudes. Different synthetic scenarios with SNR level 0.4 are tested. To reduce the uncertainty, we may use data with larger offset, improve the quality and repeatability of time-lapse seismic data, and introduce additional constraints (such as PS-data, well data, rock physics models).

Our analysis is based on the assumption that decrease in porosity in a compacting reservoir occur due to hydrocarbon production (leading to an increase in effective stress) and water injection. This is an irreversible process, since the increased effective stress leads to fractures and the increased water saturation leads to a weakening of the chalk. Therefore, for the reverse case, with decrease in effective stress or decrease in water saturation, we expect negligible porosity changes.

6.6 Conclusions

The proposed method uses time-lapse AVO seismic data to estimate pressure and saturation changes in compacting reservoirs. According to laboratory measure-

ments, the porosity loss due to reservoir compaction is related to the pressure and saturation changes. By assuming that the porosity changes of the reservoir rock can be treated independently of the changes in framework and pore-fluid density, approximate formulas for computing pressure- and saturation-related changes from time-lapse AVO data have been derived. Rock physics models calibrated to the Gassmann equation and Hertz-Mindlin model are necessary input to relate the changes in seismic parameters to changes in pressure and water saturation.

The method is tested on synthetic time-lapse seismic data for 10 different production scenarios, representing various degrees of pressure and saturation changes and corresponding compaction. The uncertainties in the estimated changes in pressure and saturation changes increase as the modeled pressure changes increase. However, for pressure changes below 2 kpsi, the method captures the modeled changes well, even in cases with large saturation changes (up to 40%).

6.7 Acknowledgments

Thomas Røste acknowledges TOTAL for financial support. We thank Alexey Stovas for providing programs for the synthetic models. Rune Holt is acknowledged for valuable discussions. Martin Landrø acknowledges the support from the ROSE-project at NTNU, sponsored by the Norwegian Research Council.

6.A The inversion procedure

The total changes in seismic parameters for a compacting reservoir are found by adding together the changes in seismic parameters due to porosity changes ($\Delta\phi$) and due to moduli and pore-fluid density changes independent of porosity changes (ϕ_c); that is,

$$\Delta\alpha_2 = [\Delta\alpha_2]_{\Delta\phi} + [\Delta\alpha_2]_{\phi_c}\,, \tag{6.A-1}$$
$$\Delta\beta_2 = [\Delta\beta_2]_{\Delta\phi} + [\Delta\beta_2]_{\phi_c}\,, \tag{6.A-2}$$
$$\Delta\rho_2 = [\Delta\rho_2]_{\Delta\phi} + [\Delta\rho_2]_{\phi_c}\,. \tag{6.A-3}$$

Substituting for $[\Delta\alpha_2]_{\Delta\phi}$, $[\Delta\beta_2]_{\Delta\phi}$, and $[\Delta\rho_2]_{\Delta\phi}$ (given by equations (6.8), (6.9), and (6.10)) and $[\Delta\alpha_2]_{\phi_c}$, $[\Delta\beta_2]_{\phi_c}$, and $[\Delta\rho_2]_{\phi_c}$ (given by equations (6.17), (6.18), and (6.19)) gives the following for the total relative changes in reservoir P-wave velocity, S-wave velocity, and density:

$$\tfrac{\Delta\alpha_2}{\alpha_2} = P_\alpha \Delta S_w + Q_\alpha \Delta\sigma + Z_\alpha \Delta S_w \Delta\sigma, \tag{6.A-4}$$
$$\tfrac{\Delta\beta_2}{\beta_2} = P_\beta \Delta S_w + Q_\beta \Delta\sigma + Z_\beta \Delta S_w \Delta\sigma, \tag{6.A-5}$$
$$\tfrac{\Delta\rho_2}{\rho_2} = P_\rho \Delta S_w + Q_\rho \Delta\sigma + Z_\rho \Delta S_w \Delta\sigma, \tag{6.A-6}$$

where

$$\begin{aligned}
P_\alpha &= \frac{B_{\alpha\phi}}{\alpha_2}(A_{\phi S} + A_{\phi S\sigma}\sigma_i) + L_{\alpha S},\\
Q_\alpha &= \frac{B_{\alpha\phi}}{\alpha_2}(A_{\phi\sigma} + A_{\phi S\sigma}S_{wi}) + M_{\alpha K}N_{K\sigma} + M_{\alpha G}N_{G\sigma},\\
Z_\alpha &= \frac{B_{\alpha\phi}}{\alpha_2}A_{\phi S\sigma},\\
P_\beta &= \frac{B_{\beta\phi}}{\beta_2}(A_{\phi S} + A_{\phi S\sigma}\sigma_i) + L_{\beta S},\\
Q_\beta &= \frac{B_{\beta\phi}}{\beta_2}(A_{\phi\sigma} + A_{\phi S\sigma}S_{wi}) + M_{\beta G}N_{G\sigma},\\
Z_\beta &= \frac{B_{\beta\phi}}{\beta_2}A_{\phi S\sigma},\\
P_\rho &= \frac{B_{\rho\phi}}{\rho_2}(A_{\phi S} + A_{\phi S\sigma}\sigma_i) + L_{\rho S},\\
Q_\rho &= \frac{B_{\rho\phi}}{\rho_2}(A_{\phi\sigma} + A_{\phi S\sigma}S_{wi}),\\
Z_\rho &= \frac{B_{\rho\phi}}{\rho_2}A_{\phi S\sigma},
\end{aligned} \tag{6.A-7}$$

where S_{wi} and σ_i denote the initial water saturation and stress, respectively. For a compacting reservoir with rock physical properties similar to Ekofisk Field, we find

$$\begin{aligned}
&A_{\phi S} = 0.128,\ A_{\phi\sigma} = -0.00283 \text{ kpsi}^{-1},\ A_{\phi S\sigma} = -0.064 \text{ kpsi}^{-1},\\
&B_{\alpha\phi} = -5500 \text{ m/s},\ B_{\beta\phi} = -3000 \text{ m/s},\ B_{\rho\phi} = -3.362 \text{ g/cm}^3,\\
&L_{\alpha S} = 0.054,\ L_{\beta S} = -0.030,\ L_{\rho S} = 0.060,\\
&M_{\alpha K} = 0.045 \text{ GPa}^{-1},\ M_{\alpha G} = 0.065 \text{ GPa}^{-1},\ M_{\beta G} = 0.181 \text{ GPa}^{-1},\\
&N_{K\sigma} = 0.231 \text{ GPa/kpsi},\ N_{G\sigma} = 0.115 \text{ GPa/kpsi}. \qquad \text{(6.A-8)}
\end{aligned}$$

Based on the Smith and Gidlow (1987) approximation for the PP-reflection coefficient, the change in PP-reflectivity can be expressed in terms of relative changes in P- and S-wave velocities and density, as given by equation (6.33). Assuming $\tan^2\theta \approx \sin^2\theta$, the change in PP-reflectivity can be expressed in one intercept and one gradient term; that is, $\Delta R^{PP}(\theta) \approx \Delta R_0^{PP} + \Delta G^{PP}\sin^2\theta$, where

$$\Delta R_0^{PP} = \frac{1}{2}\left(\frac{\Delta\alpha_2}{\alpha_2} + \frac{\Delta\rho_2}{\rho_2}\right), \qquad \text{(6.A-9)}$$

$$\Delta G^{PP} = -2Y^2\left(\frac{2\Delta\beta_2}{\beta_2} + \frac{\Delta\rho_2}{\rho_2}\right) + \frac{\Delta\alpha_2}{2\alpha_2}. \qquad \text{(6.A-10)}$$

Substituting equations (6.A-4), (6.A-5), and (6.A-6) into equations (6.A-9) and (6.A-10), the intercept and gradient terms become functions of pressure and water saturation changes; that is, $\Delta R_0 = f_1(\Delta\sigma, \Delta S_w)$ and $\Delta G = f_2(\Delta\sigma, \Delta S_w)$. By direct inversion, the estimated saturation change can be written

$$\Delta S_w = \frac{-b + \sqrt{b^2 - 4ac}}{2a}. \qquad \text{(6.A-11)}$$

where

$$\begin{aligned}
a &= P_\alpha(Z_\rho + 4Y^2Z_\rho + 8Y^2Z_\beta) - 8Y^2P_\beta(Z_\alpha + Z_\rho) - P_\rho(Z_\alpha + 4Y^2Z_\alpha - 8Y^2Z_\beta),\\
b &= 2\Delta R_0(Z_\alpha - 4Y^2Z_\rho - 8Y^2Z_\beta) - 2\Delta G(Z_\alpha + Z_\rho) + P_\alpha(Q_\rho + 4Y^2Q_\rho + 8Y^2Q_\beta)\\
&\quad - 8Y^2P_\beta(Q_\alpha + Q_\rho) - P_\rho(Q_\alpha + 4Y^2Q_\alpha - 8Y^2Q_\beta),\\
c &= 2\Delta R_0(Q_\alpha - 4Y^2Q_\rho - 8Y^2Q_\beta) - 2\Delta G(Q_\alpha + Q_\rho). \qquad \text{(6.A-12)}
\end{aligned}$$

The corresponding expression for change in stress (given in kpsi) can be written as

$$\Delta\sigma = \frac{2\Delta R_0 - \Delta S_w(P_\alpha + P_\rho)}{\Delta S_w(Z_\alpha + Z_\rho) + Q_\alpha + Q_\rho}. \qquad \text{(6.A-13)}$$

The parameters P_α, P_β, P_ρ, Q_α, Q_β, Q_ρ, Z_α, Z_β, and Z_ρ are given by equation (6.A-7).

6.B Synthetic models undergoing overburden changes

In the methodology we have assumed that changes in the overburden layer are negligible compared with the changes in the reservoir layer. To test the validity of this approximation, we have made synthetic models with overburden time-lapse changes. The changes in seismic parameters of the overburden are dependent on the reservoir compaction. Using the uniaxial strain relationship (e.g. Guilbot and Smith, 2002), the change in reservoir thickness can be given as

$$\Delta z_2 \approx z_2 \frac{\Delta \phi_2}{1-\phi_2}, \tag{6.B-1}$$

where ϕ_2 and z_2 denote initial porosity and thickness of the reservoir layer. The change in porosity ($\Delta\phi_2$) is calculated from a quantitative model of Ekofisk chalk behavior, given by equation (6.7). A normal assumption for Ekofisk is that the subsidence of the seabed is 4/5 of the subsidence of the top reservoir horizon. Keeping the base reservoir horizon constant during the reservoir compaction will then give the following relation between the thickness change of the overburden layer (1) and the thickness change of the reservoir layer (2):

$$\Delta z_1 \approx -\frac{1}{5}\Delta z_2. \tag{6.B-2}$$

As a first order approximation, we assume that the relation between relative velocity and thickness changes is proportional to each other (Røste et al., 2005; Hatchell and Bourne, 2005):

$$\frac{\Delta v_1}{v_1} = -R_1 \frac{\Delta z_1}{z_1}, \tag{6.B-3}$$

where R_1 is a positive constant and v_1 represents both the P-wave and S-wave velocities for the overburden layer. Substituting equation (6.B-2) into equation (6.B-3) and using $R_1 = 5$ for the overburden, gives the following changes in P- and S-wave velocities:

$$\Delta\alpha_1 = \alpha_1 \frac{R_1}{5}\frac{\Delta z_2}{z_1} = \alpha_1 \frac{\Delta z_2}{z_1}, \tag{6.B-4}$$

$$\Delta\beta_1 = \beta_1 \frac{R_1}{5}\frac{\Delta z_2}{z_1} = \beta_1 \frac{\Delta z_2}{z_1}, \tag{6.B-5}$$

Assuming mass conservation, the change in density can be expressed as

$$\Delta\rho_1 = -\rho_1 \frac{\Delta z_1}{z_1} = \frac{\rho_1}{5}\frac{\Delta z_2}{z_1}, \tag{6.B-6}$$

by substitution of equation (6.B-2).

6.C Using PP and PS time shifts

For a reservoir layer with thickness z_2, the relative PP-traveltime change for zero offset can be expressed in terms of the relative thickness and velocity change (Landrø and Stammeijer, 2004; Røste et al., 2005; Hatchell and Bourne, 2005); that is,

$$\frac{\Delta T_{N,2}^{PP}}{T_{N,2}^{PP}} = \frac{\Delta z_2}{z_2} - \frac{\Delta \alpha_2}{\alpha_2}, \tag{6.C-1}$$

where $T_{N,2}^{PP}$ represents seismic two-way vertical traveltime for PP-waves within the reservoir layer and α_2 is the reservoir velocity. The basic assumption in equation (6.C-1) is that all relative changes are small; that is, $\frac{\Delta z_2}{z_2} \ll 1$ and $\frac{\Delta \alpha_2}{\alpha_2} \ll 1$. For far offsets, we assume the following approximate expression for relative PP-traveltime shift (Landrø and Stammeijer, 2004):

$$\frac{\Delta T_{F,2}^{PP}}{T_{F,2}^{PP}} = \left(\frac{T_{N,2}^{PP}}{T_{F,2}^{PP}}\right)^2 \frac{\Delta z_2}{z_2} - \frac{\Delta \alpha_2}{\alpha_2}, \tag{6.C-2}$$

where $T_{F,2}^{PP}$ represents far offset two-way traveltime for PP-waves within the reservoir layer. Assuming small relative change in the S-wave velocity (that is, $\frac{\Delta \beta_2}{\beta_2} \ll 1$) the relative SS-traveltime shift for zero offset can be given as

$$\frac{\Delta T_{N,2}^{SS}}{T_{N,2}^{SS}} = \frac{\Delta z_2}{z_2} - \frac{\Delta \beta_2}{\beta_2}, \tag{6.C-3}$$

where $T_{N,2}^{SS}$ denotes zero offset two-way traveltime for SS-waves within the reservoir layer. Note that SS-traveltimes do not exist for zero offset, but can approximately be estimated from near- or full-offset SS-stacks. For PS-waves, we use Grechka and Tsvankin's (2002) to find the following approximate expression for the relative traveltime shift for zero offset:

$$\frac{\Delta T_{N,2}^{PS}}{T_{N,2}^{PS}} = \frac{\Delta T_{N,2}^{PP} + \Delta T_{N,2}^{SS}}{T_{N,2}^{PP} + T_{N,2}^{SS}}. \tag{6.C-4}$$

Substituting equations (6.C-1) and (6.C-3) into equation (6.C-4), the PS-traveltime shift for the reservoir layer is given as

$$\frac{\Delta T_{N,2}^{PS}}{T_{N,2}^{PS}} = \frac{T_{N,2}^{PP}}{T_{N,2}^{PS}}\left(\frac{\Delta z_2}{z_2} - \frac{\Delta \alpha_2}{\alpha_2}\right) + \frac{T_{N,2}^{SS}}{T_{N,2}^{PS}}\left(\frac{\Delta z_2}{z_2} - \frac{\Delta \beta_2}{\beta_2}\right). \tag{6.C-5}$$

Based on laboratory measurements of chalk and Ekofisk parameters calibrated to Gassmann and Hertz-Mindlin models (e.g. figures 6.2, 6.3, 6.4, and 6.6), the relative changes in P- and S-wave velocities ($\frac{\Delta \alpha_2}{\alpha_2}$ and $\frac{\Delta \beta_2}{\beta_2}$) can be expressed in terms of

stress and saturation changes, as given by equations (6.27) and (6.28). Inserting equations (6.27) and (6.28) into equations (6.C-1), (6.C-2), and (6.C-5), gives the relative near and far PP-traveltime shifts and near PS-traveltime shift expressed in terms of stress and saturation changes and relative thickness changes; that is,

$$\frac{\Delta T_{N,2}^{PP}}{T_{N,2}^{PP}} = f_1(\Delta\sigma, \Delta S, \frac{\Delta z_2}{z_2}), \tag{6.C-6}$$

$$\frac{\Delta T_{F,2}^{PP}}{T_{F,2}^{PP}} = f_2(\Delta\sigma, \Delta S, \frac{\Delta z_2}{z_2}), \tag{6.C-7}$$

$$\frac{\Delta T_{N,2}^{PS}}{T_{N,2}^{PS}} = f_3(\Delta\sigma, \Delta S, \frac{\Delta z_2}{z_2}). \tag{6.C-8}$$

By direct inversion, we are then able to find explicit expressions for changes in stress and saturation and relative reservoir compaction.

Chapter 7

Closing remarks

Monitoring reservoir and overburden changes during hydrocarbon production leads to production enhancement by optimizing well placement and by improving production and injection operations. Time-lapse seismic data is an important tool for monitoring. Several researches have developed methods based on time-lapse seismic data to monitor changes in layer thickness and velocity (Landrø and Stammeijer, 2004; Røste et al., 2005; Hatchell and Bourne, 2005b) and changes in reservoir pressure and saturation (Tura and Lumley, 1998, 1999; Landrø, 2001; Landrø et al., 2003). The focus of this thesis has been to develop new methods based on prestack time-lapse seismic data to monitor compacting reservoirs and overburden layers. Before this work started, I tried to develop a method based on *stacked* time-lapse data to discriminate between layer thickness and velocity changes. By testing this method on several synthetic models undergoing reservoir compaction, I concluded that changes in stacking velocities poorly describe cases with large lateral variations in the layer changes. Since lateral variations most likely occur in fields with compacting reservoirs, a method based on stacked PP-seismic data only was rejected and a theory based on prestack seismic data was initiated (chapter 3).

This new theory introduces a dilation factor (α), which discriminates the relative thickness changes and relative velocity changes. The introduction of the dilation factor seems both practical and useful, and during the writing of this thesis I also discovered that other researches (Hatchell and Bourne, 2005b) used (independently of my work) a similar dilation factor in their work. The proposed method given in chapter 3 was initially tested on a synthetic model with large lateral variations in velocity and thickness changes, and then later tested on real prestack 2D streamer data (chapter 3) and real prestack 2D ocean bottom cable (OBC) data (chapter 4). An advantage of this method is that no information or model is required for the mechanism creating the velocity and thickness changes. Chapter 4 proposes an extended method which handles vertical (in addition to lateral) variations in velocity and thickness changes. This can be viewed as a simplified version of time-

lapse tomography (Vesnaver et al., 2003). However, for cases with significant and heterogeneous variations in both vertical and horizontal velocity changes, a full 4D tomographic method is required.

In chapter 5, I try to extend the proposed method given in chapter 3 to handle anisotropic cases. The given approximate anisotropic expression for relative prestack seismic time shifts shows that static anisotropy can be neglected (also discussed in chapter 3). However, time-lapse changes in anisotropy influence the time shifts. To avoid large, complex terms in the anisotropic expression, several approximations were necessary in the derivations. Due to these approximations, the methodology given in chapter 5 does not handle cases with relative anisotropic changes larger than 3%. It is possible to compute expressions for relative prestack time shifts that include anisotropy changes more accurately. However, this leads to more complex expressions, and, in addition, more input parameters become necessary.

In chapter 4, time-lapse distortion patterns with characteristic time shift versus offset signatures are observed. The distortion zones are correlated to fault movements. As far as I know, distortions in time-lapse seismic are not so common. Monitoring fault movements is important for several reasons. Most important, hazards are associated with wells crossing reactivated faults (Alsos et al., 2002). In addition, reactivation of faults in the reservoir zone might lead to leakage of hydrocarbons and affect the reservoir drainage patterns (see for example Gaarenstroom et al., 1993; Finkbeiner et al., 2001). For future work, an automatic procedure for detecting time-lapse distortions and correlate them to growing faults will be helpful.

There are still unexplored methods for time-lapse seismic analysis. In all time-lapse seismic studies, low signal to noise ratio and high repeatability are crucial. In the future, improved acquisition equipment will increase the quality of seismic data. In addition, installation of ocean bottom cables (OBC) is expected to be more frequently used. Permanent cable installations lead to improved seismic quality and repeatability, and make it possible to acquire PS-seismic data. This means that the use of time-lapse seismic data will be even more valuable in future monitoring.

References

Allan, U.S., 1989, Model for hydrocarbon migration and entrapment within faulted structures: American Association of Petroleum Geologists Bulletin, **73**, 803-811.

Allen, J.L., and J.M. Bruso, 1989, A case history of velocity problems in the shadow of a large growth fault in the Frio formation, Texas Gulf Coast: Geophysics, **54**, 426-439.

Alsos, T., A. Eide, D. Astratti, S. Pickering, M. Benabentos, N. Dutta, S. Mallick, G. Schultz, L. den Boer, M. Livingston, M. Nickel, L. Sonneland, J. Schlaf, P. Schoepfer, M. Sigismondi, J.C. Soldo, and L.K Stronen, 2002, Seismic Applications Throughout the Life of the Reservoir: Oilfield Review, **14**, 48-65.

Angerer, E., S. Crampin, and X.-Y. Li, 2000, Changes in shear wave anisotropy in time-lapse data: A case study: 62nd Meeting, EAGE, Expanded Abstracts, X-38.

Angerer, E., S. Crampin, X.-Y. Li, and T.L. Davis, 2002, Processing, modelling and predicting time-lapse effects of overpressured fluid-injection in a fractured reservoir: Geophysical Journal International, **149**, 267-280.

Avseth, P., T. Mukerji, and G. Mavko, 2005, Quantitative seismic interpretation: Cambridge.

Barkved, O.I., 2004, Continuous seismic monitoring: 74th Annual International Meeting, SEG, Expanded Abstracts, 2537-2540.

Barkved, O., P. Heavey, R. Kjelstadli, T. Kleppan, and T.G. Kristiansen, 2003, Valhall Field - Still on plateau after 20 years of production: SPE 83957.

Barkved, O.I., and T. Kristiansen, 2005, Seismic time-lapse effects and stress changes: Examples from a compacting reservoir: The Leading Edge, **24**, 1244-1248.

Batzle, M., and Z. Wang, 1992, Seismic properties of pore fluids: Geophysics, **57**, 1396-1408.

Bickel, S.H., 1990, Velocity-depth ambiguity of reflection traveltimes: Geophysics, **55**, 266-276.

Boggs, S., 2001, Principles of sedimentology and stratigraphy, 3rd edition: Prentice Hall.

Brevik, I., 1999, Rock model based inversion of saturation and pressure changes from time lapse seismic data: 69th Annual International Meeting, SEG, Expanded Abstracts, 1044-1047.

Bube, K.P., J.A. Kane, T. Nemeth, D. Medwedeff, and O. Mikhailov, 2004, The influence of stacking velocity uncertainties on structural uncertainties: 74th Annual International Meeting, SEG, Expanded Abstracts, 2192-2195.

Carcione, J., H.B. Helle, N.H. Pham, and T. Toverud, 2003, Pore pressure estimation in reservoir rocks from seismic reflection data: Geophysics, **68**, 1569-1579.

Carcione, J.M., M. Landrø, A.F. Gangi, and F. Cavallini, 2006, Determining the dilation factor in 4D monitoring of compacting reservoirs by rock-physics models: Geophysical Prospecting, (submitted Jan 30, 2006)

Castagna, J.P., M.L. Batzle, and R.L. Eastwood, 1985, Relationships between compressional-wave and shear-wave velocities in clastic silicate rocks: Geophysics, **50**, 571-581.

Cerveny, K., R. Davies, G. Dudley, P. Kaufman, R. J. Knipe, and B. Krantz, 2004, Reducing uncertainty with fault-seal analysis: Oilfield Review, **16**, 38-51.

Chen, Z., and W. Bai, 2006, Fault creep growth model and its relationship with occurrence of earthquakes: Geophysical Journal International, **165**, 272-278.

Chin, L.Y., and N.B. Nagel, 2004, Modeling of subsidence and reservoir compaction under waterflood operations: International Journal of Geomechanics, **4**, 28-34.

Chin, L.Y., L.K. Thomas, J.E. Sylte, and R.G. Pierson, 2002, Iterative coupled analysis of geomechanics and fluid flow for rock compaction in reservoir simulation: Oil & Gas Science and Technology, **57**, 485-497.

Dix, C.H., 1955, Seismic velocities from surface measurements: Geophysics, **20**, 68-86.

Dutta, N., T. Mukerji, M. Prasad, and J. Dvorkin, 2002, Seismic detection and estimation of overpressures Part II: Field applications, Recorder, **27**, 58-73.

Dvorkin, J., and A. Nur, 1996, Elasticity of high-porosity sandstones: Theory for two North Sea data sets: Geophysics, **61**, 1363-1370.

Ewing, T.E., 1985, Subsidence and surface faulting in the Houston-Galveston area, Texas related to deep fluid withdrawal. *In*: Dorfman, M.H., R.A. Morton (Eds.), Geopressured Geothermal Energy: Proceedings of the 6th U.S. Gulf Coast Geopressured-Geothermal Energy Conference, Pergamon Press, 289-298.

Fagin, S., 1996, The fault shadow problem: Its nature and elimination: The Leading Edge, **15**, 1005-1013.

Faust, L.Y., 1953, A velocity function including lithologic variation: Geophysics, **18**, 271-288.

Finkbeiner, T., M. Zoback, P. Flemings, and B. Stump, 2001, Stress, pore pressure, and dynamically constrained hydrocarbon columns in the South Eugene Island 330 field, northern Gulf of Mexico: American Association of Petroleum Geologists Bulletin, **85**, 1007-1031.

Fjær, E., R.M. Holt, P. Horsrud, A.M. Raaen, and R. Risnes, 1992, Petroleum related rock mechanics: Elsevier.

Gaarenstroom, L., R.A.J. Tromp, M.C.D. Jong, and A.M. Brandenburg, 1993, Overpressures in the Central North Sea: implications for trap integrity and drilling safety. *In*: Parker, J.R. (Ed.), Petroleum geology of northwest Europe: Proceedings of the 4th Conference. Geological Society London, 1305-1313.

Gabriels, P.W., N.A. Horvei, J.K. Koster, A. Onstein, and R. Staples, 1999, Time-lapse seismic monitoring of the Draugen field: 69th Annual International Meeting, SEG, Expanded Abstracts, 2035-2037.

Gassmann, F., 1951, Elastic waves through a packing of spheres: Geophysics, **16**, 673-685.

Gauer, P.R., J.E. Sylte, N.B. Nagel, 2002, Ekofisk field well log decompaction: SPE/ISRM 78177.

Geertsma J., 1973, Land subsidence above compacting oil and gas reservoirs: Journal of Petroleum Technology, **25**, p734-744.

Grechka, V., and I. Tsvankin, 2002, PP + PS = SS: Geophysics **67**, 1961-1971.

Guerrero, C., J. Wookey, M. Van der Baan, and J-M. Kendall, 2002, VTI anisotropy parameter in the tau-p domain: An example from the North Sea: 72nd Annual International Meeting, SEG, Expanded Abstracts, 137-140.

Guilbot, J., and B. Smith, 2002, 4-D constrained depth conversion for reservoir compaction estimation: Application to Ekofisk Field: The Leading Edge, **21**, 302-308.

Hall, S.A., C. MacBeth, O.I. Barkved, and P. Wild, 2005, Cross-matching with interpreted warping of 3D streamer and 3D ocean-bottom-cable data at Valhall for time-lapse assessment: Geophysical Prospecting, **53**, 283-297.

Han, D.-H., 1986, Effects of porosity and clay content on acoustic properties of sandstones and unconsolidated sediments: Ph.D. dissertation, Stanford University.

Han, D., A. Nur, and D. Morgan, 1986, Effects of porosity and clay content on wave velocities in sandstones: Geophysics, **51**, 2093-2107.

Harlan, W.S., 1994, Tomographic correction of transmission distortions in reflected seismic amplitudes: 64th Annual International Meeting, SEG, Expanded Abstracts, 968-971.

Hashin, Z., and S. Shtrikman, 1963, A variational approach to the elastic behaviour of multiphase materials: Journal of the Mechanics and Physics of Solids, **11**, 127-140.

Hatchell, P.J., 2000, Fault whispers: Transmission distortions on prestack seismic reflection data: Geophysics, **65**, 377-389.

Hatchell, P., and S. Bourne, 2005a, Rocks under strain: Strain-induced time-lapse time shifts are observed for depleting reservoirs: The Leading Edge, **24**, 1222-1225.

———, 2005b, Measuring reservoir compaction using time-lapse timeshifts: 75th Annual International Meeting, SEG, Expanded Abstracts, 2500-2503.

Hatchell, P.J., R.S. Kawar, and A.A. Savitski, 2005, Integrating 4D seismic, geomechanics and reservoir simulation in the Valhall oil field: 67th Meeting, EAGE, Expanded Abstracts, C012.

Hill, R., 1963, Elastic properties of reinforced solids: Some theoretical principles: Journal of the Mechanics and Physics of Solids, **11**, 357-372.

Jack, I.G., 1997, Time-lapse seismic in reservoir management: SEG Distinguished Instructor Series, **1**, SEG.

Jenkins, S.D., M.W. Waite, and M.F. Bee, 1997, Time-lapse monitoring of the Duri steamflood: A pilot and case study: The Leading Edge, **16**, 1267-1273.

Jones, R.M., P. Boult, R.R. Hillis, S.D. Mildren, and J. Kaldi, 2000, Integrated hydrocarbon seal evaluation in the Penola Trough, Otway Basin: Australian Petroleum Production and Exploration Association Journal, **40**, 194-211.

Kjartansson, E., 1979, Constant Q-wave propagation and attenuation: Journal of Geophysical Research, **84**, 4737-4748.

Klimentos, T., 1991, The effects of porosity-permeability-clay content on the velocity of compressional waves: Geophysics, **56**, 1930-1939.

Kommedal, J.H., O.I. Barkved, and D.J. Howe, 2004, Initial experience operating a permanent 4C seabed array for reservoir monitoring at Valhall: 74th Annual International Meeting, SEG, Expanded Abstracts, 2239-2242.

Kristiansen, T.G., 1998, Geomechanical characterization of the overburden above the compacting chalk reservoir at Valhall: SPE/ISRM 47348.

———, 2004, Drilling wellbore stability in the compacting and subsiding Valhall Field: SPE/IADC 87221.

Kristiansen, T.G., O. Barkved, and P.D. Pattillo, 2000, Use of passive seismic monitoring in well and casing design in the compacting and subsiding Valhall Field, North Sea: SPE 65134.

Landrø, M., 1999a, Discrimination between pressure and fluid saturation changes from time-lapse seismic data: 69th Annual International Meeting, SEG, Expanded Abstracts, 1651-1654.

———, 1999b, Repeatability issues of 3-D VSP data: Geophysics, **64**, 1673-1679.

———, 2001, Discrimination between pressure and fluid saturation changes from time-lapse seismic data: Geophysics, **66**, 836-844.

———, 2002, Uncertainties in quantitative time-lapse seismic analysis: Geophysical Prospecting, **50**, 527-538.

Landrø, M., and R. Janssen, 2002, Estimating compaction and velocity changes from time-lapse near and far offset stacks: 64th Meeting, EAGE, Expanded Abstracts, P036.

Landrø, M., O.A. Solheim, E. Hilde, B.O. Ekren, and L.K. Strønen, 1999, The Gullfaks 4D seismic study, Petroleum Geoscience, **5**, 213-226.

Landrø, M., and J. Stammeijer, 2004, Quantitative estimation of compaction and velocity changes using 4D impedance and traveltime changes: Geophysics, **69**, 949-957.

Landrø, M., H.H. Veire, K. Duffaut, and N.F. Najjar, 2003, Discrimination between pressure and fluid saturation changes from marine multicomponent time-lapse seismic data: Geophysics, **68**, 1592-1599.

Le Rousseau, J.H., and M.V. De Hoop, 2001, Scalar generalized-screen algorithms in transversely isotropic media with a vertical symmetry axis: Geophysics, **66**, 1538-1550.

Love, A.E.H., 1944, A treatise on the mathematical theory of elasticity: Dover.

Maury, V.M.R., J.R. Grasso, and G. Wittlinger, 1992, Monitoring of subsidence and induced seismicity in the Larq gas field (France): the consequences on gas production and field operation: Engineering Geology, **32**, 123-135.

Mavko, G., T. Mukerji, and J. Dvorkin, 1998, The rock physics handbook: Cambridge.

Mildren, S.D., R.R. Hillis, and J. Kaldi, 2002, Calibrating predictions of fault seal reactivation in the Timor Sea: Australian Petroleum Production and Exploration Association Journal, **42**, 187-202.

Mindlin, R.D., 1949, Compliance of elastic bodies in contact: Journal of Applied Mechanics, **16**, 259-268.

Minkoff, S.E., C.M. Stonez, S. Bryant, and M. Peszynska, 2004, Coupled geomechanics and flow simulation for time-lapse seismic modeling: Geophysics, **69**, 200-211.

Morton, R.A., C.B. Julie, and A.B. John, 2006, Evidence of regional subsidence and associated interior wetland loss induced by hydrocarbon production, Gulf Coast region, USA: Environmental Geology, **50**, 261-274.

Murphy, W.F., A. Reischer, and K. Hsu, 1993, Modulus decomposition of compressional and shear velocities in sand bodies: Geophysics, **58**, 227-239.

Nur, A., 1992, Critical porosity and the seismic velocities in rocks: EOS, Transactions. American Geophysical Union, **73**, 43-66.

Nur, A., G. Mavko, J. Dvorkin, and D. Gal, 1995, Critical porosity: The key to relating physical properties to porosity in rocks: 65th Annual International Meeting, SEG, Expanded Abstracts, 878-881.

———, 1998, Critical porosity: A key to relating physical properties to porosity in rocks: The Leading Edge, **17**, 357-362.

Pattillo, P.D., T.G. Kristiansen, G.V. Sund, and R.M. Kjelstadli, 1998, Reservoir compaction and seafloor subsidence at Valhall: SPE 47274.

Rafavich, F., C.H.St.C. Kendall, and T.P. Todd, 1984, The relationship between acoustic properties and the petrographic character of carbonate rocks: Geophysics, **49**, 1622-1636.

Raymer, L.L., E.R. Hunt, and J.S. Gardner, 1980, An improved sonic transit time to porosity transform: 21st Annual Logging Symposium, SPWLA, Paper P.

Reuss, A., 1929, Berechnung der fließgrenze von mischkristallen auf grund der plastizitätsbedingung für einkristalle: Zeitschrift für angewandte mathematik und mechanik, **9**, 49-58.

Revil, A., and L.M. Cathles, 2002, Fluid transport by solitary waves along growing faults - A field example from the South Eugene Island Basin, Gulf of Mexico: Earth and Planetary Science Letters, **202**, 321-335.

Reynolds, S.D., R.R. Hillis, and G.W. O'Brien, 2003, Stress analysis, fault reactivation and fault seal integrity in the Bight Basin. *In*: O'Brien, G.W., E. Paraschivoiu, J.E. Hibburt, and J.F. Drexel (Eds.), in prep., The petroleum geology of South Australia, Volume 5: Great Australian Bight. South Australia. Department of Primary Industries and Resources. Petroleum Geology of South Australia Series, Ch. 9.

Rhett, D.W., 1998, Ekofisk Revisited: A new model of Ekofisk reservoir geomechanical behavior: SPE 47273.

Røgen, B., I.L. Fabricius, P. Japsen, C. Høier, G. Mavko, and J.M. Pedersen, 2005, Ultrasonic velocities of North Sea chalk samples: influence of porosity, fluid content and texture, Geophysical Prospecting, **53**, 481-496.

Røste, T., A. Stovas, and M. Landrø, 2005, Estimation of layer thickness and velocity changes using 4D prestack seismic data: 67th Meeting, EAGE, Expanded Abstracts, C010.

———, 2006, Estimation of layer thickness and velocity changes using 4D prestack seismic data: Geophysics, **71**, S219-S234.

Saunders, M., D. Howe, and J. Kommedal, 2004, Source signature repeatability and source array directivity - Measurements from the Valhall 4D survey: 74th Annual International Meeting, SEG, Expanded Abstracts, 37-40.

Sheriff, R.E., and L.P. Geldart, 1995, Exploration seismology: Cambridge.

Smith, G.C., and P.M. Gidlow, 1987, Weighted stacking for rock property estimation and detection of gas: Geophysical Prospecting, **35**, 993-1014.

Stewart, R.R., P.D. Huddleston, and T.K. Kan, 1984, Seismic versus sonic velocities: A vertical seismic profiling study: Geophysics, **49**, 1153-1168.

Stovas, A., M. Landrø, and B. Arntsen, 2003, Use of PP and PS time-lapse stacks for fluid-pressure discrimination: 65th Annual Conference and Exhibition, EAGE, Extended Abstracts, A-23.

Sylte, J.E., L. Thomas, D. Rhett, D. Bruning, and N. Nagel, 1999, Water induced compaction in the Ekofisk Field: SPE 56426.

Thomsen, L., 1986, Weak elastic anisotropy: Geophysics, **51**, 1954-1966.

Timoshenko, S.P., and J.N. Goodier, 1934, Theory of elasticity: McGraw-Hill.

———, 1951, Theory of elasticity: McGraw-Hill.

Tosaya, C., and A. Nur, 1982, Effects of diagenesis and clays on compressional velocities in rocks: Geophysical Research Letters, **9**, 5-8.

Tura, A., T. Barker, P. Cattermole, C. Collins, J. Davis, P. Hatchell, K. Koster, P. Schutjens, and P. Wills, 2005, Monitoring primary depletion reservoirs using amplitudes and time shifts from high-repeat seismic surveys: The Leading Edge, **24**, 1214-1221.

Tura, A., and D.E. Lumley, 1998, Subsurface fluid-flow properties form time-lapse elastic-wave reflection data: 43rd Annual Meeting, SPIE, Proceedings, 125-138.

———, 1999a, Estimating pressure and saturation changes from time-lapse AVO data: 61st Annual Conference and Exhibition, EAGE, Extended Abstracts, paper 1-38.

———, 1999b, Estimating pressure and saturation changes from time-lapse AVO data: 69th Annual International Meeting, SEG, Expanded Abstracts, 1655-1658.

Vesnaver, A.L., F. Accaino, G. Bohm, G. Madrussani, J. Pajchel, G. Rossi, and G.D. Moro, 2003, Time-lapse tomography: Geophysics, **68**, 815-823.

Vidal, S., P. Longuemare, F. Huguet, and P. Mechler, 2002, Reservoir parameters quantification from seismic monitoring integrating geomechanics: Oil & Gas Science and Technology, **57**, 555-568.

Vikram, S., and A. Settari, 2005, Coupled geomechanical and flow modeling of compacting reservoirs: The Leading Edge, **24**, 1284-1286.

Voigt, W., 1910, Lehrbuch der kristallphysik: Teubner.

Wang, Z., and A. Nur, 1992, Seismic and acoustic velocities in reservoir rocks, Volume 2: SEG, Geophysics Reprint Series 10.

Watts, G.F.T., D. Jizba, D.E. Gawith, and P. Gutteridge, 1996, Reservoir monitoring of the Magnus field through 4D time-lapse seismic analysis: Petroleum Geoscience, **57**, 361-372.

White, W.A., and R.A. Morton, 1997, Wetland losses related to fault movement and hydrocarbon production, southeastern Texas coast: Journal of Coastal Research, **13**, 1305-1320.

Wood, A.B., 1941, A textbook of sound: MacMillan.

Wyllie, M.R.J., A.R. Gregory, and L.W. Gardner, 1956, Elastic wave velocities in heterogeneous and porous media: Geophysics, **21**, 41-70.

Yerneni, S., D. Bhardwaj, and S. Chakraborty, 2002, Finite difference forward modeling for complex geological models: 72nd Annual International Meeting, SEG, Expanded Abstracts, 1987-1990.

Yilmaz, O., 1987, Seismic data processing: SEG.

Yin, Y., 2002, Constraining Ekofisk geomodels using 4D seismic modeling: Diploma Thesis, NTNU, Trondheim.

Yongyi, L., 2004, Anisotropic parameter prediction in clastic rocks: CSEG National Convention.

Zoback, M.D., and J.C. Zinke, 2002, Production-induced normal faulting in the Valhall and Ekofisk oil fields: Pure and Applied Geophysics, **159**, 403-420.